Università degli Studi di Milano
Facoltà di Scienze Matematiche, Fisiche e Naturali

Dottorato di Ricerca in Fisica

Energy reconstruction and calibration algorithms for the ATLAS electromagnetic calorimeter

Coordinatore: Prof. Rodolfo Bonifacio

Tutore: Prof. Luciano Mandelli

Tesi di Dottorato di

Marco Delmastro

XV Ciclo

Anno Accademico 2001-2002

Energy reconstruction and calibration algorithms for the ATLAS electromagnetic calorimeter

by

Marco Delmastro

A Thesis Submitted in Fulfillment
of the Requirements for the Degree of

"Dottore di Ricerca"

(Doctor of Philosophy)
in the Department of Nuclear and Subnuclear Physics
University of Milano

This thesis has been defended
on January 24$^{\text{th}}$ 2003 in Milano
in front of the jury composed by:

Prof. L.Mandelli. Supervisor.
Dipartimento di Fisica, Università degli Studi di Milano

Prof. S. Centro. Referee.
Dipartimento di Fisica, Università degli Studi di Padova

Prof. W. E. Cleland, Third Member.
Department of Physics and Astronomy, University of Pittsburgh

Introduction

ATLAS (*A Toroidal LHC ApparatuS*) [2] is a general purpose detector presently under construction. It will operate on the proton–proton collider, the Large Hadron Collider (LHC) [1], that will be installed in the LEP tunnel at CERN. LHC will provide a 14 TeV center of mass energy collision at a luminosity up to $\mathcal{L} \simeq 10^{34}$ cm^{-2}s^{-1}, with a bunch crossing frequency of 40 MHz.

ATLAS is a multi–purpose detector, with a large discovery potential for new physics such as Higgs bosons and Supersymmetric particles (SUSY) [5]. In most of these channels a crucial role in energy and position reconstruction of electrons and photons is played by the electromagnetic calorimeter (EMC). This is the case for example in the decay channels of the Standard Model (SM) Higgs boson $H \rightarrow \gamma\gamma$ and $H \rightarrow e^+e^-e^+e^-$.

The LHC experimental framework will impose severe constraints on the detectors in term of spatial coverage, response speed, radiation tolerance, background rejection capability, noise handing and time stability. The ATLAS EMC is a lead–liquid Argon (LAr) sampling calorimeter with an *accordion* geometry: this particular structure guarantees the full azimuthal coverage, while the LAr used as ionizing medium is intrinsically radiation tolerant and has a sensitivity that does not degrade in time. The system is provided with a fast readout that can cope with the LHC rate, and has been optimized to minimize the noise contributions coming from both electronics and pile–up. Each readout cell of the EMC can be calibrated with an embedded electronic system, that will be complemented at the LHC with a physics–based procedure.

It has been shown [3] that a relevant contribution to the performances of the EMC comes from the precision achievable by the calibration procedure and the signal reconstruction technique. The work of this thesis has been devoted to the study, development and optimization of the algorithms of *energy reconstruction* and *calibration* of the EMC.

A deep study of the electrical characteristics of the detector and of the signals formation and propagation is conduced: an electrical model of the detector is developed and analyzed through simulations; a hardware model (*mock–up*) of a group of the EMC readout cells has been built, allowing the direct collection and properties study of the signals emerging from the EMC cells.

We study the existing multiple–sampled signal reconstruction strategy, namely the one used for the energy reconstruction of the EMC barrel prototype module data of 2000 test–beam. By comparing the results with the *mock–up* observations and the model simulations, we show the need of an improvement in order to reach the needed performances in terms

of energy resolution and response uniformity.

The *optimal filtering* (OF) technique is studied and implemented, taking into account the differences between the ionization and calibration waveforms as emerging from the *mock–up* analysis. A *new calibration procedure* that does not need any informations from the ionization signals as collected from the physics events in the EMC is proposed; its feasibility is investigated and discussed.

An *energy weighting technique* is proposed to improve the EMC resolution and uniformity by recovering the energy lost by the developing electromagnetic shower in the upstream material and because of longitudinal leakage.

The signal reconstruction and calibration procedures, together with the energy weighting technique, are extensively applied to the EMC production modules test–beam data of 2001 and 2002. Results, future improvements and the application to the full ATLAS experimental framework are discussed.

Outline of the work

The LHC operating conditions and the ATLAS detector characteristics are reviewed in Chapter 1. Therein a short summary of the ATLAS physics program is given. The physics requirements on the EMC performances are discussed, mainly as driven by the Standard Model Higgs boson search. The EMC characteristics and operating features are discussed in Chapter 2.

In Chapter 3 we describe the results from the analysis of the ionization and calibration signal formation and propagation through the EMC cells and readout chain. The multiple–sampled signal reconstruction techniques are discussed in Chapter 4, together with the connected electronics calibration strategies. The new calibration and signal reconstruction procedure is developed and discussed in Chapter 5. The energy weighting technique is exposed in Chapter 6. Results from extensive test–beam data analysis are presented and discussed in Chapter 7.

Contents

List of Figures

List of Tables

Chapter 1

The ATLAS detector at the LHC

1.1 The Large Hadron Collider

The Large Hadron Collider (LHC) [1] is presently under construction, and will start operation in 2007. It will be installed at CERN (European Center for the Nuclear Research, Geneva, Switzerland) in the existing 27 km tunnel formerly used for LEP (Large Electron–Positron collider, Figure 1.1). LHC will provide 14 TeV center–of–mass energy proton–proton (pp) collisions, at a luminosity up to 10^{34} cm^{-2}s^{-1} with a bunch crossing frequency of 40 MHz. LHC will be also capable to produce heavy ions (e.g. Pb–Pb) collisions.

Four large–scale experiments will operate at LHC. ATLAS and CMS are general–purpose experiments, with a wide physics program; LHCb is devoted to the physics of B-hadrons and to the study of the CP violation; ALICE is a dedicated heavy–ions experiment, that will study the behavior of the nuclear matter at very high energies and densities.

The LHC physics program is broad and ambitious. The strong physics motivations that support the building of such an unprecedented collider machine can be briefly summarized as follows:

- Search for the Standard Model (SM) Higgs boson [13], that is predicted to be the responsible of the origin of the particle masses through the mechanism of spontaneous breaking of the electro–weak symmetry.
- Look for the physics beyond the SM, that for several reasons cannot be expected to be the ultimate theory of particles interactions [14, 15, 16].
- Perform precision measurements of the properties of the known particles, in order both to refine the present values and to search signals of new physics in unexpected deviations from the SM predictions [17].

1.1.1 Proton–proton collisions characteristics

Two operation phases are foreseen for LHC: in the first years the accelerator will provide a instantaneous luminosity of $\mathcal{L} \simeq 10^{33}$ cm^{-2}s^{-1} ("low" luminosity phase); the nominal

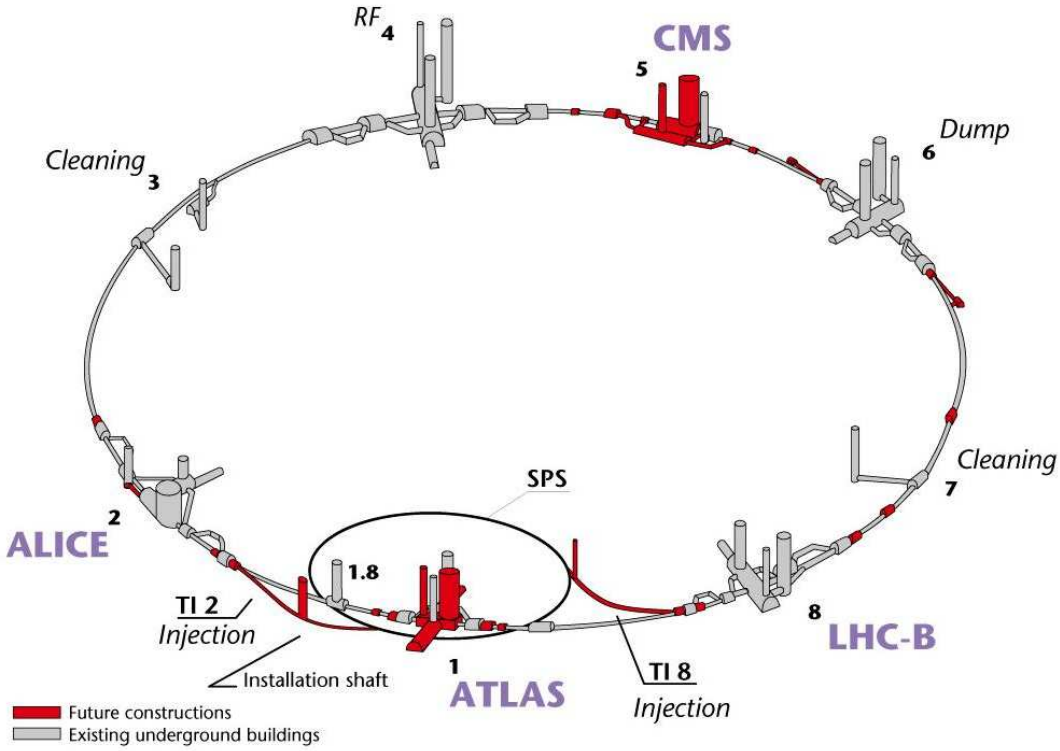

Figure 1.1: Layout of CERN LEP tunnel, including the future LHC infrastructures.

LHC parameter	nominal value
beam energy	7 TeV
beam energy at injection	450 GeV
nominal luminosity	10^{34} cm^{-2}cm^{-1}
luminosity life time	10 hours
beam life time	22 hours
number of bunches	2835
proton (p) per bunch	10^{11}
bunch spacing	25 ns (7.5 m)
p current intensity	0.54 A
beam total energy	334 MJ
energy loss per tour	6.7 keV

Table 1.1: Main LHC parameters

luminosity $\mathcal{L} \simeq 10^{34}$ cm^{-2}s^{-1} will be reached later ("high" luminosity phase). The nominal pp luminosity and center–of–mass will allow searches for new particles up to masses of ~ 5 TeV. Details on the LHC machine parameters can be found in Table 1.1 [1].

In one year (1 "year" run time $\simeq 10^7$ s) of running at high luminosity LHC will provide an integrated luminosity of:

$$L = \int_{10^7\text{s}} \mathcal{L}dt \simeq 100 \text{ fb}^{-1} \tag{1.1}$$

The total inelastic pp cross–section at $\sqrt{s} = 14$ TeV is $\sigma_{pp}^{\text{tot}} \sim 80$ mb. The LHC event rate R at high luminosity is then expected to be:

$$R = \sigma_{pp}^{\text{tot}} \times \mathcal{L} = 80\text{mb} \times 10^{34} \text{ cm}^{-2}\text{s}^{-1} \simeq 10^9\text{s}^{-1} \tag{1.2}$$

These events belong to two different classes:

- *"minimum bias events"*: they comes from long–range interactions of the incoming protons, in which the momentum transfer is small ("soft" collisions). They represent the majority of the pp collisions, their effective total cross section being $\sigma_{\text{m.b.}}^{\text{tot}} \sim 70$ mb. The study of these interactions is not foreseen in the LHC experiments physics programs. The final state products of these interactions have small transverse momentum relative to the beam line ($\langle p_T \rangle \simeq 500$ MeV): most of them escape down the beam pipe. The produced particles with p_T high enough to enter the active region of the detectors give rise to the *pile–up* phenomenon (Section 1.1.2).

- *"hard scattering events"*: they come from short–range interactions of the incoming protons. In these cases the head–on collisions between the partons constituting the protons are characterized by an high momentum transfer. Particles in the final state are produced at high angles with respect to the beam line (high p_T), and massive particles can be created. These are the physics events that will be recorded and studied; they are "rare" with respect to the soft interactions [5].

1.1.2 LHC experimental challenges

The LHC experimental framework will be highly demanding. The LHC detectors have to face severe constrains, most of them related to the machine bunch crossing frequency (response speed), luminosity (*pile–up*, radiation level), and to the physics of the pp collisions (background rejection capability).

Pile–up

The LHC protons are grouped in bunches of $\sim 10^{11}$, colliding at each interaction point every 25 ns. According to the interaction rate at high luminosity (equation 1.2), on average 25 *minimum bias* events (soft interactions) will occur simultaneously every bunch crossing.

These interactions will produce $\sim$ 700 charged particles in the detectors pseudorapidity[1] region $|\eta| < 2.5$. Each time a high p_T event is produced, $\sim$25 additional soft events will overlap to the interesting one (*pile–up*).

The *pile–up* is one of the most difficult challenges for the LHC detectors design. In order to minimize the *pile–up* impact on the physics events detection, the LHC sub-detector use different techniques. In general, their response must be fast, in order to avoid to integrate over more that one or two bunch crossings. This implies also a fast readout electronics. In addition, a fine granularity would minimize the probability that the *pile–up* particles cross the same region of the detector as the interesting object.

In case the sub–detectors response cannot be sped up to 25–50 ns, such in the case of the ATLAS LAr EMC, different technique of signal shaping and reconstruction has been developed, in order to be able to treat the *pile–up* events as a kind of noise that superimposes to the interesting physics signal (see Chapter 2 and Appendix B).

Radiation levels

The high flux of particles coming from the *pp* collisions represents an unavoidable source of radiation for the LHC detectors, that for this reason must be radiation resistant. The radiation level to stand will be different according to the sub–detector position with respect to the interaction point As an example, in the forward calorimeters the particles flux, integrated over 10 years of operations, will amount up to 10^{17} neutrons cm^{-2} and up to 10^7 Gy of absorbed energy.

The ATLAS electromagnetic calorimeter, to which this work is dedicated, will receive less than 10^{13} neutrons cm^{-2} and $\sim$200 Gy in 10 years at high luminosity in the worst place of the electronics [3].

QCD background

Being LHC an hadronic collider, the rate of high p_T events is dominated by QCD jets production, that is a strong process and has a large cross section. On the other hand, the most interesting physics processes are rare: indeed there is no hope to detect a rare object (e.g. the SM Higgs boson) decay into jets. Because of this reason, the main LHC physics searches will be conducted looking for rare decay channels [5]. The detectors performances must be optimized both for the background rejection and for dealing with such rare–channels detection.

1.2 The ATLAS Detector

ATLAS [2] (*A Toroidal LHC ApparatuS*, Figure 1.2) is one of the two LHC general–purpose detector presently under construction. It is designed to be a typical collider multi–purpose detector, with a large discovery potential for new physics such as Higgs bosons and SuperSymmetric particles (SUSY) [5].

[1] The pseudorapidity is defined as $\eta = -\log(\tan(\frac{\theta}{2}))$, where θ is the polar angle referred to beam direction at the detector interaction point.

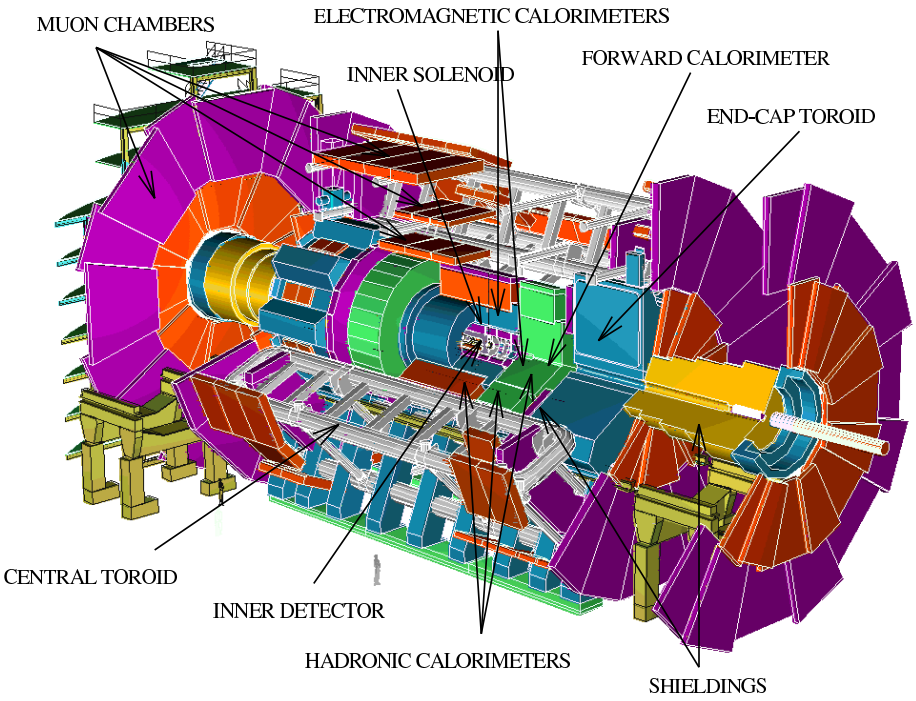

Figure 1.2: Tridimensional cut–away of the full ATLAS detector.

Among the LHC general–purpose experiments, different design philosophies have been adopted by the collaborations. The ATLAS detector uses a very large air–core toroid for the muon spectrometer. The electromagnetic calorimetry is based on the lead–liquid Argon sampling technology. The hadronic calorimetry uses an iron–scintillator detector in the barrel, and again the liquid–Argon technology in the end–caps. Integrated in the barrel electromagnetic cryostat, a superconducting coil solenoid provides a 2 T magnetic field for the inner detector. The inner tracking system is based on semiconductor detectors in the innermost part, and on straw tubes in the outer one. The philosophy that lyes underneath the ATLAS sub–detectors design can be summarized as follows:

- very good electromagnetic calorimetry, for e and γ identification and measurement; maximal ermeticity of the full calorimetry system for very accurate missing transverse momentum p_T^{miss} measurements and jets identification;

- efficient tracking system at high luminosity, for high p_T leptons measurements, and full event reconstruction capability at low luminosity.

- high–precision muon spectrometer, with the capability to perform accurate measures at the highest luminosity in stand–alone mode (i.e. without seeds from the inner tracking system).

1.2.1 Inner Detector

The Inner Detector (ID) system [6] covers the acceptance range $|\eta| < 2.5$, matching that of the rest of the ATLAS sub–detectors for precision physics [5]. The ID, thanks to the tracks bending provided by the solenoid magnet (Section 1.2.4), is responsible to measure the momentum of the charged particles coming from the interaction point. Together with the electromagnetic calorimeter, it provides the identification of electrons and photons. At low luminosity it allows the secondary vertex reconstruction in case of decay of τ leptons or b–flavored hadrons.

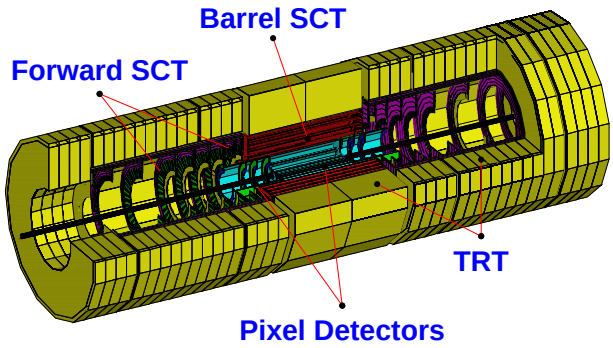

Figure 1.3: Tridimensional cut–away view of the ATLAS inner detector system.

The ATLAS ID tracking system (Figure 1.3) is composed of three different sub–detectors layers:

- **The Pixel Detector** (PD) [7] is located in a range between 4 and 22 cm from the beam line. It is based on the detection of the charge deposited by the crossing ionizing particle in a finely segmented silicon detector. The PD is composed of 3 different layers, located at increasing radii and designed to give 3 space points per track. The first pixel layer ("b–layer"), located at 4 cm from the interaction point, gives a substantial contribution to the secondary vertex measurements, and is designed to be replaceable due to the very hostile environment. At $|\eta < 0.25|$ the pixels transverse impact parameter resolution can be parametrized as $\sigma(d_0) = (11 + 60/p_T)\,\mu$m when the dedicated b–physics layer is present, the longitudinal impact parameter resolution as $\sigma(z_0) = (70 + 100/p_T)\,\mu$m [7].

- **The SemiConductor Tracker** (SCT) system follows the PD up to 56 cm from the beam line, and is again based on the silicon technique. The barrel SCT uses 4 layers of micro-strips to provide precision points in space.

- **the Transition Radiation Tracker** (TRT) is based on the use of straw tubes that can operate at very high rate. The use of Xe gas provides the TRT with electrons identification capability, that is exploited by the detection of the transition–radiation photons coming from polypropylene radiators located between the straws.

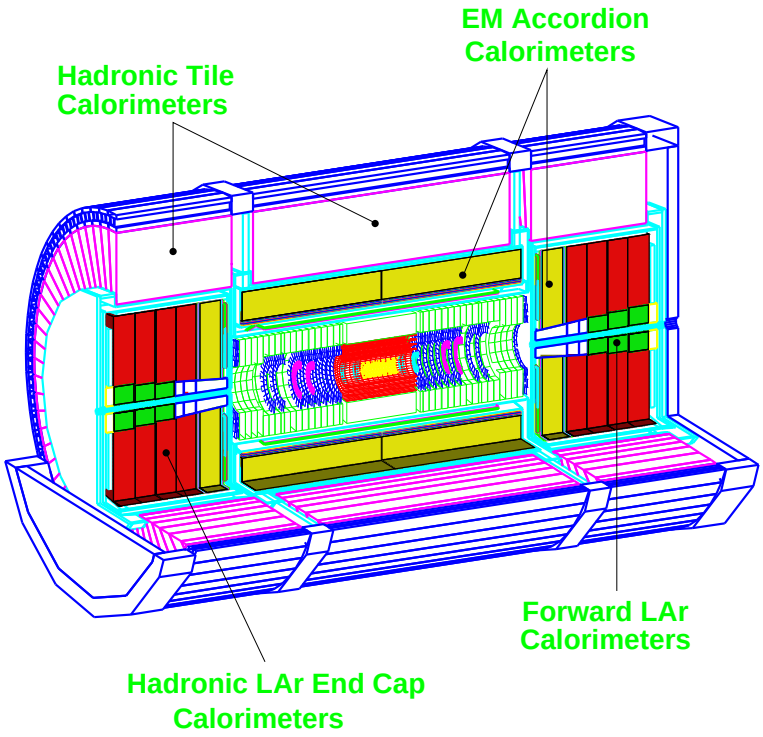

Figure 1.4: Tridimensional cut–away view of the ATLAS calorimetry system.

1.2.2 Calorimetry

A crucial role in the LHC experiments will be played by the calorimeters. They will be responsible to measure photons, electrons, isolated hadrons and jets, as well as the missing transverse energy. Furthermore, the calorimetric informations will be used by the first level trigger to discriminate if an occurring physics event is interesting or is to be rejected (Section 1.2.5). In association with the ID, the calorimetry system will be used to identify electrons and photons.

Because of the LHC operating conditions, fast detectors response and fine granularity are required to minimize the *pile–up* effect, together with high radiation resistance. Using different techniques the ATLAS calorimeters cover the range $|\eta < 5|$ (Figure 1.4). The coverage and granularity of the ATLAS calorimeters are listed in Table 1.2.

The **electromagnetic calorimeter** (EMC) is a lead–liquid Argon (LAr) sampling calorimeter [3], consisting in one barrel and two end–caps detectors covering the region $|\eta| < 3.2$. Being the main subject of this work, Chapter 2 is dedicated to a detailed discussion of its main characteristics.

The **tile hadronic calorimeter** (TILECAL) [8] consists of one barrel and two extended–barrel cylinders that cover the region $|\eta| < 1.7$. The detector is based on a sampling technique with plastic scintillator planes ("tiles"). The tiles are placed in planes perpendicular to the beam axis, and embedded in an absorbing iron matrix; the scintillation signals are read through wavelength shifting optical fibers. The TILECAL is

calorimetry system	η coverage	$\Delta\eta \times \Delta\phi$ granularity	sampling
Presampler	$\|\eta\| < 1.8$	0.025×0.1	
electromagnetic barrel	$\|\eta\| < 1.4$	0.003×0.1	(S1)
		0.025×0.025	(S2)
		0.05×0.035	(S3)
electromagnetic end-caps	$1.4 < \|\eta\| < 3.2$	as in the barrel for $\|\eta < 1.8\|$	
hadronic barrels	$\|\eta\| < 1.7$	0.01×0.1	(S1, S2)
		0.02×0.1	(S3)
hadronic end-caps	$1.5 < \|\eta\| < 2.5$	0.01×0.1	(S1, S2, S3)
	$2.5 < \|\eta\| < 3.2$	0.02×0.2	(S1, S2, S3)
forward calorimeter	$3.2 < \|\eta\| < 4.9$	∼0.02×0.2	

Table 1.2: ATLAS calorimeters coverage and granularity (see Chapter 2 for details on the EMC structure.)

longitudinally segmented in three layers. The relative energy resolution is required to be $\frac{\sigma_E}{E} = \frac{50\%}{\sqrt{E(\text{GeV})}} \oplus 3\%$, mainly driven by the jets measurements accuracy.

Two **hadronic end–caps calorimeters** (HEC) complement the hadronic calorimetry in the region $1.5 < |\eta| < 3.2$. They are based on the LAr technology because of the high radiation level to be stand [3].

The HEC's are housed in the same electromagnetic end–caps cryostats (see Chapter 2) with the **forward calorimeters** (FCAL). These detectors cover the region $3.1 < |\eta| < 4.9$, thus assuring a continuity of coverage even in a region where the radiation level is really high. For this reason they are again based on the LAr technology [3].

1.2.3 Muon spectrometer

The ATLAS detector is equipped with a high–resolution muon spectrometer [9], with momentum measurement and stand–alone triggering capability over a wide range of transverse momentum, pseudorapidity and azimuthal angle. The magnetic deflection of the muon tracks is induced by the air–core toroid magnets system (see Section 1.2.4).

The muon spectrometer system is composed by two different types of detectors (Figure 1.5): the **Monitor Drift Tubes** (MDT) perform a precision measurements of the tracks coordinates in the principal direction of the magnetic field over most of the pseudorapidity range; the **Cathode Strips Chambers** (CSC) are used in the first station of the end–cap region and for pseudorapidity $|\eta| > 2$ to sustain the demanding rate and background conditions.

The required muon transverse momentum resolution is $\frac{\Delta p_T}{p_T} \simeq 1\%$ for transverse momentum $p_T > 6$ GeV/c, and $\frac{\Delta p_T}{p_T} \simeq 10\%$ for transverse momentum $p_T > 1$ TeV/c. The expected muon identification efficiency is 90% at $p_T > 6$ GeV/c.

The muon spectrometer is also equipped with trigger chambers (**Resistive Plate Chambers** (RPC) in the barrel region $|\eta| < 1.4$, and **Thin Gap Chambers** (TGC) in

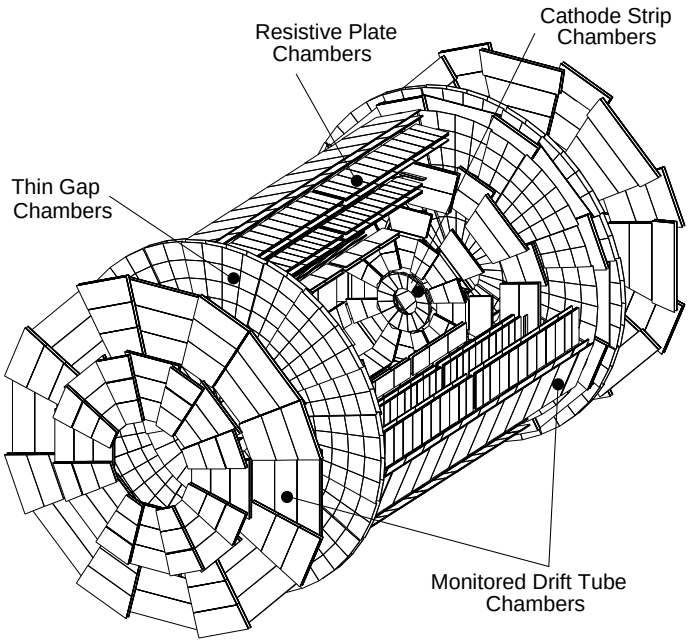

Figure 1.5: Tridimensional cut–away view of the ATLAS muon spectrometer system.

the end–cap regions), used as threshold detectors for the bunch crossing identification. These chambers have a time resolution better than the 25 ns LHC bunch spacing, and are used to trigger the acquisition of events with a definite p_T cut–off.

1.2.4 Magnets system

The ATLAS detector system is provided with two different kind of magnetic fields [10] (Figure 1.6).

A central superconducting–coil solenoid provides a 2 T field to the ID in the region $|\eta| < 1.5$. It bends the charged particles that cross the tracking system, allowing the momentum measure. The central solenoid is housed between the ID and the EMC, in the EM barrel cryostat. It represents indeed an additional amount of material in front of the EMC, that can in principle degrade the EMC performance (see Chapter 2 and 6).

The muon spectrometer is equipped with a system of three large superconducting air–core toroids (one barrel and two end–caps, Figure 1.6), that produce the magnetic deflection of the muons tracks. The large barrel toroid ($\sim$20 m diameter), consisting in eight coils that surround the hadronic calorimeter, provides the magnetic bending in the region $|\eta| < 1$. In the $1.4 < |\eta| < 2.7$ region the muon tracks are bent by the two smaller end–caps toroid, while in the $1 < |\eta| < 1.4$ range the magnetic bending is assured by a combination of the barrel and end–caps toroids fields.

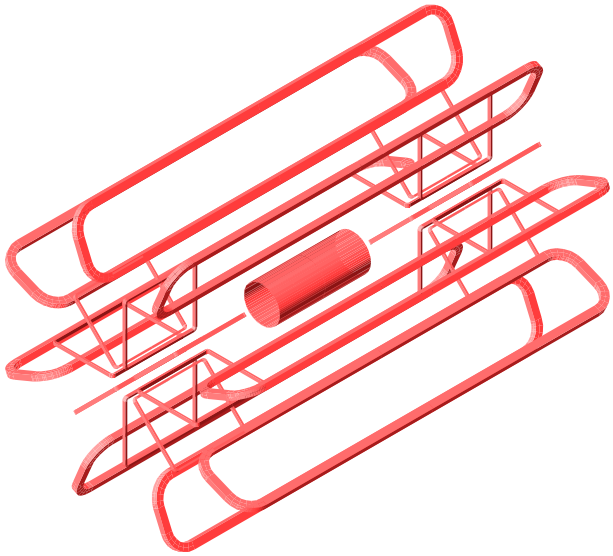

Figure 1.6: Tridimensional pictorial view of the ATLAS magnets coils system. The central cylindrical coil of the superconducting solenoid is visible, surrounded by the air–core barrel and end–caps toroids coils.

1.2.5 Trigger and DAQ

The LHC experiments need a trigger system able to reduce the huge amount of data coming from the detectors because of the high interaction rate. Only 1 event over $\sim 10^7$ is to be selected and recorded for the off–line analysis. The ATLAS trigger system is organized around three decision levels, and on the concept of the "**Region Of Interest**" (ROI).

Since it is impossible to take a decision about the event quality in the 25 ns bunch spacing, all the data from the detectors are stored in pipeline memories, while the information from the calorimetry system and from the muon spectrometer are used to make a first selection (**Level 1 trigger** (LV1) [11], Figure 1.7 left), and, in case the event seems promising, to define in which regions of the detector the event has left its main signatures (ROI, Figure 1.7 right). The LV1 computation is performed by dedicated hardware processors, and is expected to reduce the event rate from 40 MHz to 100 kHz. The latency time of the LV1 is $\sim$2 μs.

The **Level 2 trigger** (LV2)[12] refines *in the ROI's only* the raw analysis of the detector informations performed the LV1. The latency time of the LV2 is $\sim$10 ms; it is expected to reduce the event rate from 100 kHz to 1 kHz. Finally, the events selected by the LV2 are analysed by the **Level 3 trigger ("event filter")** (LV3/EF) [12]. It that reconstructs the selected event using the informations coming from the full ATLAS detector, as retrieved from the memory pipelines. The LV3/EF output rate is expected to be between 10 Hz and 100 Hz.

The scheme of the DAQ pipelines architecture along with the event selection stages is illustrated in Figure 1.8.

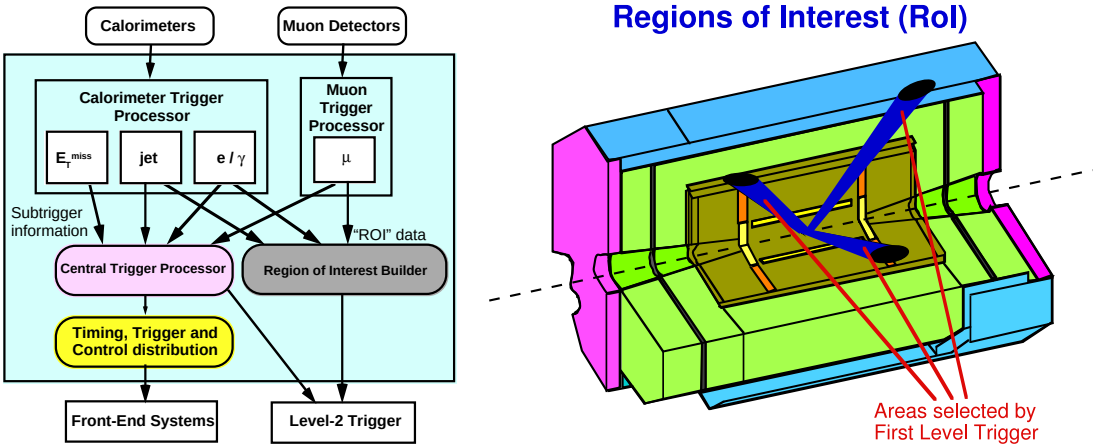

Figure 1.7: Operating principles of the ATLAS Level 1 trigger: informations flow from the ATLAS main sub-detectors (left); "Regions Of Interest" (ROI's) (right);

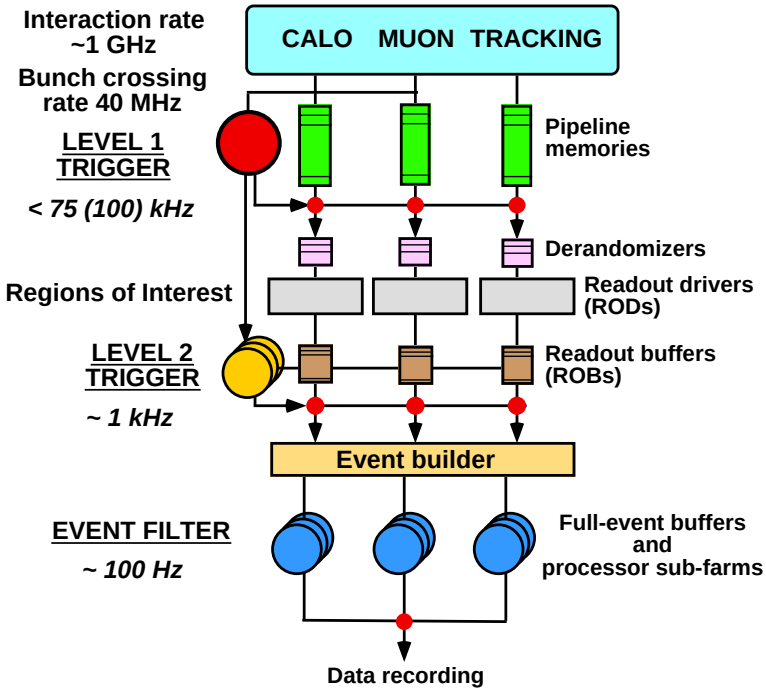

Figure 1.8: Scheme of the ATLAS DAQ pipelines, along with the trigger levels.

1.2.6 A short outline of the ATLAS physics program

The ATLAS experiment has been optimized for the detection of a large variety of physics signatures, accessible at the high luminosity and center–of–mass energy of the LHC pp collisions. We propose here a very short outline of the ATLAS physics program. It is beyond the scope of this work a detailed discussion of the full ATLAS physics potential; an exhaustive documentation of all the relevant ATLAS physics studies can be found in [5].

Being the optimization of the EMC performances the main subject of this work, a summary of the physics requirements on this detector is proposed in Section 2.4, along with a brief discussion of the physics study that will mostly take advantage of the electromagnetic calorimetry informations.

The main goals of the ATLAS physics program follow the LHC construction motivations. The main focus of the experiment is the investigation of the nature of the electro–weak symmetry breaking, and therefore the search for the Higgs bosons. Thanks to the sensibility of the different ATLAS sub–detectors to different decay channels, the Higgs bosons could be discovered over a wide mass range (see Section 2.4 and Figure 2.10).

The complementary aim of the ATLAS experiment is to find signatures of physics beyond the SM. Targets of this search are the particles predicted by SUSY or Technicolor theories, as well as new gauge bosons and composite quarks and leptons up to mass $\sim$5 TeV.

Besides the discovery potential, the ATLAS experiment has also a large capability of performing precision measurements on the SM particles properties (e.g. W mass, t mass, triple gauge coupling). As an example, the error on the W mass is expected to be 0.02 GeV in ATLAS, i.e. better than that achieved in previous experiments ($\sim$0.02 GeV).

An important part of the ATLAS physics program is constituted by the b–physics studies. A proof of direct CP violation can be established thanks to the achievable precision on the $\sin 2\beta$ and $\sin \alpha$ parameters of ± 0.01 and $\pm$ 0.05 respectively.

Chapter 2

The liquid Argon electromagnetic calorimeter

The LHC experimental framework will be highly demanding, imposing severe constraints on the detectors in terms of spatial coverage, response speed, radiation tolerance, background rejection capability, noise handling and time stability. For what concerns the electromagnetic calorimeter (EMC), the ATLAS collaboration has chosen a lead–liquid Argon (LAr) sampling calorimeter with an *accordion* geometry. This geometric feature guarantees a full azimuthal coverage without cracks and dead zones. The LAr used as ionizing medium is intrinsically radiation tolerant. The fast electronic readout can handle the LHC signal rate, and the noise contribution to the total energy, coming both from electronics and from pile–up due to minimum–bias events, is minimized using an optimized bipolar shaper and a digital filtering signal reconstruction technique (Appendix B). The whole system can be calibrated cell by cell with an embedded electronic system, and its sensitivity does not degrade in time.

A detailed description of the ATLAS LAr EMC system is found in [3]. The calorimeter performances has been deeply investigated in [4], their impact on the ATLAS physics program is discussed in [5]. In this chapter the major characteristics of the system are briefly reviewed: a particular attention is given to those directly related to this work.

2.1 General description

The ATLAS EMC is a sampling calorimeter, consisting in a sequence of active layers, in charge of recording the particles signal, and passive layers, that are the major responsibles of the shower developing, and absorb the greater part of the shower energy. In the ATLAS EMC the active medium is LAr, kept at a temperature of ~ 89 K in a cryostat (Figure 2.1), while the passive medium consists in lead absorbers, covered in stainless steel for mechanical reasons. The main properties of the EMC active and passive components are review in Table 2.1 and 2.3.

The LAr gaps between consecutive absorbers are instrumented with electrodes, which are built as sandwiches of three copper planes separated by two kapton insulator layers

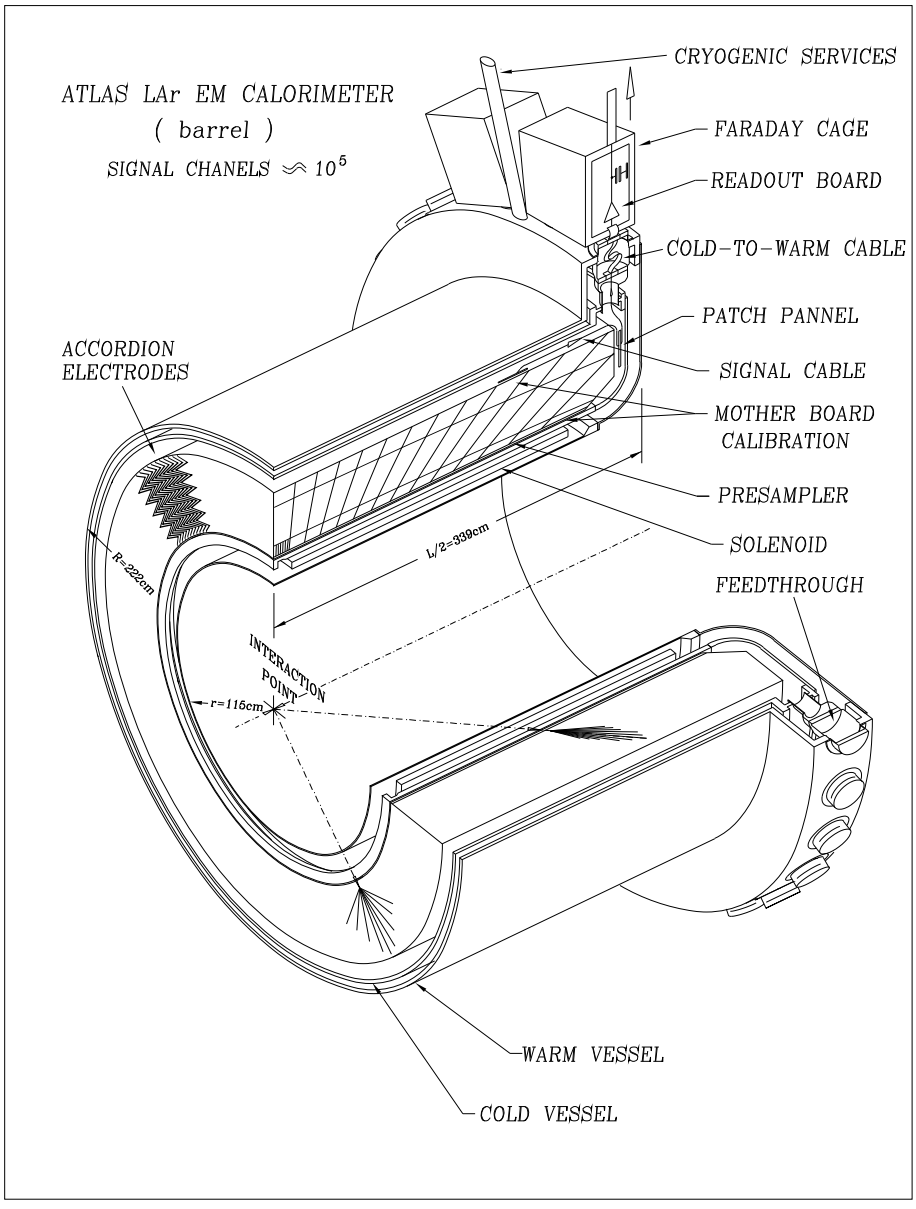

Figure 2.1: View of one half on the EMB cryostat.

		LAr	Pb
atomic number	Z	18	82
atomic weight	A	39.948	207.2
density†	ρ (g cm^{-3})	1.381	11.35
radiation length	$X_0 \simeq 180\frac{A}{Z^2}$ (g cm^{-2})	19.55	6.37
radiation lento	X_0 (cm)	14.2	0.56
Moliere radius	$R_M \simeq 7\frac{A}{Z}$ (g cm^{-2})	13.9	17.7
Moliere radius	R_M (cm)	10.1	1.55
Critical energy	$E_c \simeq \frac{560}{Z}$ (MeV)	30.5	6.82

Table 2.1: Main physical properties of the ATLAS EMC sampling calorimeter components (†LAr density at $T = 89.3$ K).

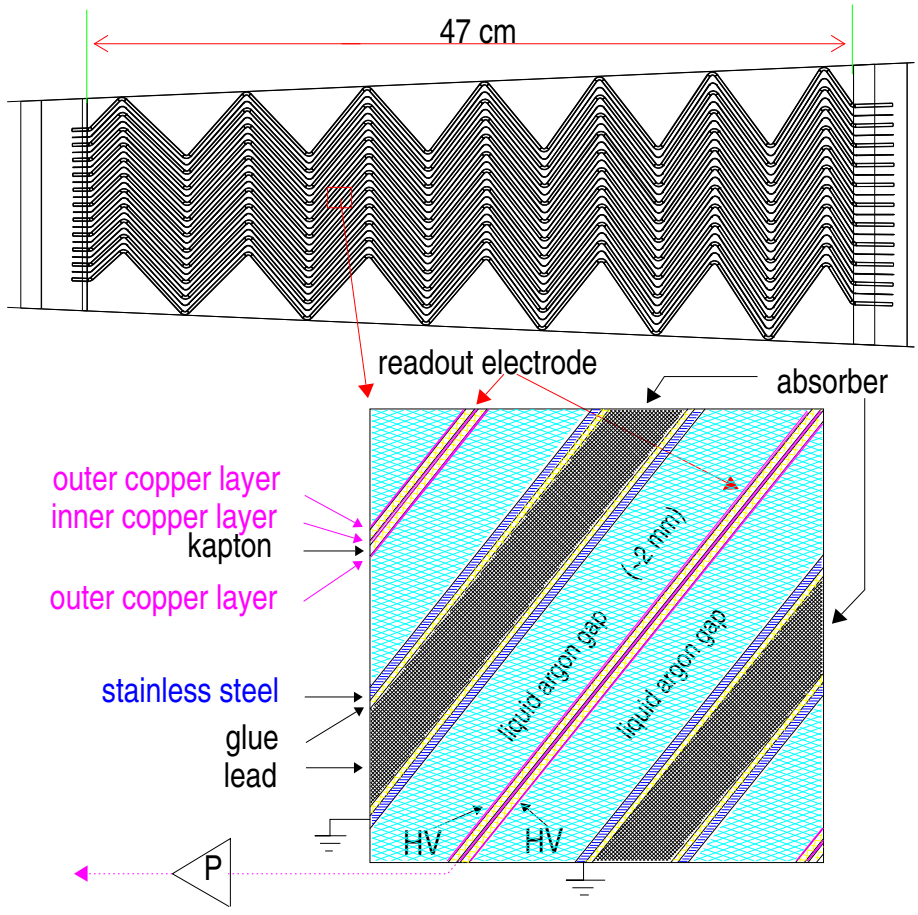

Figure 2.2: Detailed view of a EMB LAr gap section.

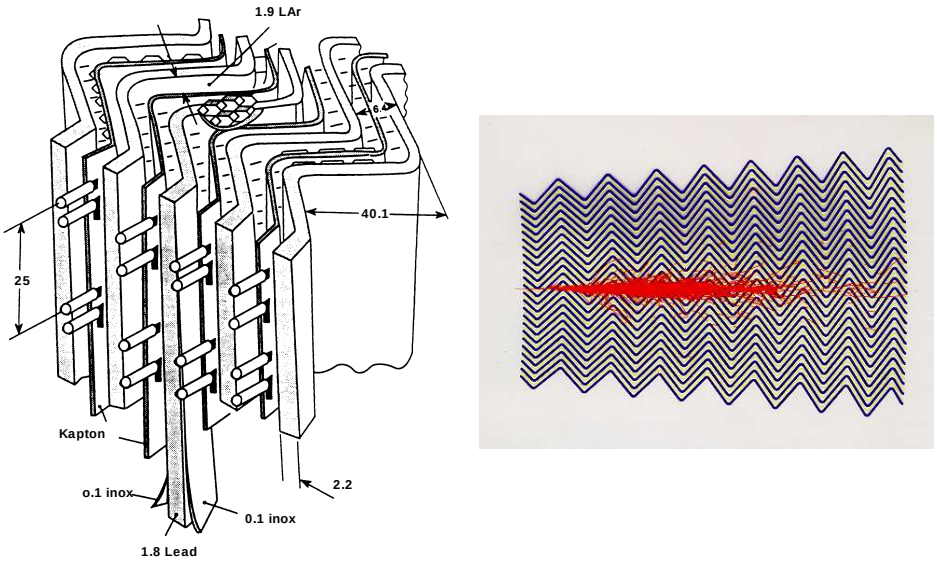

Figure 2.3: Sketch of the ATLAS LAr electromagnetic calorimeter *accordion* structure (left); GEANT simulation of an electromagnetic shower developing in the EMC.

(Figure 2.2). The two external copper planes distribute the high voltage (HV) across the LAr gap, thus forcing the drift of electrons and ions produced by the ionizing shower particles; the electrode inner plane records the ionization current by capacitive coupling. The absorbers provide the ground reference both for the HV distribution and for the ionization current. The electrodes are kept in place by means of honeycomb spacers. Both electrodes and absorbers have an *accordion* geometry (Fig. 2.3, [22]): the *accordion* shape makes the detector continuous, offering a full azimuthal acceptance $0 < \phi < 2\pi$ without dead zones. The EMC pseudorapidity coverage is $|\eta| < 3.2$ (see Section 2.2 for details). The region $|\eta| < 2.5$ is designed to be used for precision physics measurements [5].

The EMC *sampling frequency* f_{samp} computes how many times the developing shower is sampled in a radiation lent X_0:

$$f_{\text{samp}}(\eta) = \frac{X_0}{a(\eta) + p(\eta)} \tag{2.1}$$

$a(\eta)$ is the depth of a single active LAr gap, $p(\eta)$ is the depth of the passive absorber, as seen by a crossing particle at a given η position. The calorimeter effective radiation Lent is $X_0 \simeq X_0^{\text{Pb}}$, being $X_0^{\text{Pb}} \ll X_0^{\text{LAr}}$ (Table 2.1). At $\eta = 0$ $a = 0.015$ X_0 and $p = 0.28$ X_0, the sampling frequency is $f_{\text{samp}}(\eta = 0) = 3.4$. For geometrical reasons the sampling frequency decreases at large $|\eta|$, thus leading to an increase of the fluctuations in the number of secondary electron tracks in the LAr gaps, and therefore reducing the detector intrinsic resolution. This effect is compensated by a reduction of the lead thickness in the absorbers in the region $|\eta| > 0.8$ [3].

The EMC *sampling fraction* F measures the ratio between the energy deposited by Minimum Ionizing Particle (MIP) in the active medium, and the total energy lost in the

full detector (LAr gaps + passive lead absorbers). In the ATLAS EMC [3]:

$$F = \frac{\Delta E_{\mathrm{LAr}}}{\Delta E_{\mathrm{LAr}} + \Delta E_{\mathrm{Pb}}} \simeq 19\% \tag{2.2}$$

Being a sampling calorimeter, the detector intrinsic energy resolution is dominated by the poissonian fluctuations of the number N of the shower secondary electron tracks that cross the active LAr gaps:

$$\left.\frac{\Delta E}{E}\right|_{\mathrm{intr}} = \frac{\sqrt{N}}{N} = \frac{a}{\sqrt{E}} \tag{2.3}$$

being N proportional to the incoming particle energy E, at least at first order. The *sampling term* a is expected to be of order of $10\%\sqrt{\mathrm{GeV}}$ [3]. There are other effects that contributes to deteriorate the energy resolution of the EMC, that can in general be expressed as:

$$\frac{\Delta E}{E} = \frac{a}{\sqrt{E}} \oplus \frac{b}{E} \oplus c \tag{2.4}$$

The term b takes into account the fluctuation on the energy measurements due to noise from the readout electronics and the *pile–up* events (see Appendix A). The electronics readout system has been designed in order to keep $b \simeq 400$ MeV. The *constant term* c includes all the effects related to the detector imperfections (active medium impurity, absorbers or gap thickness non–uniformity, ...) and to the quality of the calibration (see Section 7.1). It is the most critical parameter in terms of high energy performance of the detector.

2.2 Segmentation and granularity

The EMC is divided in two parts: the *barrel* (EMB), that covers a pseudorapidity range $|\eta| < 1.4$, and the *end-cap* (EMEC), located in the region $1.4 < |\eta| < 3.2$. Each part covers a full azimuth acceptance $0 < \phi < 2\pi$. The detector is segmented in longitudinal samplings, that for example in the *barrel* are defined as (Fig. 2.4):

- *S1 ("Front" or "Strips")*, made of narrow strips to perform position measurement and $\gamma - \pi^0$ separation, has a 6 X_0 depth. It has a granularity $\Delta\eta \times \Delta\phi \simeq 0.003 \times 0.1$.
- *S2 ("Middle")*, made of square towers with a depth of 16 to 18 X_0, collects most of the e/γ shower energy. It has a granularity $\Delta\eta \times \Delta\phi \simeq 0.025 \times 0.025$.
- *S3, ("Back")*, with a depth of 2 to 12 X_0, is used to sample high energy showers and helps to separate hadronic to electromagnetic particle. It has a granularity $\Delta\eta \times \Delta\phi \simeq 0.05 \times 0.025$.

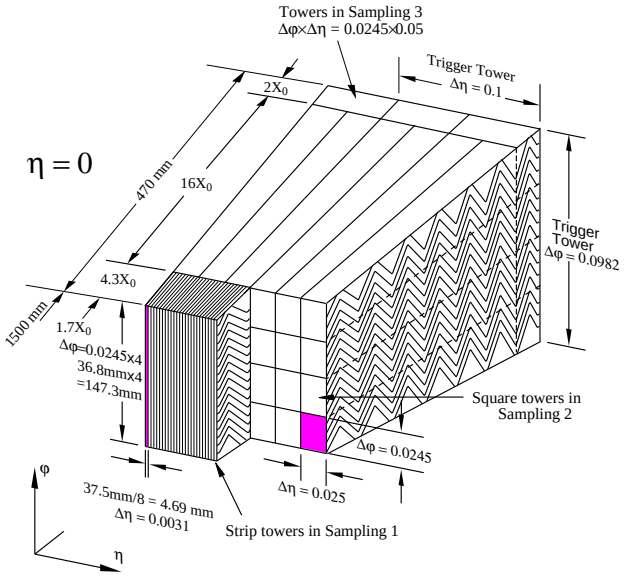

Figure 2.4: Sampling segmentation and granularity of the EMB.

In the region $|\eta| < 1.8$, Presampler detectors located in front of the EMC are used to correct for the energy lost in the material upstream (mainly the inner tracking system, the LAr cryostat and the solenoid coil).

Projectivity and granularity in pseudorapidity η are obtained by properly etching the readout electrodes (Figure 2.5). For construction reasons, two types of electrodes are used: type A for $0 < |\eta| < 0.8$ and type B for $0.8 < |\eta| < 1.4$. Along the azimuthal angle ϕ the projective geometry imposes that the *accordion* angles of absorbers and electrodes become more acute at increasing radius, thus ensuring a constant LAr gap and sampling fraction. Granularity in ϕ is defined by grouping together a proper number of electrodes: the signals coming from electrodes contiguous in azimuth are merged by the "summing boards" (SB) to form the read–out cells (Figure 2.6). The number of gaps merged for each sampling, and the relative granularity in $\eta \times \phi$, are displayed for the EMB in Table 2.2.

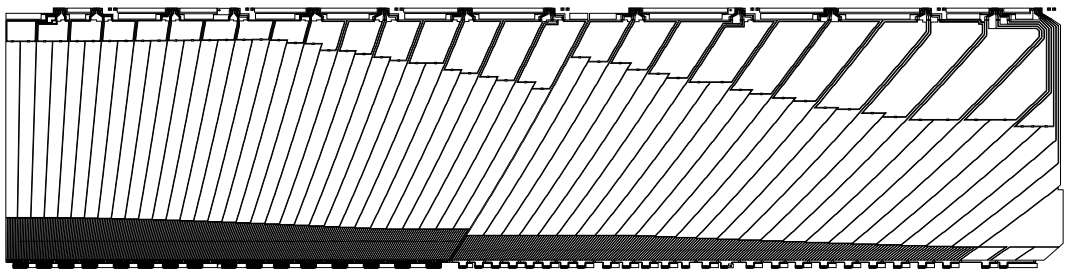

Figure 2.5: View of the signal layer of the EMB readout electrodes A and B. The readout pads for the different samplings are shown.

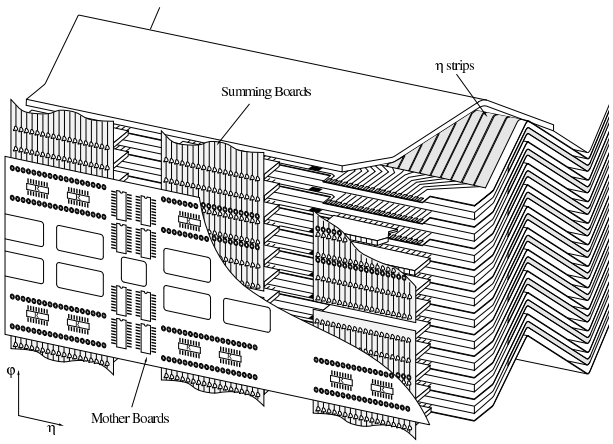

Figure 2.6: View of the front side of the *accordion*, showing the placement of the Strips summing boards (SB) and the mother board (MB). Similar connection for the Middle and Back sampling are present on the back side of the *accordion*.

Sampling	Number of merged gaps	Granularity ($\Delta\eta \times \Delta\phi$)	w.r.t. Middle
Strips	16	0.00375×0.1	$1/8 \times 4$
Middle	4	0.025×0.025	1×1
Back	4	0.050×0.025	2×1

Table 2.2: Granularity and number of merged gaps per read-out cell for the different samplings. η is pseudo-rapidity and ϕ is azimuth.

LAr property	value
normal boiling point (bp) (K)	87.27
$\langle \Delta E_{\mathrm{MIP}}(1\mathrm{cm}) \rangle$ (MeV)	2.1
W-value (1 MeV electrons) (eV/ion–pair)	23.3
electron mobility at bp ($\mathrm{m^2V^{-1}s^{-1}}$)	0.048
ion mobility at bp ($\mathrm{m^2V^{-1}s^{-1}}$)	$0.016 \cdot 10^5$
dielectric constant ϵ_r	1.6

Table 2.3: Properties of LAr related to the ionization signal generation.

The angular position, usually defined by the pseudorapidity η and the azimuthal angle ϕ (in radians), is often indicated by the coordinates $\eta_{\mathrm{cell}}, \phi_{\mathrm{cell}}$, which are expressed in units of Middle layer cells. Therefore, the Middle cell at lowest η, ϕ in the module is labeled by $\eta_{\mathrm{cell}} = 0,\ \phi_{\mathrm{cell}} = 0$, and since the granularity of this layer is $\Delta\eta \times \Delta\phi = 0.025 \times 0.025$, the following general relation holds:

$$\begin{cases} \eta &= (\eta_{\mathrm{cell}} + 0.5) \times 0.025 \\ \phi &= (\phi_{\mathrm{cell}} + 0.5) \times 0.025 \end{cases} \tag{2.5}$$

In the present work, references to Middle cells will often have the form Mx, where $x = \eta_{\mathrm{cell}}$ runs from 0 to 54 in the EMB (e.g. the first eight cells in electrodes B are named M32÷M39). Each pair of Middle cells share the same Back cell, therefore referencing will be based on the number of the associated even Middle cell (e.g. B32 refers to the Back cell shared by M32 and M33).

2.3 Readout system

2.3.1 Signal generation

After the passage of the ionizing particles produced in the electromagnetic shower, electrons and positive ions drift along the electric field. Because of mobility reasons (see Table 2.3) the fast signal is produced by the electrons drift. The resulting current has a triangular waveform [29] with a sub–nanoseconds rise time followed by a linear decay with the duration of the electron drift time T_d (Figure 2.7). In the EMB the drift time is $T_d \simeq 450$ ns for a gap thickness $g = 2.1$ mm and 2000 V HV bias. The deposited charge is collected by the readout electrodes, the absorbers provide the ground reference. The ionization electron signal generation is detailed in Appendix A.

The ionization current peak is proportional to the deposited energy: the energy-to-current nominal sensitivity for the EMB is 2.7 μA/GeV in the $0 < |\eta| < 0.8$ region, and 3.1 μA/GeV in the $0.8 < |\eta| < 1.4$ region [3]. The dynamic range is expected to range between 50 MeV (electronics noise level) and 3 TeV (energy scale of the electrons that could come from the Z' and W' decays [5]).

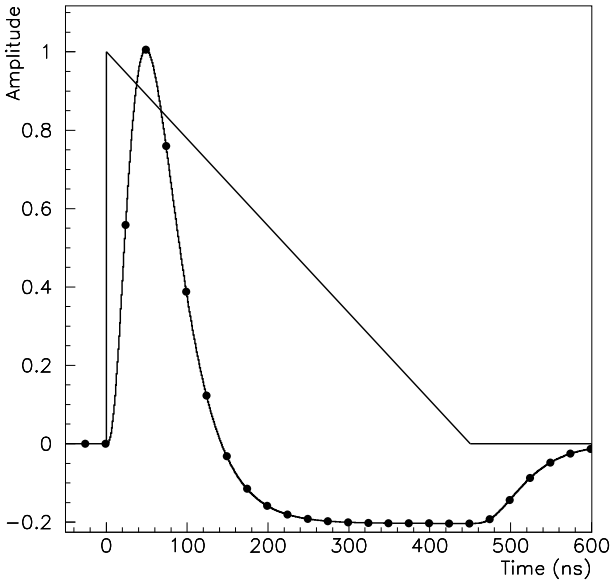

Figure 2.7: Ionization signal with amplified–and–shaped signal superimposed. Sampling points are shown.

2.3.2 Ground reference

Each SB located behind[1] the EMB covers 4×4 Middle cells and 2×4 Back cells, corresponding to an acceptance $\Delta\eta \times \Delta\phi = 0.1 \times 0.1$. For each ϕ row, the signal out of the SB is arranged in the pattern M-B-M-M-B-M, where M and B denote Middle and Back cells (Figure 2.8). Each signal line has its own ground reference; the ground plane of the SB is connected to the absorbers through paths located on the electrodes that end with springs ("ground springs") touching the absorbers. Each SB is designed to take the ground reference from the two sides; however, on the first electrodes design, the "odd" read-out connectors located near the HV connectors had only one ground return path to the absorber, located on the low-η side. The consequence of this type of grounding on the detector performances is detailed studied in Chapter 3.

2.3.3 Readout lines

The SB's are grouped in 2×2 patterns by the "mother-boards" (MB), therefore each MB covers an acceptance $\Delta\eta \times \Delta\phi = 0.2 \times 0.2$, corresponding to 8×8 Middle cells and 4×8 Back cells. An analogous structure on the detector front collects and routes the signals from the Strips. A complex chain of readout lines is in charge to carry the signals from the MB to the readout electronics, that is located in warm crates outside the EMC cryostat. The readout line elements are listed in Table 2.4, from the MB connector to the baseplane of the crate in which the readout electronics cards are plugged. The characteristic impedance of the readout cables chain is optimized for the cell capacitance in order to minimize the

[1]Similar SB's are located in front of the EMB and collect the signals from the Strips

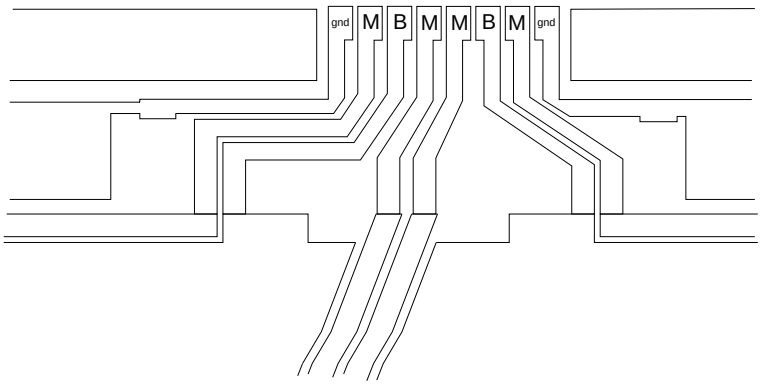

Figure 2.8: Detail of the EMB electrode back connector. The termination of the striplines in charge of the ground (gnd), Middle (M) and Back (B) cells connections with the summing board are shown.

noise contributions [3].

Readout line element	$Z_0(\Omega)$	length (ns)
Connector	40	0.3
Pigtail + Cold Cable	25	$7 \div 30$
Cold Feedthrough	50	0.2
Vacuum Cable	33	2.2
Warm Feedthrough	50	0.2
Warm Cable	33	2.2
Base Plane	75	0.3

Table 2.4: Breakdown of the read-out line elements from the MB to the front-end crate baseline preamplifier. The impedance of the pigtail and the cold cable is matched with that of the preamplifier, which is 25 Ω for Middle and Back channels. The length of the pigtail and cold cable changes according to the distance of the MB from the feedthrough.

2.3.4 Readout electronics

The active front–end (FE) readout electronics is located on the Front End Boards (FEB [24]), that are allocated in dedicated Front End Crate (FEC) immediately outside the EMC cryostat, in order to minimize the readout cables length (Figure 2.1).

A preamplifier [25] is in charge to amplify the signal emerging from the detector in order to reduce the sensitivity to the noise in the following stages of the readout system.

The amplified signal is shaped by a multi–gain $CR - RC^2$ filter [26], whose internal time constant $\tau_{\rm sh} = 15$ ns has been chosen in order to optimize the signal–to–noise ratio. The area of the shaped signal is null, thus allowing to treat the pile–up events as a noise contribution to the interesting physics signals (see Section B.1 for details).

The shaped signal is sampled at the 40 MHz LHC bunch–crossing frequency (i.e. one sample every 25 ns, Figure 2.7). The samples are stored in analog memory arrays waiting for the Level 1 trigger to accept or reject the event. When a Level 1 trigger occurs, the best gain from the 3 available at the shaper level is chosen; 5 samples in the positive lobe of the shaped signal are digitized and kept for each readout cell.

Apart from the FEB's, the FEC contains also the "tower builder" card, that uses the signal from the EMC to compute a first information about the energy released in the calorimeter to be used by the trigger processors; the calibration board (Section 2.3.5); the control electronics. A schematic view of the FE electronics is shown in Figure 2.9.

2.3.5 Calibration strategy

The ATLAS LAr EMC is a system with no internal gain. For this reason the calibration of the calorimeter can in principle be factorized in a cell–to–cell calibration of the readout system, followed by an overall energy scale determination [3].

The basic concept of the LAr EMC electronics calibration consists in injecting at the LAr gap level a known current signal that mimics "as much as possible" the ionization signal [28]. The signal emerging from the detector is read and reconstructed through the whole readout chain, thus the actual gain of each channel can be measured and monitored. This procedure takes into account the non–linearity of the gain over the full dynamic range of the readout system, thus assuring a linear behavior of the detector over the large energy range it has been designed for.

The calibration signal must have a fast rise time and a decay time similar to the ionization pulse drift time. For this scope an exponential voltage pulse with a proper decay time is generated by the calibration board (CB) [27] located in the FEC, and brought to the MB inside the LAr cryostat by a cables chain. Precision resistors located on the MB [23] convert the voltage pulse to a current signal. A detailed description of the calibration pulse can be found in Section A.2.

The aim of the electronic calibration system, together with the signal reconstruction method for the ionization signals (see Chapter 4 e 5), is to obtain a constant term c in the relative energy resolution expression (2.4) smaller than 0.5% in a region $\Delta\eta\times\Delta\phi = 0.2\times0.4$ (*local* constant term, see Section 2.4).

The electronic calibration system will be complemented at the LHC by the on–site calibration based on known physics processes, such as $Z \rightarrow e^+e^-$ ([4, 20]), in order to correct for long distance disuniformities, and to achieve a constant term of 0.7% over the calorimeter coverage that is to be used for the precision physics measurements ($0 < \phi < 2\pi$, $0 < \eta < 2.5$, *global* constant term) [5].

2.4 LHC physics requirements overview

LHC detectors will deal with a challenging experimental framework: the search for new physics implies the observation of rare decay channels over large backgrounds. In most of these channels a crucial role in energy and position reconstruction of photons and electrons is played by the EMC. This is the case for example in the decay channels of the Higgs

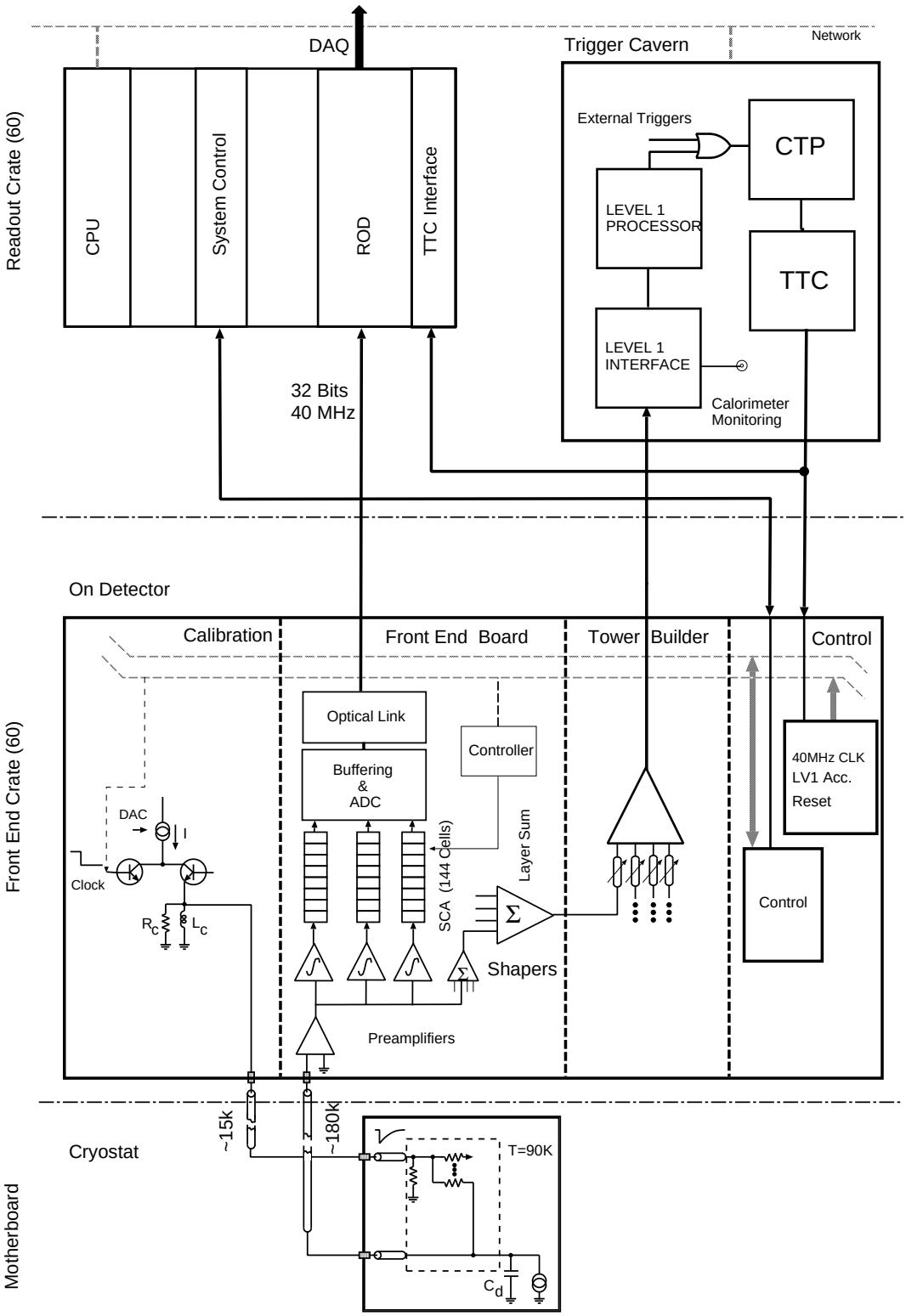

Figure 2.9: Schematic view of the EMC front–end electronics locate in the FEC.

boson $H \rightarrow \gamma\gamma$ and $H \rightarrow e^+e^-e^+e^-$. The ATLAS EMC design have been optimized for such physics searches [5].

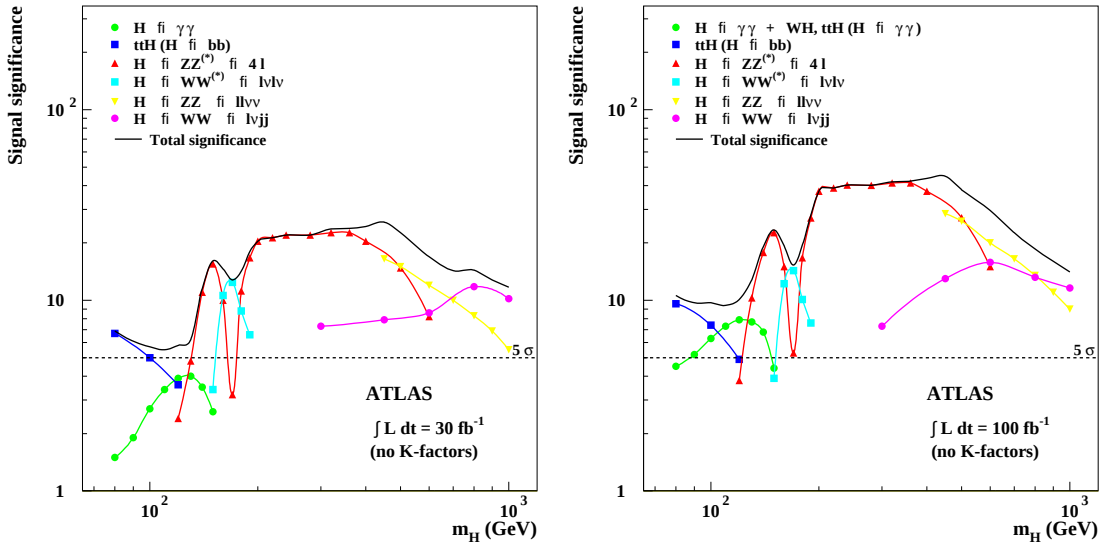

Figure 2.10: Expected significance of the SM Higgs boson signal in the ATLAS detector, as function of the Higgs mass, for an integrated luminosity of 30 pb^{-1} (left) and 100 pb^{-1} (right), for several decay channels The significance of a channel signal is defined as the ratio $\frac{S}{\sqrt{B}}$ between the signal S and the poissonian RMS of the corresponding background $\sqrt{B}$.

The SM Higgs boson will be sought over a very large mass range (100 GeV $< m_H <$ 1 TeV), its mass being an unknown parameter of the model (Figure 2.10). For $m_H \leq 150$ GeV one of the most suitable channels is $H \rightarrow \gamma\gamma$ [18]: both the energy of the two photons and their opening angle, necessary to deduce the $\gamma\gamma$ invariant mass, will be measured through the EMC, thus requiring optimal energy and angular resolution and response uniformity.

For 120 GeV$< m_H <$ 700 GeV one of the most promising search channels will be $H \rightarrow ZZ^{(*)} \rightarrow e^+e^-e^+e^-$ [19], thus challenging again the EMC on the electron energy reconstruction performances.

Another interesting search channel, that would be the only useful for $m_H > 700$ GeV, is $H \rightarrow WW \rightarrow l\nu l\nu$, in which a part on the energy is carried by undetectable neutrinos. In this case a good ermeticity of the calorimeter is required, in order to accurately reconstruct the missing transverse energy and detect the toward jets from the underlying events.

All this arguments imply the following EMC properties [5, 4]:

Response uniformity

A 0.7% constant term in the energy resolution over the whole rapidity coverage of the barrel and part of the end-cap (0$< \eta <$2.5) is required, especially driven by Higgs boson physics (see Section 2.3.5).

We shows in this work (Chapter 3 and 4) that the response uniformity of the LAr EMC is the most critical parameter to the energy reconstruction and calibration strategy; the present work is devoted to the study and to the development of such reconstruction algorithms (Chapter 4, 5 and 6). The response uniformity will be investigated in relation to the signal reconstruction and calibration methods, their effectiveness will be directly tested in the analysis of the data from the EMB production module exposed to electrons beam at CERN (Chapter 7).

Sampling term

For the decay products of a low mass Higgs boson the sampling term a is still important in the energy resolution expression (2.4). In order to obtain a good invariant mass resolution, a must be kept by design smaller than 10%.

Position measurement resolution

Several position measurements can be performed thanks to the excellent EMC granularity. The ϕ position of the shower can be measured in the $S2$ compartment, the η position both in $S1$ and in $S2$. By combining these two measurements it is possible to estimate the shower direction in θ and therefore extrapolate the primary vertex along the beam axis. The EMC angular resolution for photons scales as $\frac{d}{\sqrt{E}}$; the terms d must be kept around 50 mrad by design, in order to ensure the $\gamma\gamma$ invariant mass resolution within the SM Higgs boson H discovery limits.

Mass measurement

Beside the search for new physics, the large events statistics due to the high luminosity will allow precision measurements within the SM, such as that of the W mass. This measure implies an absolute electromagnetic energy scale of better than 0.02%. This goal can be achieved combining the linearity of the apparatus with an optimal calibration system.

Time measurement

Timing information of the reconstructed signals can be important for some supersymmetric channel identification, such as the Gauge Mediated Supersymmetry Breaking model channel $\tilde{\chi_0} \rightarrow \tilde{G}\gamma$, through the identification of showers generated by non–pointing photons. For this kind of measurement an accuracy of 100 ps is required.

Chapter 3

Electrical properties and signal shapes in the EMC

3.1 Foreword: the 2000 test-beam results

In years 1999 and 2000, a prototype of the EMB modules that will be assembled in the ATLAS experiment –the "Module 0" [43]– has been exposed to electron beams at CERN. Typical results from a position scan performed with 245 GeV electrons from year 2000 test-beam data are presented in Figure 3.1 [51]. The top plot shows the energy as a function of the impact position, for three different η-rows ($\phi_{\rm cell} = 9, 10, 11$). The total energy[1] is obtained from the standard 3×3 cluster from the Middle sampling, plus clusters of corresponding granularity from Presampler, Strips and Back samplings. The energy response as a function of the η coordinate exhibits a clear pattern with a periodicity of 8 Middle cells, over which the peak-to-peak variation is about 10 GeV (4%); the RMS over the full η range is 5 GeV (2%). The bottom left plot of Figure 3.1 shows the energy spread over cells $1 \div 47$ at $\phi_{\rm cell} = 10$; the bottom right plot shows the relative energy spread in ϕ, after removing the oscillations along η.

The general idea in the ATLAS LAr collaboration was that the cause of non–uniformity was to be sought in the electrical properties of the detector itself. In fact, as we discuss in detail along this chapter, the calibration signal is injected at the motherboards (MB) level, while the signal induced by electromagnetic cascades originates inside the detector, at the LAr gap level: this introduces differences in shape and amplitude between the two signals.

In this sense, a basic electrical model that describes each detector channel as a LC circuit is inadequate, and a complete model accounting for all the parameters is too complex to be handled with a reasonable confidence. The goal of this work consists in building both an *effective model* suitable to simulate the detector electrical behavior,

[1] The energy deposited in each cell is reconstructed from the digitized samples of the corresponding ionization signal. The "*parabola*" signal reconstruction (SR) algorithm, as implemented in the standard EMB test–beam reconstruction code EMTB [52], is used. This SR method is discussed in detail in Chapter 4.

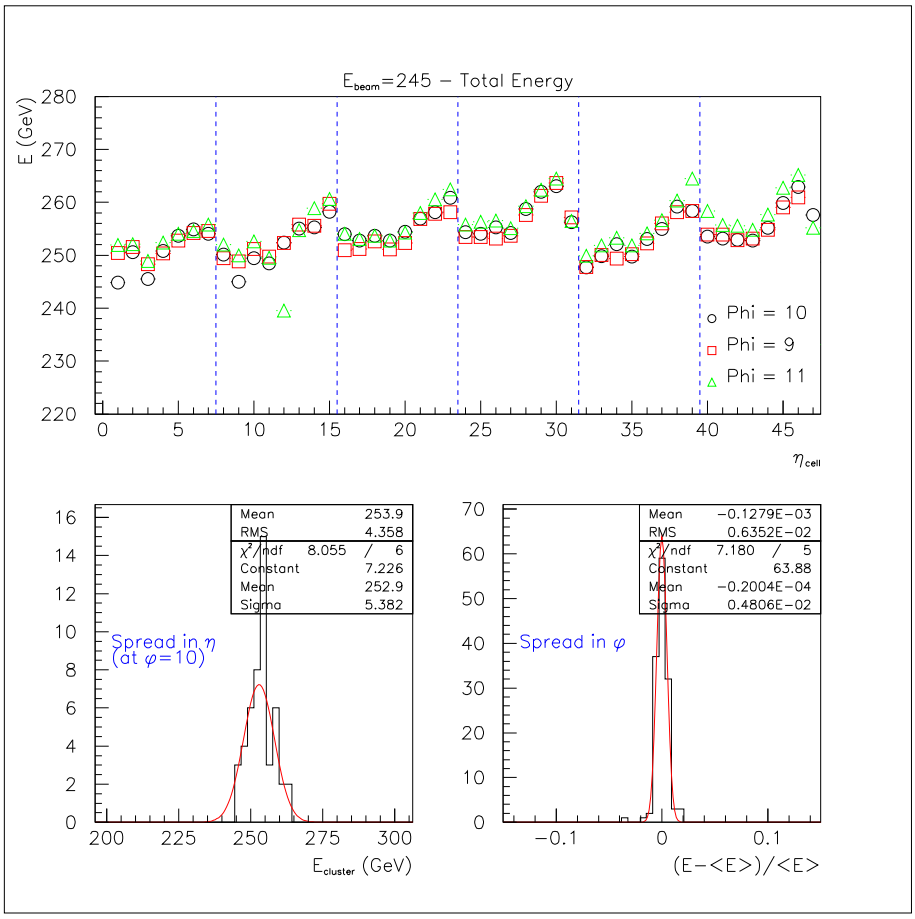

Figure 3.1: Energy response of the EMC barrel prototype "Module 0" to 245 GeV electrons, from data taken during the year 2000 test–beam session (see text for details).

and a *hardware model*, as similar as possible to the real calorimeter, to directly investigate the non–uniformity origin and to suggest a solution.

In Section 2.3.2 the asymmetry in the ground springs that causes the "odd" summing boards along one η line to have only one reference ground connected to the electrodes instead of two has been described. This was firstly believed to completely explain the 8–fold periodicity along η of the energy response as seen in Figure 3.1. We show in this chapter that the absence of the second ground contact was in fact the main source of the non–uniformity along η. This results has lead to the electrodes design modification, consisting in adding a second ground springs to the connectors lacking of the "odd" one (Section 3.7).

It is important to say that the knowledge of the electrical properties of the detector gained with this study points anyway out the need of additional corrections in the EMC signal reconstruction procedure. This holds also after that the ground spring modification has been implemented in the electrodes design. We discuss this point in detail in Chapter 4.

3.2 Detector models

3.2.1 Basic detector electrical model

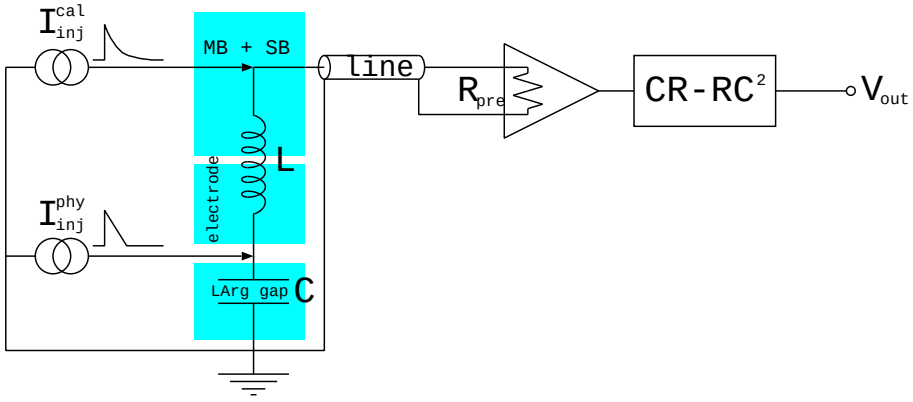

Figure 3.2: Basics electrical model of a LAr cell with schematic readout chain and simplified calibration network.

In Figure 3.2 the simplest model for a detector cell is drawn. The liquid argon (LAr) gap can be described as a capacitor C between the absorber (ground reference) and the readout electrode. The signal originated by an e.m. shower ("ionization" or "physics" signal) is represented by a *triangular* current generator applied between the two capacitor plates (see Section A.1 for details): we refers to it here as $I_{\rm inj}^{\rm phys}$. This signal is brought to the summing board (SB) and the mother board (MB) through a path on the electrode, which is inductive; L is the total inductance of such path plus the SB and MB contribution. The calibration pulse is an *exponential* current generator injected on the MB (see Section A.2 for details) with a decay time $\tau_{\rm cali} \simeq 400$ ns: we refers to it here as $I_{\rm inj}^{\rm cali}$

The readout line consists of a set of lines connected to each other and closed on a preamplifier with input impedance $R_{\rm pre} = 25\ \Omega$. The line can be described (see for example [64]) by a transfer matrix M such that:

$$\begin{aligned} \begin{pmatrix} V_{\rm line,in} \\ I_{\rm line,in} \end{pmatrix} &= M \begin{pmatrix} V_{\rm line,out} \\ I_{\rm line,out} \end{pmatrix} \\ &= \begin{pmatrix} M_{VV} & M_{VI} \\ M_{IV} & M_{II} \end{pmatrix} \begin{pmatrix} V_{\rm line,out} \\ I_{\rm line,out} \end{pmatrix} \end{aligned} \tag{3.1}$$

Since $V_{\rm line,out} = R_{\rm pre} I_{\rm line,out}$, the line presents at its input an impedance:

$$Z_{\rm line,in} = \frac{M_{VV} R_{\rm pre} + M_{VI}}{M_{IV} R_{\rm pre} + M_{II}} \tag{3.2}$$

and the voltage at the line output (i.e. at the preamplifier input) is:

$$\begin{aligned} V_{\rm line,out} = V_{\rm pre,in} &= \frac{R_{\rm pre}}{M_{IV} R_{\rm pre} + M_{II}} I_{\rm line,in} \\ &= H_{\rm line} I_{\rm line,in} \end{aligned} \tag{3.3}$$

The preamplifier provides a gain α (assumed to be constant over the relevant frequency range) and the shaper is of the type CR-RC^2, therefore the overall transfer function of the two components is:

$$H_{\rm sh} = \frac{V_{\rm out}}{V_{\rm pre,in}} = \alpha \frac{s\tau_{\rm sh}}{(1 + s\tau_{\rm sh})^3} \tag{3.4}$$

where $\tau_{\rm sh} = 15$ ns is the shaper characteristic time ($2\tau_{\rm sh}$ is the peaking time of the shaper response to a step-function input), and $s = i\omega$ represents the complex frequency in the usual Laplace notation [65].

Due to the inductive path connecting the LAr gap to the readout line, the calibration signal sees a circuit different than the physics signal. In fact, the calibration current entering the line is given by:

$$I^{\rm cali}_{\rm line,in} = I^{\rm cali}_{\rm inj} \frac{Z_{\rm det} + Z_{\rm conn}}{Z_{\rm det} + Z_{\rm conn} + Z_{\rm line,in}} \tag{3.5}$$

while the physics current entering the line is:

$$I^{\rm phys}_{\rm line,in} = I^{\rm phys}_{\rm inj} \frac{Z_{\rm det}}{Z_{\rm det} + Z_{\rm conn} + Z_{\rm line,in}} \tag{3.6}$$

where $Z_{\rm det}$ and $Z_{\rm conn}$ are the impedances offered by the detector gap and by its connection to the readout line, respectively. In this simple model, the detector and "connection" impedances are:

$$Z_{\rm det} = \frac{1}{sC} \tag{3.7}$$

$$Z_{\rm conn} = sL \tag{3.8}$$

The complete formulæ for the output voltage due to physics and calibration signals are as follows:

$$V_{\text{out}}^{\text{phys}} = H_{\text{sh}} H_{\text{line}} I_{\text{inj}}^{\text{phys}} \frac{Z_{\text{det}}}{Z_{\text{det}} + Z_{\text{conn}} + Z_{\text{line,in}}} \tag{3.9}$$

$$V_{\text{out}}^{\text{cali}} = H_{\text{sh}} H_{\text{line}} I_{\text{inj}}^{\text{cali}} \frac{Z_{\text{det}} + Z_{\text{conn}}}{Z_{\text{det}} + Z_{\text{conn}} + Z_{\text{line,in}}} \tag{3.10}$$

The ratio between physics and calibration signal at the shaper output is then:

$$\frac{V_{\text{out}}^{\text{phys}}}{V_{\text{out}}^{\text{cali}}} = \frac{I_{\text{inj}}^{\text{phys}}}{I_{\text{inj}}^{\text{cali}}} \frac{Z_{\text{det}}}{Z_{\text{det}} + Z_{\text{conn}}} \tag{3.11}$$

which, in the simple detector model described by equations (3.7), (3.8), reads:

$$\frac{V_{\text{out}}^{\text{phys}}}{V_{\text{out}}^{\text{cali}}} = \frac{I_{\text{inj}}^{\text{phys}}}{I_{\text{inj}}^{\text{cali}}} \frac{1}{1 + s^2 LC} \tag{3.12}$$

The meaning of this result is that the two signals differ for two reasons: one is the different injected shape (triangular and exponential, respectively), the other is that the two are injected at different locations. All the effects due to the readout line, the preamplifier and the shaper (described by the parameters $Z_{\text{line,in}}, H_{\text{sh}}, H_{\text{line}}$) are common to both signals and cancel out when taking the ratio.

3.2.2 Detailed electrical model of an electrode channel

The detector model described in Section 3.2.1 is very simplified. In the reality, things differ for the following reasons:

- each detector cell consists of more electrode channels connected together by the summing board (16 for the Strips, 4 for Middle and Back samplings);
- channels belonging to Strips, Middle and Back samplings are not electrically independent, being connected by resistors on the high-voltage (HV) layers; more precisely, each Middle channel has 8 Strips associated and shares a Back channel with another neighboring Middle channel (see Figure 2.5);
- the high-voltage layer of each Middle or Back cell is subdivided in pads, while the signal layer is continuous; the signal and the HV layers of each electrode channel are capacitively-coupled through the kapton layer, the overall capacitance through kapton being ≈ 80 times larger than that through the LAr gap.
- cross-capacitances and, possibly, mutual inductances exist between neighboring channels.

Figure 3.3 shows a more realistic electrical scheme of one middle channel in one electrode. The complete scheme, accounting for "all" high voltage pads, is drawn in (a),

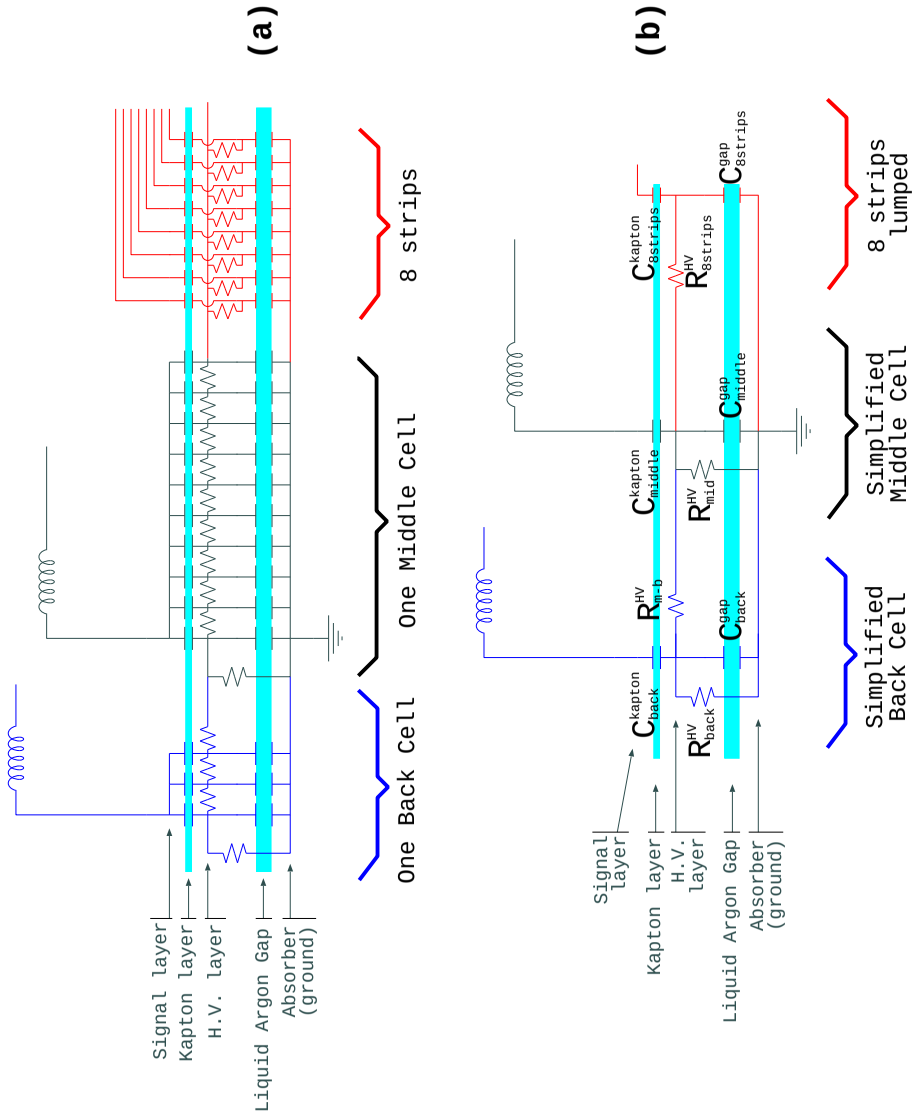

Figure 3.3: Complete schematics of an electrode Middle channel (a) and a reasonable simplification (b)

while (b) represents a reasonable simplification, in which the 8 Strips are lumped together (with effective resistance and capacitance equal to the parallels of the 8 Strips resistances and capacitances) and the Middle and Back HV layers are considered as continuous. The reason of the last assumption is that two consecutive pads are coupled through the signal layer and the two kapton capacitances, that offer an impedance much smaller than the resistor in the frequency region of interest ($\gtrsim$ 100 kHz).

As it will be shown in Section 3.4, the model proposed here is necessary to understand some results from the impedance measurements, while the simpler LC model is not adequate. In Section 3.6, the effect of adding the Strips and Back will be shown on the physics and calibration signals.

3.3 Hardware model of the EMC: the *mock–up*

3.3.1 General system layout

The detector hardware model ("*mock–up*") realized in Milano consists of 4 B–electrodes[2] and 5 absorbers piled-up and interspaced by holed polypropylene (PP) Strips in the plane portions to simulate the LAr gaps (see Figure 3.4). The PP thickness is (2.0±0.1) mm, and its plastic/air ratio was chosen in order to reproduce an average dielectric constant $\epsilon_r \simeq 1.5$[3], similar to that of LAr at 80 K temperature.

For all the measurements and analysis concerning the *mock–up* references to middle sampling cells will have the form Mx, where x represent the η_{cell} value as defined in Chapter 2. For the EMB it runs from 0 to 54 (e.g. the first eight cells in electrodes B are named M32÷M39). Each pair of Middle cells share the same Back cell, therefore referencing will be based on the number of the associated even Middle cell (e.g. B32 refers to the Back cell shared by M32 and M33).

Inside the 2$^{\text{nd}}$ gap[4] twelve Middle cells (M32÷M43, corresponding to three SB's) have been equipped with "physics injectors", described below, to simulate the electromagnetic shower that develops in the LAr gaps. The coaxial cables carrying the signal from the pulse generator to the injectors run along the electrode folds, that are free of PP.

The *mock–up* is laid on plastic supports and pushed by a pressing system that provides a better mechanics stability (it has been observed that modest pressure variations cause sizable fluctuations in the gap width, and therefore in the capacitances).

Three SB's are available to be plugged on the electrodes back connectors, to merge together Middle and Back samplings channels from the 4 different gaps. L and C measurements can be performed both on separate gaps and at the SB's level (cell grouped gaps). The electrodes in use are yet of the type with asymmetric ground returns on some

[2]The electrodes used were discarded because not satisfying the requirements for being used in an EMC module, therefore their quality is poor, especially for what concerns the HV resistors values; broken resistors were repaired with silver epoxy or resistive ink, there are no broken paths on the signal layer, and the measured kapton capacitances are regular.

[3]The value of ϵ_r has been tested to be stable to better than 0.5% over a wide frequency range: 100 kHz ÷ 100 MHz.

[4]Gaps are numbered 1 through 4 starting from that on the top.

Figure 3.4: Picture of the *mock–up* during assembling. The two bottom gaps (3^{rd} and 4^{th} in our numbering scheme) are complete, the 2^{nd} is open and the PP Strips and physics injection cables are visible.

Figure 3.5: Detail view of the *mock–up* system in its final layout; the accordion structure of the detector is visible.

Figure 3.6: View of the *mock–up* system in its final layout; the Faraday cage is visible on top of the detector model.

back connectors (see Section 2.3.2 for details): connectors 1 and 3 (Middle cells 32÷35 and 40÷43 respectively) have two ground springs, while connectors 2 and 4 (Middle cells 36÷39 and 44÷47) have only one on the small–η side. However, connector 2 has been equipped with removable extra–ground springs on the large-η side, in order to study the effects of this asymmetry.

A Faraday cage has been built to screen the system from external electromagnetic noise (see Figure 3.6). A details of the final layout of the system is shown in Figure 3.5.

For what concerns the measurements treated in this chapter the signal waveforms are read out directly from the SB's. Subsequently the layout has been completed with the full read-out chain as in the real detector (MB + cold cable + vacuum cable + warm cable) to investigate the signal reconstructions algorithms features (see Chapter 5).

3.3.2 Injection circuits

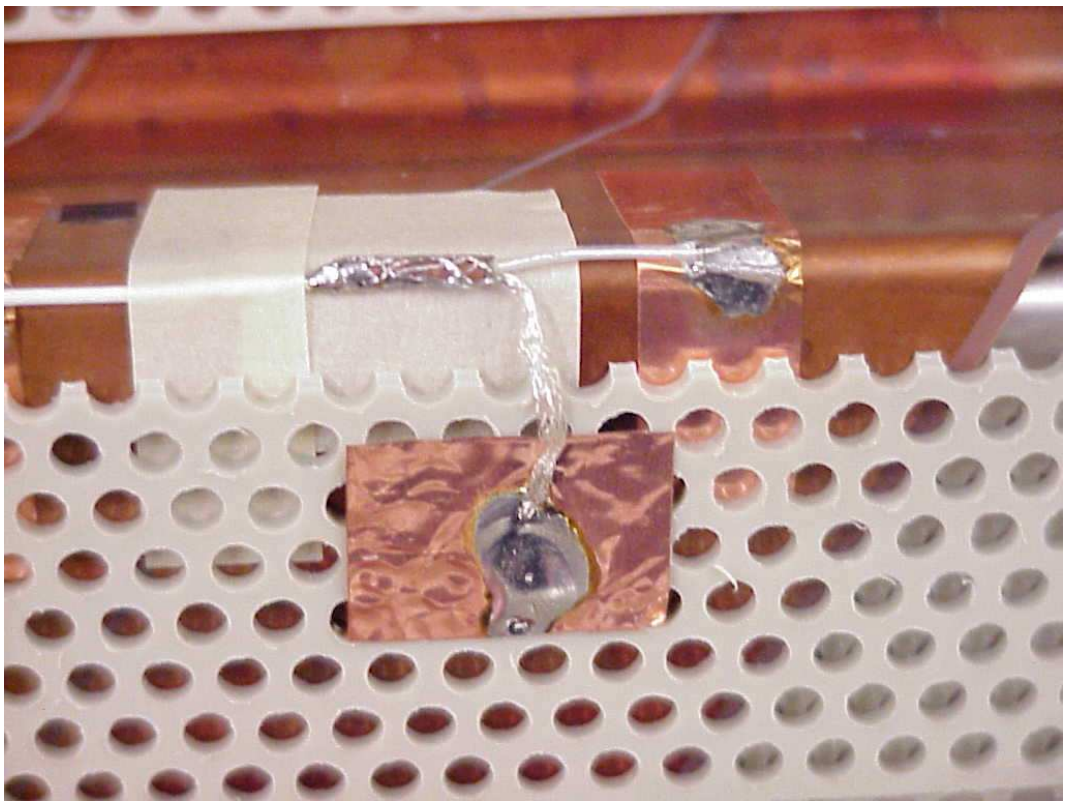

Figure 3.7: Detail of one physics injector.

For both "physics" and calibration injections, exponential pulses are used, by sending a fast step-function through an RC circuit, as shown in Figure 3.8. A step–function voltage signal is sent through a 50 Ω coaxial cable terminated at 50 Ω, and followed by an RC series circuit producing an exponential signal with a decay constant of 400 ns, which is injected

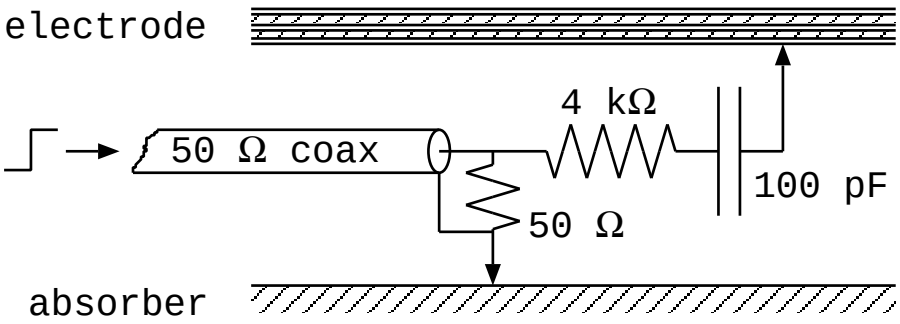

Figure 3.8: Electric scheme of a "physics" injector (see text for details).

between the absorber and the electrode HV layer. The calibration signal is produced in the same way, but is injected at the SB level.

In order to allow multiple physics injection on neighboring cells (thus simulating a cluster), 12 physics injectors are located between the electrode and the absorber (see Figure 3.4 and the detail in Figure 3.7). The calibration injector is unique and can be plugged in any channel through the SB.

All injectors are made with 4 kΩ resistors and 100 pF capacitors that have been selected from a larger set with an accuracy of $\sim 0.1\%$. Each injector has been tested closed on a 350 pF capacitor and read on the oscilloscope through a 50 Ω cable: the traces on the scope confirm the uniformity at the $\sim 0.1\%$ level.

3.3.3 Electronic instrumentation and measurement methods

An HP-4395A network/impedance/spectrum analyzer is used to perform impedance measurements in the frequency domain. Normally each measurement consists of 401 samples, equally spaced in log-scale, over the frequency interval 10 kHz ÷ 100 MHz, with a 100 Hz IF bandwidth. During such measurements, the channel under exam is read through a 50 Ω LEMO cable, while all the other channels are left open, to ensure that no current flows into them through parasitic couplings. Measurements are performed both on single gaps (i.e. on single electrodes) and at the SB level (i.e. on 4 electrodes in parallel).

Step–function pulses are generated by a LeCroy 9210 dual channel pulse generator with a 1 ns rise time and a maximum voltage of 5 V. The output signal from the SB is fed into a programmable CR-RC^2 shaper; to avoid saturation at this level, it is necessary to operate the pulse generator at 3 V maximum. When performing multiple physics injection, the two channels are used at the same time: one for the central cell, the other, by means of a power splitter, for the two neighboring cells. In such a way, it is possible to synchronize the three injections and vary the signal amplitudes independently for the central cell and the two side cells.

The signal waveforms are acquired on a Tektronix TDS 754D 8 bits, 2GSample/s, 500 MHz bandwidth digital oscilloscope, and averaged over 400 samples. The precision from digitization, achieved with this procedure, has been estimated from the smallest

appreciable output difference, and amounts to ~ 0.2 mV for a signal amplitude of 1 V. During signal injection and measurements, the SB is always used, and all channels are terminated on 25 Ω loads (obtained using either 25 Ω resistors or 50 Ω LEMO cables in parallel with 50 Ω resistors). This is done to reproduce more faithfully what happens in the real detector (i.e. cross-talk due to parasitic couplings to the neighboring channels).

3.4 Electrical parameters measurements on the *mock–up*

A precise measurement of the L, C parameters for each channel is crucial for having a good understanding of the system behavior. In this section, a critical discussion of such measurement is proposed, and results are shown.

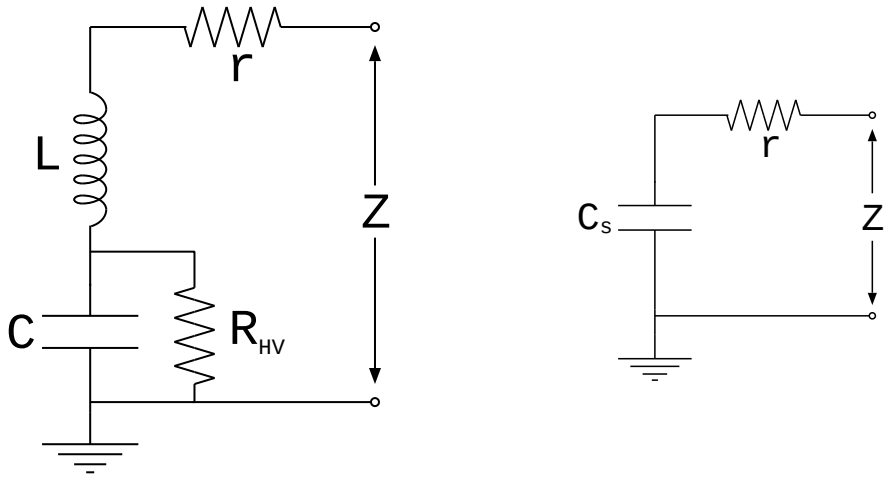

Figure 3.9: Simple schematics of a single LAr cell, as seen at the SB level (left), and simplified equivalent circuit (right).

3.4.1 Extraction of effective L and C values from impedance measurements

The expected signal-to-ground impedance for a Middle sampling channel, neglecting the presence of Strips and Back sampling (see the simplified model in Figure 3.9 left), is:

$$Z = r + j\omega L + \frac{1}{j\omega C}\left(\frac{R_{\mathrm{HV}}}{R_{\mathrm{HV}} + \frac{1}{j\omega C}}\right) \tag{3.13}$$

where r is a contact resistor ($\lesssim 1\ \Omega$), and R_{HV} is the HV distribution resistor ($\approx 1\ \mathrm{M}\Omega$), whose effect is sizable only at low frequencies ($\lesssim 10\mathrm{kHz} \sim R_{\mathrm{HV}}C$), being:

$$\lim_{\omega \gg R_{\mathrm{HV}}C} \frac{1}{j\omega C}\left(\frac{1}{1 + 1/j\omega R_{\mathrm{HV}}C}\right) = \frac{1}{j\omega C} \tag{3.14}$$

In this situation we can drop the presence of the HV distribution resistor:

$$Z_{\text{noHV}} = r + j\omega L + \frac{1}{j\omega C} \tag{3.15}$$

and define an equivalent circuits (Figure 3.9 right) where the *effective series capacitance* C_s is introduced such that:

$$\begin{cases} Z_{rC_s} &= r + \frac{1}{j\omega C_s} \\ \text{Im}(Z_{rC_s}) &= -\frac{1}{\omega C_s} \end{cases} \tag{3.16}$$

This is equivalent to assume that the circuit behaves mainly as a simple rC series (Figure 3.9 right), which is reasonable for frequencies well below the LC resonance, but high enough to neglect the effect of R_{HV}. When approaching the resonance frequency the effect of the presence of the inductance L can be modeled as a C_s dependence on the frequency. Comparing the imaginary parts of Z_{noHV} in equation (3.15) and of Z_{rC_s} in equation (3.16), we obtain an ω–dependent expression for C_s, that is related to the L and C values by the following:

$$C_s(\omega) = \frac{C}{1 - (\omega/\omega_0)^2} \qquad \omega_0 = \frac{1}{\sqrt{LC}} \tag{3.17}$$

This expression can be used to measure the L and C values: once measured C_s vs frequency, one can find the resonance ω_0 (vertical asymptote), then take a C_s value at a given ω and work out C from equation (3.17). The advantage of this method is that the measurement is independent of $\text{Re}(Z)$, hence of the contact resistor r.

In practice, the model assumed in Figure 3.9 (left) is not adequate to describe in detail the detector, as it does not account for the paths parallel to the Middle gap capacitance, introduced by the Strips and Back sampling (see Figure 3.3). This is evident when performing a C_s measurement on any Middle channel, as that shown in Figure 3.10, with SB (top) and for separate gaps (bottom). In the intermediate frequency range (20 kHz÷2 MHz) a regular slope can be observed, where a plateau was expected from equation (3.17). However, introducing Strips and Back in the model describes correctly this slope, as it is shown in Figure 3.11. This proves that the presence of Strips and Back is in principle not negligible[5].

In Figure 3.10(bottom) differences among gaps belonging to the same η are evident. First, two gaps (number 1 and 3) exhibit similar trends, but n. 3 is systematically higher than n. 1: this is due to gravity, because lower gaps are subject to larger pressure and are therefore more squeezed. Moreover, gap n. 2 (the one where physics injection is applied) shows a clearly different trend: this is due to the injection RC circuit put in parallel to the gap capacitance, as is evident from simulation in Figure 3.12. It must be noted that all these effects are well evident in a C_s-vs-freq plot, but not quite in the corresponding $|Z|$-vs-freq plot.

[5]The effects of Strips, Back and injector on the physics and calibration signals will be discussed in Section 3.6.

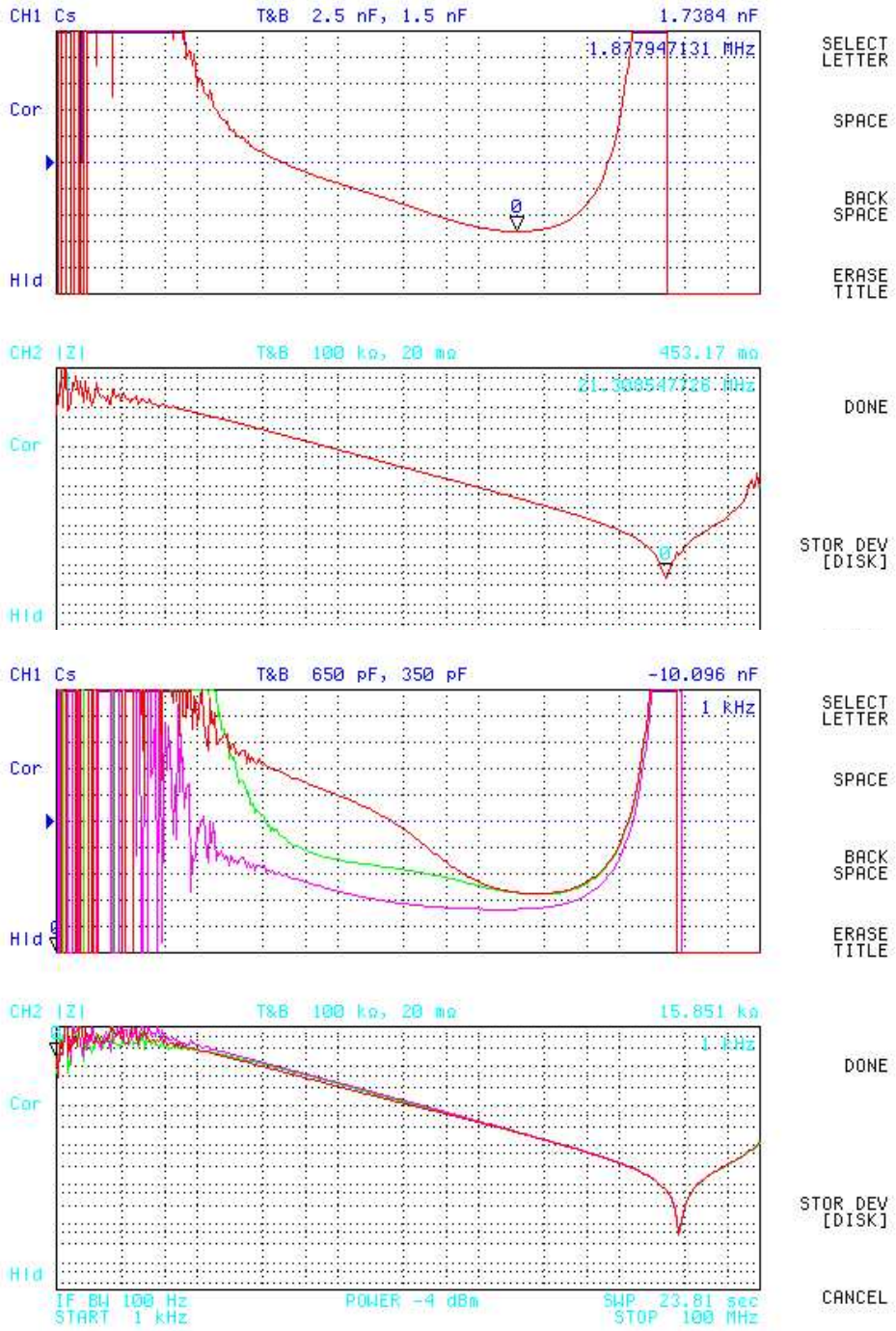

Figure 3.10: Typical measurements of C_s and $|Z|$ as functions of frequency for: (top) 4 gaps connected by the SB, and (bottom) single gaps nn. 1, 2, 3. The horizontal scale is logarithmic between 1 kHz and 100 MHz. In the bottom plot, the gap with anomalous trend (the "knee" at $\approx$ 15 kHz) is n. 2, where the physics injection is applied.

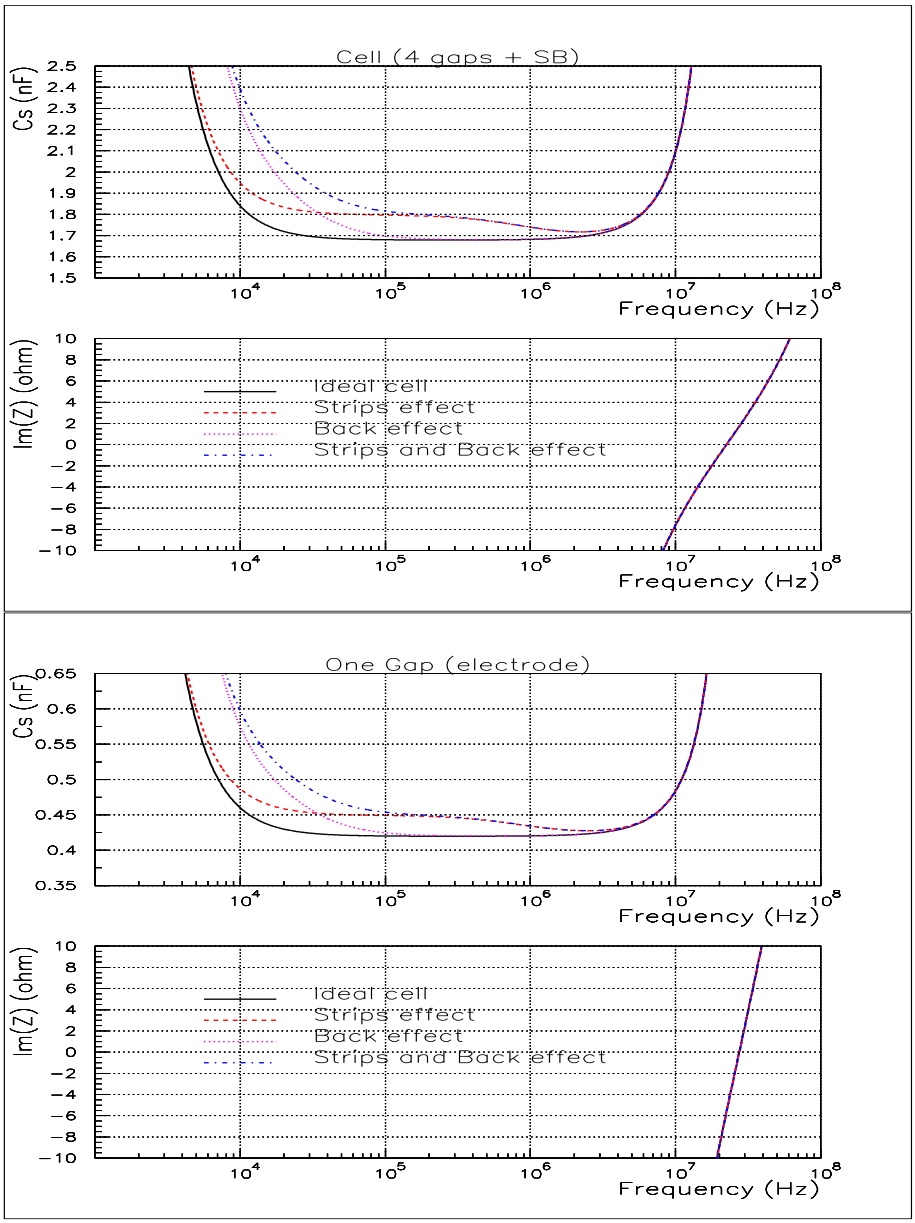

Figure 3.11: Simulation of the Strips and Back effect on C_s and $X = \mathrm{Im}(Z)$ for: (top) 4 gaps connected by the SB, and (bottom) a single gap. The four curves describe the predicted trend for Middle only (solid), Middle+strips (dashed), Middle+back (dotted) and Middle+strips+back (dash-dotted). In the simulation, typical values for the detector parameters are used.

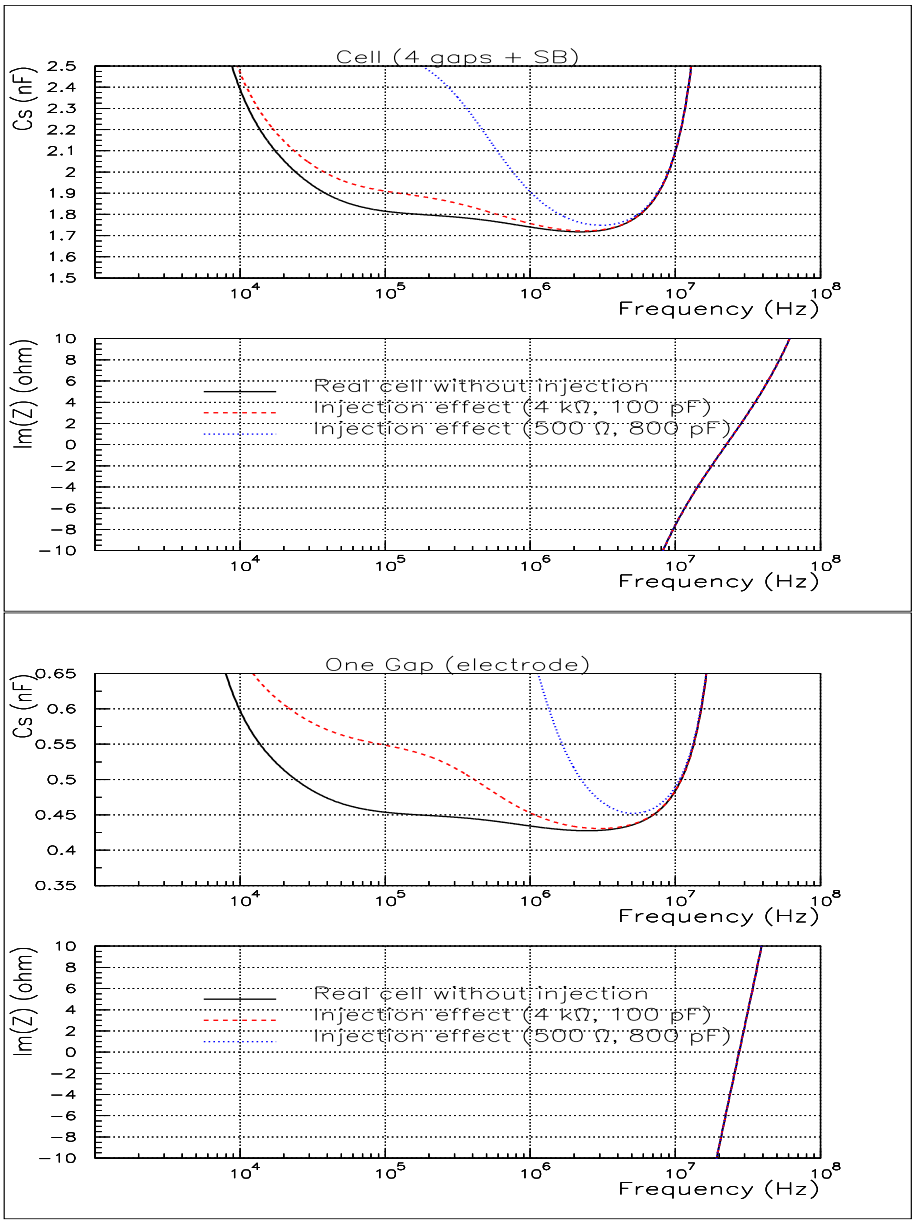

Figure 3.12: Simulation of the physics injector effect on C_s and $X = \mathrm{Im}(Z)$ for: (top) 4 gaps connected by the SB, and (bottom) a single gap. The solid line is the trend without injector; the dashed line is the distortion due to the presence of the 4 kΩ - 100 pF physics injector (i.e. the one in use); the dotted line shows that decreasing R while keeping RC constant, increases the distortion.

As shown in Figures 3.11 and 3.12, the effect of strips, Back and injector does not affect the value of $\mathrm{Im}(Z)$ near the resonance, where it can be described as:

$$X_{\mathrm{res}} = \omega L - \frac{1}{\omega C} \tag{3.18}$$

Therefore, L and C are extracted by fitting the function (3.18) to the data in a frequency range between $\pm 1.5\%$ around the zero crossing[6]. The frequency interval for the fit has been chosen in order to keep the result stable. Typical precision, estimated by repeating the frequency scan few times over the same cells and refitting, are $\delta C \approx 15$ pF and $\delta L \approx 5$ nH.

3.4.2 Results from L and C measurements

Capacitance and inductance measurements have been carried out over the first 16 middle channels and 8 Back channel of the *mock–up* corresponding to the region $0.8 \leq \eta \leq 1.2$, or to Middle cells 32÷47. For each channel, measurements have been performed both on single gaps and on the SB.

Connectors 1 and 3 (middle cells 32÷35 and 40÷43 respectively) are equipped with two ground springs each, while connector 4 (middle cells 44÷47) has only one ground spring on the low-η side. Connector 2 (middle cells 36÷39) was originally equipped with one ground spring, but a second removable one has been added, and C, L measurements have been performed both with one and two ground springs.

The C, L scan along η for single gaps, with two ground springs on connector 2, is displayed in Figures 3.13 and 3.14 for Middle and Back samplings, respectively.

The L measurements show a very good agreement, within few nH, among the different gaps, which is expected since the inductive paths are located on the electrodes, and therefore must be equal to each other. In the Middle sampling, a "high-low-low-high" pattern with periodicity 4 cells is clearly visible: this is evidently due to the readout electrode layout.

The C measurements show similar trends for gaps nn. 1, 3, 4: the absolute difference is explained by the dielectric compression due to absorbers weight, which causes lower gaps to exhibit larger capacitances. The anomalous trend on gap n. 2 in the Middle sampling is due to the presence of the coaxial cables connected to physics injectors: all cables enter the *mock–up* from the large-η edge, and each ends on a different cell, therefore there is more material in the gap at large η than at low η. This phenomenon has been understood quantitatively, and it is also a validation of the precision achieved in the measurement.

The C, L scan along η with the SB (i.e. summing together the four gaps) is displayed in Figures 3.15 and 3.16 for middle and Back samplings, respectively. Here, measurements are performed both with one and two ground springs on connector 2: the effect can be observed on cells 36÷39. When removing the ground spring on the large-η side, the measured inductances increase, especially near the side where the ground is removed, while the C values are essentially unchanged. The increase in the measured inductance indicates

[6] X_{res} is null for $\omega = \omega_0 = 1/\sqrt{LC}$, and the slope is $(\mathrm{d}X_{\mathrm{res}}/\mathrm{d}\omega)_{\omega=\omega_0} = 2L$, therefore the curve of X around the resonance contains sufficient information to extract L and C.

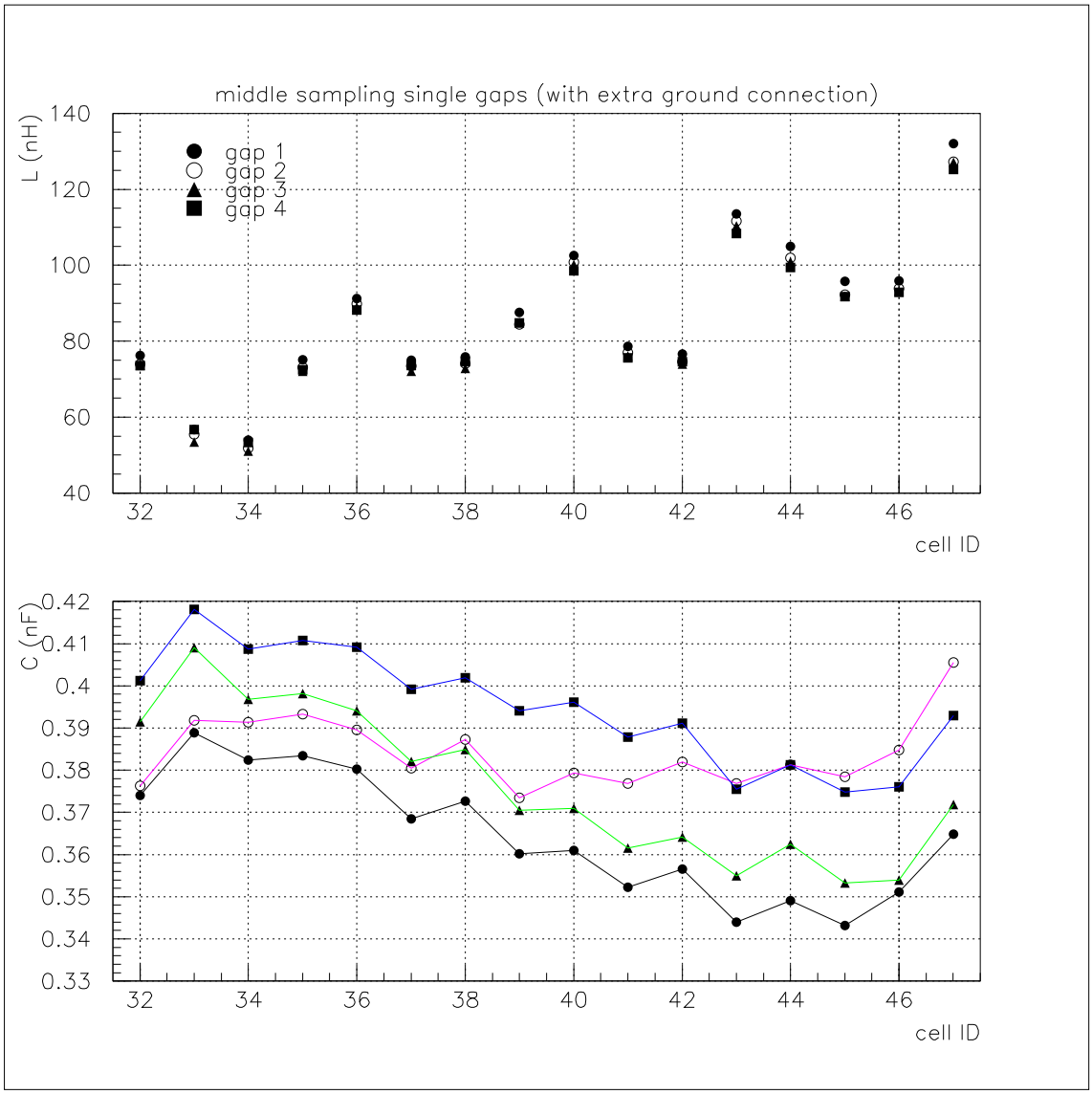

Figure 3.13: Measurements of the L,C values for single Middle gaps in the region $\eta = 0.8 \div 1.2$, corresponding to Middle cells 32÷47. Only connector 4 has one ground spring.

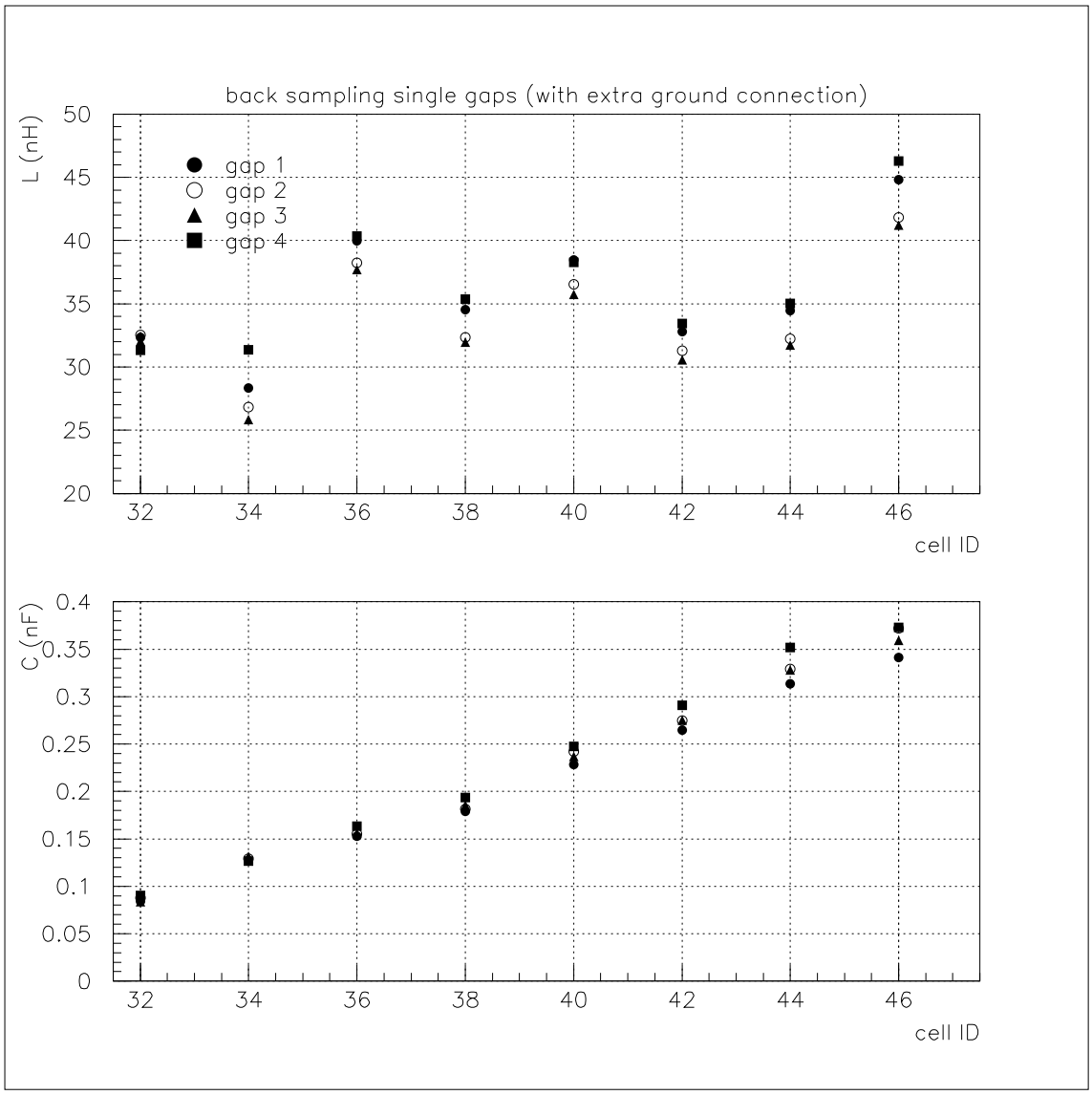

Figure 3.14: Measurements of the L,C values for single Back gaps in the region $\eta = 0.8 \div 1.2$, corresponding to Middle cells 32÷47. Only connector 4 has one ground spring. Back cells numbering refer to the corresponding "even" Middle cell.

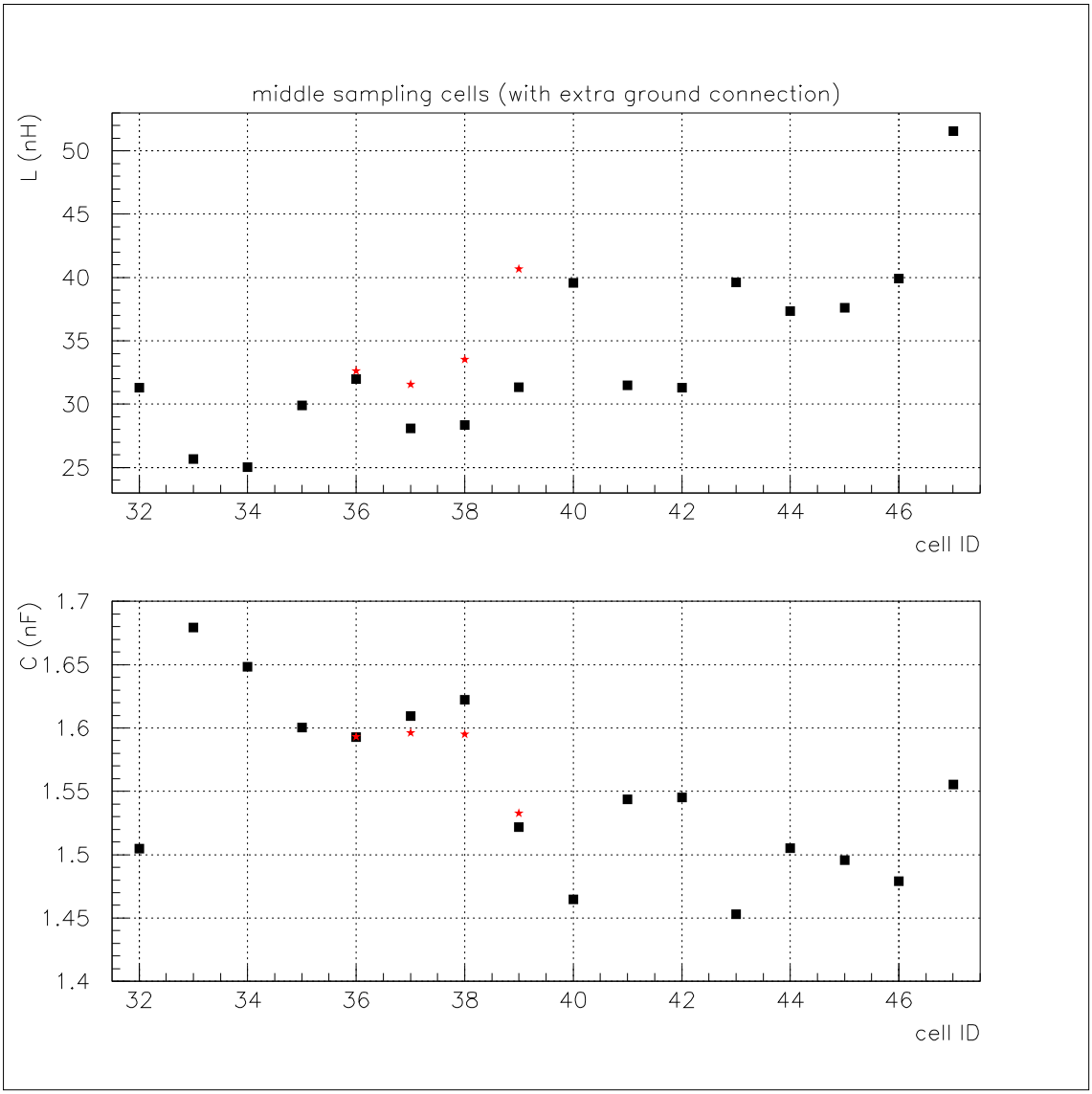

Figure 3.15: Measurements of the L,C values for Middle cells with SB, in the region $\eta = 0.8 \div 1.2$, corresponding to Middle cells 32÷47. Connector 4 has one ground spring. For connector 2 the measurement has been performed both with two and one ground spring (squares and stars, respectively).

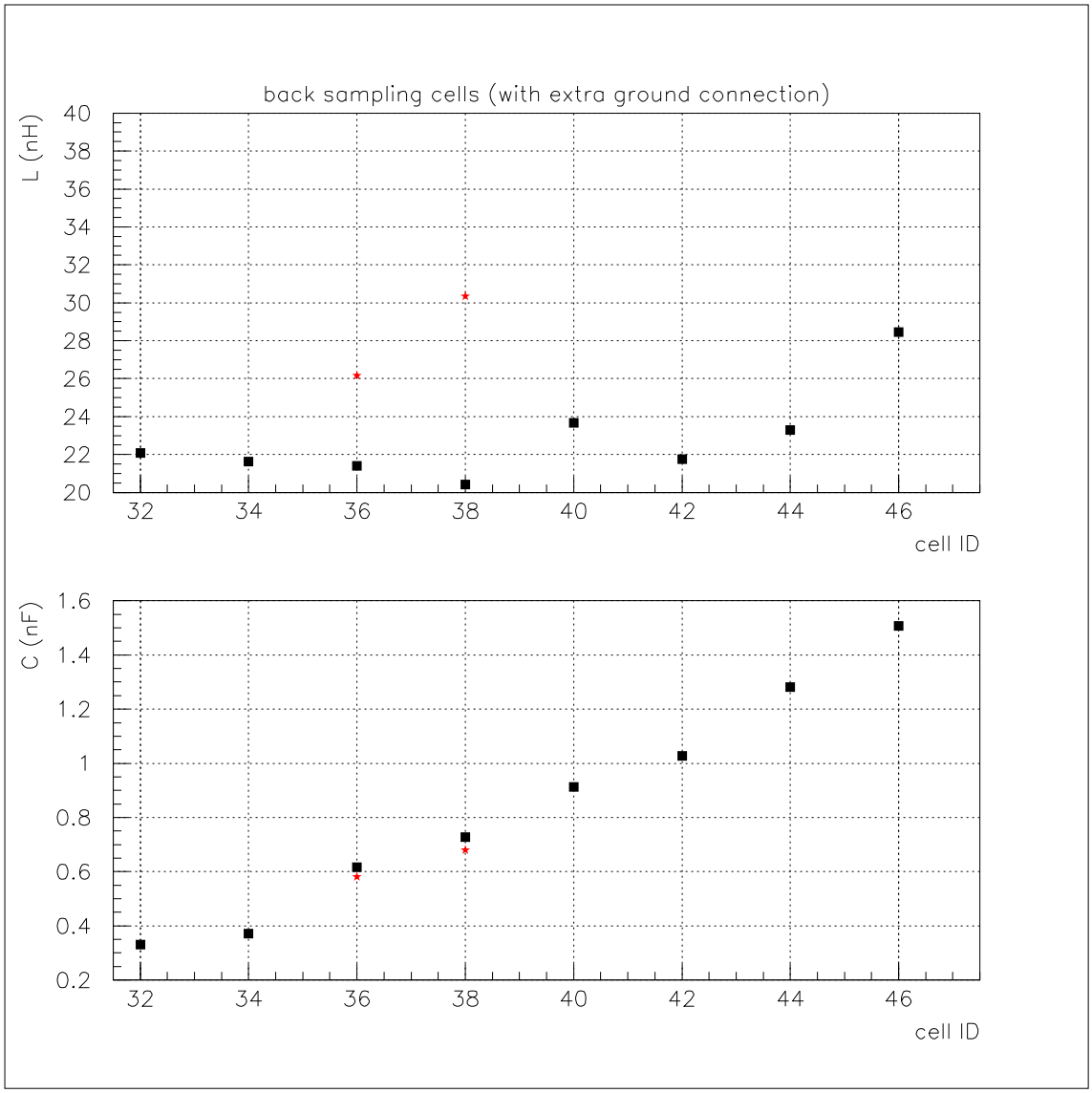

Figure 3.16: Measurements of the L,C values for Back cells with SB, in the region $\eta = 0.8 \div 1.2$, corresponding to Middle cells 32÷47. Connector 4 has one ground spring. For connector 2 the measurement has been performed both with two and one ground spring (squares and stars, respectively). Back cells numbering refer to the corresponding "even" Middle cell.

that the ground return path from the SB output to the absorber is also inductive, and more precisely the inductance is located partly on the SB "ground" plane and partly on the electrode. This feature is discussed in more detail in Section 3.6.

By comparing the measured L values with and without SB (see Figure 3.17) information can be extracted on the inductive signal path on the SB. Naively (i.e. neglecting the capacitances!) one would expect:

$$\frac{1}{L_{4\text{gaps}}} = \sum_{\text{gap}=1}^{4} \frac{1}{L_{\text{gap}}} \tag{3.19}$$

while the data show an offset between the two quantities, which could be taken as an estimate of the SB inductance (≈ 12 nH)[7].

3.5 Signal measurements on the *mock–up*

In the ATLAS LAr EMC, "physics" signals (originated by electromagnetic cascades) are like triangular current pulses closed on the detector capacitance C and read-out through a chain with input impedance Z_{ro}; therefore, the current seen is scaled by a factor $1/(1 + sCZ_{\text{ro}})$ (in the Laplace domain). This factor is not uniform over the calorimeter, since the C value varies along η. For this reason, the calorimeter has been designed to be electronically calibrated cell by cell, by sending a known current pulse in each channel and reading the output signal. Then, the physics signals must be scaled by a factor inversely proportional to the corresponding calibration signal amplitude.

This method works only in principle, since the physics and calibration current pulses are generated on different places in the detector, as already explained in Section 3.2. Therefore, the calibration procedure must be further refined. The *mock–up* provides a good tool to study these features. In particular, the dependence of physics and calibration signals on the detector capacitance and inductance have been studied, as well as the effect of having one or two ground springs on a SB connector.

3.5.1 Single physics injection

Physics and calibration signals have been injected on Middle cells 32÷39, corresponding to the region $0.8 \leq \eta \leq 1.0$. The pulse generator has been operated to generate a 3 V step-function, and the waveforms have been acquired on the Tektronix oscilloscope and then analyzed offline to find the peak amplitude and timing. For Middle cells 36÷39 the acquisition has been performed both with two and one ground spring.

Typical examples of physics and calibration waveforms after the shaping filter ($\tau_{\text{sh}} =$ 15 ns) are displayed in Figure 3.19. The calibration waveform (right) differs from the physics waveform (left) especially for the "shoulder" on the rise. This effect, which is also predicted by simulations, is due to the cell inductance, which is seen in series with the read-out by the physics signal, but in parallel by the calibration. The effect is even

[7] This inductance is located on the signal output path, and is not to be confused with the inductive ground return mentioned before.

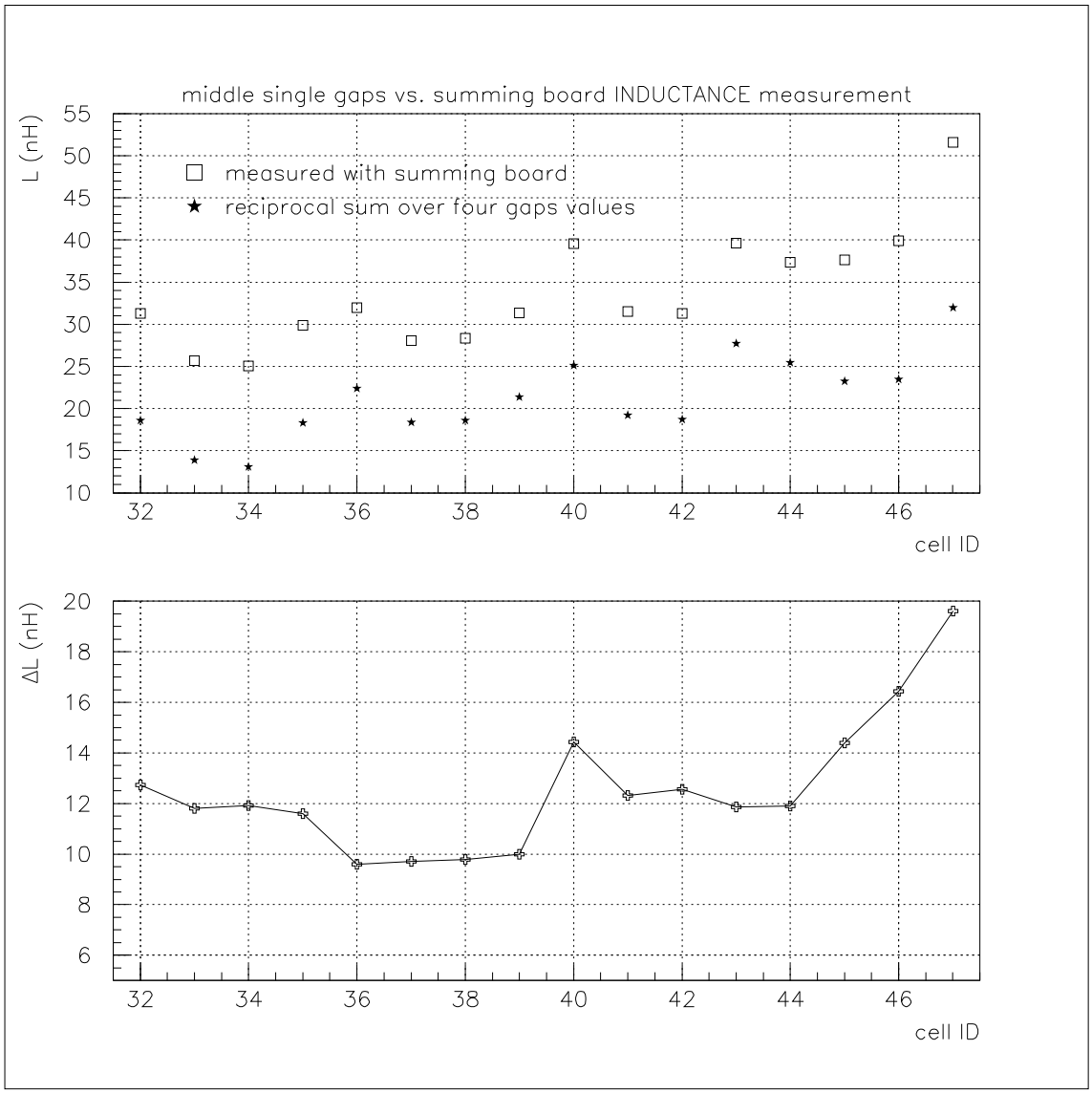

Figure 3.17: Comparison of L measurements with and without summing board.

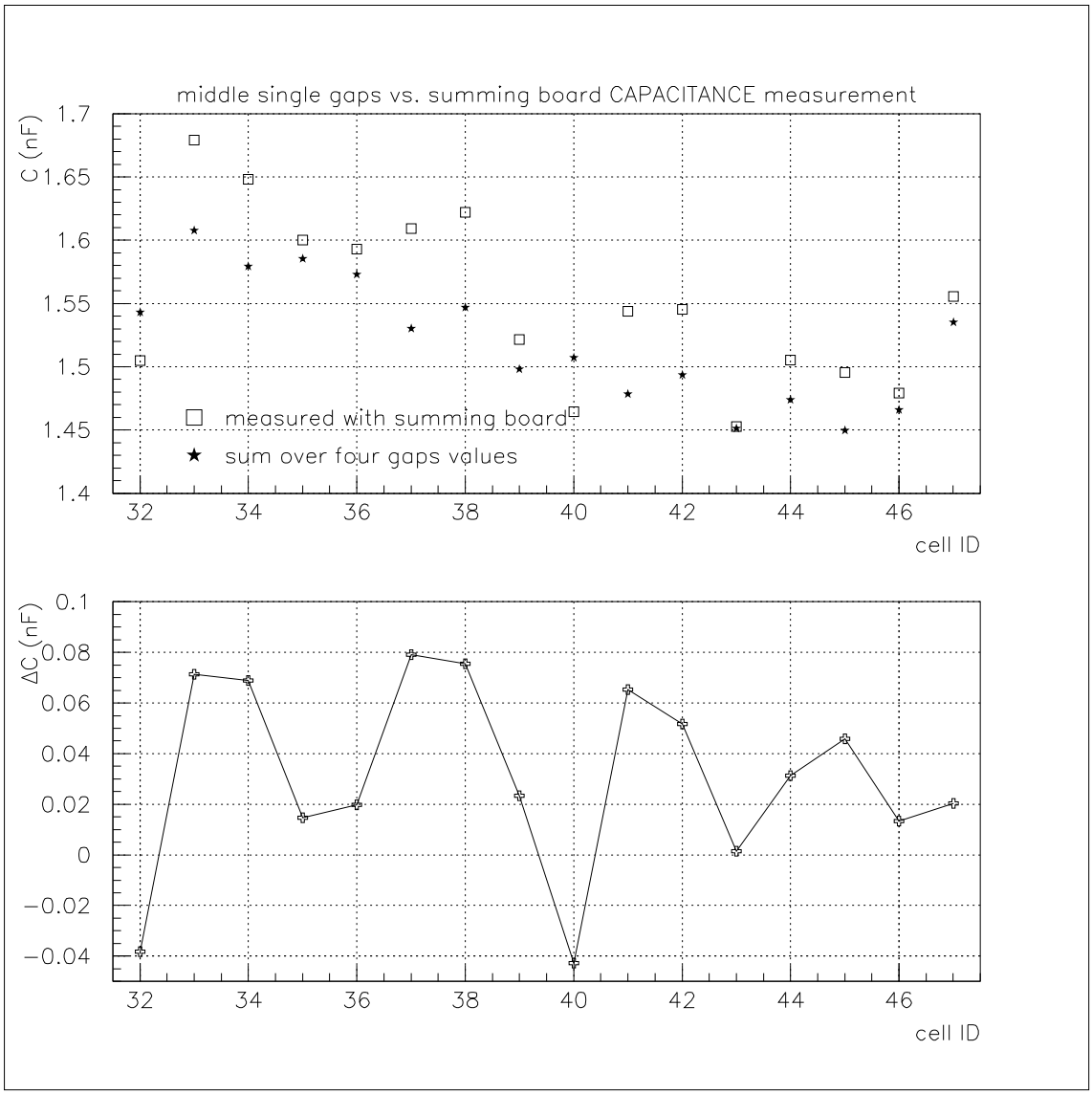

Figure 3.18: Comparison of C measurements with and without summing board.

more evident when the shaping time is decreased from 15 ns to 5 ns, in which case the "shoulder" becomes a sharp peak.

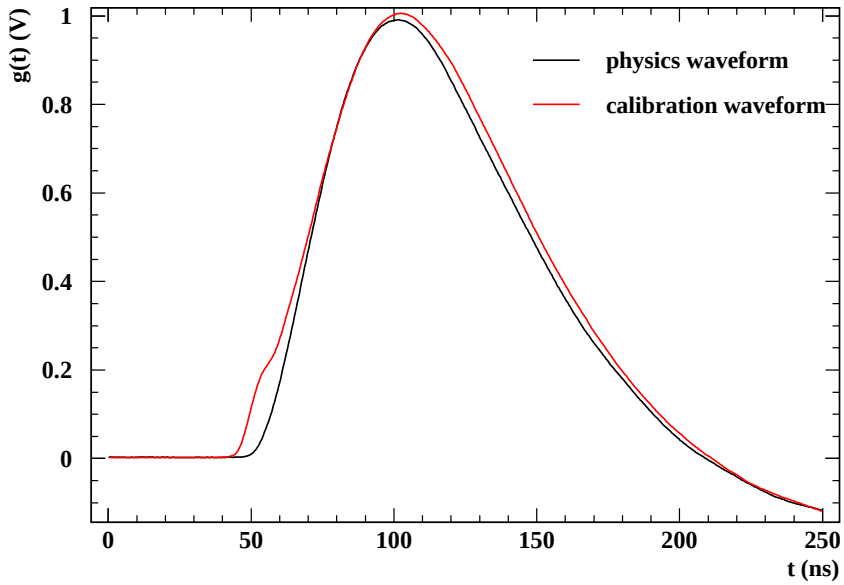

Figure 3.19: Typical waveforms shaped at $\tau_{sh} = 15$ ns, for a physics (black) and a calibration (red) signal, acquired on the same cell (middle 39 with two ground springs).

In Figure 3.20 some correlations between signal amplitudes and C, L cell parameters can be observed. Figures (a) and (b) show that an increase in C determines a decrease in both the physics and calibration peaks; here the correlation is not so evident, because the signal amplitude is influenced also by other parameters, such as L. In figure (c) the correlation between physics and calibration amplitudes is evident, which legitimates the procedure of correcting the physics signal by the inverse of the calibration. However, even after this correction, the cells equalization is not complete, as a dependence on the inductance L is still manifest, as in figure (d). Here, it is also evident that the removal of one ground spring increases the effective inductance and at the same time increases the physics-to-calibration ratio.

The η-scan for physics and calibration measurements is displayed in Figure 3.21. Physics and calibration oscillate with a peak-to-peak variation of $\sim 3\%$, following similar patterns. The effect of the 2^{nd} ground spring removal is most evident on Middle cell 39, where the inductance variation is most sizable; the signal distortion is $+0.6\%$ for the physics, -0.8% for the calibration, and $+1.4\%$ for the physics-to-calibration ratio. The removal of the 2^{nd} ground spring affects also the response uniformity over the examined 8 Middle cells: the r.m.s. non–uniformity in the physics-to-calibration ratio increases from 0.3% to 0.6%, while the peak-to-peak deviation increases from $\sim 1\%$ to $\sim 2\%$.

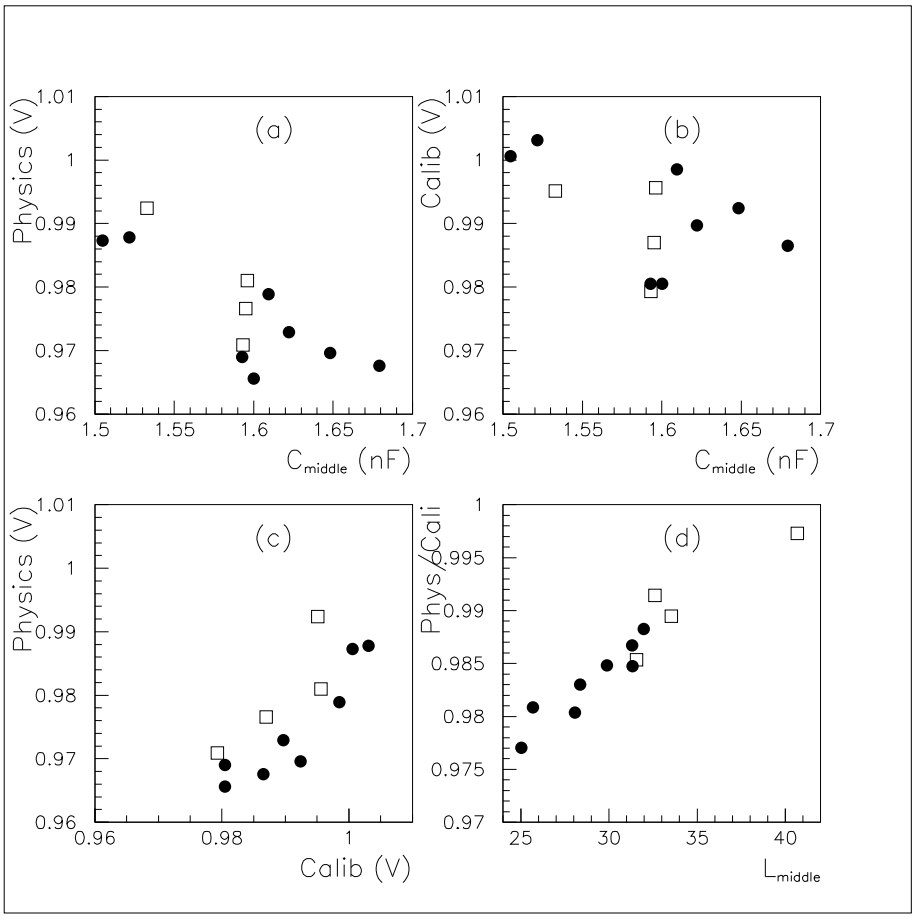

Figure 3.20: Correlations among signal amplitudes and C, L cell parameters. Measurements are displayed both for two ground springs (solid circles) and one ground spring (open squares).

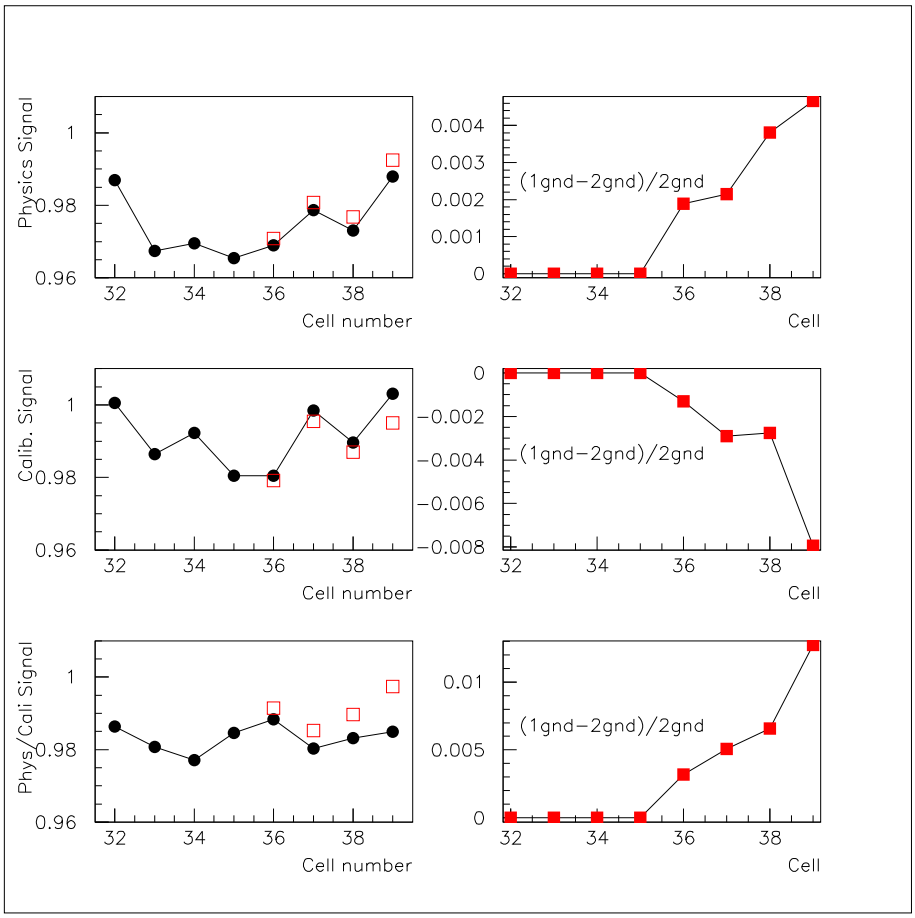

Figure 3.21: Physics and calibration signal measured as a function of η. The plots on the left show the peaks of the output shaped signals for "physics"and "calibration" injection in cells 32÷39 from Middle sampling, and the ratio between the two. Solid circles (open squares) refer to measurements performed with two (one) ground springs per connector. The corresponding plots on the right show the relative deviation between the two ground configurations.

3.5.2 Multiple physics injection

To simulate the effect of grouping neighboring cells into a "cluster", as it happens in the real detector offline analysis, a multiple "physics" injection has been performed on groups of three contiguous cells. The central cell and the two side cells of each group are injected with 2.4 V and 0.3 V step-function, respectively, in order to mimic a 10%-80%-10% energy sharing[8].The calibration signals have been injected on single cells [9].The region $0.8 \leq \eta \leq 1.05$ has been scanned, corresponding to Middle cells 32÷41.

In the *mock–up* framework the amount of current injected to generate the calibration signal is always the same for each cell: following the standard EMC calibration strategy, we define the "gain" of each readout channel as $G_m = \frac{1}{E_m^{\rm cali}}$, where $E_m^{\rm cali}$ is the calibration signal amplitudes measured at the end of the readout chain (i.e. after the shaper) on cell m. The calibrated cluster "energy" around cell k ($32 \leq k \leq 40$) is then computed as the sum of the calibrated "energy":

$$E_k^{\rm clus} = \sum_{m=k-1}^{k+1} G_m E_m^{\rm phys} = \sum_{m=k-1}^{k+1} \frac{E_m^{\rm phys}}{E_m^{\rm cali}} \tag{3.20}$$

where $E_m^{\rm phys}$ is the physics signal amplitudes measured at the end of the readout chain on cell m.

The results are shown in Figure 3.22. Clusters around cells M32 and M41 are about 10% lower than the others, because one of the side cells is missing (cell M31 and M42 respectively). Clusters around cells M33÷M38 (two consecutive connectors, excluding cell M32) exhibit a spread of 0.3% (0.45%) when two grounds are (one ground is) connected. Removing the 2$^{\rm nd}$ ground from the 2$^{\rm nd}$ connector, the maximal deviation is observable in the cluster around cell M39, amounting to 1.1%.

[8]In test–beam data analysis, clusters are obtained grouping 3×3 Middle cells. By requiring that the energy centroid be well centered with respect to the central cell, the energy sharing for a 300 GeV electron is about (in percentage):

0.75	7	0.75
7	69	7
0.75	7	0.75

therefore, projecting onto the η axis, one gets 8.5%-83%-8.5%, similar to the sharing used here.

[9]This is slightly different from what happens in the real calorimeter, where more than one cell are pulsed at the same time, according to the pattern:

3	4	1	2
1	2	3	4
3	4	1	2
1	2	3	4

This fact might induce signal distortions in the pulsed cells, due to cross-talk effects.

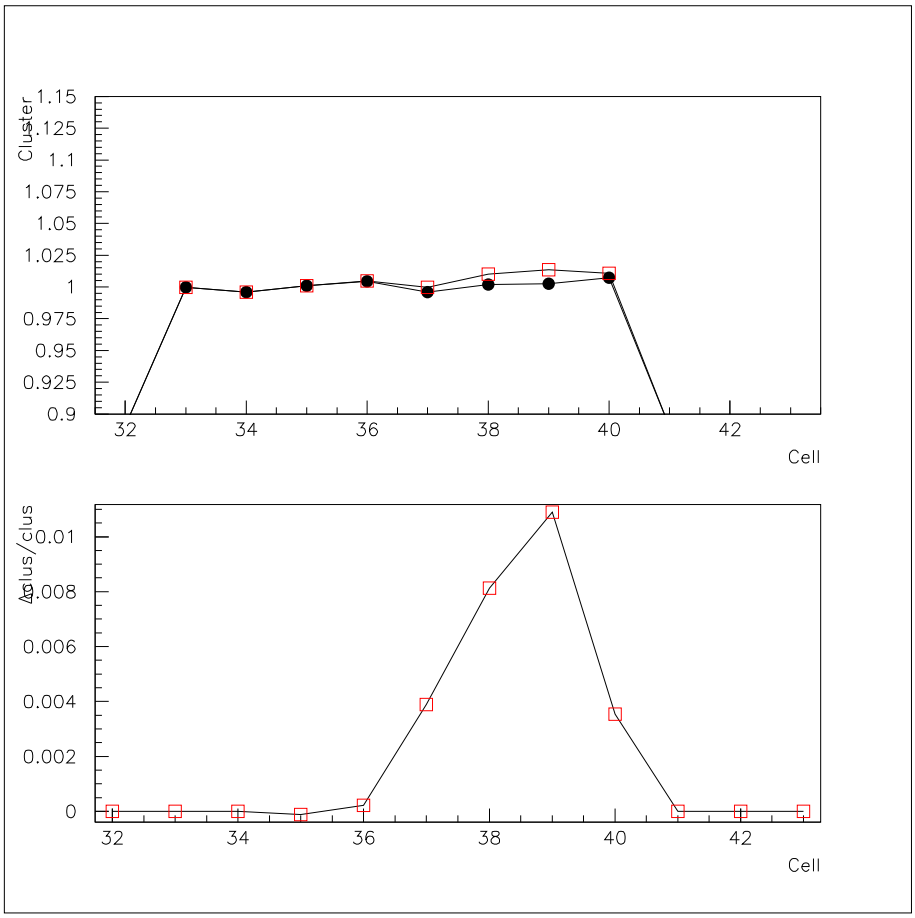

Figure 3.22: Signal amplitudes, measured as a function of η, for calibrated cluster obtained by injecting 80% of the signal in the central cell and 10% in each of the side cells. In the top figure, solid circles (open squares) refer to measurements performed with two (one) ground springs per connector. The bottom figure displays the relative variation between the two configurations.

3.6 Signals simulation

The response of the *mock–up* detector both to a "physics" and to a "calibration" pulse has been simulated using a SPICE [61] equivalent circuit model, performing a transient analysis while injecting the cells in the appropriate place of the network. The goal of the simulation is to to test the accuracy of the model used to describe the detector. It has been also possible at the same time to investigate the dependence of the response to the pulses on the values of the lumped elements of the network.

3.6.1 Effective detector description for simulation

Since the electrode model discussed in Section 3.2.2 is too complex to be suitable for a simulation, we develop an effective description of the six cells that share the same SB (four cells in the Middle and two in the Back sampling), starting from the "reasonably simplified" equivalent circuit of one detector cell shown in Figure 3.3.

The effect on the distribution of the ground voltage reference on SB itself and the capacitive coupling between neighboring cells is taken into account. This complete equivalent circuit model of the six cells is shown in Figure 3.23.

The full complexity of the circuit is anyway not necessary to accurately simulate the electrical behavior of the *mock–up* cells. The final equivalent circuit used in the simulation is somehow simpler, mainly because of the following two assumptions:

- A cell, composed by four LAr gaps joined together by a SB, is well represented in the useful frequency range by an effective single capacitance and an effective single inductance connected in serie. It is reasonable to neglect the effect of the kapton capacitances, since in the SPICE circuit the effective C and L values, measured as described in Section 3.4, are used. Mutual inductances between neighboring channels are also neglected.

- The effect of the resistive coupling between the cells of the Middle and the Strips (drawn as R-C branches in parallel to the Middle gap capacitances in Figure 3.23) causes an attenuation of -0.3% on the signal peak. This distortion is quantitatively the same (within 0.02%) for physics and calibration signal, and it does not depend on the cell parameters (L, C, etc.), therefore it does not affect the uniformity, and cancels out when evaluating the physics-to-calibration ratio. The presence of physics injectors in gap n. 2 affects the calibration signal by a -0.3%, again uniformly over the different cells. For this reason, the Strips and the physics injectors have not been included in the simulation. Similar arguments prove that the HV bias resistances can be neglected in the simulation.

Other basic characteristics of the model used in the simulation are the following:

- The six read-out lines take the ground reference from the same shared SB. This "ground return" path is naively modeled by an inductive chain, exactly as shown in Figure 3.23. The inductance between two neighboring channels is supposed to be

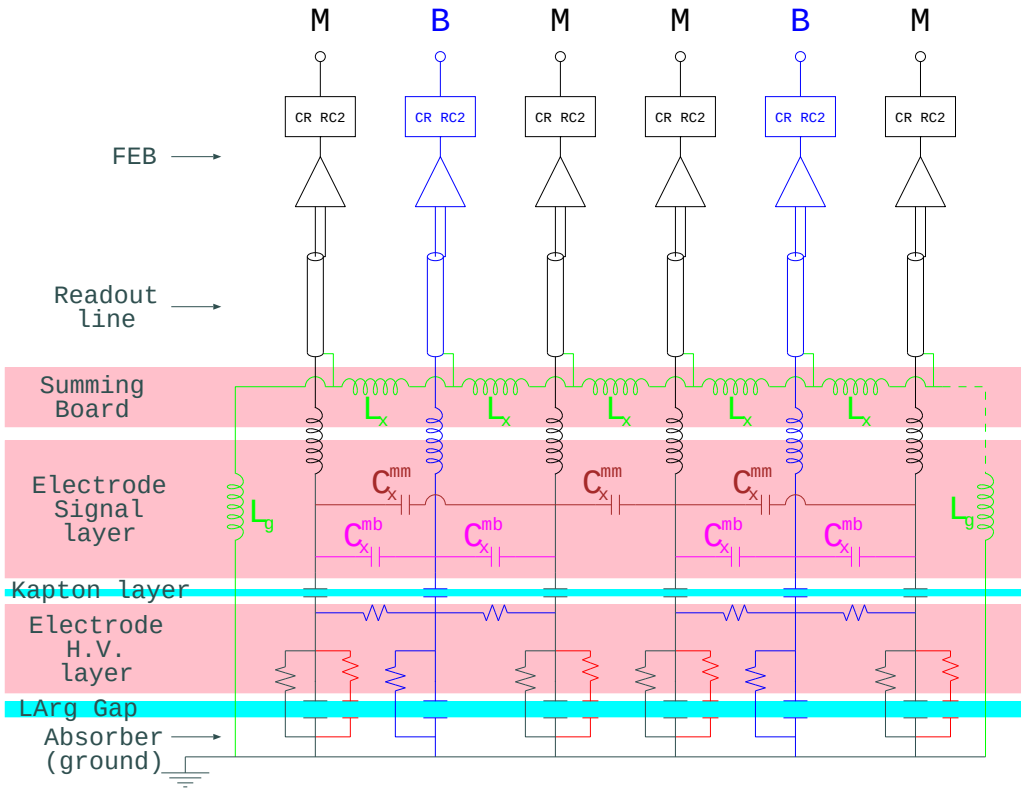

Figure 3.23: Complete equivalent circuit describing six cells (four from Middle and two from Back sampling) sharing the same SB. The inductive ground return path and the cross capacitances between neighbor cells are shown.

small and equal (L_x) for each pair of neighboring cells. The ground plane on the SB is connected to the ground reference on the absorber planes by two inductive paths (L_G) going to the ground springs (see Section 3.6.2 for details on L_x and L_G calculation). The effect of the absence of the of the second ground connection in cells 36÷39 is simulated by removing one of the two L_G in the large-η side.

- The capacitive coupling between neighboring cells has been described connecting the channels with cross capacitances (C_x). The direct measurement of the C_x values on the *mock–up* is difficult and really imprecise. In the simulation we used one single value for the C_x between every two adjacent Middle cells ($C_x^{mm} = 80$ pF), and one for the C_x between every Middle cells and its neighboring Back ($C_x^{mb} = 5$ pF). These values have been estimated from the low-voltage test measurements on the electrodes.

- For every cell the readout chain is represented by a 25 Ω resistance, that simulates the behavior of a perfectly terminated line followed by a perfect preamplifier with infinite flat bandwidth. After this termination resistance an equivalent circuit for a CR-RC^2 shaper is connected. This is modeled as a chain of CR or RC stages, each powered by a voltage source driven by the output voltage of the previous stage.

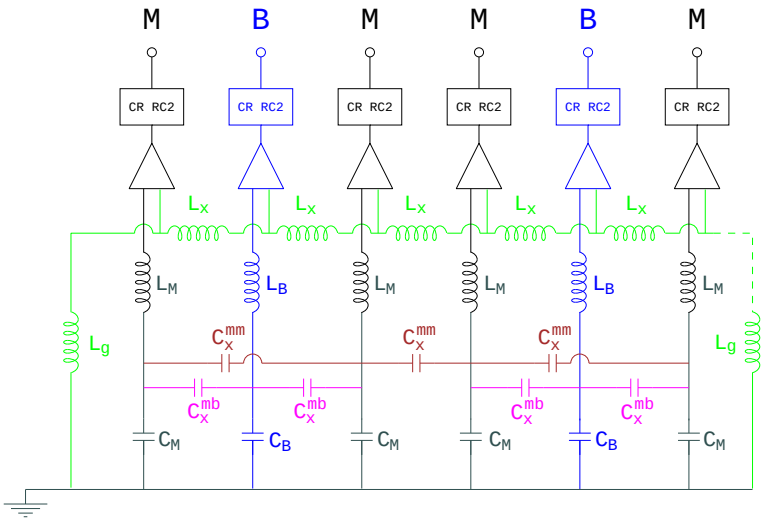

Figure 3.24: Simplified equivalent circuit used for the SPICE simulation, describing six cells (four from Middle and two from Back sampling) sharing the same SB.

The actual equivalent circuit used for the simulation is shown in Figure 3.24. The simulation is performed on a global equivalent circuit describing 12 cells of the Middle sampling (32÷43) and the corresponding 6 cells of the Back sampling. C and L values are taken from measurements described in Section 3.4. The circuit corresponds to 3 SB. The measured values for the cells effective capacitances and inductances are used for all the cells of the Middle and Back samplings of the *mock–up*. Cross-capacitances between

neighboring cells of the Middle sampling sharing different SB have been added, their values being estimate from the standard low–voltage RC tests performed on the electrodes.

Results of the simulation using this effective circuit and comparisons with measurements on the hardware model are discussed in Section 3.6.3.

3.6.2 Inductive ground return estimate

For the cells belonging to the second SB (middle cells from 36 to 39) the measurements of the effective values of capacitances and inductances has been performed both with and without the second ground connection. We find compatible values for the effective capacitance, and, as expected, different values for the effective inductance. These pairs of different L values are used to estimate the components L_x and L_G of the inductive ground return path.

Calling L_k the specific inductance, located on the electrode, of the k-th cell out of the n sharing the same SB, according to the model shown in Figure 3.23 the k-th channel sees an effective total inductance amounting to:

$$\begin{aligned} L_k^{\text{2gnd}} &= L_k + (L_G + (k-1)L_x) \parallel (L_G + (n-k)L_x) \\ &= L_k + \frac{L_G^2 + (n-1)L_G L_x + (n-k)(k-1)L_x^2}{2L_G + (n-1)L_x} \end{aligned} \tag{3.21}$$

in the case where both of the ground springs are connected, or

$$L_k^{\text{1gnd}} = L_k + L_G + (k-1)L_x \tag{3.22}$$

in the case where only one is connected. In this evaluation, possible effects due to mutual inductances have been neglected. The difference between these two values is:

$$\Delta L_k = \frac{(L_G + (k-1)L_x)^2}{2L_G + (n-1)L_x} \tag{3.23}$$

from which it is possible to calculate the values of L_x and L_G, since:

$$\Delta L_n - \Delta L_1 = (n-1)L_x \tag{3.24}$$

$$L_G^2 = \Delta L_1 \, (2L_G + (n-1)L_x) \tag{3.25}$$

The values of the effective inductance measured on the *mock–up* for cells 36÷39 of the Middle sampling and 36 and 38 of the Back sampling are shown in Figure 3.25, versus their relative position on the SB itself (M36, B36, M37, M38, B38, M39). An increasing trend is clearly visible when removing the second ground connection.

The estimate of L_x and L_G has been done using the global variation of L between the two edge channels on the SB ($k = 1$, Middle cell 36; $k = 6$, middle cell 39): $(\Delta L_6 - \Delta L_1) = 5L_x \simeq 8.7$ nH from which we obtain the values:

$$\begin{aligned} L_x &\simeq 1.7 \text{ nH} \\ L_G &\simeq 3 \text{ nH} \end{aligned}$$

that are used in the SPICE equivalent circuit.

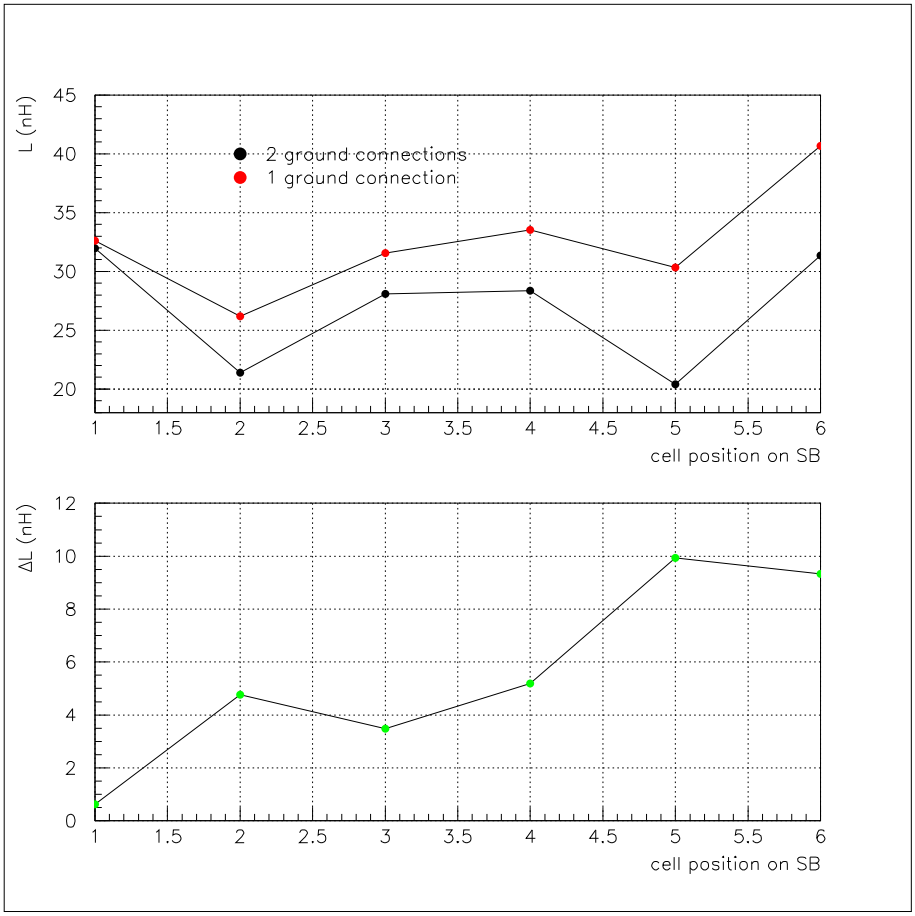

Figure 3.25: Effective L values of *mock–up* cells 36÷39 of the Middle sampling and 36 and 38 of the Back sampling, versus their relative position on the SB itself (M36, B36, M37, M38, B38, M39). On top the values measured with and without the second ground connection, on bottom the difference between the two series.

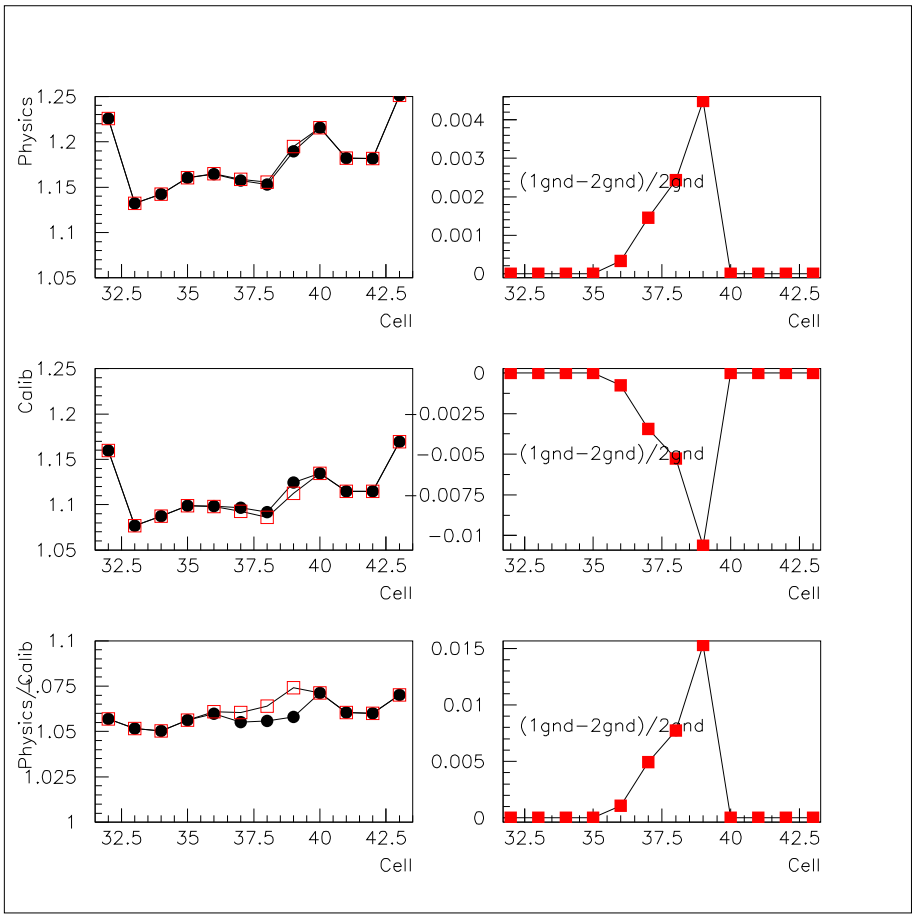

Figure 3.26: Results of simulation using the detector SPICE model. The plots on the left show the peaks of the output shaped signals for "physics"and "calibration" injection in cells 32÷39 from Middle sampling, and the ratio between the two. The two series in each plot refer to two-grounds (solid circles) and one-ground (open squares) configurations on the second connector. The corresponding plots on the right show the relative deviation between the two ground configurations.

3.6.3 Results and comparison with measurements

Results of the simulation are shown in Figure 3.26. The first two plots on the left show the peaks of the output shaped signals for "physics" and "calibration" injection in cells 32÷39 from Middle sampling. The two series of data in each plot refer to the values obtained using one or two ground connections in the second connector. The third plot on the left shows the ratio between the "physics" and "calibration" output signal peaks, again both for the one-ground and two-grounds configurations. The corresponding plots on the right show the relative deviation between the two ground configurations.

The trend of the "physics" and "calibration" output signals peaks is mainly driven by both the cell capacitances and the cross-capacitances values. The effect of the capacitance values is the same for both "physics" and "calibration" signals, and cancels out when calculating the ratio.

The output of cell 32 is significantly higher then the others, both in "physics" and in "calibration". This is due to the absence of a capacitive coupling to a neighboring cell on the small-η side: this is in agreement with what observed in the data collected on the *mock–up*.

The simulation predicts an increase of the "physics" signals, due to the absence of the second ground connection, that is roughly linearly dependent on the position of the cell in the SB. The maximum value of the relative increase is $+0.4\%$ for cell 39, which is farthest from the ground spring. A similar behavior is predicted for "calibration" output signals, that shows a linear decrease whose maximum value is -1.2% for cell 39. The overall effects of the absence of the second ground connection on the ratio between "physics" and "calibration" signal is $+1.6\%$ for cell 39. This result is in fair agreement with what observed on the *mock–up* (see Section 3.5). This leads to conclude that the set-up used to simulate the detector is correct, both in the equivalent circuit model and in the parameters values used.

Simulations similar to the one described above have been performed using different values of the equivalent circuit parameters. As mentioned before, the results are not sensitive to cell capacitances or cross capacitances values, at least in the ratio between "physics" and "calibration" output signals. On the other hand, this ratio is very sensitive to the inductance values, especially to the ground return path component L_x, as can be noticed from Figure 3.27.

The plots report the percentage variation on the output signal peaks on cell 39 from Middle sampling, between the configuration with one and two ground connections. It is evident that the effect increases linearly with the value of L_x; the proportionality constant is approximately 0.9% /nH[10]

3.6.4 Multiple physics injection

Similarly to what has been done for the signal measurements, a simulation has been carried out to study the performances of clusters. Three cells are injected at the same time, with

[10]This refers to a variation on the value of each L_x out of the five in the inductive ground chain. In every simulation the value of the two L_G is left equal to 3 nH each.

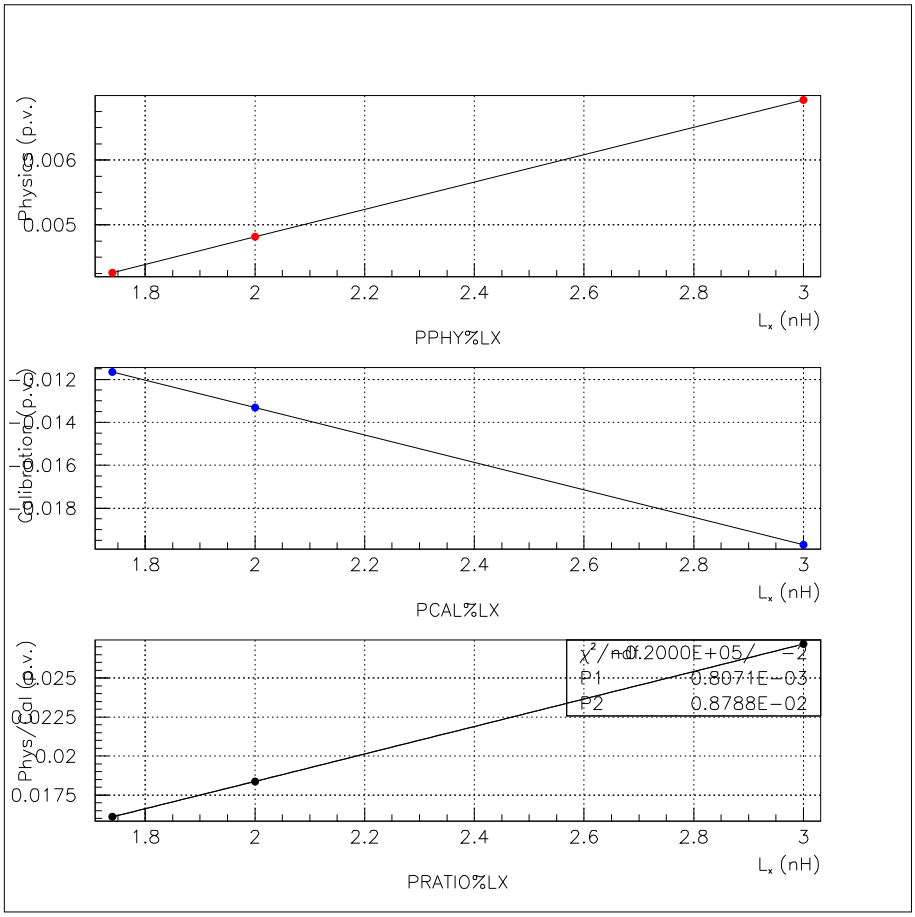

Figure 3.27: Percentage variation on the output signal peaks ("physics", "calibration", ratio between the two) on cell 39 from Middle sampling, between the configuration with one and two ground connections.

80% of the overall energy in the central cell and 10% in each side cell. The cell around which the cluster is built runs from M32 to M43.

The results are shown in Figure 3.28. Clusters around cells M32 and M43 are about 10% lower than the others, because one of the side cells is missing (cell M31 and M44 respectively). Clusters around cells M33÷M38 exhibit a spread of 0.3% (0.7%) when two grounds are (one ground is) connected. Removing the 2nd ground from the 2nd connector, the maximal deviation is observable in the cluster around cell M39, amounting to 1.5%.

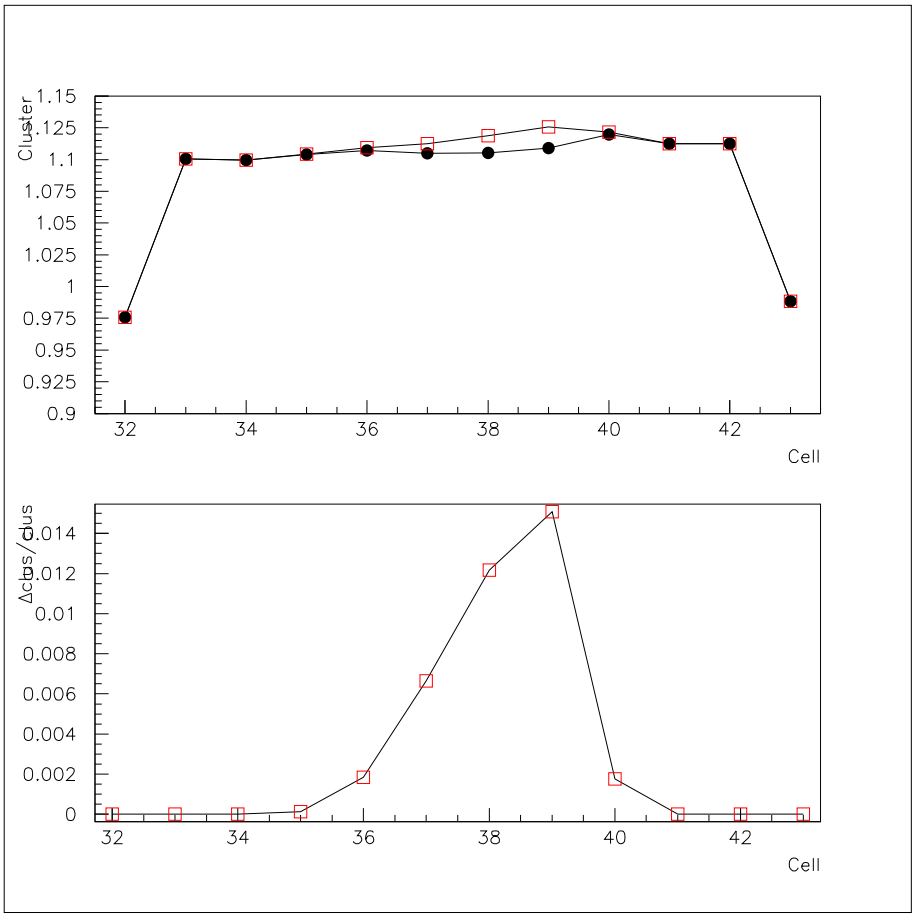

Figure 3.28: Signal amplitudes, predicted for calibrated cluster obtained by injecting 80% of the signal in the central cell and 10% in each of the side cells. In the top figure, solid circles (open squares) refer to measurements performed with two (one) ground springs per connector. The bottom figure displays the relative variation between the two configurations.

3.7 Summary and perspectives

The *mock–up* built in Milano proved to be a good apparatus to test in detail the electrical properties of the ATLAS LAr EMC. It has been possible to better understand the electrical behavior of the electrodes, and create a model with lumped elements that reasonably describes the observations. Signal waveforms are understood, both for ionization and calibration signals.

The system exhibits an *intrinsic non–uniformity* over the first eight Middle cells of electrode B (corresponding to $0.8 < \eta < 1.0$) of about 0.3%. This value is worsened when removing one ground spring from the 2^{nd} electrode-to-SB connector, becoming 0.6% for single injection and 0.45% for cluster-like injection. The effect of this distortion is mostly evident on Middle cell 39 ($0.975 < \eta < 1$), where the ground spring removal causes an increase of the physics-to-calibration ratio of 1.4% for single cell injection and of 1.1% for cluster-like injection. The values are in fair agreement with simulations, that predict respectively 1.6% and 1.5%. The simulations prove that the effect of removing one ground spring is due to the inductive nature of the ground reference on the SB, and amounts to $\sim 0.9\%/\text{nH} \times L_x$, where L_x is the inductance on the SB ground plane existing between two adjacent channels. As a direct consequence of the results of this study, the design of the EMB electrodes as been changed adding a second ground–connection spring to the connectors lacking of one. A picture of the modification is shown in Figure 3.29.

These results go in the right direction to explain the disuniformities observed in the 2000 EMB test-beam data, which are however at least a factor of two larger than observed on the *mock–up*. There are several reasons why we can expect the *mock–up* to give a better performance of a real module at the test-beam:

- In the "*mock–up*" we mimic the ionization signals with a single exponential pulse injected on a single LAr gap; in the test-beam the real ionization signal is triangular (see Appendix A for details), and it is generated by the charge released by the developing electromagnetic shower. No cross–talk is directly taken into account in the *mock–up*.

- The *mock–up* signals are not acquired through full readout chain (MB + cables + analogic and digital electronics), they do not suffer of reflections and electronics noise as in the test-beam.

- Finally, the *mock–up* signals are not digitized at the ATLAS 40 MHz sampling frequency as in the test-beam: the peak reconstruction is easier and more precise, since the oscilloscope provide a 1 GHz sampling, and we keep the whole extension of the signals up to 1 μs. As in the ATLAS experiment, in the test-beam only 5 samples every 25 ns are kept and used to reconstruct the signals amplitudes.

In the next chapters we devote our attention to this last point: we show how the signal reconstruction algorithm can magnify the system intrinsic non–uniformity, then we move to study how this non–uniformity can be cured by an *ad–hoc* improved reconstruction and calibration procedure.

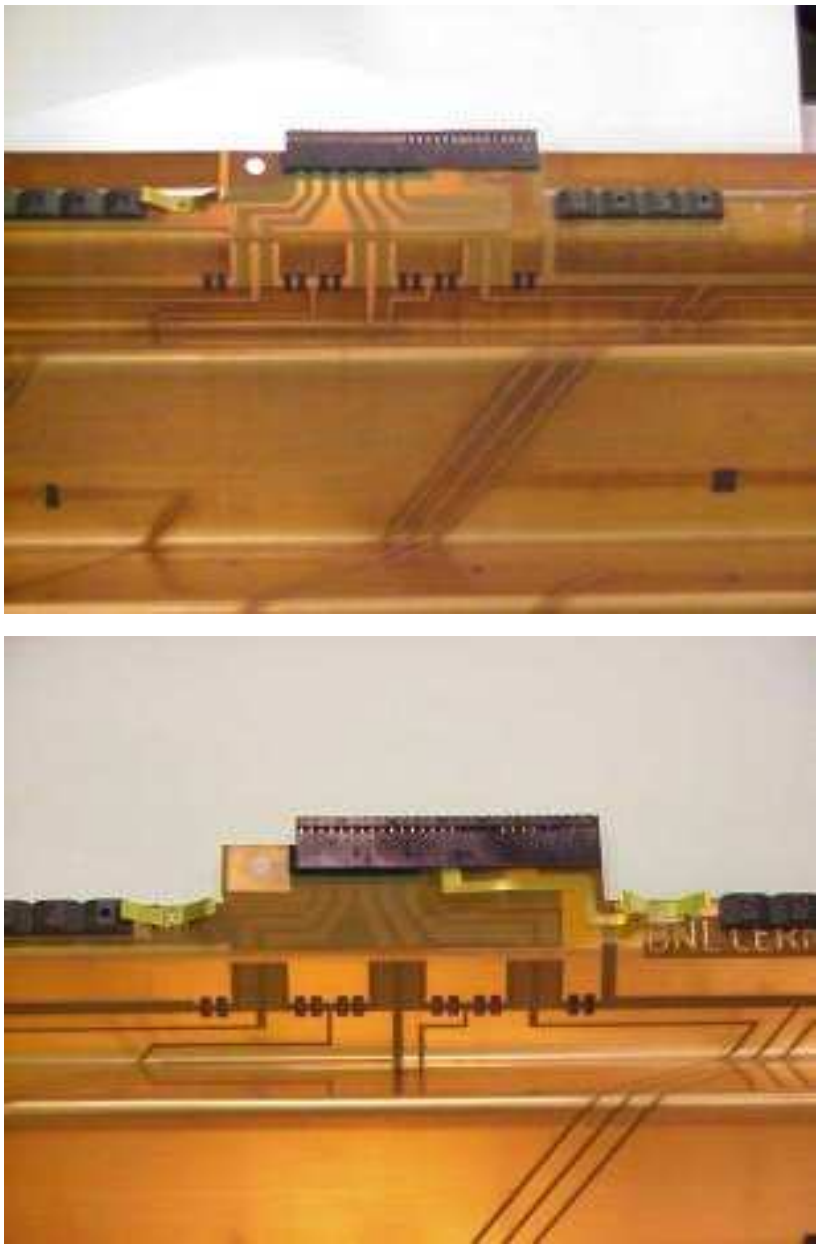

Figure 3.29: Ground connection spring modification on the EMB readout electrodes: (top) missing–spring old layout; (bottom) new symmetric layout.

Chapter 4

Signal reconstruction algorithms study

The EMC system intrinsic non–uniformity, that we showed to be related to the detector electrical properties, has been discussed in Chapter 3. We now focus the attention to the *signal reconstruction* (SR) algorithms.

In Section 4.1 we show the uniformity results when the same SR algorithm that is used to reconstruct the energy with the test-beam data discussed in Section 3.1 (Figure 3.1) is applied to the *mock–up* signals. We show that this SR algorithm ("*parabola*" SR) magnifies the intrinsic system non–uniformity. Using aagain the *mock–up* signals, we demonstrate then how the non–uniformity can be cured applying an *ad–hoc* correction (Section 4.2). We finally discuss how this correction can be applied to the data coming from the real detector system, in the framework of the *optimal filtering* SR technique (Section 4.3).

4.1 Analysis of the "*parabola*" SR algorithm

The ATLAS EMC data acquisition (DAQ) system is synchronized on the 40 MHz LHC bunch–crossing frequency; for obvious reasons, the same holds for the EMC test-beam DAQ system. In this case however the beam particles come asynchronous with respect to the DAQ clock: the ionization signals are therefore uniformly randomly distributed with respect to the 25 ns sampling period. The test-beam framework needs a SR system able to reconstruct the peak of the signals, whatever the delay between the sampling clock and the signal arrival time is. The so-called "*parabola*" algorithm is the first and simplest SR system that as been implemented in the reconstruction software for the EMC test-beam [52].

4.1.1 Algorithm working principles

The ionization signals emerging from each EMC readout cell are continuously sampled every 25 ns. When a physics event is accepted by the trigger system, 5 samples are digitized and saved. The "*parabola*" SR algorithm uses 3 out of the 5 saved samples to reconstruct

the amplitude and peak time of the signal. It is the SR technique used to analyze the data discussed in Section 3.1. The "*parabola*" SR algorithm attempts to retrieve the signal amplitude and arrival time values performing an interpolation of the digitized samples. The 25 ns sampling period is too long to allow a direct peak reconstruction through a fit procedure. The "*parabola*" strategy consists in obtaining a first "raw" informations from the 3 samples interpolation, and coming then to the refined values in applying an *ad–hoc* correction:

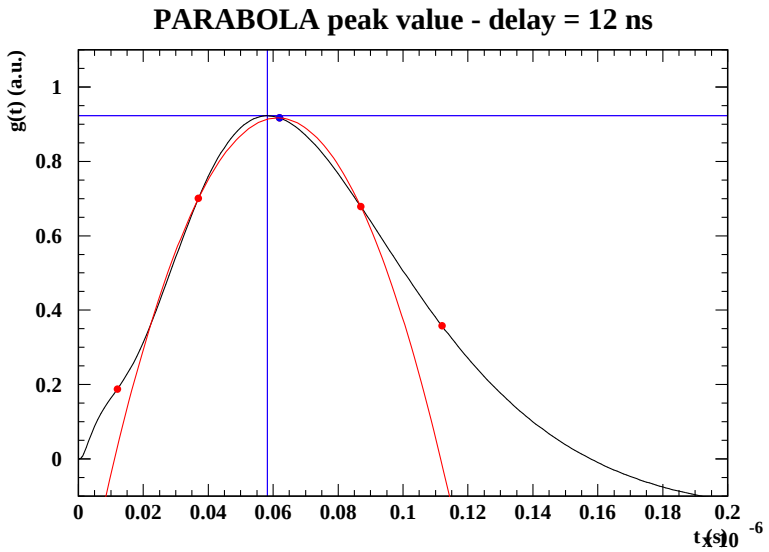

Figure 4.1: First step of the "*parabola*" SR algorithm: a "raw" timing information is computed interpolating 3 sampled points of the signal.

- 3 signal samples out of the 5 saved (the greater one and its two neighbors) are interpolated with a parabolic function (Figure 4.1). The time corresponding to the vertex of the interpolating parabola is used as a first "raw" timing information.
- The signal waveform after the shaping filter is assumed to be perfectly known (*reference* signal, Figure 4.2); two correction functions are computed from this reference waveform. The first function correlates *the reference signal peak time to the "raw" timing information* that can be obtained through the "*parabola*" interpolation (Figure 4.3 (top)). The second function correlates *the ratio between the reference signal real amplitude and the maximum signal sample* to the same "raw" timing information (Figure 4.3 (bottom)).
- The two correction function are stored in a software look-up table. During the EMC test-beam data reconstruction, for each signal the "raw" timing information is computed from the 3 samples. The "true" peak time of the digitized signal is directly obtained from the first correction function. The digitized signal amplitude is computed applying to the maximum signal sample the proper correction value from the second function.

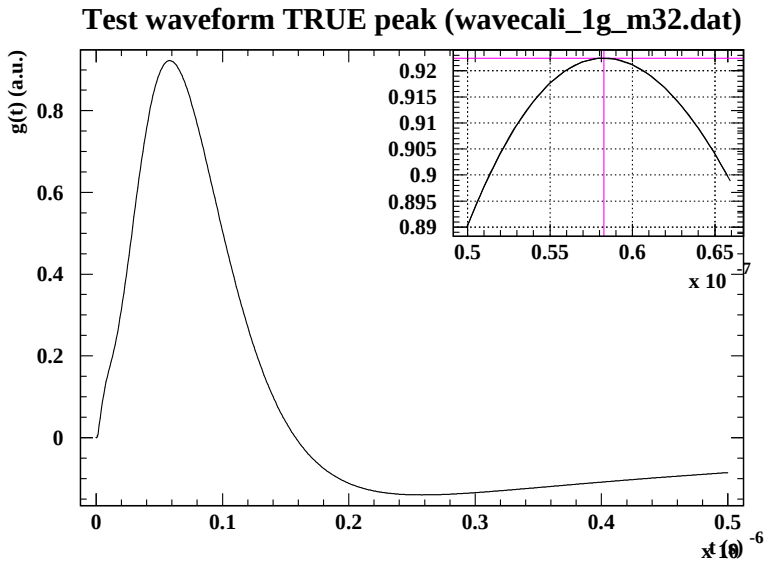

Figure 4.2: Reference signal waveform after the shaping filter. In the "*parabola*" SR algorithm the shape of this reference waveform is assumed to be perfectly known.

Two concurrent problems affect this system: the set of correction functions used in the test–beam data reconstruction software EMTB [52] is the same for all the cell of the same sampling, thus the system does not take into account the cell-to-cell signal difference we showed in Chapter 3; the reference waveform used to compute the correction functions is a *calibration* waveform, thus it does not take into account the ionization-to-calibration difference we showed in Chapter 3.

4.1.2 Test on *mock–up* signals

We take a *mock–up* calibration waveform from cell M32 (according to the numbering explained in Section 3.3.1) and compute the correction functions as a function of the delay value. We use then these correction functions with the "*parabola*" SR algorithm, and reconstruct peak and arrival time of:

- the *same* waveform used to compute the functions (Figure 4.4);
- the "*ionization*[1]" waveform collected from the *same cell* (Figure 4.5);
- the *calibration* waveform from a different cell (M39) (Figure 4.6);
- the "*ionization*" waveform collected from a *different cell* (M39) (Figure 4.7).

[1]Here "ionization" is used according to the *mock–up* standard, e.g. an exponential pulse injected on the detector gap.

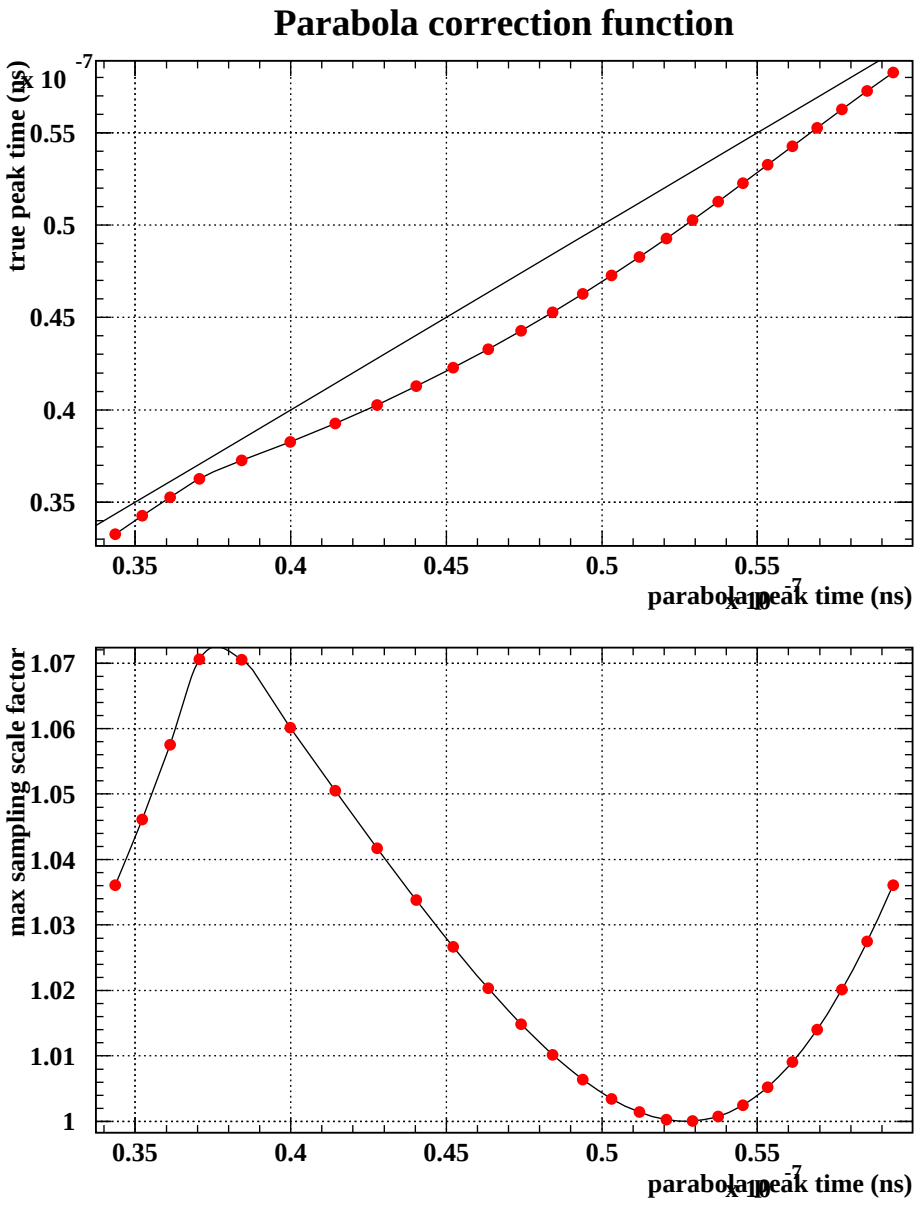

Figure 4.3: "*Parabola*" SR algorithm time (top) and amplitude (bottom) correction functions.

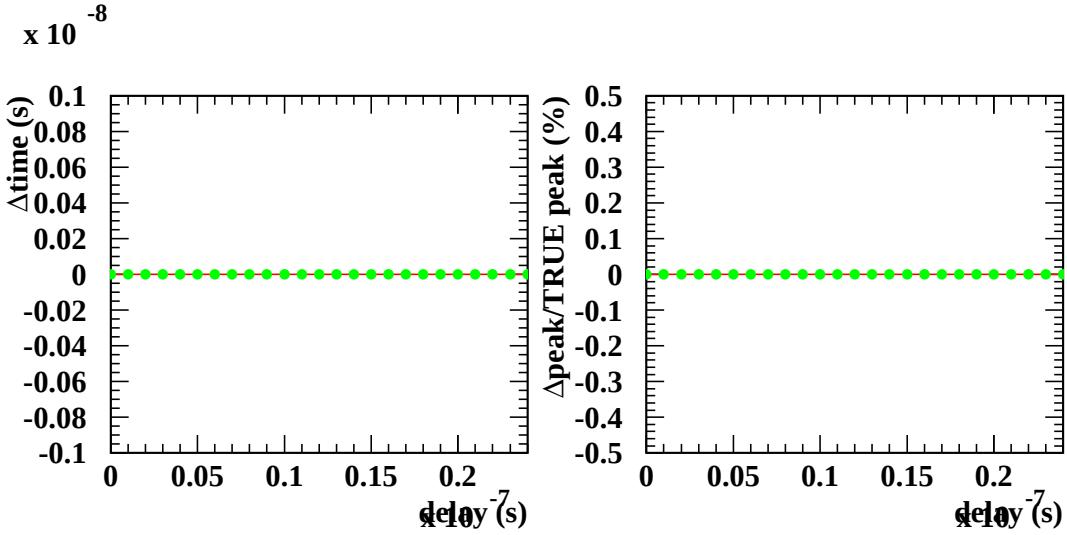

Figure 4.4: "*Parabola*" SR algorithm performances, when the correction functions obtained from a *mock–up* calibration waveform are used to reconstruct the same sampled calibration signal: difference between "true" and reconstructed peak time, as a function of the signal delay value (left); percentage difference between "true" and reconstructed signal amplitude, as a function of the signal delay value (right).

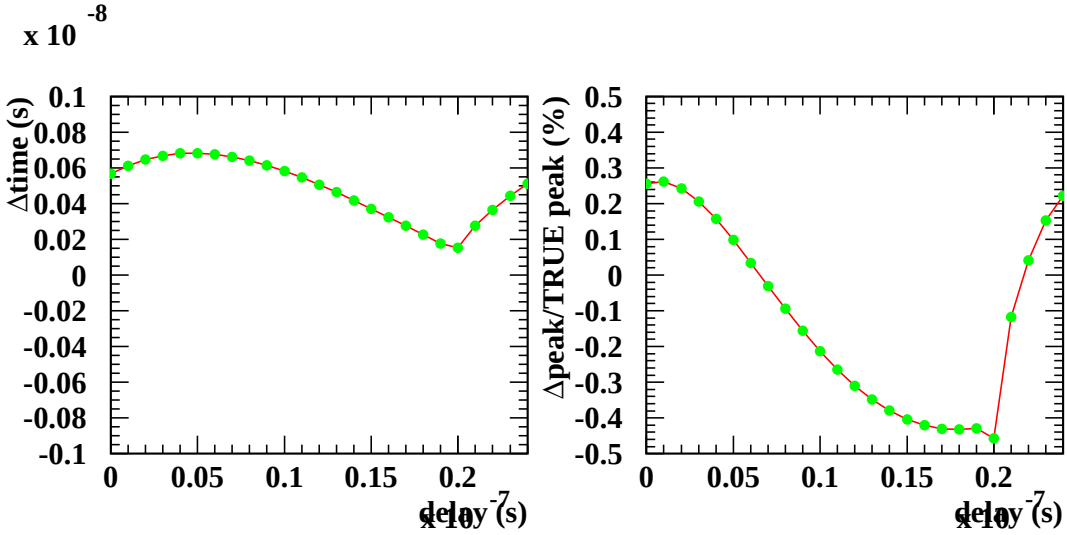

Figure 4.5: "*Parabola*" SR algorithm performances, when the correction functions obtained from a *mock–up* calibration waveform are used to reconstruct the sampled "ionization" signal from the same cell: difference between "true" and reconstructed peak time, as a function of the signal delay value (left); percentage difference between "true" and reconstructed signal amplitude, as a function of the signal delay value (right).

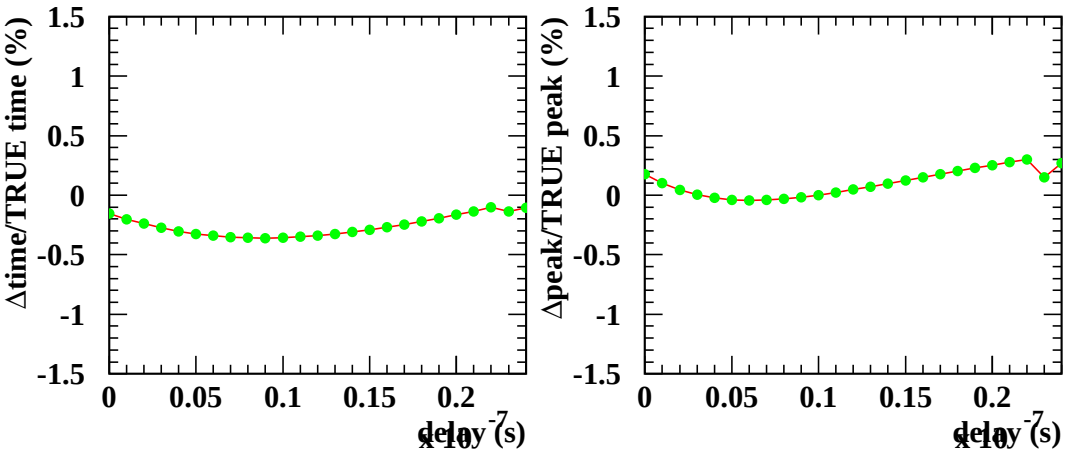

Figure 4.6: "*Parabola*" SR algorithm performances, when the correction functions obtained from a *mock–up* calibration waveform are used to reconstruct the a sampled calibration signal from a different *mock–up* cell: difference between "true" and reconstructed peak time, as a function of the signal delay value (left); percentage difference between "true" and reconstructed signal amplitude, as a function of the signal delay value (right).

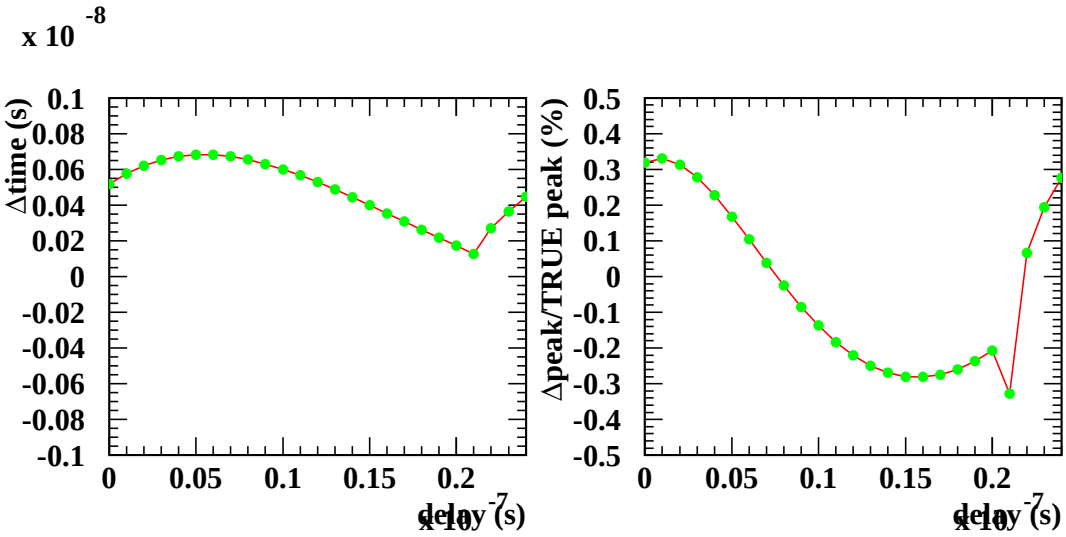

Figure 4.7: "*Parabola*" SR algorithm performances, when the correction functions obtained from a *mock–up* calibration waveform are used to reconstruct the sampled "ionization" signal from a different *mock–up* cell: difference between "true" and reconstructed peak time, as a function of the signal delay value (left); percentage difference between "true" and reconstructed signal amplitude, as a function of the signal delay value (right).

If for the same waveform the accuracy of the reconstruction method is virtually perfect (Figure 4.4), when it is applied to a different waveform (for cell or type) it shows its weakness. The reconstructed signal amplitude and time strongly depend in fact on the signal delay. The different electrical properties of the readout cells distort the signals, leading to a deviations up to ∼0.3% in the amplitude estimation, and up to ∼700 ps in the time estimation (Figure 4.6). The effect is similar and even greater due to the fact that the ionization and the calibration signals have not the same shape: a deviation in the time estimation up to ∼700 ps is again found, the amplitude estimation can be incorrect up to ∼0.4% (Figure 4.7).

A further step consists in trying to simulate the test-beam SR conditions along the 8 *mock–up* Middle sampling cells, similarly to what we did in Chapter 3. In this case:

- the "ionization" signals are multiply–injected in order to simulate the shower energy sharing among the neighboring cells (this procedure has been described in detail in Section 3.5.2;
- the "ionization" signals peaks are reconstructed with the "*parabola*" SR algorithm for the 25 different possible delay values, the resulting peak values are averaged;
- since calibration signals are supposed to be synchronous with the DAQ, the maximum of every signal is forced to directly correspond to a sample.

Results of this procedure are shown in Figure 4.8, where the "ionization" peaks, calibration peaks and "ionization"–over–calibration peak ratios are reconstructed using a polynomial fit on the 1 GHz oscilloscope samplings ("true" reconstruction, as used in Chapter 3), and through the "*parabola*" SR algorithm. The procedure has been applied to the signals collected both with 1 and 2 ground springs on the second *mock–up* connector.

The effect of removing the second ground connection on cell M39 pass from 1.1% ("true" reconstruction) quoted in Section 3.5.2 to 1.4% ("*parabola*" reconstruction). The uniformity (RMS/mean) of the 8 Middle cells system pass from 0.3% to 0.4% when the second ground is connected, from 0.6% to 0.8% when it is removed. The intrinsic non–uniformity of the system is evidently magnified by the "*parabola*" SR algorithm. For this reason the "*parabola*" SR algorithm is presently used only for the raw on-line monitoring of energy deposited in the EMC modules during test-beams data takings.

A final remark is necessary: apart from its non–uniformity–magnifying properties, the "*parabola*" SR algorithm use a single sample to compute the amplitude of the signal. For this reason the quantities obtained using this technique are more affected by the noise fluctuations than the ones computed with techniques using more than one sample. It would therefore not be suitable to be used at the LHC, while running at low luminosity $\mathcal{L} \simeq 10^{33}$ cm^{-2}s^{-1}. At that condition in fact the EMC readout electronics is not optimized to minimize the noise (see Appendix B for details).

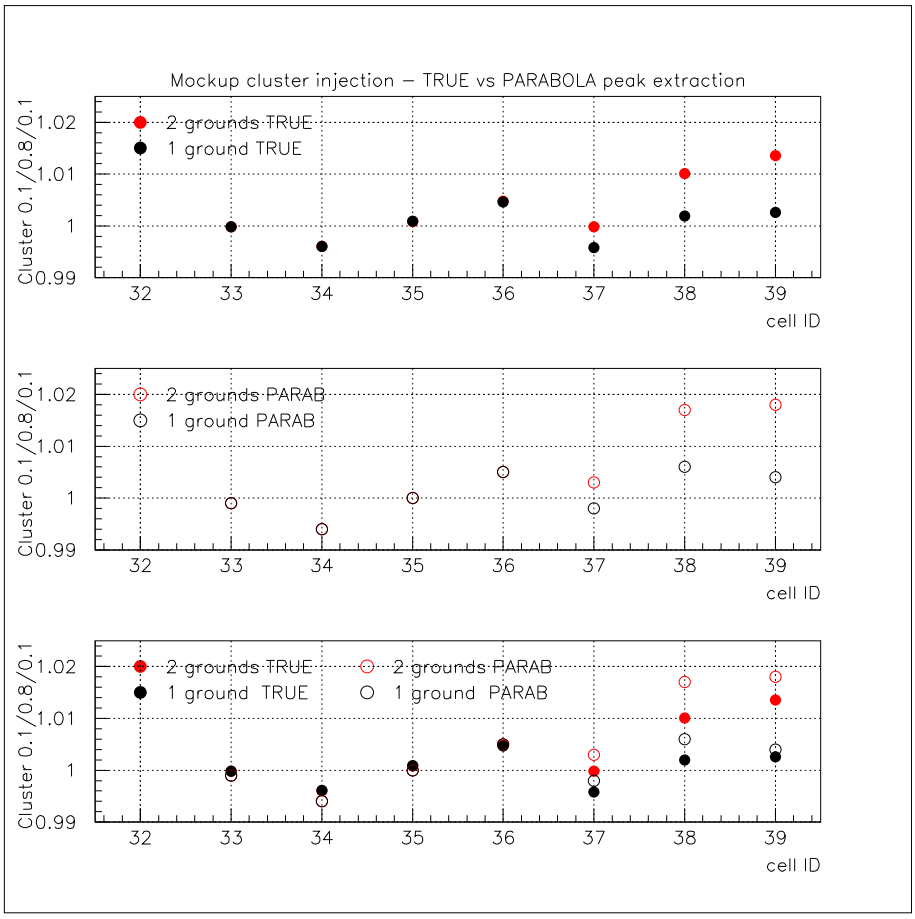

Figure 4.8: Comparison between "*parabola*" (empty symbols) and "true" (full symbols, corresponding to a polynomial fit on the peak region) peak reconstruction of the *mock–up* signals, in case of multiple "physics" injection (*cluster* 10%/80%/10%): "ionization" vs. Middle cell position (top); calibration (middle); "ionization" over calibration ratio (bottom). Red symbols refer to the *mock–up* having only 1 ground returns connected in the second connector; black symbols to 2 ground returns connected.

4.2 Injection point correction

4.2.1 Basics

The intrinsic non–uniformity of the EMC system can be cured with a cell–dependent correction to be applied on the signals. The ionization and calibration pulses differ in *shape* (Appendix A), and they are *generated in different place* of the detector, as it is showed in Figure 3.2. Since the gain of each readout cell is computed through the reconstruction of a calibration pulse (see Section 2.3.5), this gain should be applied to the ionization signal emerging from the cell *after is has been corrected for its difference respect to the calibration signal*. The non–uniformity due to the cells electrical properties is reduced if corrections for the ionization–to–calibration shape difference and for the different injection points are applied to the ionization signals during the peak reconstruction.

If we consider the simplest model of an EMC cell discussed in Section 3.2.1, from equation (3.12) we know that at the end of the readout chain the ionization pulse differs from the calibration pulse by two factors:

$$V_{\rm out}^{\rm phys}(s) = V_{\rm out}^{\rm cali}(s) \times \underbrace{\left(\frac{I_{\rm inj}^{\rm phys}(s)}{I_{\rm inj}^{\rm cali}(s)}\right)}_{\substack{\text{ionization–}\\ \text{to–calibration}\\ \text{signal shape ratio}}} \times \underbrace{\left(\frac{1}{1+s^2LC}\right)}_{\substack{\text{injection–point}\\ \text{difference}}} \tag{4.1}$$

being L the effective inductance and C the effective capacitance of the cell. The readout gain obtained from the calibration pulse should then be applied to the *corrected ionization signal*:

$$V_{\rm out}^{\rm phys}(s)\Big|^{\rm corr} = V_{\rm out}^{\rm phys} \times \underbrace{\left(\frac{I_{\rm inj}^{\rm cali}(s)}{I_{\rm inj}^{\rm phys}(s)}\right)}_{\substack{\text{ionization–}\\ \text{to–calibration}\\ \text{shape correction}}} \times \underbrace{\left(1+s^2LC\right)}_{\substack{\text{injection–point}\\ \text{correction}}} \tag{4.2}$$

The injection–point correction needs the knowledge of the LC parameter for each readout cell. We'll come later to the details of the ionization–to–calibration signal shape difference correction $\left(I_{\rm inj}^{\rm cali}/I_{\rm inj}^{\rm phys}\right)$.

4.2.2 Injection point correction on *mock–up* signals

The effectiveness of the injection–point correction can be easily tested on the *mock–up* signals. In the *mock–up* framework we mimic the ionization signal injecting at the detector gap level a pulse that is identical to the calibration exponential one (see Section 3.3.2). The *mock–up* corrected "ionization" signal is then:

$$I_{\rm inj}^{\rm phys}(s) = I_{\rm inj}^{\rm cali}(s) \quad \Rightarrow \quad V_{\rm out}^{\rm phys}(s)\Big|^{\rm corr} = V_{\rm out}^{\rm phys}(s) \times \left(1+s^2LC\right) \tag{4.3}$$

or, in the time domain:

$$V_{\rm out}^{\rm phys}(t)\Big|^{\rm corr} = \left(1 + LC\frac{d^2}{dt^2}\right) V_{\rm out}^{\rm phys}(t) \tag{4.4}$$

We proceed as the following (see Figure 4.9):

- The correction (4.4) is applied to the *mock–up* "physics" signals $V_{\rm out}^{\rm phys}(t)$;
- The peak of the *corrected* "physics" signal $A^{\rm phys} = \max\left\{V_{\rm out}^{\rm phys}(t)\Big|^{\rm corr}\right\}$ is reconstructed as in Chapter 3 (polynomial fit on the 1 GHz oscilloscope samplings);
- The peak $A^{\rm cali} = \max\left\{V_{\rm out}^{\rm cali}(t)\right\}$ of the corresponding *mock–up* calibration signals is reconstructed in the same way;
- The "calibrated" signal is computed as the ratio $\frac{A^{\rm phys}}{A^{\rm cali}}$ as for the *mock–up* uniformity study of Chapter 3.

The injection–point correction to the "physics" signals is applied using the LC values measured from the *mock–up* Middle cells, according to the procedure described in Section 3.4.

The "calibrated" signals along the 8 *mock–up* Middle cells are shown in Figure 4.10 both in the 1–ground and 2–ground connection configuration; they are compared with the non–corrected results discussed in Chapter 3. The uniformity values are listed in Table 4.1.

uniformity (%)	non–corrected	with LC correction
1 ground	0.36	0.14
2 ground	0.60	0.15

Table 4.1: *Mock–up* uniformity (RMS %) with and without injection–point (LC) correction.

Since after the correction the 8 Middle cells residual non–uniformity is compatible with the *mock–up* signal injectors non–uniformity (see Section 3.3.2), we can state that *the injection–point correction eliminates almost perfectly the intrinsic non–uniformity of the system*, in both the two ground connections configurations. Being in fact the ground spring effect of inductive nature (Chapter 3), the correction is able to flatten the detector response for the cells the second *mock–up* connector (M36÷M39), even if the second ground spring is not present (Figure 4.11).

The corrected calibrated response is systematically lower than the non–corrected one (Figure 4.10): the cell effective inductance L is in fact responsible for the systematic increase of the ionization signals peak, as in has been shown in Figure 3.20. If the injection–point correction is not applied, even after the calibration procedure the cells equalization is not complete, and the reconstructed energy is in general overestimated.

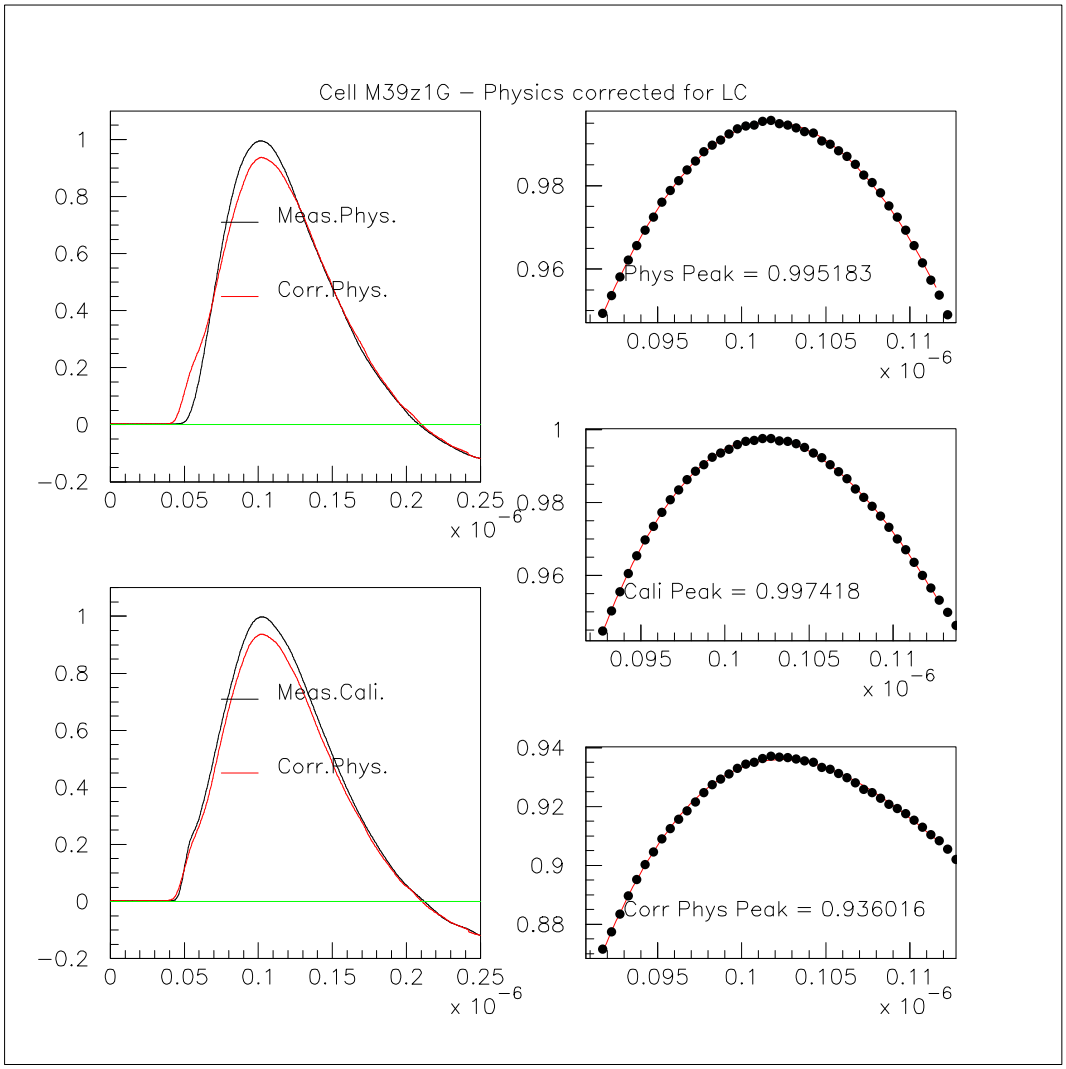

Figure 4.9: Injection–point correction on the *mock–up* M39 cell signals: measured "ionization" signal (black) and corrected "ionization"signal (red) comparison (top left); measured calibration signal (black) and corrected "ionization" signal (red) comparison (bottom left); measured "ionization" signal peak detail (top right); corrected "ionization" signal peak detail (middle right); measured calibration signal peak detail (bottom right).

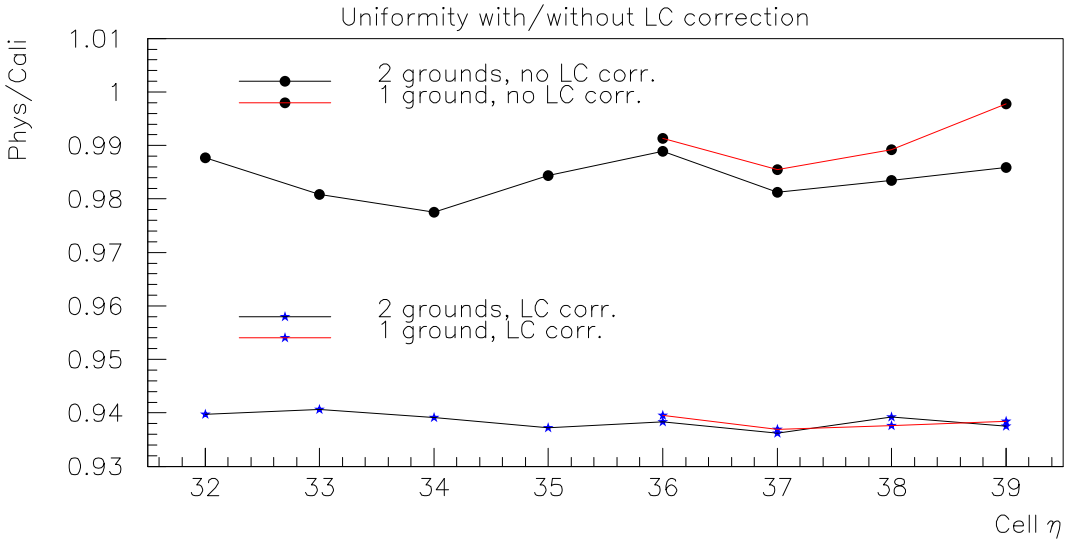

Figure 4.10: *Mock–up* "calibrated" signals with and without injection–point (*LC*) correction.

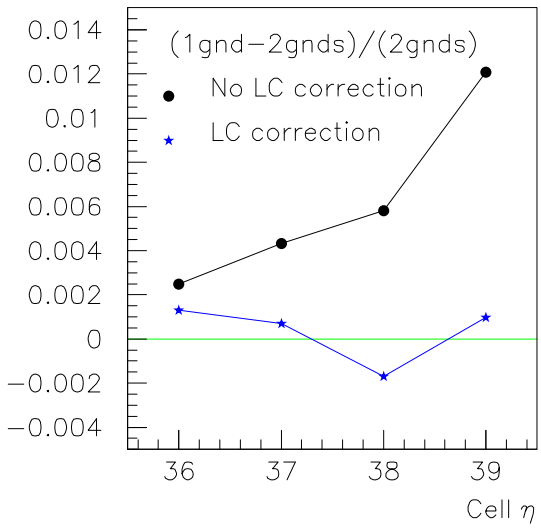

Figure 4.11: Response variation $\left(\frac{\text{(1 gnd - 2 gnds)}}{\text{2 gnds}}\right)$ in the second *mock–up* connector (Middle cells M36÷M39) adding the second ground spring, with and without injection–point (*LC*) correction.

4.3 Electronic calibration using the *optimal filtering* technique

4.3.1 Basics

The injection–point correction is a powerful calibration tool for the EMC, since it can flatten the intrinsic non–uniformity of the system due to its electrical properties. This correction, together with the ionization–to–calibration shape correction, is to be applied to the EMC test-beam data, and then extended to the ATLAS EMC data reconstruction.

The correction can be directly applied using the *optimal filtering* (OF) SR technique. The OF reconstructs the ionization signal amplitude S and starting time τ as the weighted sums of the 5 signal samples s_i:

$$\left\{ \begin{array}{rcl} S & = & \sum_{k=1,5}^{n} a_k s_k \\ S\tau & = & \sum_{k=1,5}^{n} b_k s_k \end{array} \right. \tag{4.5}$$

The details of the $\{a_k\}$ and $\{b_k\}$ coefficients sets computation are discussed in Appendix B. The important thing to be pointed out is anyway that, in order to complete the OF coefficients computation, *the normalized shape of the ionization signal* $g^{\text{phys}}(t)$ *is needed*. The injection–point correction and the ionization–to–calibration shape correction can then be directly implemented during the OF coefficients computation, through the correct definition of "normalized" ionization waveform. *The ionization waveform is "normalized" when it corresponds to a calibration pulse of unitary peak*, according to the following relation derived from equation (4.1):

$$\left\{ \begin{array}{l} g^{\text{phys}}(s) = g^{\text{cali}}(s) \times \left(\frac{I_{\text{inj}}^{\text{phys}}(s)}{I_{\text{inj}}^{\text{cali}}(s)} \right) \times \left(\frac{1}{1+s^2 LC} \right) \\ \max \left\{ g^{\text{cali}}(t) \right\} = 1 \end{array} \right. \tag{4.6}$$

In this way the predicted "normalized" ionization waveform $g^{\text{phys}}(t)$ would in general have a peak greater than 1 ($\max \left\{ g^{\text{phys}}(t) \right\} > 1$), due mainly to the injection–point correction to be applied to the calibration waveform. When the OF coefficients sets $\{a_k\}$ are computed using this $g^{\text{phys}}(t)$, the peak estimator would be $S = \sum_{k=1,5}^{n} a_k \; g^{\text{phys}}(t_k) = 1$, for the OF technique intrinsic properties. This ensures that the disuniformities due to the cell electrical properties are reduced during the peak reconstruction, and the electronics gain computed using the calibration pulses can be safely applied.

4.3.2 Test-beam OF4 SR implementation

The OF SR technique have been implemented in the EMC test-beam data reconstruction software [52] in different incarnations. The corrections (4.6) have been firstly implemented through the OF SR technique by [32] (OF4). This is presently the official SR technique used for the EMB test-beam data analysis.

The OF4 coefficients are computed using the ionization waveform prediction (4.6), according to the following strategy [32]:

- The ionization signal is supposed to be triangular (equationA.6) with drift time T_d; the calibration signal is supposed to be a simple exponential (equationA.8) with decay time τ_{cali}. The ionization-to-calibration signal shape difference correction is then (see Appendix A for the signals different analytic descriptions):

$$\left(\frac{I_{\text{inj}}^{\text{phys}}(s)}{I_{\text{inj}}^{\text{cali}}(s)} \right) = \frac{(1 + s\tau_{\text{cali}})(sT_d - 1 + e^{-sT_d})}{s^2 T_d \tau_{\text{cali}}} \tag{4.7}$$

- The cell–dependent parameter LC is obtained through a fit procedure, that attempts to adjust the $g^{\text{phys}}(t)$ waveform to the average ionization pulse profile that can be reconstructed from the test-beam electrons data. This is possible because the test-beam particles are asynchronous with respect to the DAQ: thanks to the TDC [45] external information, that provides the time difference between the DAQ clock and the particle arrival time, a mean ionization pulse can be reconstructed over a range of 175 ns with a 1 ns step, similarly to what is done with the calibration pulses.

- The ionization signal prediction is performed in the frequency domain and then converted to the time domain using a Fast Fourier Transform (FFT) procedure.

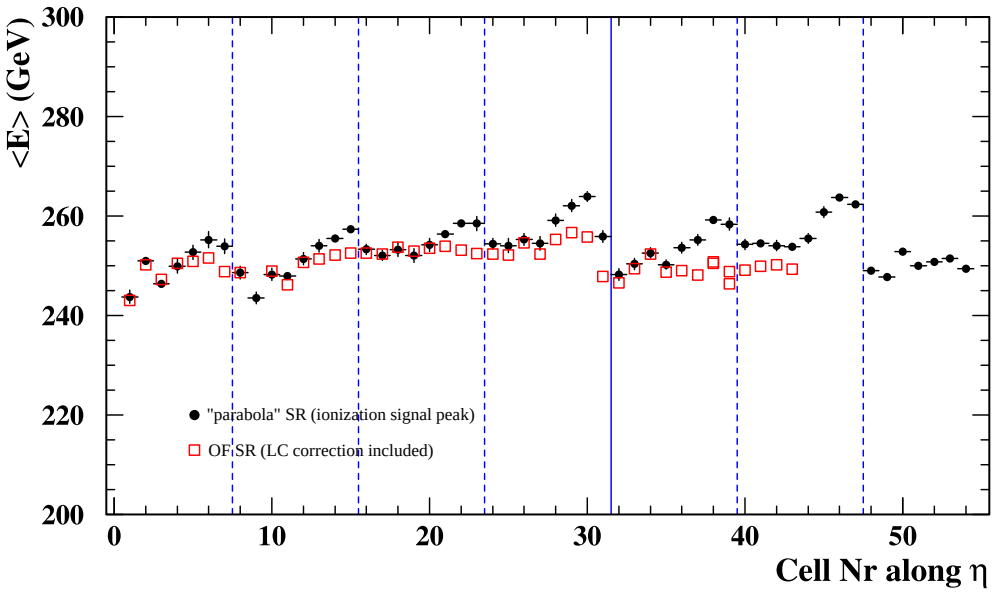

Figure 4.12: Energy response of the EMC barrel prototype "Module 0" cells line $\phi_{\text{cell}} = 10$ to 245 GeV electrons, from data taken during the year 2000 test–beam session: signal reconstructed and calibrated using the "*parabola*" SR method (full black dots) and with the OF4 SR method (open red squares).

The "Module 0" 2000 test-beam data presented in Section 3.1 have been re–reconstructed and analyzed using the OF4 SR technique ([51, 53]) and compared with

the results obtained using the "*parabola*" SR method. The energy response of the EMC barrel prototype "Module 0" obtained with the two different SR methods is showed in Figure 4.12 for cells line $\phi_{\text{cell}} = 10$. As for the *mock–up* data, the energy response 8–fold periodicity along η is suppressed thanks to corrections implemented in the SR method. The overestimation of the ionization signals peaks due to the cell effective inductance L presence is avoided. The $\phi_{\text{cell}} = 10$ cells line uniformity improvements are listed in Table 4.2 for the electrode A and B regions [51]. The table shows also the additional improvement that can be obtained applying the "dead–material and longitudinal–leakage" correction, that is discussed in detail in Chapter 6.

Uniformity (%)	$0 \leq \eta_{\text{cell}} < 32$	$32 \leq \eta_{\text{cell}} \leq 55$
"*parabola*"	1.8	1.7
OF4	1.1	1.2
OF4 + leakage corr.	0.7 ($0 \leq \eta_{\text{cell}} \leq 55$)	

Table 4.2: Energy response uniformity (RMS %) of the EMC barrel prototype "Module 0" cells line $\phi_{\text{cell}} = 10$.to 245 GeV electrons.

4.4 Summary and perspectives

The EMC system intrinsic non–uniformity can be corrected through the SR and calibration procedure. A SR algorithm that takes into account the detector cell–dependent electrical properties discussed in Chapter 3 is needed to flatten the detector energy response. Such a need has been extensively demonstrated using the *mock–up* signals; the power of the injection-point correction and of the ionization–to–calibration signal shape difference correction has been demonstrated.

The extension of such corrections to the test-beam data reconstruction found its natural way in the framework of the OF SR technique. The 2000 barrel "Module 0" test-beam data, reconstructed with the OF technique implementing the necessary corrections (OF4), do not show anymore the 8–fold non–uniformity.

The limits and the possible improvements of the OF4 SR and calibration procedure are discussed in Chapter 5, where a possible extension to the ATLAS experimental framework is studied.

Chapter 5

A stand–alone SR and calibration procedure for the ATLAS EMC

5.1 Possible improvements in the OF SR procedure

The corrections for the detector cell–dependent electrical properties and for the ionization–to–calibration signal shape differences can be included in the OF SR procedure (OF4, [32]). This strategy proved to be a powerful tool to calibrate and reconstruct the energy in the EMC, as it is shown in Section 4.3 and in [53]. On the other hand, the OF4 SR procedure has some intrinsic limitations that would not let it be suitable for the ATLAS experimental framework:

1. The OF4 *LC* parameter extraction uses the mean ionization pulse that can be obtained from the test-beam electrons asynchronous data. It is not obvious that this could be done in the ATLAS framework: at the LHC the incoming particles will be synchronous to the DAQ clock, thus a complete reconstruction of the ionization pulse will not be directly possible. The ionization pulse prediction should be based only on information that would be available at LHC.

2. Due to the way the calibration signal is generated, it can be more complex than a simple exponential (Section A.2). The signals description used to compute the ionization–to–calibration correction can be refined, in order to take into account these smaller effects that can affect the precision of the method.

3. Like every Fast Fourier Transform based algorithm, the procedure used to predict the OF4 "normalized" ionization signal waveform is very sensitive to the signal window choice (see for example [63]). A *time–domain convolution* should get rid of this dependence, and use the whole extension of the signals.

The goal of this study is to demonstrate that each of the problems posed in the previous list can be solved, and to propose then an improved OF SR reconstruction and calibration procedure that can be directly extended to the ATLAS framework.

5.2 Ionization signal prediction

We take as a starting point the relation (4.6) between the "normalized" ionization pulse and the normalized calibration pulse expressed in equation . Once the normalized calibration waveform $g^{\text{cali}}(s)$ is known, the "normalized" ionization pulse can predicted through the following:

$$g^{\text{phys}}(s) = g^{\text{cali}}(s) \times \left(\frac{I_{\text{inj}}^{\text{phys}}(s)}{I_{\text{inj}}^{\text{cali}}(s)} \right) \times \left(\frac{1}{1 + s^2\tau_0^2} \right) \tag{5.1}$$

being:

$$\begin{cases} \tau_0 = \sqrt{LC} = \frac{1}{\omega_0} \\ \max\left\{ g^{\text{cali}}(t) \right\} = 1 \end{cases} \tag{5.2}$$

The parameter $\omega_0 = \frac{1}{\sqrt{LC}} = \frac{1}{\tau_0}$ is the detector cell *characteristic frequency*. In order to get rid of the limitation described in point 3. of the previous section, the expression (5.13) can be converted to a time domain relation:

$$g^{\text{phys}}(t) = g^{\text{cali}}(t) * \underbrace{\mathcal{L}^{-1}\left\{ \frac{I_{\text{inj}}^{\text{phys}}(s)}{I_{\text{inj}}^{\text{cali}}(s)} \right\}}_{g^{\text{exp} \rightarrow \text{tri}}(t)} * \underbrace{\mathcal{L}^{-1}\left\{ \frac{1}{1 + s^2\tau_0^2} \right\}}_{g^{\text{MB} \rightarrow \text{det}}(t)} \tag{5.3}$$

the two corrections being factorized in two different time–domain convolutions[1].

The ionization waveform is still supposed to be triangular with drift time T_d (equation A.6). The calibration signal is described by the complete analytical expression (A.11); in this case the signal shape is characterized by the decay time τ_{cali} and saturation fraction f_{step} (see Appendix A for a detailed description of the parameters meaning in the different cases). The ionization-to-calibration signal shape difference correction function

[1] For rigorous mathematical details about the direct and inverse Laplace transforms and their properties, see for example [65]. We recall that the time domain convolution of two function $f(t)$ and $g(t)$ is defined as:

$$f(t) * g(t) = \int f(t-t')g(t')\theta(t-t')dt' = \int_0^t f(t-t')g(t')dt' \tag{5.4}$$

In our case the n samples $g_i = g(t_i)$ of the $g(t)$ function, and the analytic expression of the $f(t)$ function, are known. The i-th sample of the convolution function $f(t) * g(t)$ can be then numerically estimated as:

$$\{f(t) * g(t)\}_i = \left(\sum_{j=1}^{i} f(t_i - t_j) \times g_j \right) \times \Delta t \tag{5.5}$$

being Δt the sampling interval (in our case $\Delta t = 1$ ns).

is then:

$$g^{\text{exp} \rightarrow \text{tri}}(t) = \mathcal{L}^{-1}\left\{\frac{I_{\text{inj}}^{\text{phys}}(s)}{I_{\text{inj}}^{\text{cali}}(s)}\right\} \tag{5.6}$$

$$= \mathcal{L}^{-1}\left\{\frac{(1+s\tau_{\text{cali}})(sT_d - 1 + e^{-sT_d})}{sT_d(f_{\text{step}} + s\tau_{\text{cali}})}\right\} \tag{5.7}$$

$$= \delta(t) + \left[\frac{1-f_{\text{step}}}{\tau_{\text{cali}}}e^{-f_{\text{step}}\frac{t}{\tau_{\text{cali}}}} - \frac{1-f_{\text{step}}}{f_{\text{step}}}\left(e^{-f_{\text{step}}\frac{t}{\tau_{\text{cali}}}} - 1\right)\right]\theta(t) + \frac{1-f_{\text{step}}}{f_{\text{step}}}\left(e^{-f_{\text{step}}\frac{t-T_d}{\tau_{\text{cali}}}} - 1\right)\theta(t-T_d) \tag{5.8}$$

being:

$$\begin{cases} \mathcal{L}^{-1}\left\{\frac{1+s\tau_{\text{cali}}}{f_{\text{step}}+s\tau_{\text{cali}}}\right\} = \delta(t) + \frac{1-f_{\text{step}}}{\tau_{\text{cali}}}e^{-f_{\text{step}}\frac{t}{T_d}} \\ \int_0^t dt \frac{1-f_{\text{step}}}{\tau_{\text{cali}}}e^{-f_{\text{step}}\frac{t}{\tau_{\text{cali}}}} = \frac{1-f_{\text{step}}}{f_{\text{step}}}\left(e^{-f_{\text{step}}\frac{t}{\tau_{\text{cali}}}} - 1\right) \end{cases}$$

The case in which the calibration pulse is a simple exponential (equation A.8) corresponds to the limit of (5.8) in which the saturation fraction $f_{\text{step}} = 0$:

$$g^{\text{exp} \rightarrow \text{tri}}(t)|_{f_{\text{step}}=0} = \mathcal{L}^{-1}\left\{\frac{(1+s\tau_{\text{cali}})(sT_d - 1 + e^{-sT_d})}{s^2 T_d \tau_{\text{cali}}}\right\} \tag{5.9}$$

$$= \delta(t) + \left(\frac{1}{\tau_{\text{cali}}} - \frac{1}{T_d} - \frac{t}{\tau_{\text{cali}}T_d}\right)\theta(t) + \left(\frac{1}{T_d} + \frac{t-T_d}{\tau_{\text{cali}}T_d}\right)\theta(t-T_d) \tag{5.10}$$

The injection–point correction function is:

$$g^{\text{MB} \rightarrow \text{det}}(t) = \mathcal{L}^{-1}\left\{\frac{1}{1+s^2\tau_0^2}\right\} \tag{5.11}$$

$$= \frac{1}{\tau_0}\sin\left(\frac{t}{\tau_0}t\right)\theta(t) \tag{5.12}$$

The connection between the detector cell and the readout line has always a small resistive component ($r \sim \Omega$, see Chapter 3), at least because of the contact resistance between the connectors. This resistive behavior of the cell can be modeled by a resistance r added to the cell equivalent circuit of Figure 3.2, as in Figure 5.1). The expression (5.1) becomes:

$$g^{\text{phys}}(s) = g^{\text{cali}}(s) \times \left(\frac{I_{\text{inj}}^{\text{phys}}(s)}{I_{\text{inj}}^{\text{cali}}(s)}\right) \times \underbrace{\left(\frac{1}{1+s\tau_r+s^2\tau_0^2}\right)}_{g^{\text{MB} \rightarrow \text{det}}|_{r\neq 0}} \tag{5.13}$$

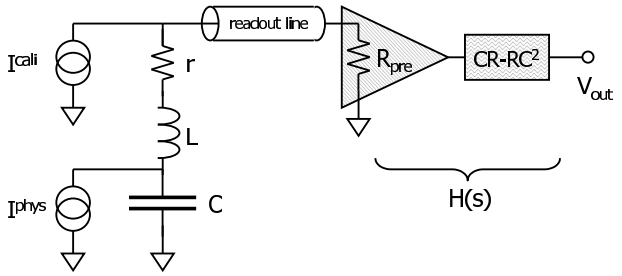

Figure 5.1: Basic detector cell equivalent circuit, taking into account the resistive component r of the connection between the electrodes and the readout line.

being $\tau_r = rC$ the additional parameter to be taken into account with the (5.2) conditions. The injection–point correction function is in this case:

$$g^{\text{MB} \rightarrow \text{det}}|_{r\neq 0} = \mathcal{L}^{-1}\left\{\frac{1}{1+s\tau_r+s^2\tau_0^2}\right\} \tag{5.14}$$

$$= \frac{2}{\tau_a} e^{-\frac{\tau_r}{2\tau_0^2}t} \sin\left(\frac{\tau_a}{2\tau_0^2}t\right)\theta(t) \quad ; \quad \text{when } (\tau_r^2 - 4\tau_0^2) < 0 \tag{5.15}$$

being:

$$\begin{cases} \tau_a = \sqrt{4\tau_0^2 - \tau_r^2} \\ \mathcal{L}^{-1}\left\{\frac{1}{(s-a)(s-b)}\right\} = \frac{e^{-bt}-e^{-at}}{a-b} \\ \frac{1}{2i}\left(e^{ix} - e^{-ix}\right) = \sin(x) \end{cases}$$

The case $(\tau_r^2 - 4\tau_0^2) < 0$ is always fulfilled for the r, L and C detector typical values (see Chapter3).

5.3 Parameters extraction from the calibration waveform

The time–domain correction functions to be used used in (5.3) or in then analogous (5.13) depend on several parameters:

$$\begin{cases} g^{\text{exp} \rightarrow \text{tri}}(t) = g^{\text{exp} \rightarrow \text{tri}}(t, \{T_d, \tau_{\text{cali}}, f_{\text{step}}\}) \\ g^{\text{MB} \rightarrow \text{det}}(t) = g^{\text{MB} \rightarrow \text{det}}(t; \{\tau_0\}) \\ g^{\text{MB} \rightarrow \text{det}}(t)|_{r\neq 0} = g^{\text{MB} \rightarrow \text{det}}(t; \{\tau_0, \tau_r\}) \end{cases}$$

Some of them (i.e. τ_{cali}, f_{step}) are typical of the calibration line that generates the calibration pulse; the others (i.e. T_d, τ_0 and eventually τ_r) are related to the detector cell properties.

According to what we discuss at point 1. of Section 5.1, in the ionization waveform prediction procedure we do not want to use any information that would not be similarly available at the LHC. Some of the necessary parameters could be gathered from the calibration pulse itself, as it as been firstly proposed by [34] and [33]. This is the case for

the calibration pulse shape parameters $\tau_{\rm cali}$ and $f_{\rm step}$, and of the detector cell characteristic parameter τ_0 (and eventually τ_r), that can in principle be extracted from the calibration waveform.

The drift time T_d is a specific characteristic of the ionization electrons motion in the LAr gap. It has no direct influence on the calibration waveform, it is then to be retrieved from a different source. It can anyway be shown (Section 5.5.3) that the ionization waveform prediction is rather insensitive to the T_d value, at least in the region of interest for the OF coefficients computation: for this reason the nominal T_d value can be used.

5.3.1 Calibration output transformation strategy

Recalling the simple model of a LAr readout cell shown in Figure 5.1, the calibration pulse at the end of the readout chain can be written in the frequency domain as:

$$V_{\rm out}^{\rm cali}(s) = I_{\rm inj}^{\rm cali}(s) \times H^{\rm det}(s) \times H^{\rm readout}(s) \tag{5.16}$$

The function $H^{\rm det}(s)$ describes the effects of the detector cell properties on the injected calibration signal $I_{\rm inj}^{\rm cali}(s)$, while $H^{\rm readout}(s)$ is the readout (line + preamplifier + shaper) transfer function.

The strategy to retrieve the needed parameters is based on the computation and analysis of what would be the response of the system (detector cell + readout system) to a signal different from the standard "exponential" calibration pulse. The system response can in fact be sensitive to a particular injected waveform, the output showing in some case easily recognizable characteristics. Let a generic current pulse $Y_{\rm inj}(s)$ be injected on the system at the MB level, exactly as it is done with the calibration pulse $I_{\rm inj}^{\rm cali}(s)$. The response $W_{\rm out}(s)$ of the system to this signal would be:

$$\begin{aligned} W_{\rm out}(s) &= Y_{\rm inj}(s) \times H^{\rm det}(s) \times H^{\rm readout}(s) && (5.17)\\ &= \frac{Y_{\rm inj}(s)}{I_{\rm inj}^{\rm cali}(s)} \times I_{\rm inj}^{\rm cali}(s) \times H^{\rm det}(s) \times H^{\rm readout}(s) \\ &= \frac{Y_{\rm inj}(s)}{I_{\rm inj}^{\rm cali}(s)} \times V_{\rm out}^{\rm cali}(s) && (5.18) \end{aligned}$$

or, in the time domain:

$$\begin{aligned} W_{\rm out}(t) &= \mathcal{L}^{-1}\left\{\frac{Y_{\rm inj}(s)}{I_{\rm inj}^{\rm cali}(s)}\right\} * V_{\rm out}^{\rm cali}(t) \\ &= f_{\rm tran}^{Y}(t) * V_{\rm out}^{\rm cali}(t) && (5.19) \end{aligned}$$

The "transformed" response $W_{\rm out}(t)$ to the test signal $Y_{\rm inj}(t)$ can be then computed as the (numeric) time–domain convolution of the sampled calibration signal $V_{\rm out}^{\rm cali}(t)$ and a proper *transformation function* $f_{\rm tran}^{Y}(t) = \mathcal{L}^{-1}\left\{\frac{Y_{\rm inj}(s)}{I_{\rm inj}^{\rm cali}(s)}\right\}$.

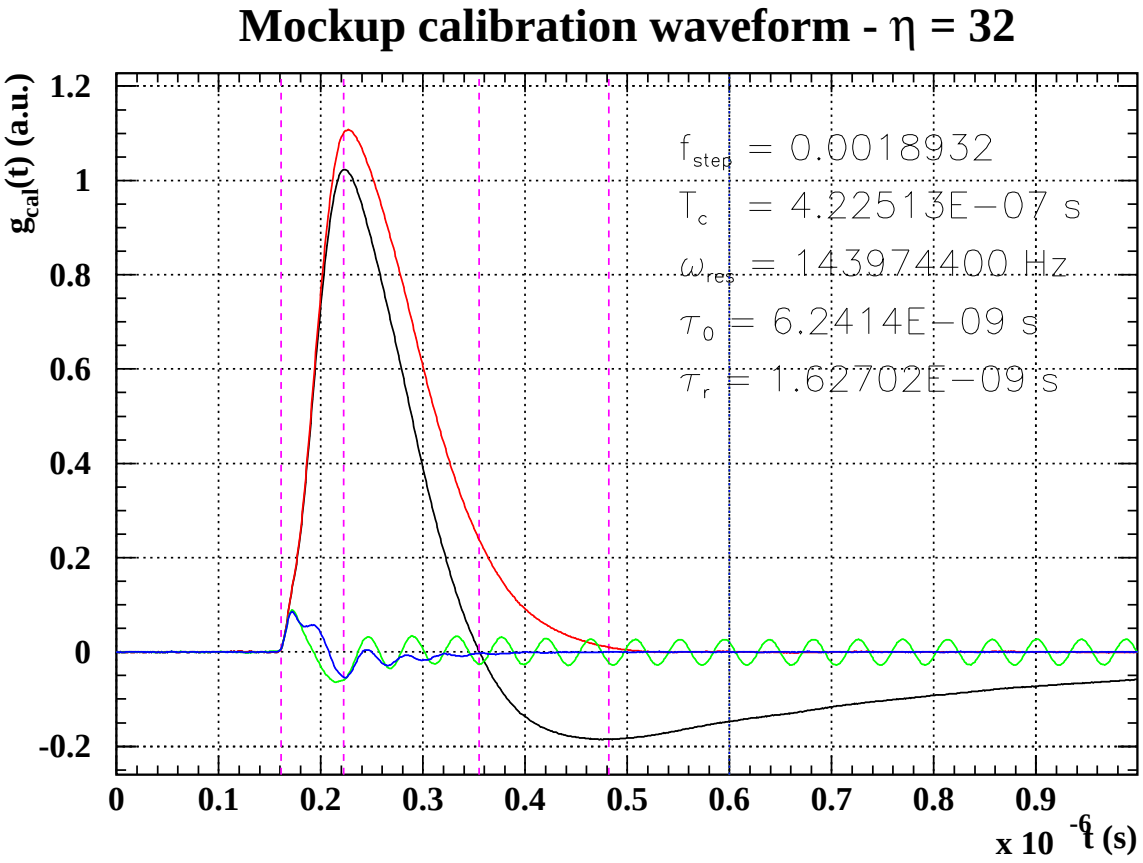

Figure 5.2: Calibration waveform collected from the *mock–up* cell M32 (black). The extracted parameters and the relative transformed waveforms are shown: step–response transformation (red); cosine–response transformation (green); injection–point–correction residual oscillation (blue). The tail starting point is $t_{\min} = 600$ ns for all the transformed waveform tail minimizations (see text for details).

5.3.2 Calibration pulse parameters through the *step–response* transformation

The calibration pulse parameters τ_{cali} and f_{step} can be obtained computing the response of the system to a *step function* S_{inj} [34]:

$$S_{\text{inj}}(s) = \frac{1}{s} \tag{5.20}$$

In the frequency domain the relative transformation function is:

$$\begin{aligned} f_{\text{tran}}^{\text{step}}(s, \tau'_{\text{cali}}, f'_{\text{step}}) &= \frac{S_{\text{inj}}(s)}{I_{\text{inj}}^{\text{cali}}(s, \tau'_{\text{cali}}, f'_{\text{step}})} \\ &= \frac{1}{s} \times \frac{s(1 + s\tau'_{\text{cali}})}{s\tau'_{\text{cali}} + f'_{\text{step}}} = \frac{1 + s\tau'_{\text{cali}}}{s\tau'_{\text{cali}} + f'_{\text{step}}} \end{aligned} \tag{5.21}$$

being τ'_{cali} and f'_{step} the assumed values of the calibration pulse parameters. It can be easily verified that, when the conditions $\tau'_{\text{cali}} = \tau_{\text{cali}}$ and $f'_{\text{step}} = f_{\text{step}}$ are verified, the output function is exactly the response of the system to a step function:

$$U_{\text{out}}(s) = \frac{1}{s} \times H^{\text{det}}(s) \times H^{\text{readout}}(s) \tag{5.22}$$

The function $U_{\text{out}}(s)$ has the property to *go to zero in the tail*, at least after a sufficient portion of the signal, since the functions $H^{\text{det}}(s)$ and $H^{\text{readout}}(s)$ contain only short time constants and do not give rise to a long tail in the waveform.

This null–tail property of the step–response can be used to recognize when the conditions $\tau'_{\text{cali}} = \tau_{\text{cali}}$ and $f'_{\text{step}} = f_{\text{step}}$ are verified. A χ^2–like function can be built summing the squares of the step–response function values over the tail of the pulse, the tail being defined as the portion of pulse after the time t_{min}. The values of τ_{cali} and f_{step} values are extracted finding the minimum of this function:

$$\begin{cases} Q^2(\tau'_{\text{cali}}, f'_{\text{step}}) = \sum_{t > t_{\text{min}}} U_{\text{out}}^2(t, \tau'_{\text{cali}}, f'_{\text{step}}) \\ \min\left\{Q^2(\tau'_{\text{cali}}, f'_{\text{step}})\right\} \Rightarrow \begin{cases} \tau'_{\text{cali}} = \tau_{\text{cali}} \\ f'_{\text{step}} = f_{\text{step}} \end{cases} \end{cases} \tag{5.23}$$

The time domain transformation function to be used in the convolution (5.19) to obtain the step–response $U_{\text{out}}(t)$ is:

$$\begin{aligned} f_{\text{tran}}^{\text{step}}(t, \tau'_{\text{cali}}, f'_{\text{step}}) &= \mathcal{L}^{-1}\left\{\frac{1 + s\tau'_{\text{cali}}}{s\tau'_{\text{cali}} + f'_{\text{step}}}\right\} \\ &= \delta(t) + \left(\frac{(1 - f'_{\text{step}})}{\tau'_{\text{cali}}}\right) e^{-\frac{f'_{\text{step}} t}{\tau'_{\text{cali}}}} \end{aligned} \tag{5.24}$$

Since the convolution with a δ–function simply reproduces the original function, the step–response transformation can be computed as a correction on the original calibration output

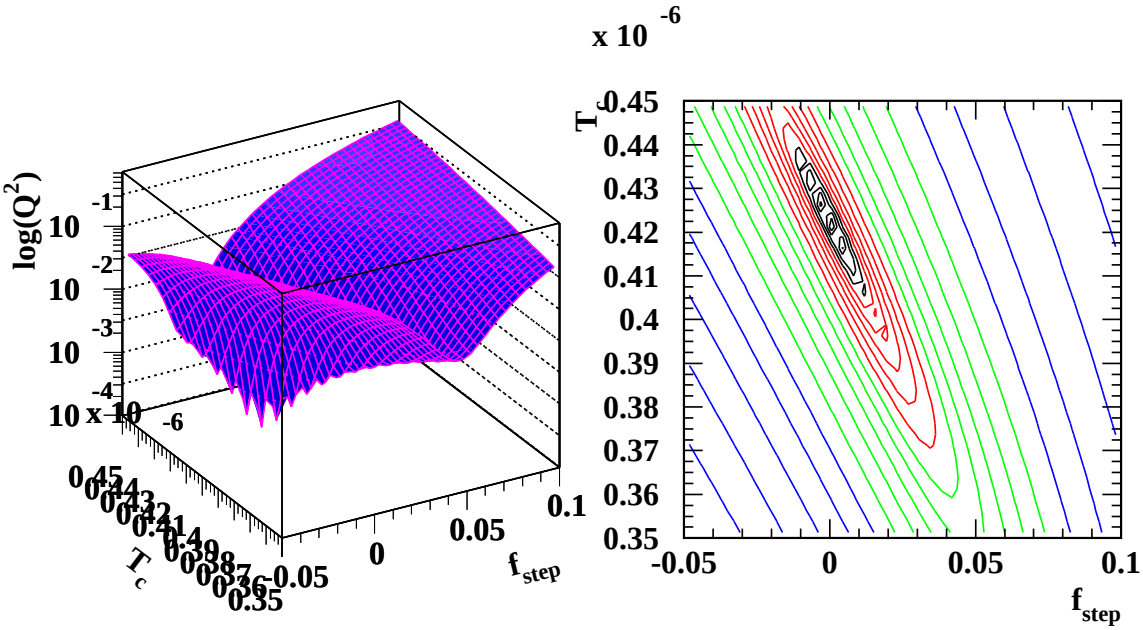

Figure 5.3: Surface (left) and contour (right) plot of the function $\log\left\{Q^2(\tau'_{\rm cali}, f'_{\rm step})\right\}$ in the ($\tau'_{\rm cali}$,$f'_{\rm step}$) parameters space. The "saw–teeth" structure around the minimum in left plot is not real, being due to the chosen number of points in the plot.

waveform:

$$\begin{aligned} U_{\rm out}(t, \tau'_{\rm cali}, f'_{\rm step}) &= f^{\rm step}_{\rm tran}(t, \tau'_{\rm cali}, f'_{\rm step}) * V^{\rm cali}_{\rm out}(t) \\ &= V^{\rm cali}_{\rm out}(t) + \left(\frac{(1 - f'_{\rm step})}{\tau'_{\rm cali}}\right) e^{-\frac{f'_{\rm step} t}{\tau'_{\rm cali}}} * V^{\rm cali}_{\rm out}(t) \\ &= V^{\rm cali}_{\rm out}(t) + \Delta U^{\rm step}(t, \tau'_{\rm cali}, f'_{\rm step}) \end{aligned} \tag{5.25}$$

Figure 5.3 shows the surface of $\log\left\{Q^2(\tau'_{\rm cali}, f'_{\rm step})\right\}$ in the ($\tau'_{\rm cali}$,$f'_{\rm step}$) parameters space. The $Q^2(\tau'_{\rm cali}, f'_{\rm step})$ function is computed from the *mock–up* calibration waveform shown in Figure 5.2; the signal is sampled every 1 ns for a 1 μs interval (1000 points), the tail starting point is $t_{\rm min} = 600$ ns. The $Q^2(\tau'_{\rm cali}, f'_{\rm step})$ function has indeed a minimum, that is located in a narrow flat valley of the ($\tau'_{\rm cali}$,$f'_{\rm step}$) parameters space. The $\tau'_{\rm cali}$ and $f'_{\rm step}$ parameters are strongly correlated. The function properties suggest that it is better to directly perform the minimization of $\log\left\{Q^2(\tau'_{\rm cali}, f'_{\rm step})\right\}$, in order to increase the numerical procedure convergence speed.

We wrote a numerical code that, given the sampled calibration signal $V^{\rm cali}_{\rm out}(t)$, computes the transformation convolution (5.25), then builds the χ^2–like function and performs the minimization (5.23) using a set of the MINUIT routines [62], in order to extract the correct $\tau_{\rm cali}$ and $f_{\rm step}$ values. The results are given with the relative uncertainties due to the numerical algorithms used in the minimization procedure. The starting point of the signal tail $t_{\rm min}$ can be set as an external parameter. The MINUIT routines show to

be able to handle the log $\left\{Q^2(\tau'_{\rm cali}, f'_{\rm step})\right\}$ function properties and the strong parameters correlation, the step–response code is able to converge to reasonable results. An example of the output of this routine is showed in Figure 5.2, where the step–response minimization is applied to a *mock–up* calibration signal. The calibration signal $V_{\rm out}^{\rm cali}(t)$ is shown, together with the $Q^2(\tau'_{\rm cali}, f'_{\rm step})$–minimizing step–response transformation. The tail starting point is $t_{\rm min} = 600$ ns. For a detailed discussion of the parameters results and of the algorithm accuracy see Section 5.4.

Since the results of the minimization procedure depend in principle on the tail starting point value $t_{\rm min}$, the correlation between this parameter and the final $\tau_{\rm cali}$ and $f_{\rm step}$ values is studied. In Figure 5.4, together with the usual trial *mock–up* calibration signal (top), the final parameters $f_{\rm step}$ (middle) $\tau_{\rm cali}$ (bottom) are shown as a function of the signal tail starting point value $t_{\rm min}$. Even if there is a clear correlation between the parameters results and the $t_{\rm min}$ value, we believe that there is a $t_{\rm min}$ region for which the $\tau_{\rm cali}$ and $f_{\rm step}$ values are stable enough. In the example case, this is for $t_{\rm min} \in [\sim$500 ns, $\sim$600 ns].

We found that a robust criterion to choose the "stable" $t_{\rm min}$ value to be used in the step–response minimization consists in correlating it with a signal–dependent parameter. We compute the tail starting point as $t_{\rm min} = t_{\rm min}^{\text{neg. lobe}} + 100$ ns, being $t_{\rm min}^{\text{neg. lobe}}$ the minimum of the negative lobe of the shaped signal. This choice proves to be effective and is automatically implemented in the numerical minimization code.

5.3.3 Detector cell characteristic frequency through the *cosine* transformation

According to the equivalent circuit of Figure 3.2, the detector transfer function $H^{\rm det}(s)$ is:

$$H^{\rm det}(s) = \frac{1 + s^2 LC}{1 + sCZ_{\rm line} + s^2 LC} Z_{\rm line} \tag{5.26}$$

The function $H^{\rm det}(s)$ has a *zero* in $\omega_0 = \frac{1}{\sqrt{LC}}$. If a *monochromatic* pulse of frequency ω_0 is injected on the detector cell, the response of the detector at the end of the readout system is null. We compute the response of the system to a monochromatic *cosine pulse* $C_{\rm inj}$ of frequency ω:

$$\begin{cases} C_{\rm inj}(t, \omega) = \cos(\omega t) \\ C_{\rm inj}(s, \omega) = \frac{s}{s^2 + \omega^2} \end{cases} \tag{5.27}$$

The relative frequency–domain transformation function is:

$$\begin{aligned} f_{\rm tran}^{\cos}(s, \omega, \tau'_{\rm cali}, f'_{\rm step}) &= \frac{C_{\rm inj}(s, \omega)}{I_{\rm inj}^{\rm cali}(s, \tau'_{\rm cali}, f'_{\rm step})} \\ &= \frac{s}{s^2 + \omega^2} \times \frac{s(1 + s\tau'_{\rm cali})}{s\tau'_{\rm cali} + f'_{\rm step}} \end{aligned} \tag{5.28}$$

If the conditions $\tau'_{\rm cali} = \tau_{\rm cali}$ and $f'_{\rm step} = f_{\rm step}$ are satisfied, the output function is exactly the response of the system to a cosine pulse of frequency ω:

$$X_{\rm out}(s) = C_{\rm inj}(s) \times H^{\rm det}(s) \times H^{\rm readout}(s) \tag{5.29}$$

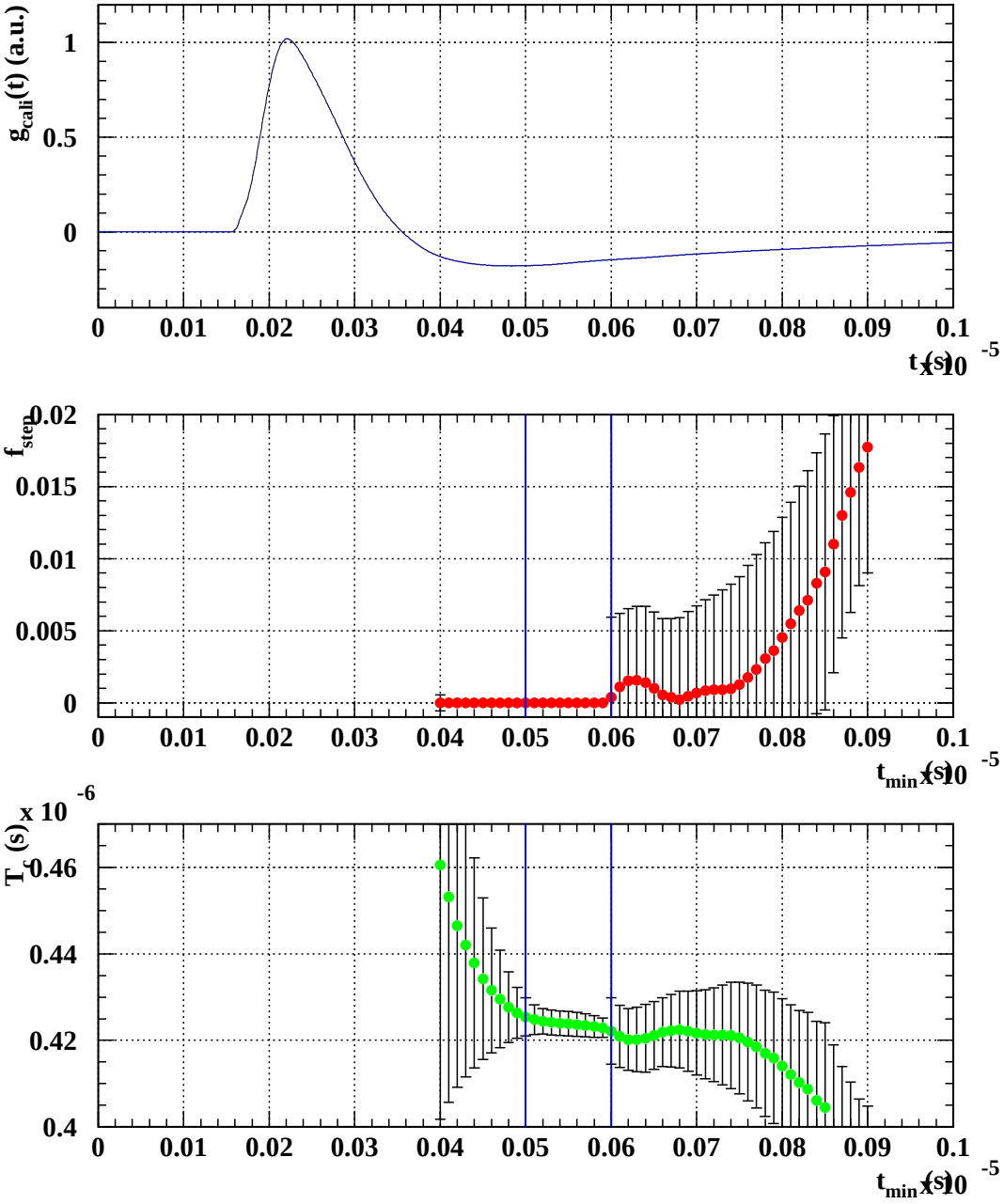

Figure 5.4: Step–response minimization final parameters τ_{cali} and f_{step} correlation with the signal tail starting point value t_{min}. The region of t_{min} for which the final τ_{cali} and f_{step} values are stable is show.

For this purpose the $\tau_{\rm cali}$ and $f_{\rm step}$ values computed with step–response analysis (Section 5.3.2) are used.

The property of the cosine–response to be null when the $\omega = \omega_0$ condition is verified is used to extract the LC parameter. Again, a χ^2–like function can be built summing the squares of the cosine–response function values along the tail of the pulse, the tail being defined as the portion of pulse after the time $t_{\rm min}$. The values of ω_0 can be extracted finding the minimum of this function:

$$\begin{cases} Q^2(\omega) = \sum_{t>t_{\rm min}} X^2_{\rm out}(t,\omega) \\ \min\left\{Q^2(\omega)\right\} \Rightarrow \omega = \omega_0 = \frac{1}{\sqrt{LC}} \end{cases} \tag{5.30}$$

The time domain transformation function to be used in the convolution (5.19) to obtain the cosine–response $X_{\rm out}(t)$ is:

$$\begin{aligned} f^{\cos}_{\rm tran}(t,\omega,\tau'_{\rm cali},f'_{\rm step}) &= \mathcal{L}^{-1}\left\{\frac{s}{s^2+\omega^2}\times\frac{s(1+s\tau'_{\rm cali})}{s\tau'_{\rm cali}+f'_{\rm step}}\right\} \\ &= \delta(t) + \frac{1}{f'^2_{\rm step}+\omega^2\tau'^2_{\rm cali}}\times\left\{e^{\frac{-tf'_{\rm step}}{\tau'_{\rm cali}}}(f'^2_{\rm step}-f'^3_{\rm step}) - \right. \\ &\quad \omega\times\left[\left(f'_{\rm step}+\omega^2\tau'^2_{\rm cali}\right)\sin(\omega t) + \right. \\ &\quad \left.\left.\left(\omega\tau'_{\rm cali}(f'_{\rm step}-1)\right)\cos(\omega t)\right]\right\} \end{aligned} \tag{5.31}$$

Since the convolution with a δ–function simply reproduces the original function, the cosine–response transformation can be computed as a correction on the original calibration output waveform:

$$\begin{aligned} X_{\rm out}(t,\omega,\tau'_{\rm cali},f'_{\rm step}) &= f^{\cos}_{\rm tran}(t,\omega,\tau'_{\rm cali},f'_{\rm step}) * V^{\rm cali}_{\rm out}(t) \\ &= V^{\rm cali}_{\rm out}(t) + \left\{\frac{1}{f'^2_{\rm step}+\omega^2\tau'^2_{\rm cali}}\times\left\{e^{\frac{-tf'_{\rm step}}{\tau'_{\rm cali}}}(f'^2_{\rm step}-f'^3_{\rm step}) - \right.\right. \\ &\quad \omega\times\left[\left(f'_{\rm step}+\omega^2\tau'^2_{\rm cali}\right)\sin(\omega t) + \right. \\ &\quad \left.\left.\left.\left(\omega\tau'_{\rm cali}(f'_{\rm step}-1)\right)\cos(\omega t)\right]\right\}\right\} * V^{\rm cali}_{\rm out}(t) \\ &= V^{\rm cali}_{\rm out}(t) + \Delta U^{\cos}(t,\omega,\tau'_{\rm cali},f'_{\rm step}) \end{aligned} \tag{5.32}$$

In Figure 5.5 (top) the cosine–response χ^2–like function (5.30) is shown versus the ω frequency value. The $Q^2(\omega)$ function does not shows a clear minimum: this is due to the contribution in the original calibration waveform of the readout transfer function $H_{\rm readout}(s)$, that in the ideal case is:

$$H^{\rm readout}(s) = \alpha\frac{s\tau_{\rm sh}}{(1+s\tau_{\rm sh})^3} \tag{5.33}$$

where α is the preamplifier gain and $\tau_{\rm sh}$ the shaper internal constant. The shaper acts as pass-width filter that blocks the higher frequency components. It prevents the $Q^2(\omega)$ function to rise at increasing frequency, making the minimum search impossible. This problem can be solved deconvolving the shaper transfer function from the transformed detector output. It can be easily done after the cosine transformation has been computed, since the cosine output function $X_{\rm out}(t,\omega)$ depends only on the single frequency value ω. The shaper transfer function contribution can be eliminated using a single correction factor, computed as the inverse of the absolute magnitude of (5.33) at the given frequency ω:

$$X'_{\rm out}(t,\omega,\tau_{\rm sh}) = X_{\rm out}(t,\omega)\sqrt{\frac{\left(1+(\omega\tau_{\rm sh})^2\right)^3}{(\omega\tau_{\rm sh})^2}} \tag{5.34}$$

The minimization as a function of ω can then be performed on the corrected χ^2–like function (see Figure 5.5 (bottom)), the shaper internal constant $\tau_{\rm sh}$ being given as an external parameter:

$$\begin{cases} Q'^2(\omega,\tau_{\rm sh}) = \sum_{t>t_{\rm min}} X'^2_{\rm out}(t,\omega,\tau_{\rm sh}) = Q^2(\omega)\left(\frac{\left(1+(\omega\tau_{\rm sh})^2\right)^3}{(\omega\tau_{\rm sh})^2}\right) \\ \min\left\{Q'^2(\omega,\tau_{\rm sh})\right\} \Rightarrow \omega = \omega_0 = \frac{a}{\sqrt{LC}} \end{cases} \tag{5.35}$$

The $Q'^2(\omega,\tau_{\rm sh})$ function plotted in Figure 5.5 shows a principal minimum around $\omega \sim$ 150 MHz, corresponding to the $\frac{1}{\sqrt{LC}}$ characteristic frequency. The $Q'^2(\frac{1}{\sqrt{LC}})$ value is not strictly zero, due to the fact that a detector cell is fairly more complex than a simple LC–circuit, and there is always at least a small resistive component r that should be considered. The electrode complex structure and its transmission–line behavior at high frequency produce the other local minima of the $Q'^2(\omega,\tau_{\rm sh})$ function.

We wrote a numerical code that, given the sampled calibration signal $V^{\rm cali}_{\rm out}(t)$ and the parameters $\tau_{\rm cali}$, $f_{\rm step}$ and $\tau_{\rm sh}$, computes the transformation convolution (5.32), then builds the χ^2–like function and performs the minimization (5.35) using a set of the MINUIT routines [62], in order to extract the correct ω_0 value. The result is given with the relative uncertainty due to the numerical algorithms used in the minimization procedure. The starting point of the signal tail $t_{\rm min}$ can be set as an external parameter. An example of the output of this routine is showed in Figure 5.2, where the cosine–response minimization is applied to a *mock–up* calibration signal. The calibration signal $V^{\rm cali}_{\rm out}(t)$ is shown, together with the $Q^2(\omega,\tau_{\rm sh})$–minimizing cosine–response transformation. The tail starting point is $t_{\rm min} = 600$ ns, the shaper constant is $\tau_{\rm sh} = 15$ ns. For a detailed discussion of the parameters results and of the algorithm accuracy see Section 5.4.

Since the result of the procedure depends in principle on the tail starting point value $t_{\rm min}$, the correlation between this parameter and the final ω_0 value is studied. In Figure 5.6, together with the trial *mock–up* calibration signal (top), the final parameter ω_0 is shown as a function of the signal tail starting point value $t_{\rm min}$ (bottom). The ω_0 parameter is clearly uncorrelated with the $t_{\rm min}$ value, its final value being stable in the limit of the numerical algorithm precision. We arbitrary decide to chose $t_{\rm min} = t^{\rm neg.\ lobe}_{\rm min}$, being $t^{\rm neg.\ lobe}_{\rm min}$ the minimum of the negative lobe of the shaped signal. This choice is automatically implemented in the numerical minimization code.

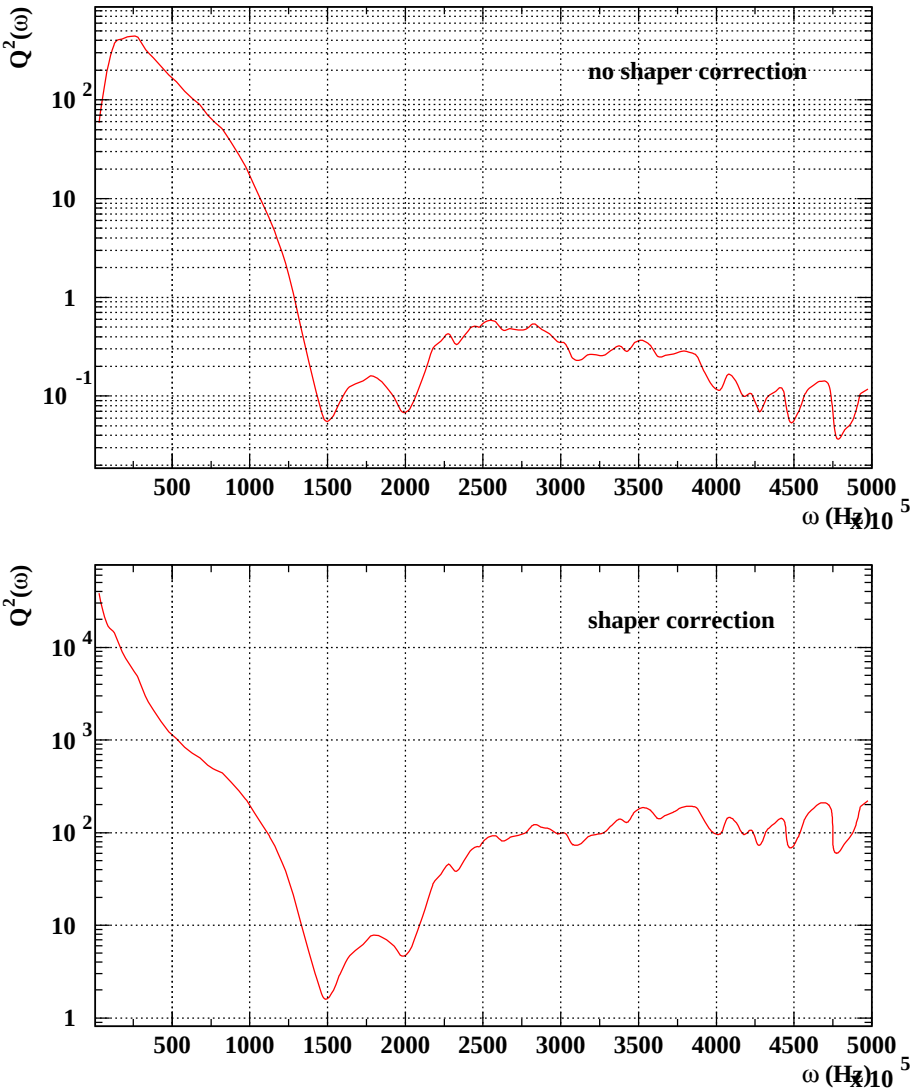

Figure 5.5: Profile of $Q^2(\omega)$ (top) and $Q'^2(\omega, \tau_{\rm sh})$ (bottom) as a function of the frequency ω.

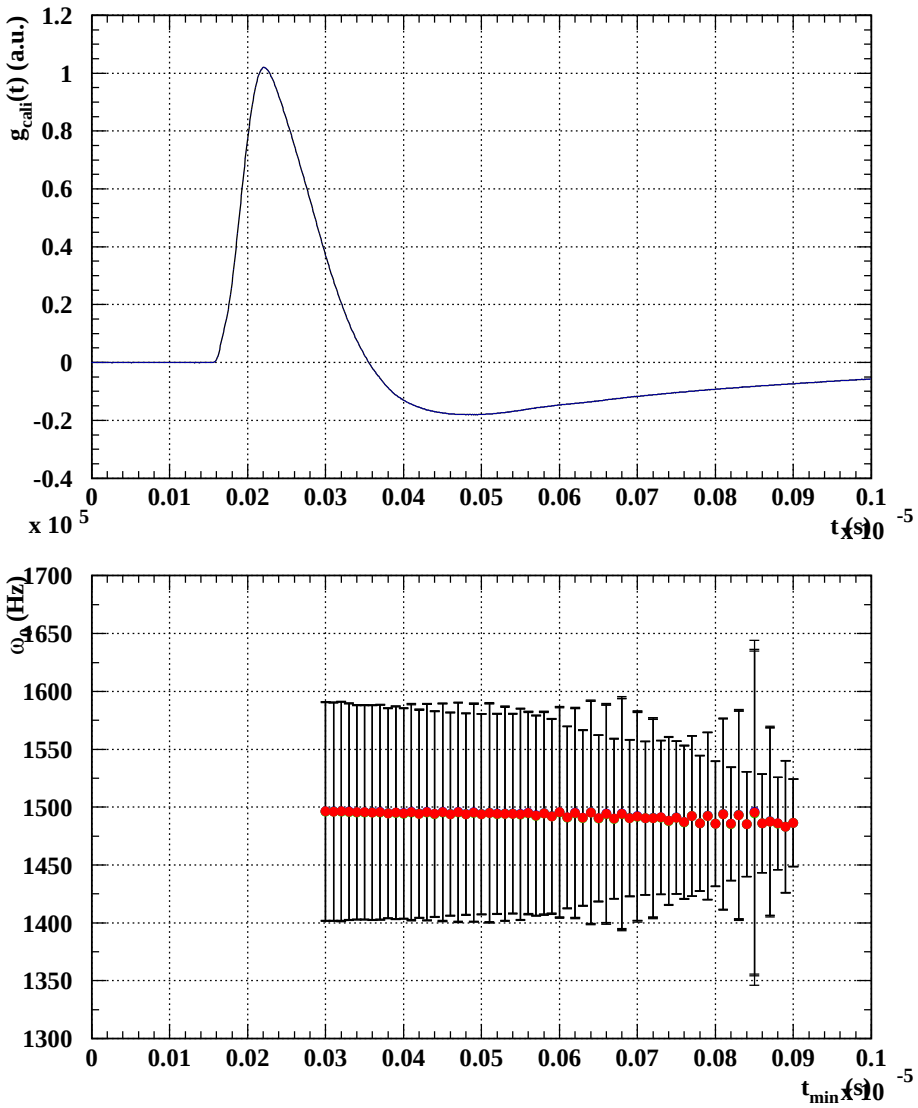

Figure 5.6: Cosine–response minimization final parameter ω_0 correlation with the signal tail starting point value $t_{\min}$.

5.3.4 Detector contact resistance through the injection–point correction residual oscillation minimization

If the resistive component r is taken into account in the detector cell description (Figure 5.1) the detector transfer function $H^{\mathrm{det}}(s)|_{r\neq 0}$ becomes:

$$H^{\mathrm{det}}(s)|_{r\neq 0} = \frac{1 + srC + s^2LC}{1 + \mathrm{s(r + Z_{line})C + s^2LC}} Z_{\mathrm{line}} \tag{5.36}$$

An attempt to simultaneously extract both the $\tau_0 = \sqrt{LC}$ and $\tau_r = rC$ parameters can be done, implementing a zero–cancellation procedure in the transformation–and–minimization framework [34]. The calibration waveform can be corrected for the "injection–point" factor:

$$\begin{aligned} V_{\mathrm{out}}^{\mathrm{cali}}(t)|^{\mathrm{corr}} &= f_{\mathrm{tran}}^{\mathrm{i.p.}}(t, \tau_0', \tau_r') * V_{\mathrm{out}}^{\mathrm{cali}}(t) \\ &= \mathcal{L}^{-1}\left\{\frac{1}{1 + s\tau_r' + s^2\tau_0'}\right\} * V_{\mathrm{out}}^{\mathrm{cali}}(t) \end{aligned} \tag{5.37}$$

the transformation function being:

$$f_{\mathrm{tran}}^{\mathrm{i.p.}}(t, \tau_0, \tau_r) = \mathcal{L}^{-1}\left\{\frac{1}{1 + s\tau_r' + s^2\tau_0'}\right\} \tag{5.38}$$

$$= e^{-\frac{t}{\tau_1}} \sin\frac{t}{\tau_2} \tag{5.39}$$

where:

$$\begin{cases} \tau_1 = \frac{2\tau_0'^2}{\tau_r'} \\ \tau_2 = \frac{2\tau_0'^2}{\sqrt{4\tau_0'^2 - \tau_r'^2}} \end{cases} \tag{5.40}$$

If the condition $\{\tau_0' = \tau_0, \tau_r' = \tau_r\}$ is verified, the factor $(1 + srC + s^2LC)$ embedded in the original calibration waveform because of the detector transfer function $H^{\mathrm{det}}(s)|_{r\neq 0}$ is canceled. Otherwise the zero–cancellation is incomplete, and oscillations of frequency $\omega_{\mathrm{res}} = \frac{1}{2\pi\tau_0'}$ are produced in the transformed waveform $V_{\mathrm{out}}^{\mathrm{cali}}(t)|^{\mathrm{corr}}$.

The correct values of the τ_0 and τ_r parameters are sought searching the minimum of this residual oscillations. A χ^2–like function can be built summing the squares of the difference between the observed calibration signal and the correct one in the tail region on the pulse, the tail being defined as the portion of pulse after the time t_{min}:

$$\begin{cases} \Delta V_{\mathrm{out}}^{\mathrm{cali}}(t) = V_{\mathrm{out}}^{\mathrm{cali}}(t) - V_{\mathrm{out}}^{\mathrm{cali}}(t)|^{\mathrm{corr}} \\ Q^2(\tau_0', \tau_r') = \sum_{t>t_{\mathrm{min}}} \left(\Delta V_{\mathrm{out}}^{\mathrm{cali}}(t, \tau_0', \tau_r')\right)^2 \\ \min\left\{Q^2(\tau_0', \tau_r')\right\} \Rightarrow \begin{cases} \tau_0' = \tau_0 \\ \tau_r' = \tau_r \end{cases} \end{cases} \tag{5.41}$$

Figure 5.7 shows the surface of $\log\left\{Q^2(\tau_0', \tau_r')\right\}$ in the (τ_0', τ_r') parameters space. The $Q^2(\tau_0', \tau_r')$ function is computed from the *mock–up* calibration waveform shown in

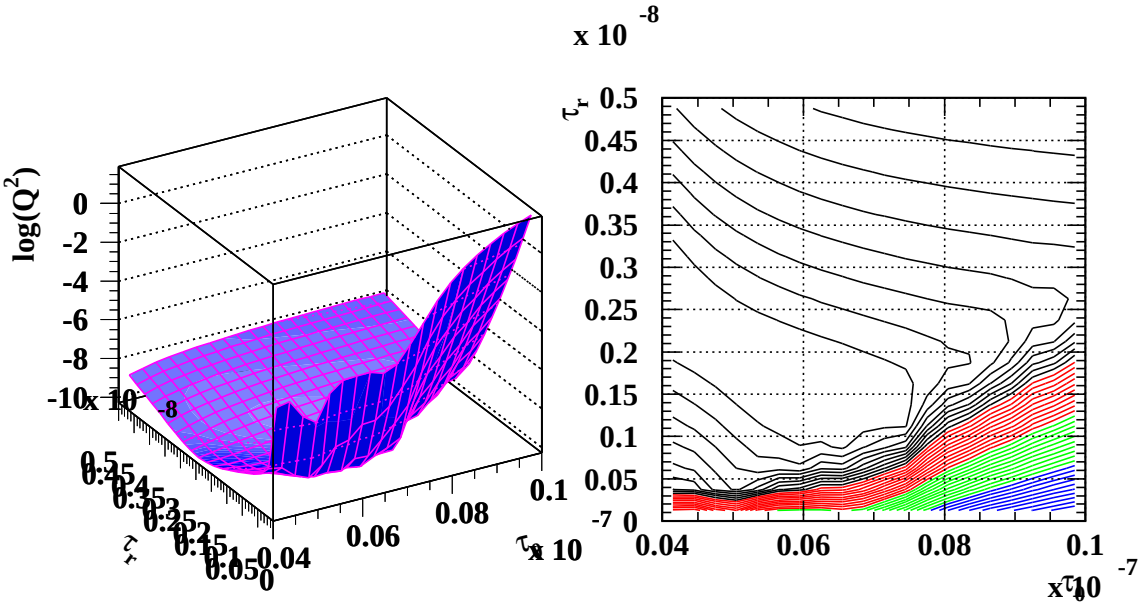

Figure 5.7: Surface (left) and contour (right) plot of the function $\log\left\{Q^2(\tau_0', \tau_r')\right\}$ in the (τ_0', τ_r') parameters space.

Figure 5.2; the signal is sampled every 1 ns for a 1 μs interval (1000 points), the tail starting point is $t_{\min} = 600$ ns. The minimum of the $Q^2(\tau_0', \tau_r')$ function is hardly found: even in logarithmic scale there is a wide and nearly flat (τ_0', τ_r') region in which the $\log\left\{Q^2(\tau_0', \tau_r')\right\}$ variation is so small that a numerical minimization procedure would result long and rather imprecise. Furthermore, the τ_0 and τ_r parameters are strongly correlated: even if a numeric algorithm succeeds in converging to a minimum value, we can expect large errors on the extracted parameters.

We wrote a numerical code that, given the sampled calibration signal $V_{\text{out}}^{\text{cali}}(t)$, computes the transformation convolution (5.37), then builds the χ^2–like function and performs the minimization (5.41) using a set of the MINUIT routines [62], in order to extract the correct τ_0 and τ_r values. The results are given with the relative uncertainties due to the numerical algorithms used in the minimization procedure. The starting point of the signal tail $t_{\min}$ can be set as an external parameter. An example of the output of this routine is showed in Figure 5.2, where the injection–point correction residual oscillation minimization is applied to a *mock–up* calibration signal. The calibration signal $V_{\text{out}}^{\text{cali}}(t)$ is shown, together with the $Q^2(\tau_0, \tau_r)$–minimizing residual oscillation. The tail starting point is $t_{\min} = 600$ ns. In this case the results appears quite promising, since $\tau_0 \sim \frac{1}{\omega_0}$, the ω_0 parameters being obtained with the cosine transformation algorithm (the actual values are shown in Figure 5.2). On the other hand, for other calibration waveform the MINUIT routines fail in finding a reasonable convergence.

As for the previous algorithms, we investigate the correlation between the tail starting point value $t_{\min}$ and the final τ_0 and τ_r values. In Figure 5.8, together with the usual trial *mock–up* calibration signal (top), the final parameters τ_0 (middle) and τ_r (bottom) are

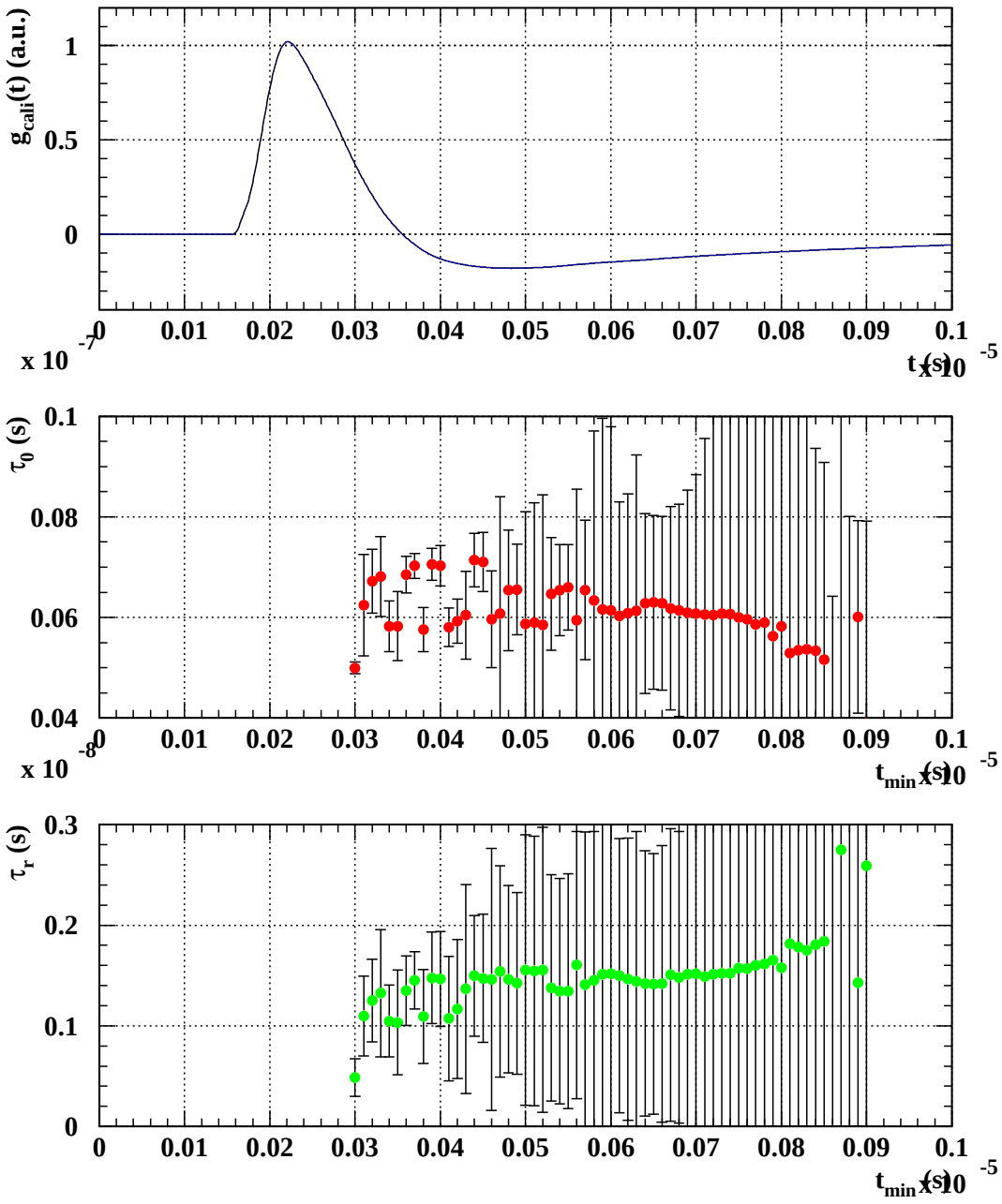

Figure 5.8: Step–response minimization final parameters τ_{cali} and f_{step} correlation with the signal tail starting point value t_{min}.

shown as a function of the signal tail starting point value $t_{\min}$. The algorithm shows again its weakness: the strong correlation between the final parameters values is confirmed, and a nearly–random dependence on the $t_{\min}$ value appears.

For these reasons this parameters–extraction method is judged not to be robust enough to be used in a EMC calibration algorithm. The τ_r estimate remains a problem to be further investigate.

5.4 Parameters extraction from *mock–up* signals

The parameters extraction algorithms described in Section 5.3.2 and 5.3.3 are applied on the calibration signals collected from the *mock–up* Middle cells. For this validation study the *mock–up* system has been completed with the full calibration–injection and signal–readout warm–to–cold cables chains (Section 2.3). The new system setup is shown in Figure 5.9. All the measures relative to this section are taken with the *mock–up* second removable ground spring connected (two ground connections in the second connector).

Figure 5.9: *Mock–up* system setup, complemented with the full calibration–injection and signal–readout cables chains.

Since the calibration and the readout cables are supposed to be used in LAr, and

some of their characteristics (e.g. the skin effect) change with the temperature, during the signals injection and measure we eventually allow the cables to be immerse in liquid nitrogen (LN_2) from the MB connection up to the warm–to–cold pin carrier (Figure 5.10). In this Section we refer to a "*warm*" measure (or result) when the calibration and the readout cables are kept at room temperature, to a "*cold*" measure (or result) when they are immerse in the LN_2 dewar.

Figure 5.10: Calibration–injection and signal–readout cables, kept in a LN_2 dewar from the MB connection up to the warm–to–cold pin carrier.

Because of the cables presence, the calibration injection system has been slightly modified with respect to the one used in Chapter 3. The exponential signal is (again) obtained by the injection of a voltage step through a RC circuit (Figure 5.11). In this case a discrete capacitive component ($C = 3.97$ nF $\simeq 4$ nF) is directly plugged between the beginning of the calibration cables chain and the voltage step generator, whose internal resistance is $r_{\rm int} = 50\ \Omega$. The cables are supposed to be correctly terminated, their effective impedance Z acts (mostly) as a resistance. The voltage pulse at the cables termination resistance on the MB is then an exponential, with characteristic decay time $\tau_{\rm cali} = (r_{\rm int} + Z)C$. The injector resistance on the MB is in charge to convert the voltage signal into a current pulse. We estimate the calibration cables effective impedance Z with a Time Domain Reflectometer, both at warm and at cold. The expected values of $\tau_{\rm cali}$

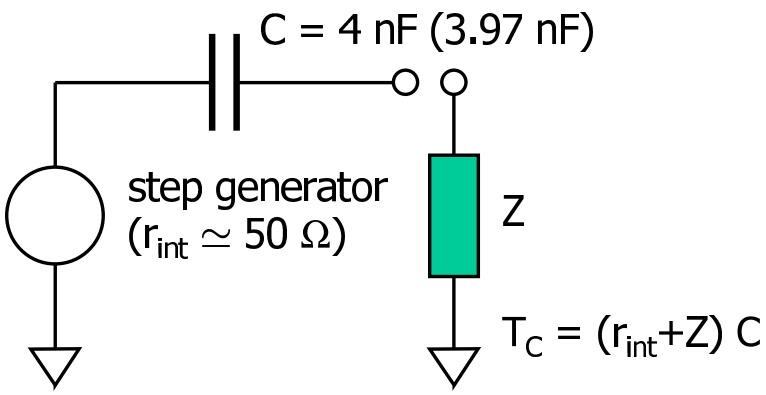

Figure 5.11: *Mock–up* calibration pulse injection circuit. The exponential decay time is obtained as $\tau_{\rm cali} = (r_{\rm int} + Z)C$, Z being the effective characteristic impedance of the calibration cables chain.

are listed in Table 5.1. When the injection circuit is directly plugged to the oscilloscope ($Z = r_{\rm int} = 50\Omega$), we measured the exponential pulse decay time to be $\tau_{\rm cali} \simeq 400$ ns.

	Z (Ω)	$\tau_{\rm cali}^{\rm expected}$ (ns)
oscilloscope	~ 50	~ 400
warm cables	~ 57	~ 425
cold cables	~ 54	~ 415

Table 5.1: Expected *mock–up* calibration decay time value, as a function of the the cables effective characteristic impedance Z.

The calibration signals are injected on the *mock–up* Middle cells M32÷M39 at warm and cold, and acquired with an oscilloscope according to the procedure already described in Chapter 3. The output signal sampling frequency is 1 GHz (Δt=1ns), the pulse are recorded for a 1 μs interval. The step–response and the cosine–response of the collected signals are computed, the $f_{\rm step}$, $\tau_{\rm cali}$ and ω_0 parameters are extracted for each of the 8 Middle cells at warm and cold.

The calibration pulse characteristic parameters $f_{\rm step}$ and $\tau_{\rm cali}$ are shown in Figure 5.12. The extracted $f_{\rm step}$ and $\tau_{\rm cali}$ values are compatible for all the different *mock–up* cells, as expected since they are related to the same injection circuit. This proves that the step–response algorithm is capable to handle the cell-dependent signal properties. The average values of the parameters are listed in Table 5.2; the exponential decay time $\langle\tau_{\rm cali}\rangle$ is indeed compatible with the prediction of Table 5.1, both at warm and at cold. As expected, the extracted $f_{\rm step}$ values are really small, and compatible with zero at least for the warm measures. This is in agreement with the theoretic description of the *mock–up* calibration pulse, as discussed in Appendix A.

In Figure 5.13 the cell characteristic frequency $\omega_0 = \frac{1}{\sqrt{LC}}$ is shown, and compared with the LC direct measure discussed in Section 3.4. The extracted values of the ω_0 parameter

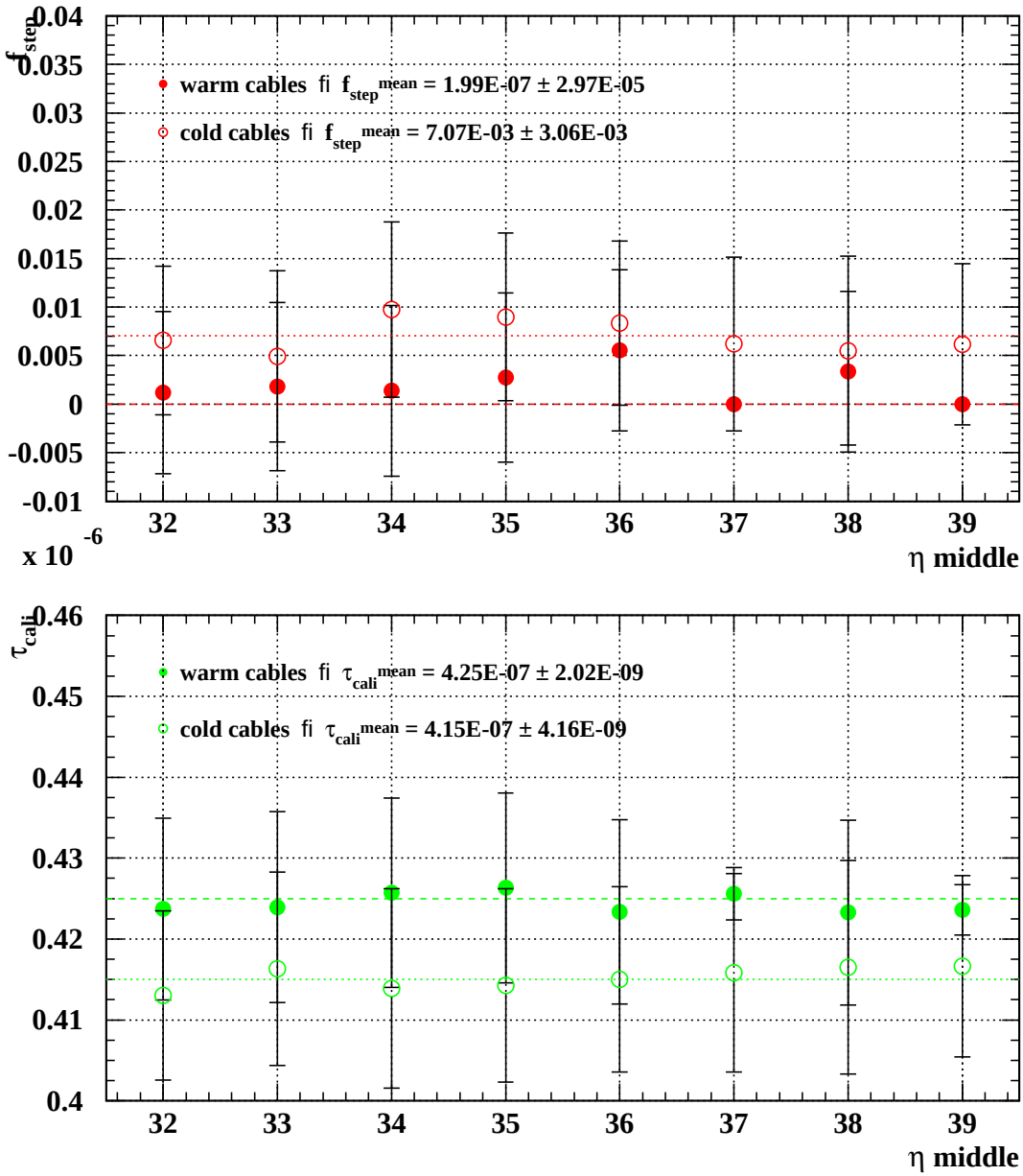

Figure 5.12: Calibration pulse characteristic parameters $f_{\rm step}$ (top) and $\tau_{\rm cali}$ (bottom), as extracted by the step–response transformation algorithm applied to the *mock–up* Middle cells M32÷M39. Empty points refer to signals collected at warm, full points at cold.

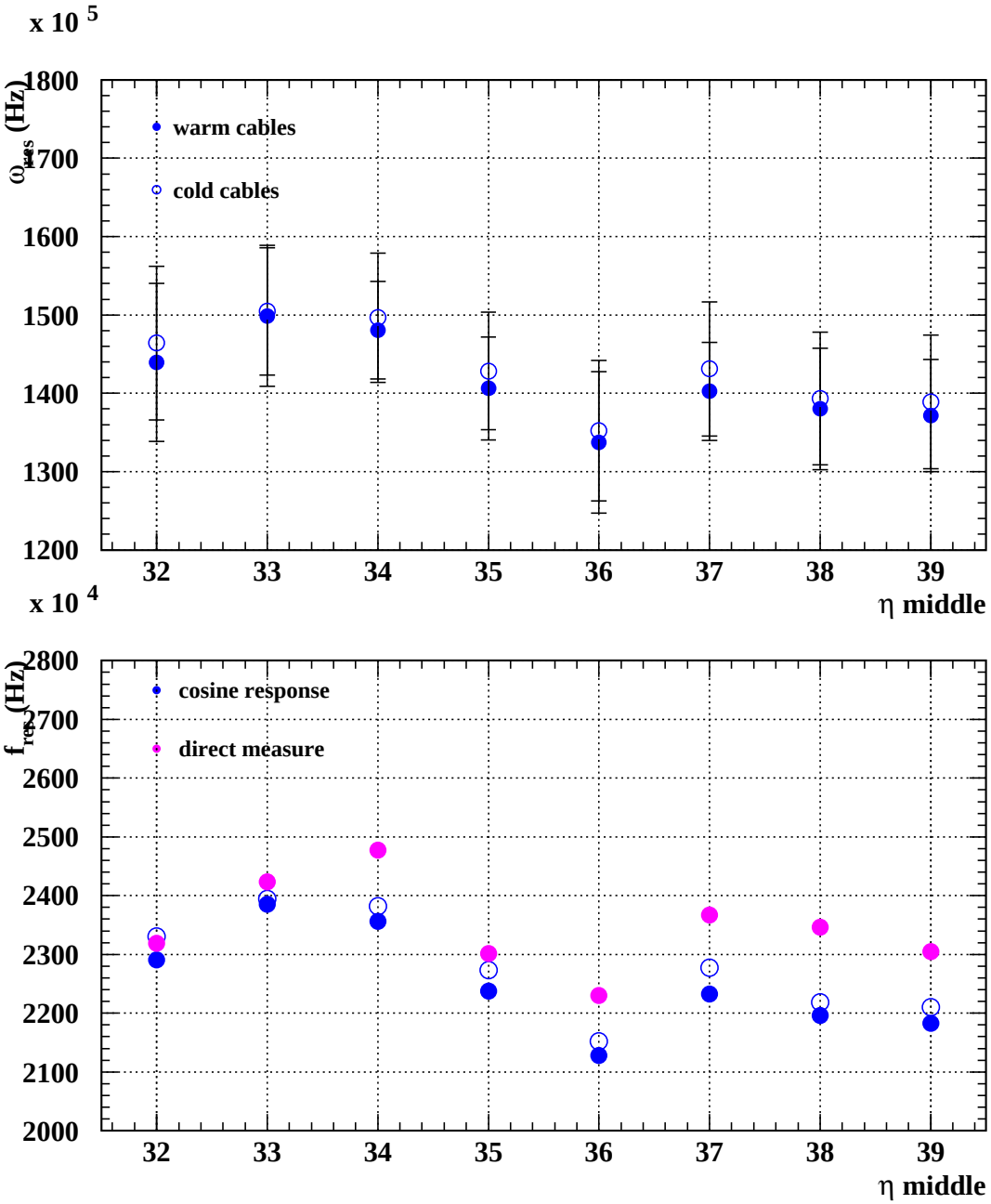

Figure 5.13: Detector cell characteristic frequency $\omega_0 = \frac{1}{\sqrt{LC}}$ as extracted by the cosine–response transformation algorithm applied to the *mock–up* Middle cells M32÷M39 calibration signals: results and relative uncertainties (top); comparison with the direct measure (bottom) are shown. Empty points refer to signals collected at warm, full points at cold.

	$\langle\tau_{\rm cali}\rangle$ (ns)	$\langle f_{\rm step}\rangle$
warm	425 ± 2	$1.99 \cdot 10^{-7} \pm 2.97 \cdot 10^{-5}$
cold	415 ± 4	$7.07 \cdot 10^{-3} \pm 3.06 \cdot 10^{-3}$

Table 5.2: Average $\tau_{\rm cali}$ and $f_{\rm step}$ calibration parameters values, as extracted at warm and cold from the 8 *mock–up* Middle cells with the step–response transformation.

show the expected trend along the 8 Middle cell positions. They are systematically smaller than the direct measures. This effect can be explained by the presence of the MB, that provides each cell with an additional $\sim$ 10 nH inductive contribution [23]. The direct L and C measures of Chapter 3 were in fact performed at the SB level. There is no significant difference between the warm and cold ω_0 values: the cosine–response algorithm proves to be able to estimate the cell-dependent LC parameters directly from the calibration signal pulses.

5.5 Parameters extraction from the test–beam 32–samples delay waveforms

The parameters extraction procedures are applied to the EMC delay calibration waveforms. The goal is to extract the $\{\tau_{\rm cali}, f_{\rm step}, \omega_0\}$ parameters set for each readout cells, to predict the ionization waveform and to compute the corresponding OF coefficients to be used for the energy reconstruction. The calibration waveforms used for this procedures come from the delay curves generated from the test-beam calibration data [27].

In the standard test-beam setup the delay waveforms are built using a 7–samples readout configuration: the resulting curves are defined over a 175 ns interval. Since a long tail portion of the calibration signal is needed to apply the algorithms of Section 5.3.2 and 5.3.3, some special calibration runs have been acquired for this purpose, using a 32–samples readout configuration: the resulting curves are defined over a 800 ns interval. The 32–samples delay runs have been acquired during the test–beam periods for the EM barrel production modules M10 (October 2001), in the region $\{\eta_{\rm cell} \in [16, 23], \phi_{\rm cell} \in [0, 7]\}$, and P15 (June 2002), in the region $\{\eta_{\rm cell} \in [0, 55], \phi_{\rm cell} \in [8, 15]\}$.

This analysis is presently concentrated on the Middle cells, since this is indeed the sampling that is mostly responsible for the detector non–uniformity. The greater part of the electromagnetic shower energy is in fact released in the Middle cells; the Middle cells shows the greatest effective inductance L, they are indeed the cells in which the most appreciable difference between the calibration and the ionization signal shapes is found.

5.5.1 Master Waveform computation

Each delay curve is usually built from the calibration data generated by the injection of a calibration pulse of defined normalization, corresponding to a definite Digital–to–Analogic–Converter (DAC) setting on the calibration board (CB) [27]. The calibration

data are acquired in defined readout gain region (Low, Medium or High) [24]. The aim of this work is to come to a single set of OF coefficients for each gain region, assuming that in each of these the response of the detector is *linear*.

The CB output is sensitive to the card clock feed–through [27]: even when the CB is supposed to inject a null signal (DAC = 0), in fact, there is a non–zero signal emerging from the board (DAC0 signal). Since the response of the detector is not dependent on this residual signal, its effect should be subtracted from the delay curves.

The linearity assumption and the need of the DAC0 signal subtraction are implemented through the use of the Master Waveform (MW) for the calibration analysis. The MW values m are determined by the linear response of the system for several DAC values at a given time bin t, from which the input current can be computed:

$$y = m \times \mathrm{DAC} + \mathrm{DAC0} \quad \forall t \in [0, 800]\mathrm{ns} \tag{5.42}$$

where y is the system response in ADC counts for the relative DAC setting, as extracted from the corresponding delay curve. The m and DAC0 values are obtained through a linear fit to the delay data at each time t. For this purpose only the delay curves in the linear–response region of the calorimeter are used. This procedure allows to map the detector response $m(t)$ to a calibration pulse, averaged on the different DAC values and independent of the DAC0 offset.

The final MW $m(t)$ is measured in ADC/DAC units. An example of the MW computation in the Medium gain region is proposed in Figure 5.14, 5.15 and 5.16, where the input 32–samples delay curves, four examples of the (5.42) fits for different t values, and the final $m(t)$ and DAC0(t) results are shown.

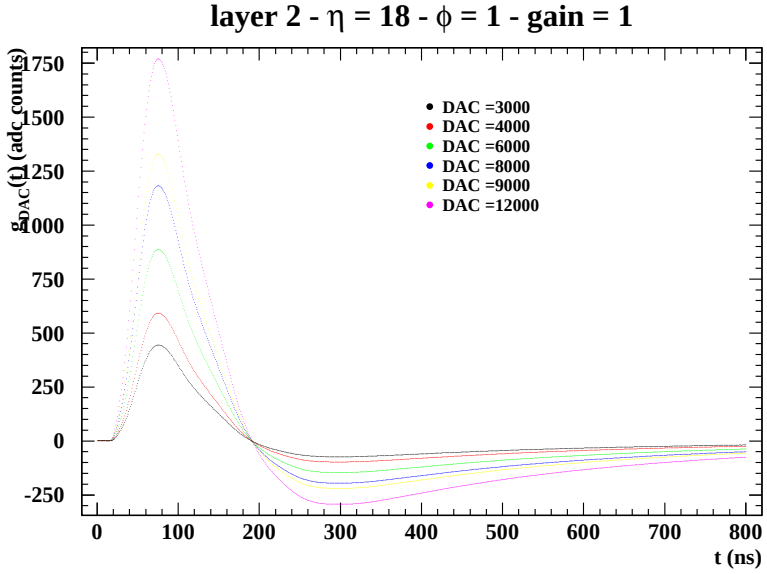

Figure 5.14: 32–samples delay curves for different DAC values, acquired from the EMB module M10 Middle cell $\eta_{\mathrm{cell}} = 16$, $\phi_{\mathrm{cell}} = 1$ in Medium gain.

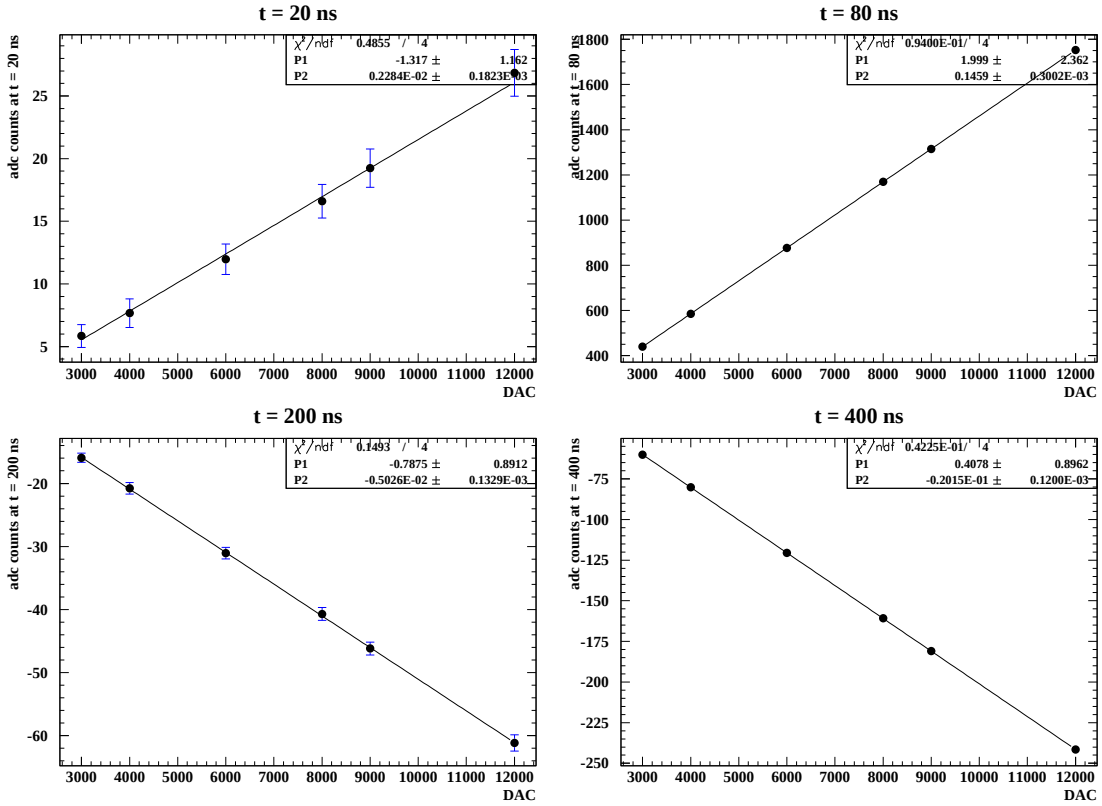

Figure 5.15: Examples of the (5.42) fit on the DAC-dependent delay curves values at different time t. The values are taken from the delay curves shown in Figure 5.14

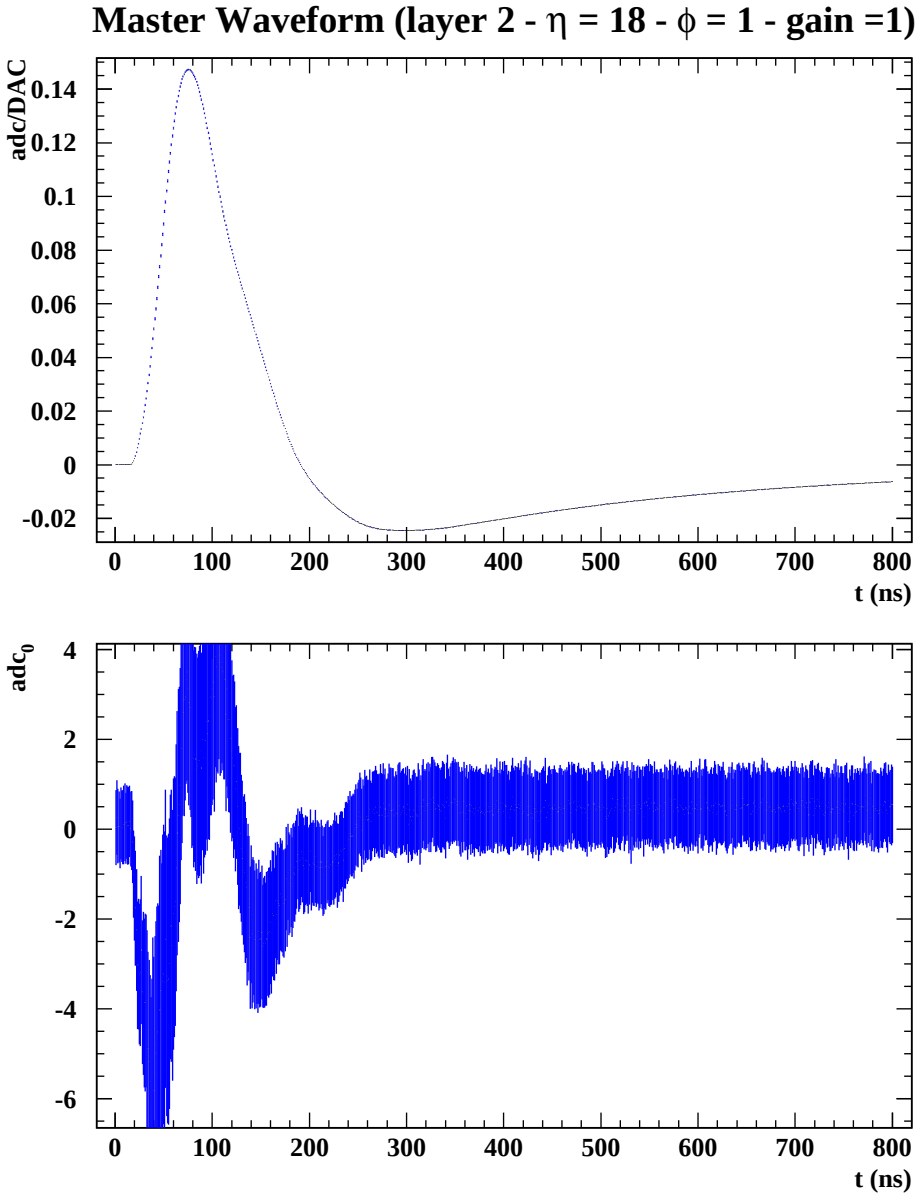

Figure 5.16: Master Waveform values $m(t)$ (top) and residual signal DAC0(t) (bottom), computed for the EMB module M10 Middle cell $\eta_{\text{cell}} = 16$, $\phi_{\text{cell}} = 1$ in Medium gain.

5.5.2 Parameters extraction results

The parameters extraction procedure is applied to the EM barrel production module M10 Middle cells, in the region $\{\eta_{\text{cell}} \in [16, 23], \phi_{\text{cell}} \in [0, 7]\}$, and to the P15 module Middle cells in the region $\{\eta_{\text{cell}} \in [0, 55], \phi_{\text{cell}} \in [8, 15]\}$.

Calibration pulse parameters

The calibration pulse characteristic parameters τ_{cali} and f_{step} values are shown in Figure 5.17 for module M10 cells, and in Figure 5.18 for module P15 cells. The obtained values are compatible with the direct measures on the production CB's [38], from which $\tau_{\text{cali}} = 347$ ns $\pm$ 5.7 RMS and $fstep \simeq 7\%$ is obtained (see Appendix A).

The parameters distributions show a consistent spread, and a structure can be noticed at least in the M10 results. The total distributions accumulate parameters values relative to different calibration lines: each calibration board is in fact equipped with 8 different pulsers. Since the calibration injection pattern is known (see [3] and Chapter 3), each pair of f_{step} and τ_{cali} values can be attributed to a specific CB channel. Examples of the parameters clustering is shown in Figure 5.19 for the M10 values coming from Sector 4 ($24 \leq \eta_{\text{cell}} \leq 31$), and in Figure 5.20 for the P15 values coming from Sector 1 ($0 \leq \eta_{\text{cell}} \leq 7$). The extracted parameters group well around a line–dependent central value, that is computed as the weighted mean, and shown superimposed with the relative uncertainty. Similar results are obtained for all the other module sectors. This is an additional prove of the precision of the step–response parameters extraction algorithm.

A direct comparison between the values extracted from the two different modules data for the same calibration lines it is presently not possible, since the 32–samples delay runs have been acquired from two completely non–superposing $\{\eta, \phi\}$ regions.

Cell characteristic frequency

The cell characteristic frequency values $\omega_0 = \frac{1}{\sqrt{LC}}$ are shown as a function of η_{cell} for the different ϕ_{cell} lines in Figure 5.21 for module M10 cells, and in Figure 5.22 for module P15 cells. The results reproduce well the electrode structure. The 4–η_{cell} pattern due to the effective inductance L located on the connection strips (see Chaper 3) is clearly evident in both cases.

Figure 5.23 (Figure 5.24) shows the same ω_0 values for the module M10 (P15), as function of the ϕ_{cell} position . A perfect symmetry would be expected, but a trend appears once the η dependence connection show smaller ω_0 (greater LC) value. This effect can be due a non–perfectly equalized inductive contribution on the MB or on the SB, but its study is behind the scope of this work. More details on this effect are discussed in the comparison with the direct LC measures on the P15 module cells.

Comparison with the LC values from direct measure and OF4 fit

Direct measures of the cells effective L and C parameters (L_{meas}, C_{meas}) has been performed on the prototype module M0, and on some of the production modules (M15,

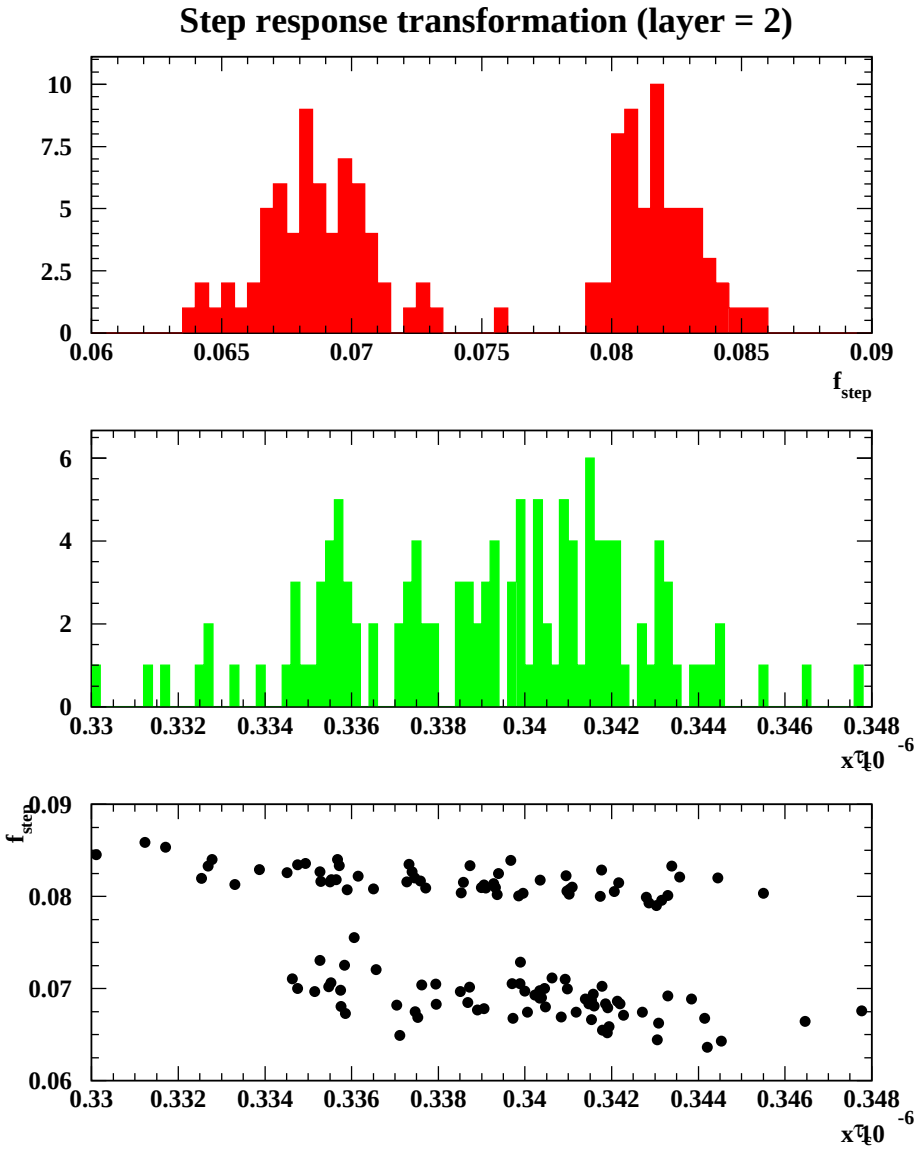

Figure 5.17: Calibration pulse characteristic parameters f_{step} (top) and τ_{cali} (middle) distributions, as extracted from the EM barrel production module M10 Middle cells 32–samples MW, in the region $\{\eta_{\text{cell}} \in [16, 23], \phi_{\text{cell}} \in [0, 7]\}$. The parameters correlation is shown in the bottom plot.

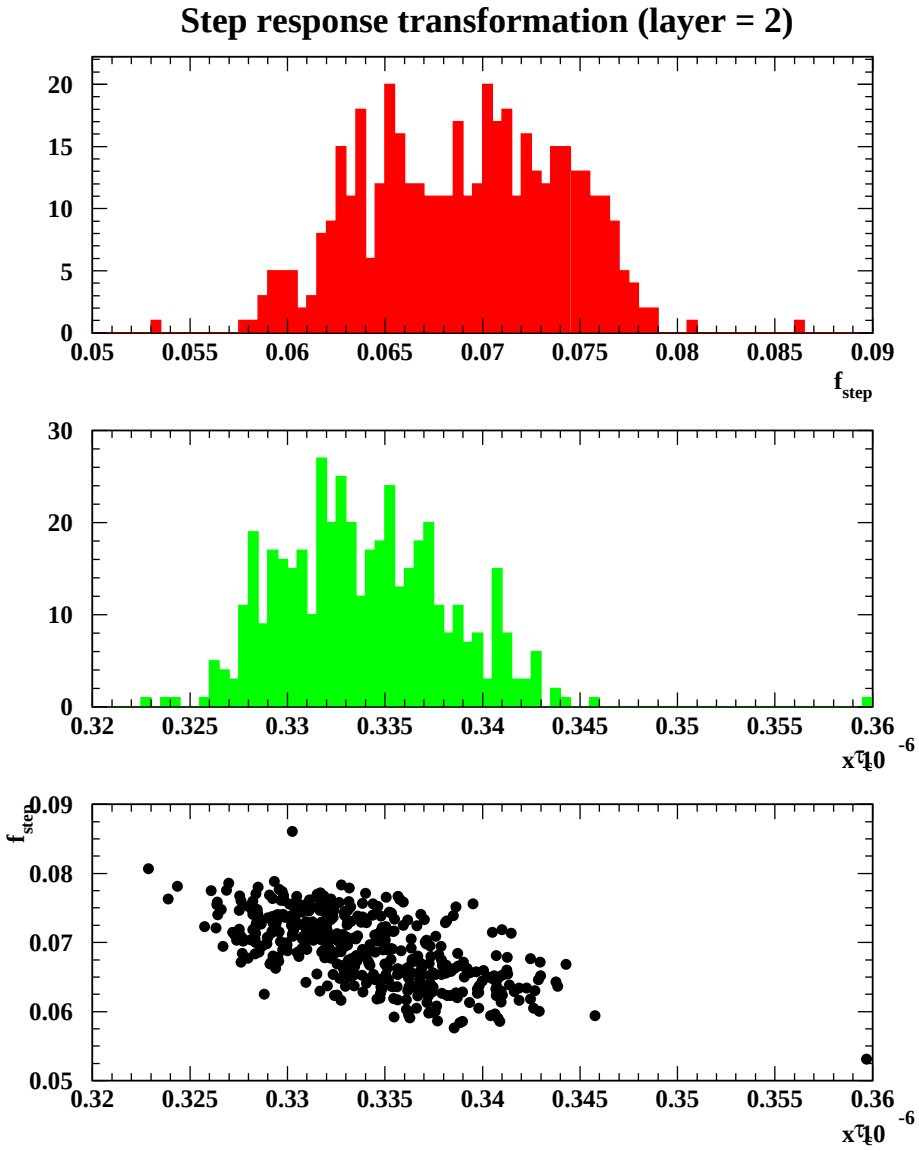

Figure 5.18: Calibration pulse characteristic parameters f_{step} (top) and τ_{cali} (middle) distributions, as extracted from the EM barrel production module P15 Middle cells 32–samples MW, in the region $\{\eta_{\text{cell}} \in [0, 55], \phi_{\text{cell}} \in [8, 15]\}$. The parameters correlation is shown in the bottom plot.

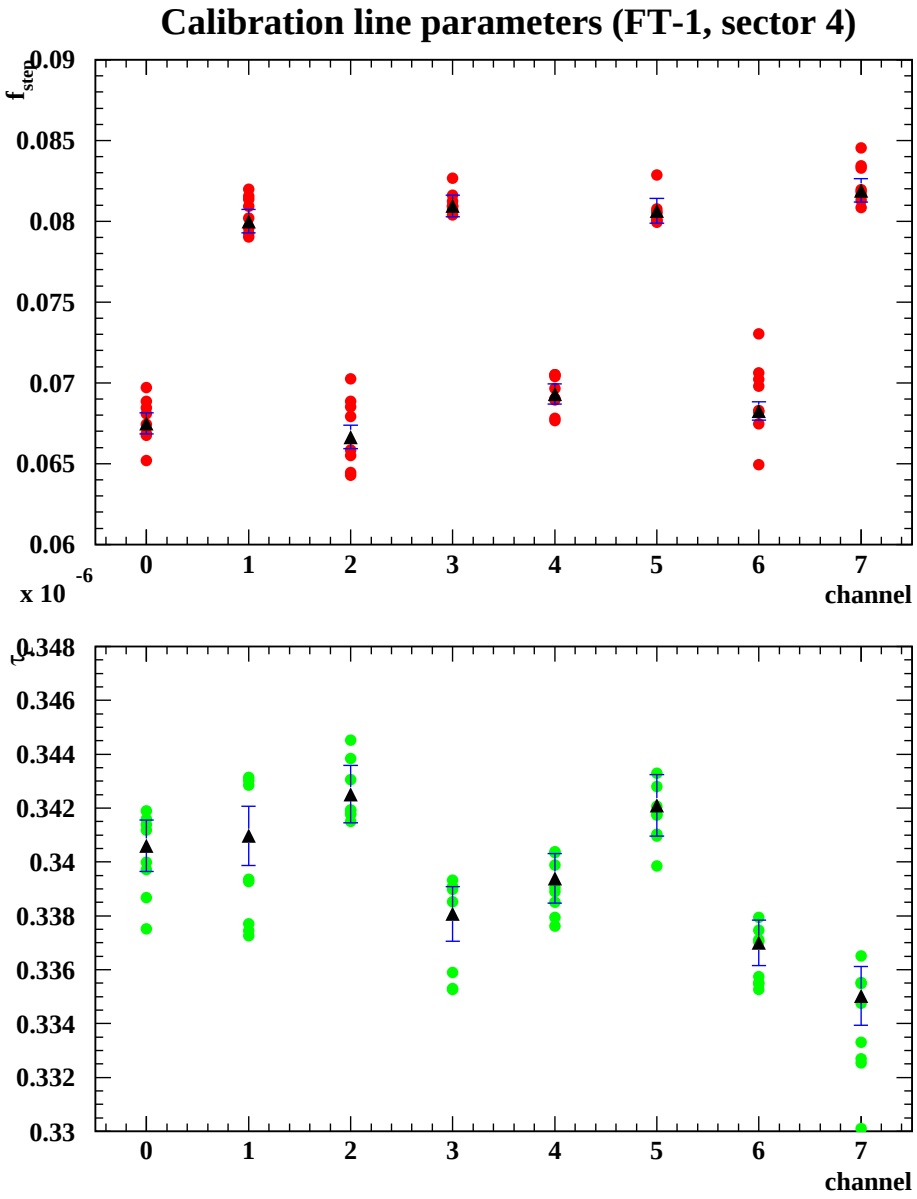

Figure 5.19: Calibration pulse characteristic parameters f_{step} (top) and τ_{cali} (bottom) as a function of the calibration board line number. The values refers to the Middle cells of Sector 4 of the EM barrel production module M10 ($24 \leq \eta_{\text{cell}} \leq 31$). The weighted means of each line groups of values are shown superimposed (black triangle) with the relative uncertainties.

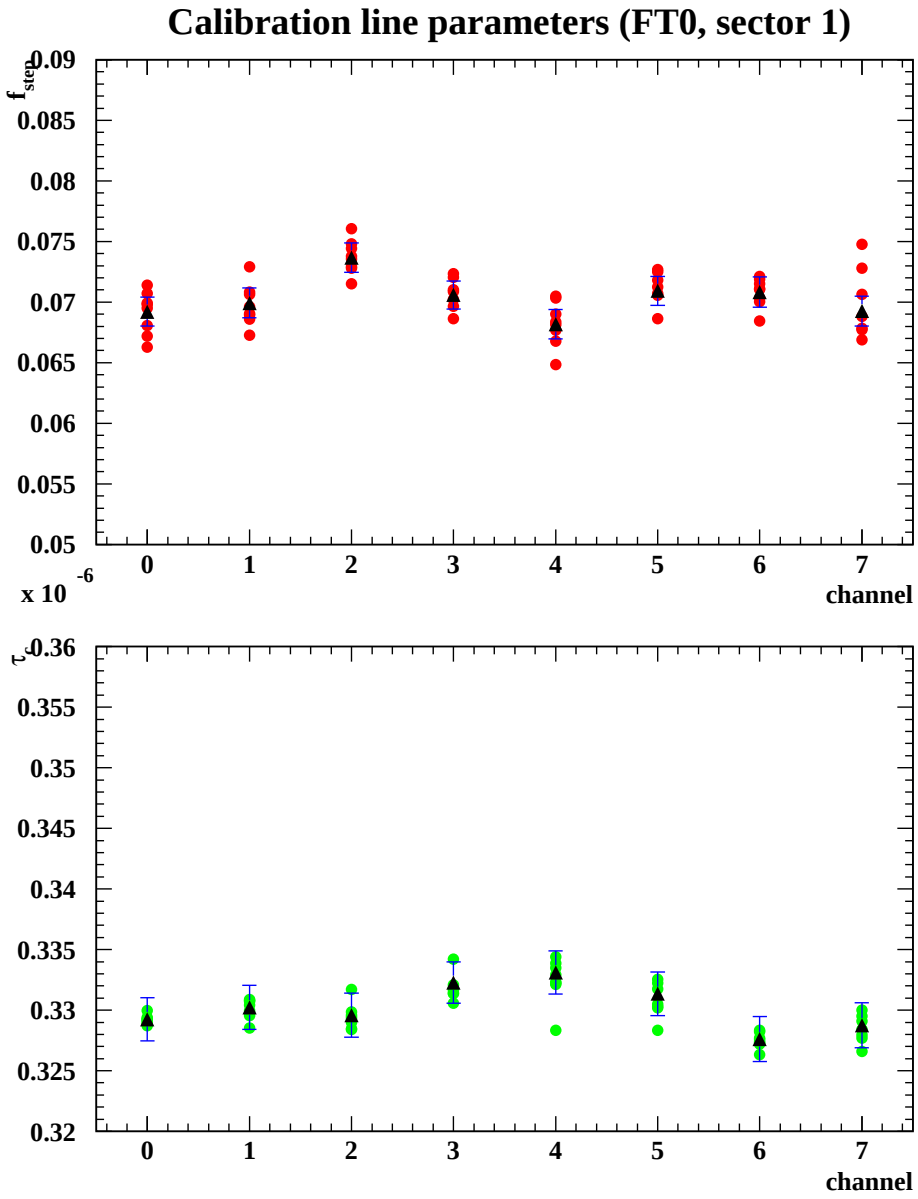

Figure 5.20: Calibration pulse characteristic parameters f_{step} (top) and τ_{cali} (bottom) as a function of the calibration board line number. The values refers to the Middle cells of Sector 1 of the EM barrel production module P15 ($0 \leq \eta_{\text{cell}} \leq 7$). The weighted means of each line groups of values are shown superimposed (black triangle) with the relative uncertainties.

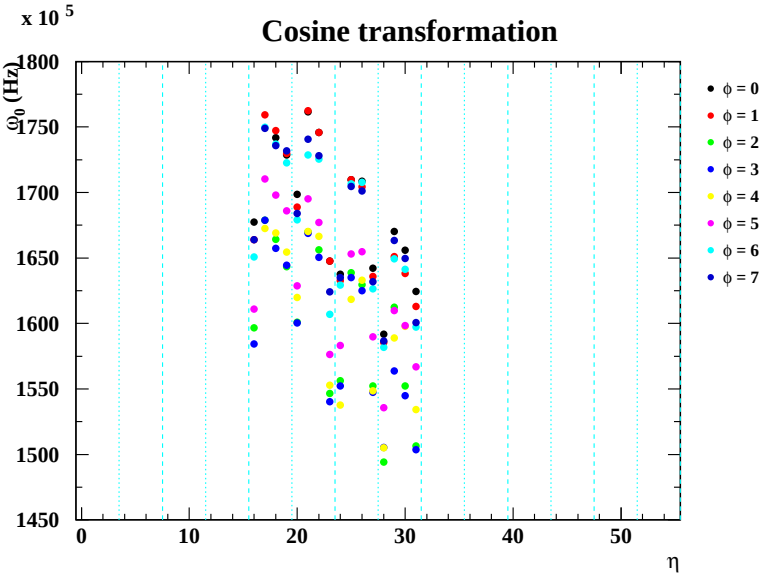

Figure 5.21: EM barrel production module M10 Middle cells characteristic frequencies $\omega_0 = \frac{1}{\sqrt{LC}}$ values, as a function of η_{cell} for the different ϕ_{cell} lines. The values have been extracted from the 32–samples MW with the cosine–response algorithm.

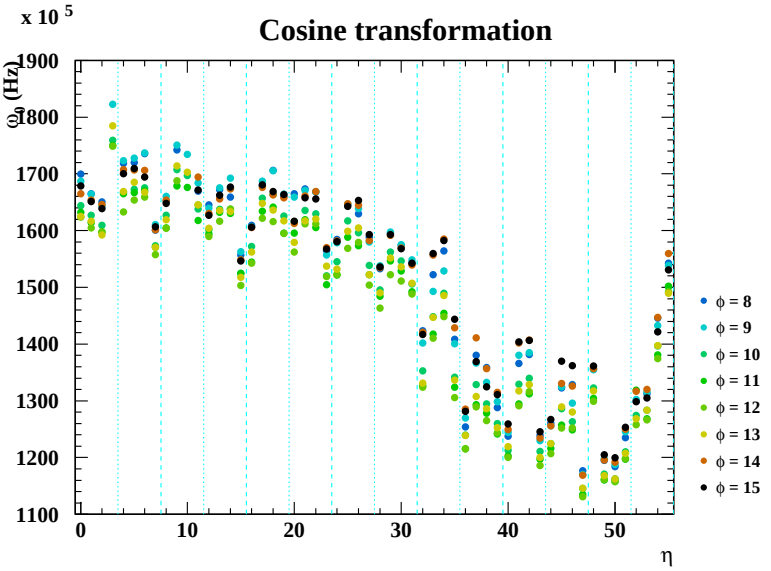

Figure 5.22: EM barrel production module P15 Middle cells characteristic frequencies $\omega_0 = \frac{1}{\sqrt{LC}}$ values, as a function of η_{cell} for the different ϕ_{cell} lines. The values have been extracted from the 32–samples MW with the cosine–response algorithm.

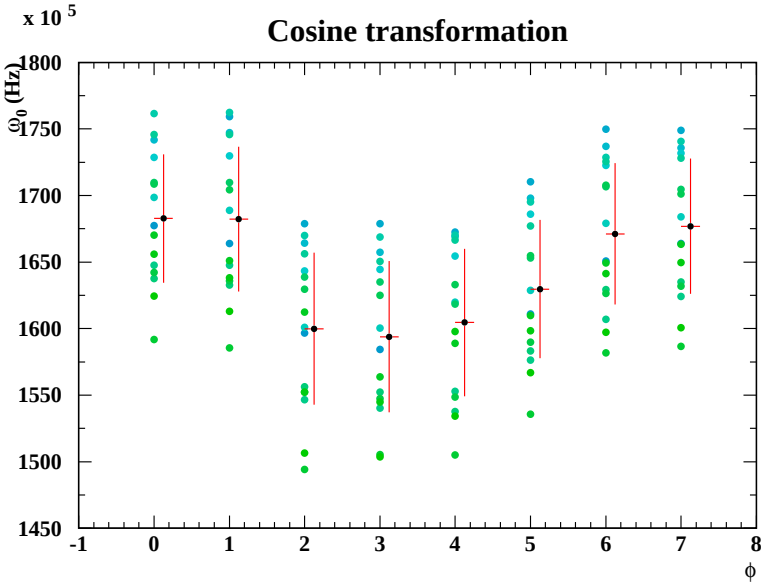

Figure 5.23: EM barrel production module M10 Middle cells characteristic frequencies $\omega_0 = \frac{1}{\sqrt{LC}}$ values, as a function of ϕ_{cell} for the different η_{cell} positions, and averaged along η. The values have been extracted from the 32–samples MW with the cosine–response algorithm.

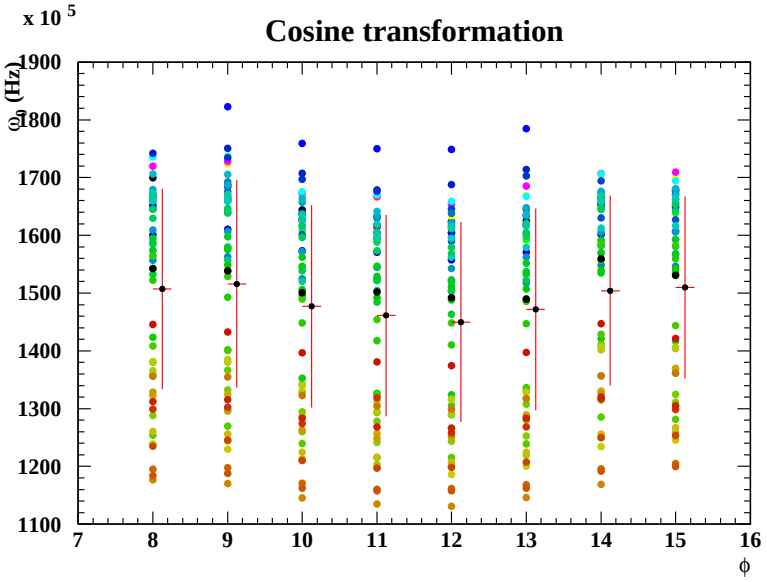

Figure 5.24: EM barrel production module P15 Middle cells characteristic frequencies $\omega_0 = \frac{1}{\sqrt{LC}}$ values, as a function of ϕ_{cell} for the different η_{cell} positions, and averaged along η. The values have been extracted from the 32–samples MW with the cosine–response algorithm.

P13 and P15) [39]. These measures are performed with a RCL–meter on all the Middle and Back cells at the SB level. The module is in air (i.e. not filled with LAr) at room temperature. For different ν frequency values the impedance Z and the relative phase are obtained. The $L_{\rm meas}(\nu)$ and $C_{\rm meas}(\nu)$ values are extracted with a fit procedure on ${\rm Im}(Z)$. According to [39], the $L_{\rm meas}(\nu)$ and $C_{\rm meas}(\nu)$ values are strongly correlated; their fit values depend on the used frequency range. The product $L_{\rm meas}(\nu)C_{\rm meas}(\nu)$ seems more stable (~ 0.5 %). Part of the modules (e.g. P15) are known to have bad measurements ore cells in which the ${\rm Im}(Z)$ fit fails.

In order to perform a comparison with the ω_0 parameters extracted with the cosine–response algorithm, a frequency–averaged value $\omega_{\rm meas} = \frac{1}{\sqrt{\langle L_{\rm meas} C_{\rm meas}\rangle_\nu}}$ is computed for the module P15 Middle cells. Because of the way the direct LC measurement are performed (SB connection, no MB and cables, air dielectric module at warm), only a qualitative comparisons is possible. A scaling of the $\omega_{\rm meas}$ to the LAr temperature could in principle be possible [39]:

$$\omega^{\rm cold}_{\rm meas} = \frac{1}{\sqrt{\langle L_{\rm meas} C^{\rm cold}_{\rm meas}\rangle_\nu}} \tag{5.43}$$

$$C^{\rm cold}_{\rm meas} = \epsilon_r^{\rm LAr}\left(C_{\rm meas} - C^{\rm eff}_{\rm SB}\right) + C^{\rm eff}_{\rm SB} \tag{5.44}$$

being $\epsilon_r^{\rm air} \simeq 1$ and $\epsilon_r^{\rm LAr} = 1.53$. $C^{\rm eff}_{\rm SB} \simeq 0.077$ nF represents the capacitive contribution of the SB to the cell measured capacitance [39]. The $\omega^{\rm cold}_{\rm meas}$ values could anyway not be suitable, since the single $\langle C_{\rm meas}\rangle_\nu$ value proved not to a stable and trustable measurements.

The ω_0 parameters should also be compared with the corresponding one obtained by the OF4 coefficients computation with a fit procedure involving the ionization pulse [40]. These $\omega_{\rm OF4} = \frac{1}{\sqrt{L_{\rm OF4} C_{\rm OF4}}}$ parameters are expected to represent the correct value to be used in the ionization waveform prediction, at least according in the (5.1) model, since they are computed fitting the mean ionization pulse obtained from the test–beam data [32] with a function of the $L_{\rm OF4}C_{\rm OF4}$ parameter.

The P15 ω parameters obtained through the 32–samples delay runs analysis, from the direct impedance measure scaled to LAr temperature, and through the OF4 computation procedure using the ionization pulses are compared in Figure 5.25. The values are shown as a function of $\eta_{\rm cell}$, for the 8 different ϕ lines from which the 32–sample delay runs has been acquired. The ω_0 values are systematically greater than the $\omega_{\rm OF4}$ ones, while the $\omega^{\rm cold}_{\rm meas}$ ones are systematically smaller; but there is anyway a significant qualitative agreement between the extracted, measured and fitted values, expecially in the local patternswhich are well reproduced in the three approaches.

The systematical differences between the ω values obtained with the different approches need indeed to be further studied. An indipendent study of the 32–sampled delay runs [41, 33], based on the FFT frequency analysis of the cell resonance, returns ω values compatible at the 0.5% level with the ones obtained with the cosine–response algorithm. On the other hand the $\omega_{\rm OF4}$ parameter, being obtained through a fit procedure on the ionization pulse extracted from the electrons test–beam data, could take into account both

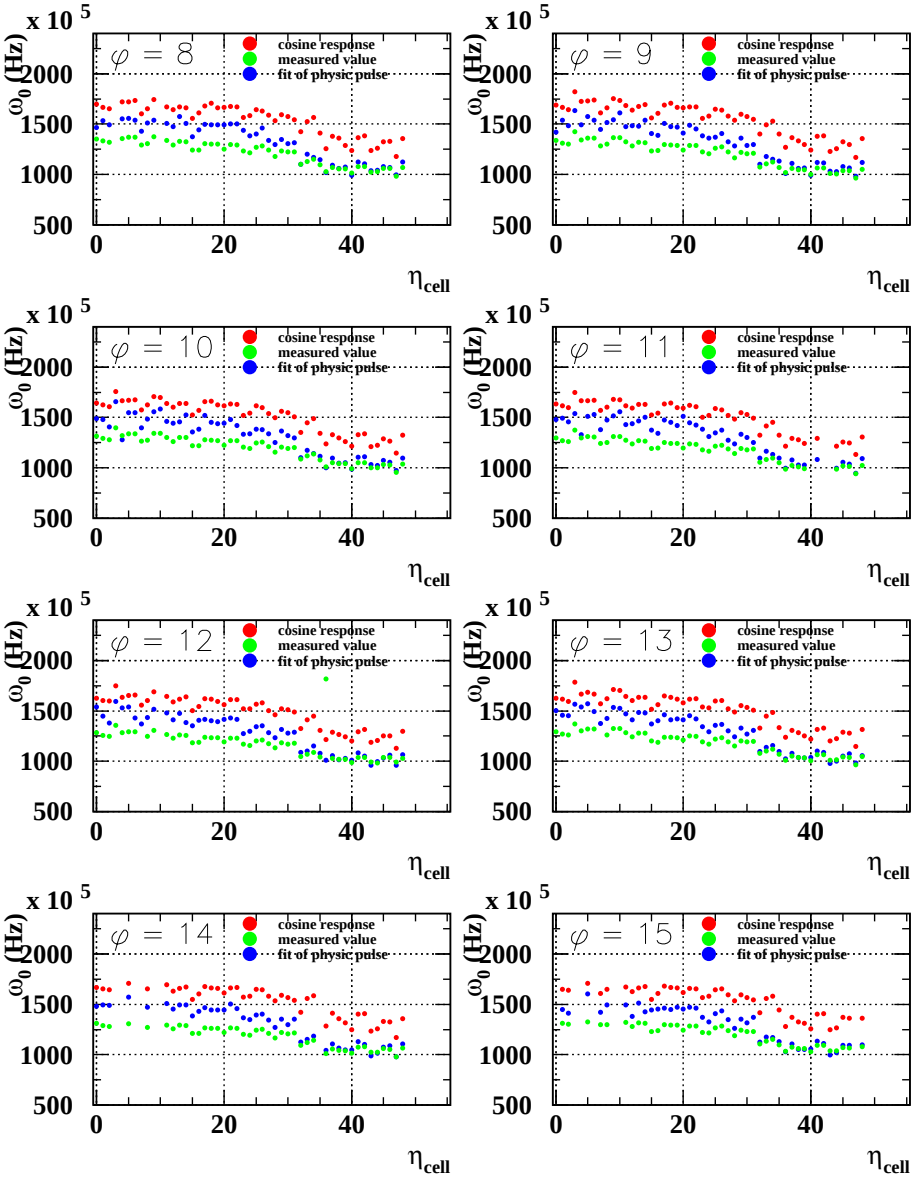

Figure 5.25: EM barrel production module P15 Middle cells characteristic frequencies, as a function of η_{cell} for 8 different ϕ lines. The cosine–response extracted ω_0 values are compared with the direct measure $\omega_{\text{meas}}^{\text{cold}}$ and with the ω_{OF4} values obtained through the OF4 fit procedure on the ionization pulses.

the injection point effect, related to the real LC values, and other smaller contributions that are not directly included in the model (5.1) (e.g. the τ_r parameter related to the contact resitance), assuming the role of a sort of effective parameter. We return on this point in the conclusive remarks summary at the end of this work.

In Figure 5.26 the ω values are compared as a function of ϕ_{cell} for 8 different η position. Similar results are obtained for all the other η positions. The ϕ behavior that was noticed on the extracted ω_0 parameters is reproduced by both the measured ω_{meas} values and the ω_{OF4} values obtained through the OF4 fit procedure on the ionization pulses. The Middle cells connected at the center of the SB show a lower characteristic frequency. It is behind the present aims of this work to investigate the origin of this effect; the fact that the cosine–response algorithm is able to recognize such a property is anyway a further prove of the accuracy of the method.

5.5.3 Ionization signal prediction and OF coefficients computation

Once the set of parameters $\{\tau_{\text{cali}}, f_{\text{step}}, \omega_0\}$ has been extracted from the 32–samples MW, the calibration waveform can be easily normalized to its peak values, and the corresponding "normalized" ionization pulse can be computed through the (5.3). An example of this procedure is shown in Figure 5.27.

As it has been mentioned before, the nominal T_d value is to be used; in the EM barrel, $T_d \simeq 450$ ns. This choice does not represent a real limitation to the precision of the procedure, since the ionization signal prediction is not really sensitive to the T_d value, at least in the region of the signal that is used for the OF coefficients computation. In Figure 5.28 the ionization signal prediction is computed using the $T_d = 450$ ns EMB nominal value, and the test values $T_d^1 = 430$ ns and $T_d^2 = 470$ ns. It is immediately noticed that the peak region of the ionization signal prediction it is not affected by such strong variations in the T_d value, while the biggest differences are registered in the tail of the signal.

Once the ionization pulse has been computed from the calibration MW on a time range of 800 ns, the positive lobe region is selected in a 125 ns interval, and the OF coefficients sets are computed for each of the 25 possible delay values according to the procedure exposed in Appendix B. An example of the OF coefficients obtained for the Medium gain region from the ionization waveform of Figure 5.27 is shown in Figure 5.29.

A naive test of these OF coefficients is proposed in Figure 5.30. The peak of the "normalized" ionization waveform that was used to compute the coefficients sets is reconstructed using the OF SR technique itself. For each possible delay value 5 samples are selected, one every 25 ns. Peak and arrival time of the signal are reconstructed using the first OF coefficient set available, the obtained time is used as a correction to choose the following set to be used. The iterative procedure is stopped when the computed time correction is smaller than 0.5 ns. In this case the OF coefficients set is the one to be used. The convergence is always reached after 3 iterations at maximum. The distribution of the reconstructed peak, each value being obtained for the different signal delays, is well centered around 1 with a 10^{-5} RMS. There is no evident correlation between the signal delay and the reconstructed peak value. Analogous considerations hold for the

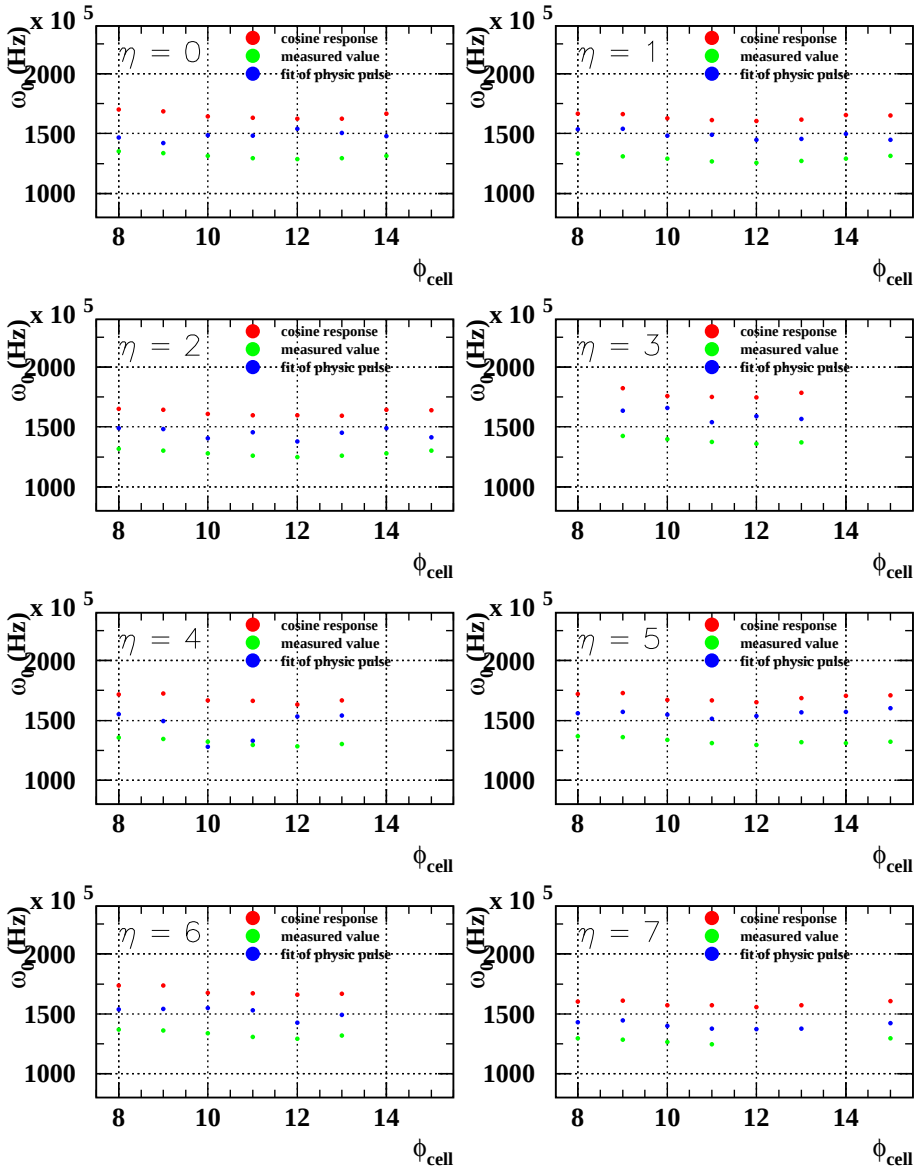

Figure 5.26: EM barrel production module P15 Middle cells characteristic frequencies, as a function of ϕ_{cell} for 8 different η lines. The cosine–response extracted ω_0 values are compared with the direct measure $\omega_{\text{meas}}^{\text{cold}}$ and with the ω_{OF4} values obtained through the OF4 fit procedure on the ionization pulses.

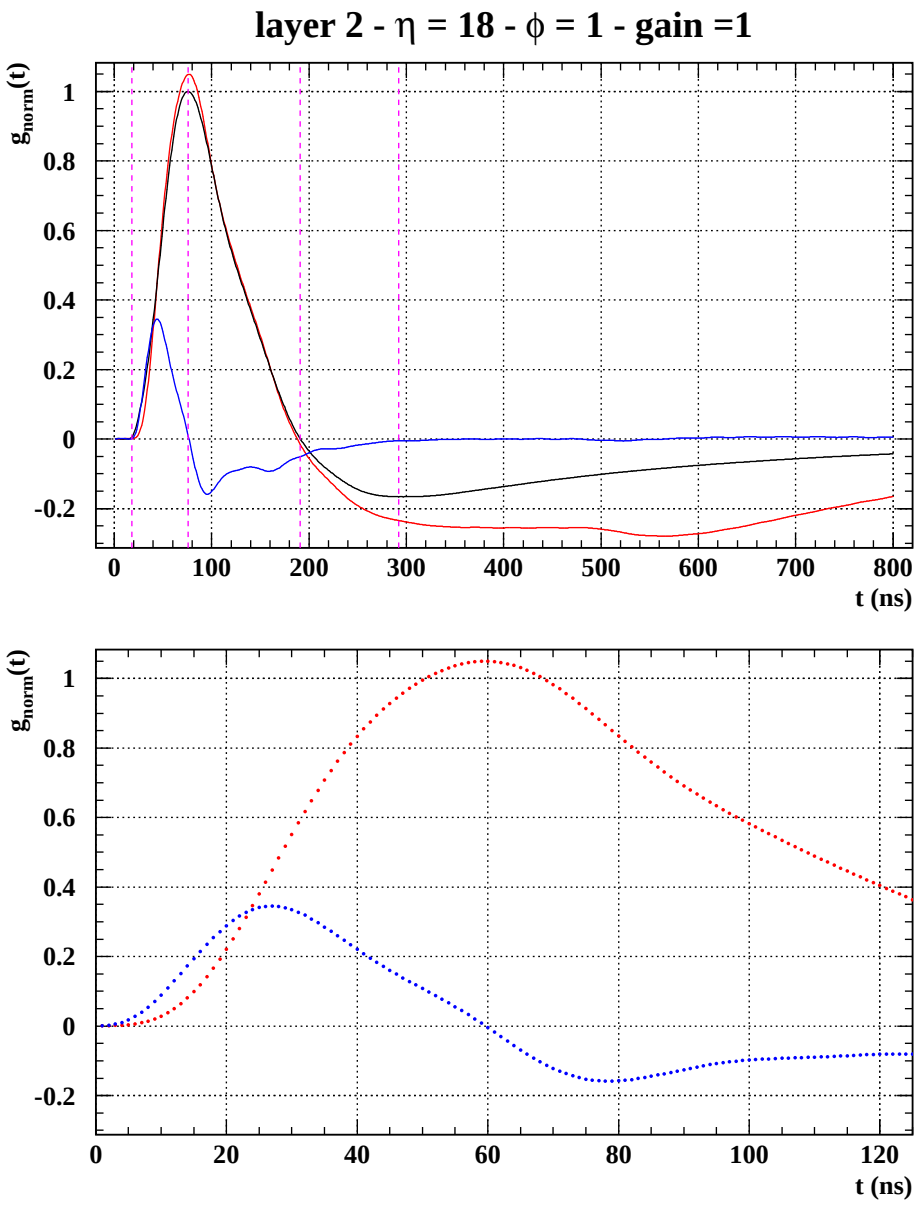

Figure 5.27: Ionization pulse prediction computed for the EMB module M10 Middle cell $\eta_{\text{cell}} = 18$, $\phi_{\text{cell}} = 1$, using the parameters $\{\tau_{\text{cali}}, f_{\text{step}}, \omega_0\}$ extracted from the 32–samples calibration MW, and the nominal value of the drift time $T_d = 450$ ns. The calibration MW (black), the ionization pulse prediction (red) and its derivative (blue) are shown on the full 800 ns interval (top), and in the restricted 125 ns zone of the positive lobe that is to be used for the OF coefficients computation (bottom).

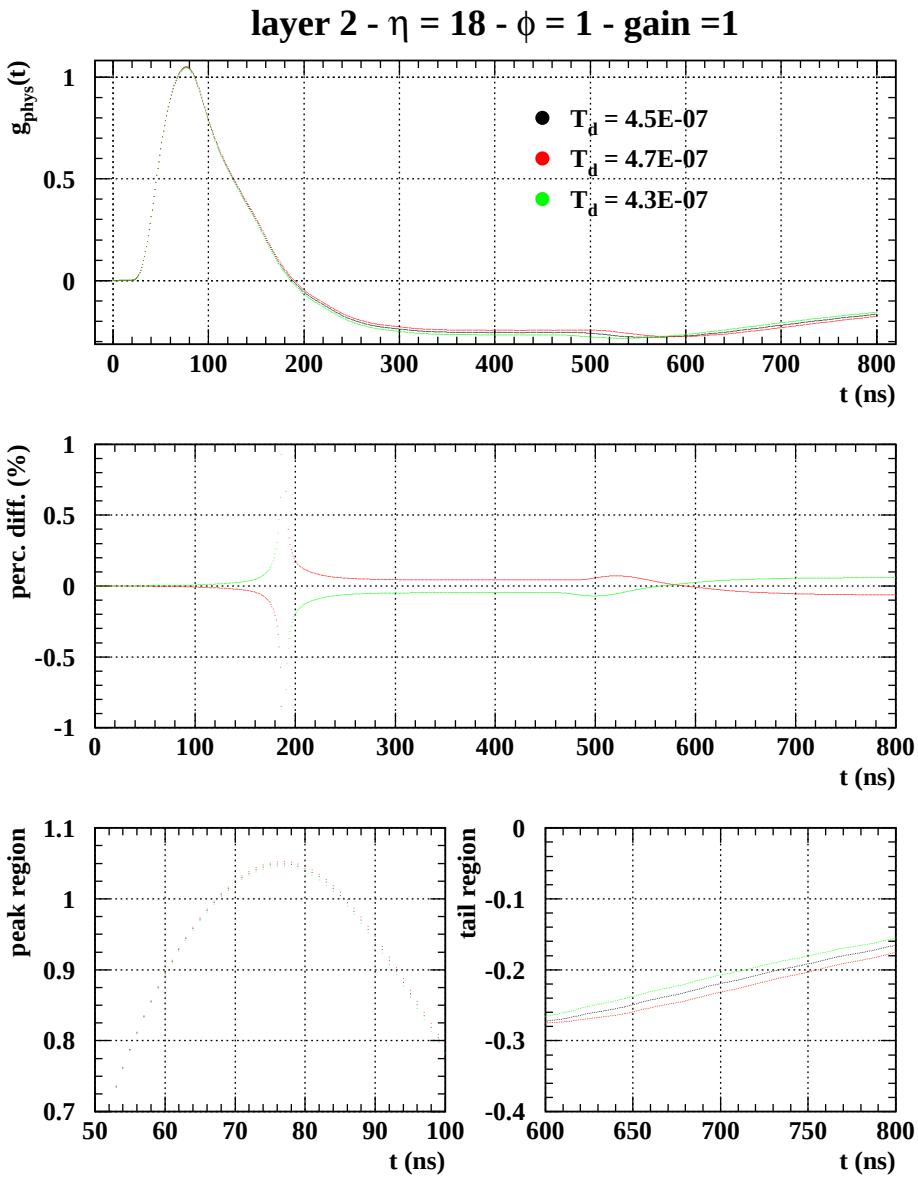

Figure 5.28: Ionization pulse predictions dependence on the T_d drift time value (top). The pulse are computed for the EMB module M10 Middle cell $\eta_{\text{cell}} = 18$, $\phi_{\text{cell}} = 1$, using the parameters $\{\tau_{\text{cali}}, f_{\text{step}}, \omega_0\}$ extracted from the 32–samples calibration MW, together with the nominal value of the drift time $T_d = 450$ ns (black), or the test values $T_d^1 = 430$ ns (green) and $T_d^2 = 470$ ns (red). The percentage differences between the "nominal" and the two test predicted signal (middle), the zone of the signals peaks (bottom left) and of the signals tails (bottom right) are shown.

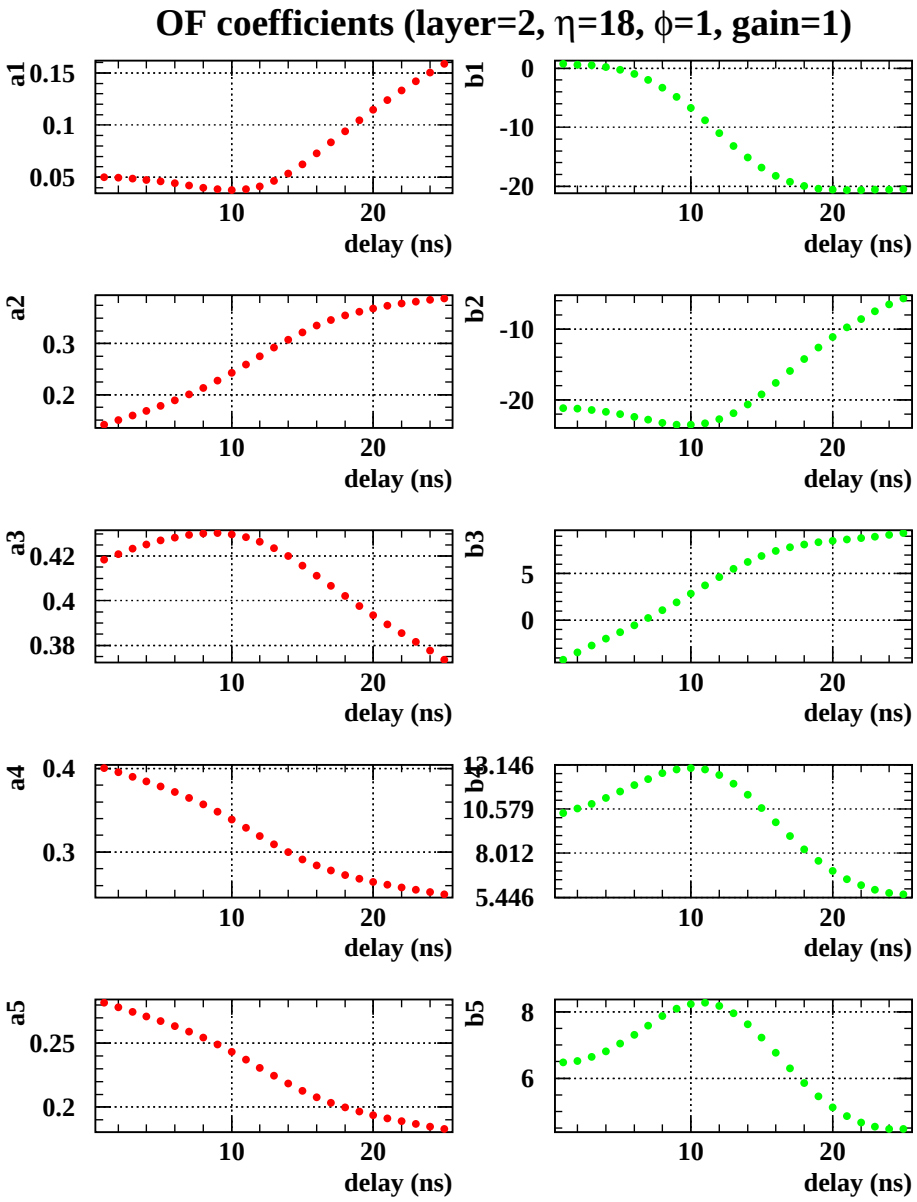

Figure 5.29: OF coefficients sets computed for the EMB module M10 Middle cell $\eta_{\text{cell}} = 18$, $\phi_{\text{cell}} = 1$ in the Medium gain region, using the ionization pulse prediction shown in Figure 5.27. The $\{a_i\}$ coefficients are shown in the left column of plots, as a function of the possible delay values. The $\{b_i\}$ coefficients are shown in the right column.

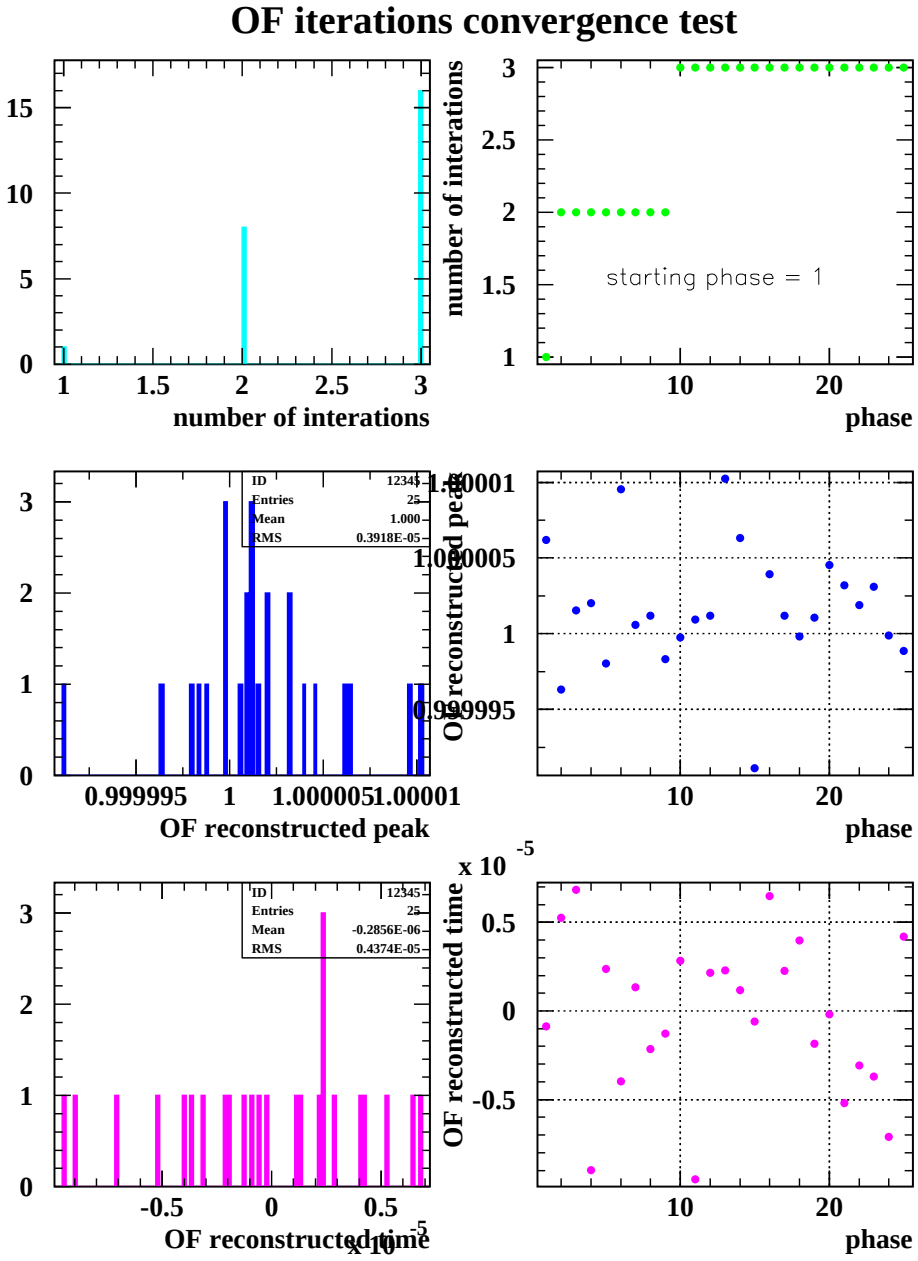

Figure 5.30: Test of the OF SR iterative procedure. The peak of the "normalized" ionization waveform used to compute the coefficients is reconstructed using the OF SR system itself: number of iteration distribution (top left); number of iterations as a function of the delay value (top right); reconstructed peak distribution (middle left); reconstructed peak as a function of the delay value (middle right); reconstructed time distribution (bottom left); reconstructed time as a function of the delay value (bottom right).

reconstructed time.

The OF coefficients obtained with the ionization waveform predicted using the *LC* values from the cosine–response algorithm are presently not to be considered as "production" values for the EMB modules test-beam data analysis, at least until the systematic differences from the OF4 values pointed out in Section 5.5.2 have been solved, or the physics pulse prediction model has been sufficiently refined (see the conclusive remarks summary for details).

5.5.4 A possible EMC calibration scenario at the LHC

In conclusion we try to imagine a possible EMC calibration scenario at the LHC. The actual gain of each readout channel is computed injecting and reconstruction calibration pulses of different normalization (ramp runs). The noise (electronics + pile–up) is measured during the pedestal runs. The full shape of the calibration signal is reconstructed through the analysis of several 32–samples delay curves, acquired for different injected current (DAC) values (at least 3); a MW is obtained for each cell. The step–response transformation and the cosine–response transformation are computed from the MW, the parameters set $\{\tau_{\rm cali}, f_{\rm step}, \omega_0\}$ is extracted[2]. The MW is normalized to its peak value, and the "normalized" ionization waveform is computed (e.g. using the nominal drift time T_d value). Using this ionization pulse prediction and the noise autocorrelation information

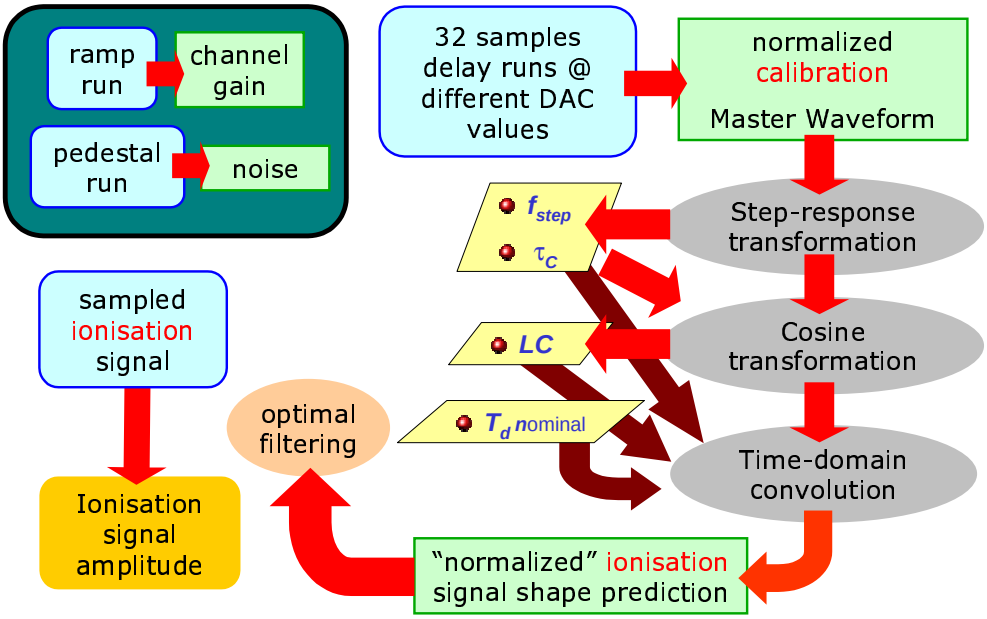

Figure 5.31: Pictorial flowchart of a possible EMC calibration scenario at the LHC.

[2] Any other parameter needed to complete the ionization pulse prediction (e.g. τ_r) is to be extracted from the MW at this point of the procedure, or inferred from nominal value or first–principles computation.

A pictorial summary of the procedure is proposed in Figure 5.31. The evident advantage of this algorithm is to be fast and completely stand–alone. The calibration steps can be performed once in a while, the final OF coefficients sets would be (nearly) immediately available at the end of the computation procedure.

5.6 Open questions

5.6.1 Ionization signal prediction

It has been shown in this chapter that the EMC ionization signal prediction, needed to complete the OF coefficients computation and therefore the EMC energy reconstruction, can in principle be performed using only the calibration waveform. Most of the needed information, represented by the parameters used in the ionization pulse prediction from the calibration waveform, can be retrieved directly from the calibration waveform itself. There are anyway some open problems which are not directly faced in this thesis, but that need to be solved if the advertised calibration accuracy is to be achieved.

We already mentioned the systematic difference between the OF4 LC values obtained through a direct fit procedure on the ionization mean pulse [32], and the ones we obtain from the MW's cosine–response analysis. This systematic difference might be related to some intrinsic property of the cosine algorithm; it is anyway reasonable to believe that the ω_{OF4} value could take into account both the injection point effect related to the real LC value, and other effect contributions that are not directly included in the cell model described by equation (5.1).

Some of the open questions that need to be solved and included in the stand–alone ionization waveform prediction are:

- **The problem of the resistive term in the electrode.** The EMC cell model proposed Figure 3.2 does not take into account the unavoidable presence of at least a contact resistance between the readout electrodes and the SB. The model in Figure 5.1 should instead be used. The relative importance of the $\tau_r = rC$ parameter in the detector transfer function can be estimated using typical values of the circuit model components of a Middle cell. If $r = 1\ \Omega$, $L = 25$ nH and $C = 2$ nF one obtains:

$$\begin{cases} \tau_r = 2 \text{ ns} \\ \tau_0 \simeq 7 \text{ ns} \end{cases} \quad \Rightarrow \quad \frac{\tau_r}{\tau_0} \simeq 28\%$$

  Indeed the resistive term cannot be ignored while performing the ionization signal prediction. Since the algorithm based on the output transformation proposed in Section 5.3.4 is not able to converge to reasonable results, a different approach must be tempted. A possible strategy could be the frequency analysis of the resonance width around the cell characteristic frequency [33, 41].

- **The change in rise time of the calibration pulse due to the skin effect.** The calibration pulses must travel over a cable of about 4 m in length that connects the

CB to the MB. This path induces a distortion on the signal, that therefore should be corrected before being analysed and transformed. This distortion is mainly due to the cable skin effect [34], that in the frequency domain produces an attenuation proportional to $e^{-\sqrt{st_{\rm se}}}$ on the calibration signal, $t_{\rm se}$ being a characteristic parameter related to the calibration cable length and properties. The main effect of this distortion is to slow the rise time of the calibration pulse, that in all the analysis in this work is always considered to be null.

- **The determination of the drift time.** The T_d value is shown to weakly contribute to the precision of the ionization physics waveform (Section 5.5.3), for this reason we suggest that the nominal value can be used in the ionization waveform prediction. Nevertheless, it could be useful to investigate more deeply this point, especially if the algorithm is to be applied to the EMC end–caps data, where the non–uniformity of the LAr gap thickness give rise to different drift time along the detector [3].

- **The cross-talk contribution to the ionization signal.** As we show in Chapter 3, the neighboring EMC cells are electrically coupled in different way (capacitively, inductively and resistively). These couplings produce a "cross–talk" effect that in principle distorts the ionization signals. Some attempt are presently being done to understand if the "cross–talk" effects can be corrected in the framework of the OF signal reconstruction [42].

5.6.2 Signals normalization and readout gain

It is worth to add here a short remark about the way the signal normalization is carried out. In this work we followed the EMC test–beam data reconstruction framework approach: since the actual gain of each readout channel is computed using the ramp runs [52] and applied by default, the peak of the calibration MW, from which the ionization waveform is predicted, must be normalized to 1. Nevertheless, if the linearity assumption that is made in the calibration MW computation is valid, it should be possible from the MW data alone (i.e. not normalized) to derive OF coefficients in units of DAC/ADC (corresponding to μA/ADC), which would directly give the reconstructed ionization signal in current units (DAC). The channel gain information is in fact fully contained in the MW itself. The only additional constant that would have to be applied would be the sensitivity (DAC/GeV or μA/GeV), which should be a constant for each type of LAr calorimeter in ATLAS.

Chapter 6

Energy calibration using a layer–weighting technique

The shower energy response of a calorimeter with a longitudinal multi–layer segmentation, evaluated as a simple sum of the energies recorded by all layers, is affected by several effects which deteriorate the total energy resolution and bias the measured value of the total energy. Some of these effects can be recovered by reconstructing the total energy $E_{\rm tot}$ as a *weighted* sum of the energy measurements in all the longitudinal layers:

$$E_{\rm tot} = \sum_{i}^{n} w_i E_i \tag{6.1}$$

n being the numbers of sampling layers. The problem can be studied on the ATLAS EMC, which has three longitudinal layers (Strips, Middle, Back) and is complemented in the region $0< \eta <1.8$ by a thin Presampler layer put in front [3]. Referring to this setup:

- The energy loss due to the amount of material in front of the EMB can be recovered by weighting the energy deposited in the Presampler (and potentially even in the Strips).
- A small fraction of the shower energy is deposited in the material between the Presampler and the Strips. It can be potentially recovered by weighting the energy deposited in the Strips.
- For showers of hundred GeV or more, the energy resolution loss due to a longitudinal leakage can be recovered by weighting the energy deposited in the Back compartment.

Since the loss of energy in non–active zones of the calorimeter worses the detector measurement accuracy, one of the possible approach is to choose the weights w_i's in order to *minimize the relative energy resolution* $\sigma[E_{\rm tot}]/\langle E_{\rm tot}\rangle$.

A preliminary study of the energy losses is conducted using a "toy" MonteCarlo (MC) simulation of electromagnetic shower development and energy deposit in a EM barrel

(EMB) module (Section 6.1). An analytic solution for the optimal weights is proposed in Section 6.2, together with a numerical method to estimate their statistics fluctuations (Section 6.3). Furthermore, this technique is applied to the electrons test–beam data from an EMB production module exposed to electrons of $E_0 = 245$ GeV. The optimal weights are studied as functions of the η, ϕ coordinates, and the improvements on the energy scale, resolution and uniformity are presented (Section 6.4).

6.1 Energy losses estimate using a "toy" MC

The EMB modules setup is described in detail in a simulator program [56] based on GEANT [57], both for the ATLAS and for the test–beam framework. Using this simulation code [54, 55], the mean amount of material in the calorimeter for the EMB test–beam setup has been computed, in term of radiation lengths X_0 as a function of η. In Figure 6.1 the X_0 longitudinal boundaries of the detector samplings are shown. Apart from the active zones (Presampler, Strips, Middle and Back samplings), the shower energy can be deposited (and lost) in three non–active ("dead") regions: in the material in front of the Presampler (E_{cryostat}), in the material between the Presampler and the Strips (E_{front}), and behind the Back sampling (E_{leakage}).

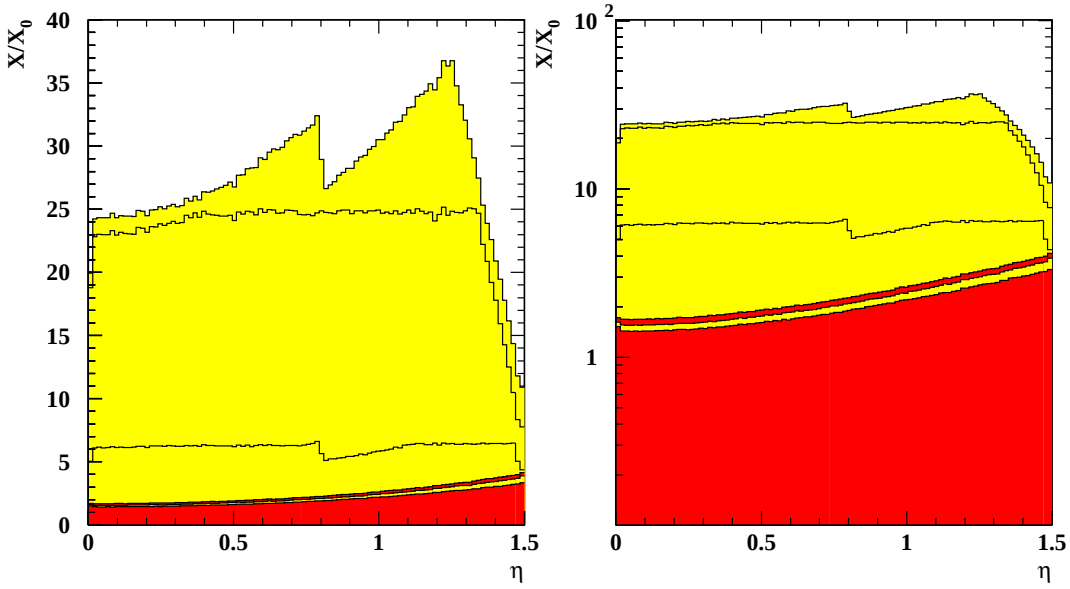

Figure 6.1: Amount of material in term of radiation lengths X_0 (linear scale, left, and logarithmic scale, right) in the EMB calorimeter in the test-beam setup, as a function of η. The boundaries of the different samplings are shown. The active samplings (from bottom, Presampler, Strips, Middle and Back) are drawn in yellow, the non–active ("dead") regions (before the Presampler and between the Presampler and the Strips) are drawn in red.

The mean longitudinal profile of the energy deposition in an electron–induced

electromagnetic shower is reasonably described by the function [58, 59]:

$$\frac{dE}{dt} = E_0 \frac{b^{(a+1)} t^a e^{-bt}}{\Gamma(a+1)} \tag{6.2}$$

where E_0 is the incoming electron energy, and:

$$\begin{cases} t &= \frac{X}{X_0} & \text{material depth} \\ t_{\max} &= \ln \frac{E_0}{E_c} - 1 & \text{peak of the shower} \\ b &\simeq 0.5 & \text{(for very different kind of material)} \\ a &= b t_{\max} & \\ E_c &\simeq \frac{560 \text{ MeV}}{Z} & \text{critical energy of the crossed material} \end{cases} \tag{6.3}$$

In the ATLAS EMC case a reasonable approximation is $E_c \simeq E_c^{\text{Pb}} \simeq 6.8$ MeV. An example of the curve (6.2) for an electron of $E_0 = 245$ GeV is shown in Figure 6.2.

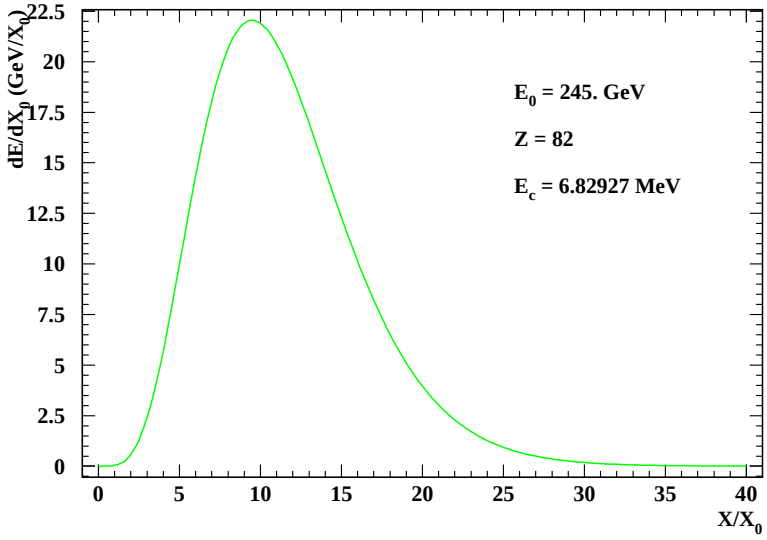

Figure 6.2: Mean longitudinal profile of the energy deposition in an electromagnetic shower generated by a $E_0 = 245$ GeV electron in lead ($Z_{\text{Pb}} = 82$, $E_c^{\text{Pb}} \simeq 6.8$ MeV).

A mean estimate of energy deposited in each of the active samplings and in the "dead" regions can be computed as a function of η, integrating[1] the function (6.2) between the proper X_0 boundaries shown in Figure 6.1. The results for an electron of $E_0 = 245$ GeV are shown in Figure 6.3 (active samplings) and Figure 6.4 ("dead" regions).

The energy losses can in principle be recovered by weighting the proper sampling measurements. The energy lost in front of the module is recover by weighting the Presampler measure, the energy lost between the Presampler and the Strips by weighting the Strips measure, the longitudinal energy leakage by weighting the Back measure. The

[1] The Gauss-Legendre numerical integration formula [63] is used.

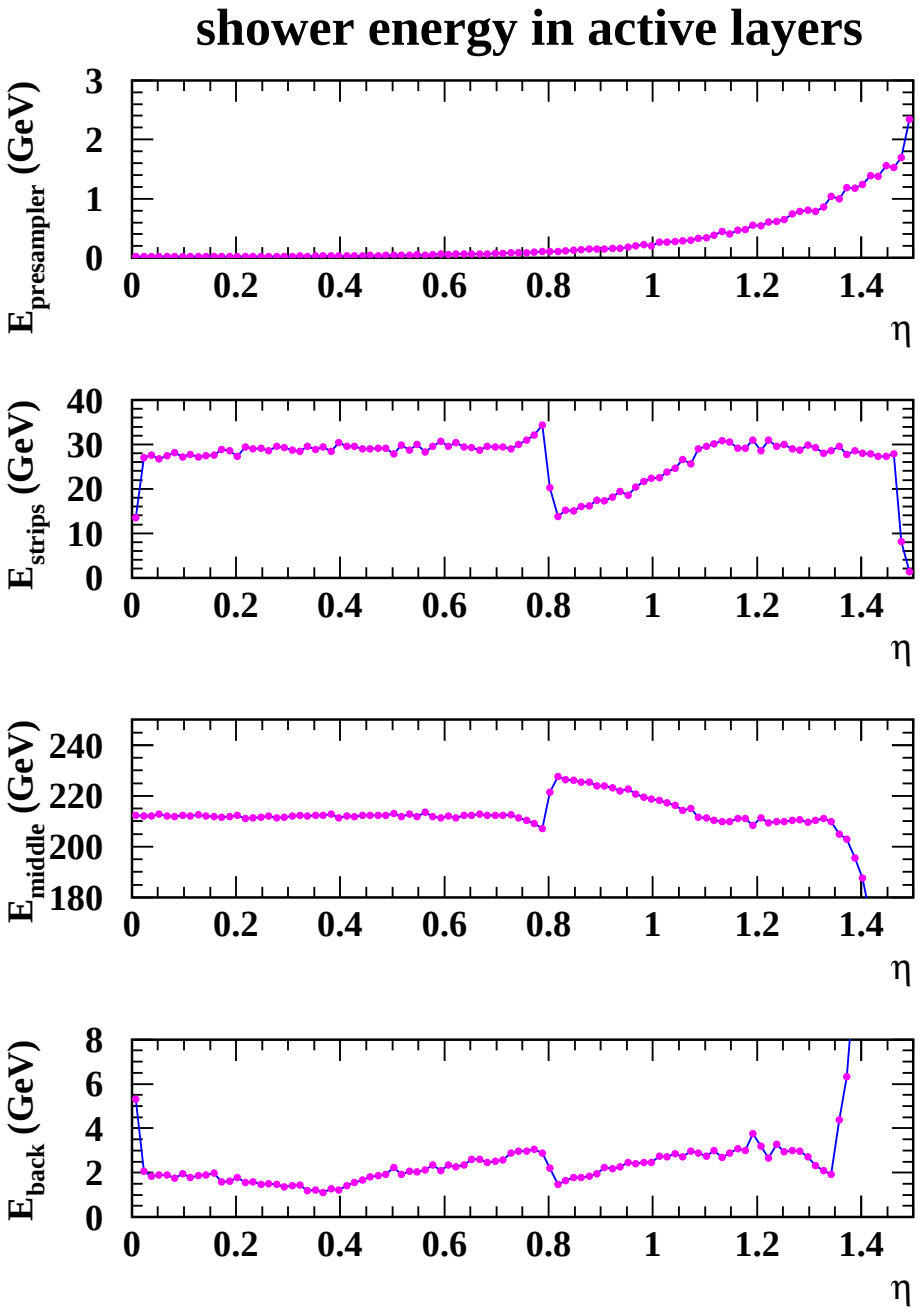

Figure 6.3: Mean energy loss in the EMB active samplings as a function of η, for an e.m. shower induced by a 245 GeV electron. From top to bottom, Presampler, Strips, Middle and Back.

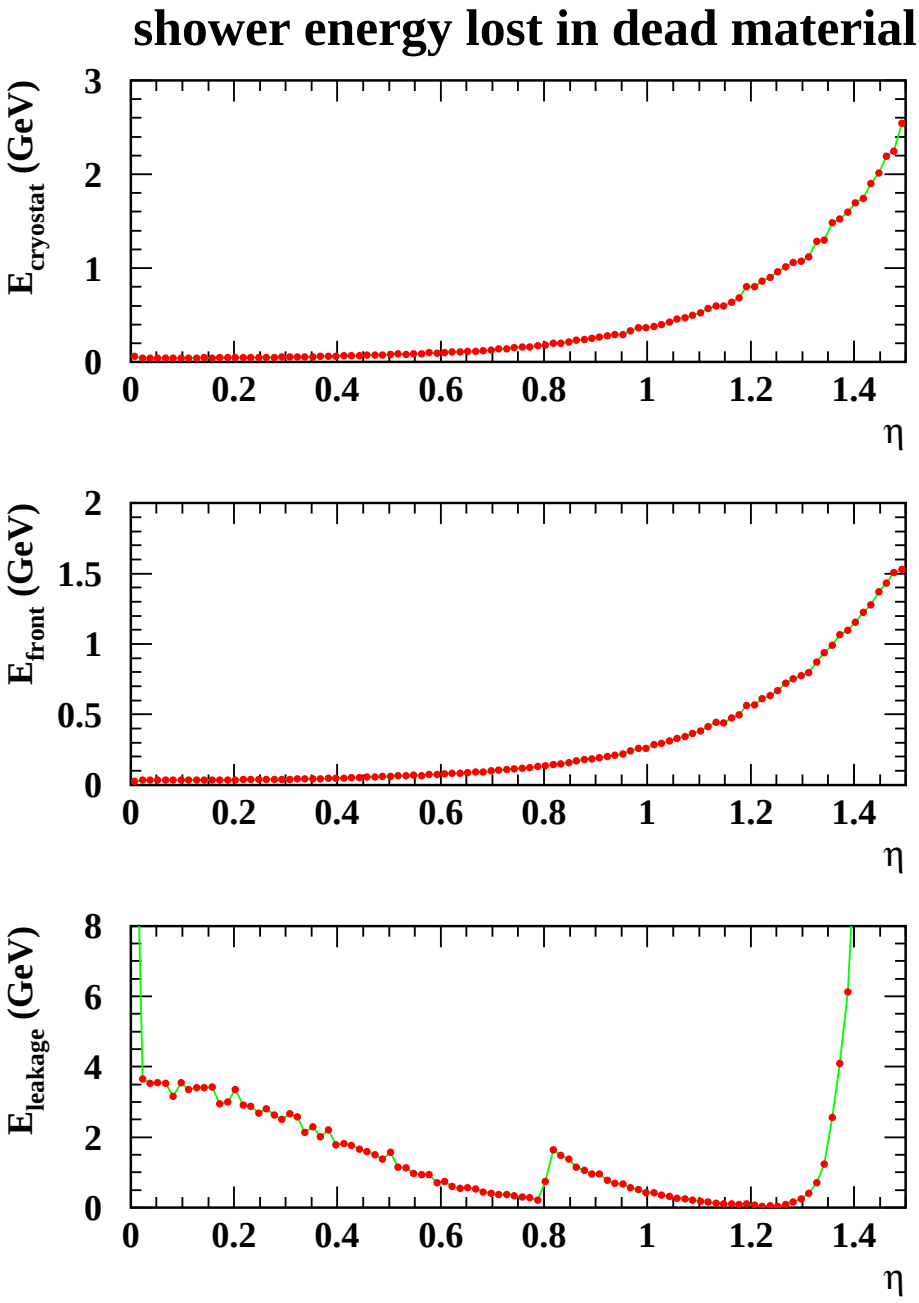

Figure 6.4: Mean energy loss in the EMB "dead" regions as a function of η, for an e.m. shower induced by a 245 GeV electron. Form top to bottom, mean energy deposited in the material in front of the Presampler, in the material between the Presampler and the Strips, and behind the Back.

weights are defined as:

$$\begin{cases} w_0 = 1 + \frac{E_{\text{cryostat}}}{E_{\text{Presampler}}} \\ w_2 = 1 + \frac{E_{\text{front}}}{E_{\text{Strips}}} \\ w_3 = 1 + \frac{E_{\text{leakage}}}{E_{\text{Back}}} \end{cases} \tag{6.4}$$

The weights values obtained from the "toy" MC computation for a shower induced by a 245 GeV electron are shown in Figure 6.6.

A real shower is known to increases more rapidly than the (6.2) parametrization, being the Γ distribution very flat near the origin: equation (6.2) fails badly for about the first two radiation lengths [59]. For this reasons the weights values obtained from this "toys" MC analysis can only give a qualitative information about what the optimal weights should be. Some considerations are anyway possible:

- The Presampler weight can be reasonably expected to be greater than 1. The energy lost in front of the EMC is well correlated with the one measured in Presampler (Figure 6.5). The Presampler weight can be also expected to be slightly varying as a function of η.

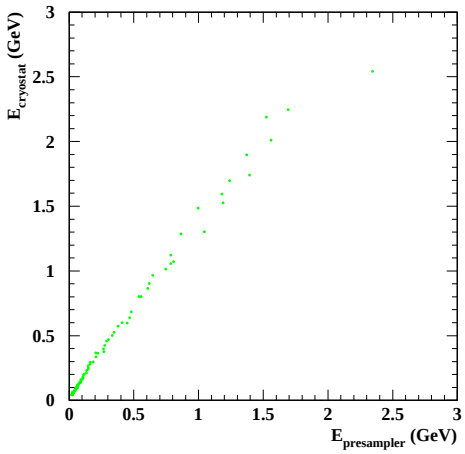

Figure 6.5: Correlation between the energy lost in material in front of the EMB and the energy deposited in the Presampler, for an e.m. shower induced by a 245 GeV electron, according to the "toy" MC analysis.

- The Strips weight is to be expected to be slightly greater than 1 at high η only, where the amount of "dead" material between the Presampler and the Strips crossed by the incoming particles increases because of a geometric effect. The fraction of energy to be recovered is in fact small compared to the amount measured in the Strips themselves.

  Furthermore, in the real experimental framework, the Strips energy measurement would have a finite resolution. This resolution can be expected to be comparable with the amount of energy to be recovered weighting the Strips measurement itself,

at least for high energy showers. According to the "toy MC" in fact, the energy lost between the Presampler and the Strips by a shower of $E_0 = 245$ GeV is <4% of the Strips mean measurement. It is therefore to be verified if a Strips weight can really improve the accuracy of a high energy shower measure.

- The Back weight should show a structure that respects the detector total X_0 depth as a function of η.

6.2 Energy resolution minimization

The *total optimized energy* defined in expression (6.1) is a function of the stochastic variables E_i's, whose averages are $\langle E_i \rangle = \mu_i$. Their RMS's and correlations are described by the covariance matrix $\mathrm{Cov}[E_i, E_j] = C_{ij}$. These parameters can be derived from the data set with the usual formulæ:

$$\mu_i = \frac{\sum_{k=1}^{N} E_i^{(k)}}{N} \tag{6.5}$$

$$C_{ij} = \frac{\sum_{k=1}^{N} (E_i^{(k)} - \mu_i)(E_j^{(k)} - \mu_j)}{N-1} \tag{6.6}$$

where N is the number of events collected, and the superscript $^{(k)}$ flags the event number. The average and variance of E_{tot} are:

$$\langle E_{\mathrm{tot}} \rangle = \sum_{i=1}^{n} w_i \mu_i \tag{6.7}$$

$$\mathrm{Var}[E_{\mathrm{tot}}] = \sum_{i,j} w_i w_j C_{ij} \tag{6.8}$$

A possible approach to estimate the optimal weights w_i consists in minimize the quantity $\sigma[E_{\mathrm{tot}}]/\langle E_{\mathrm{tot}} \rangle$, where $\sigma[E_{\mathrm{tot}}] = \sqrt{\mathrm{Var}[E_{\mathrm{tot}}]}$. The energy losses in the material in front of the EMC and the shower longitudinal leakage contribute in fact to deteriorate the total energy resolution of the detector. The energy resolution minimization problem can be analytically solved in different ways; an elegant solution is found using a matricial approach. The following notation is used:

- C = covariance matrix $C_{ij} = \mathrm{Cov}[E_i, E_j]$
- $\vec{\mu}$ = mean energies μ_i vector
- $\vec{w}$ = weights w_i vector
- $\vec{w}^T$ = transpose of the $\vec{w}$ vector

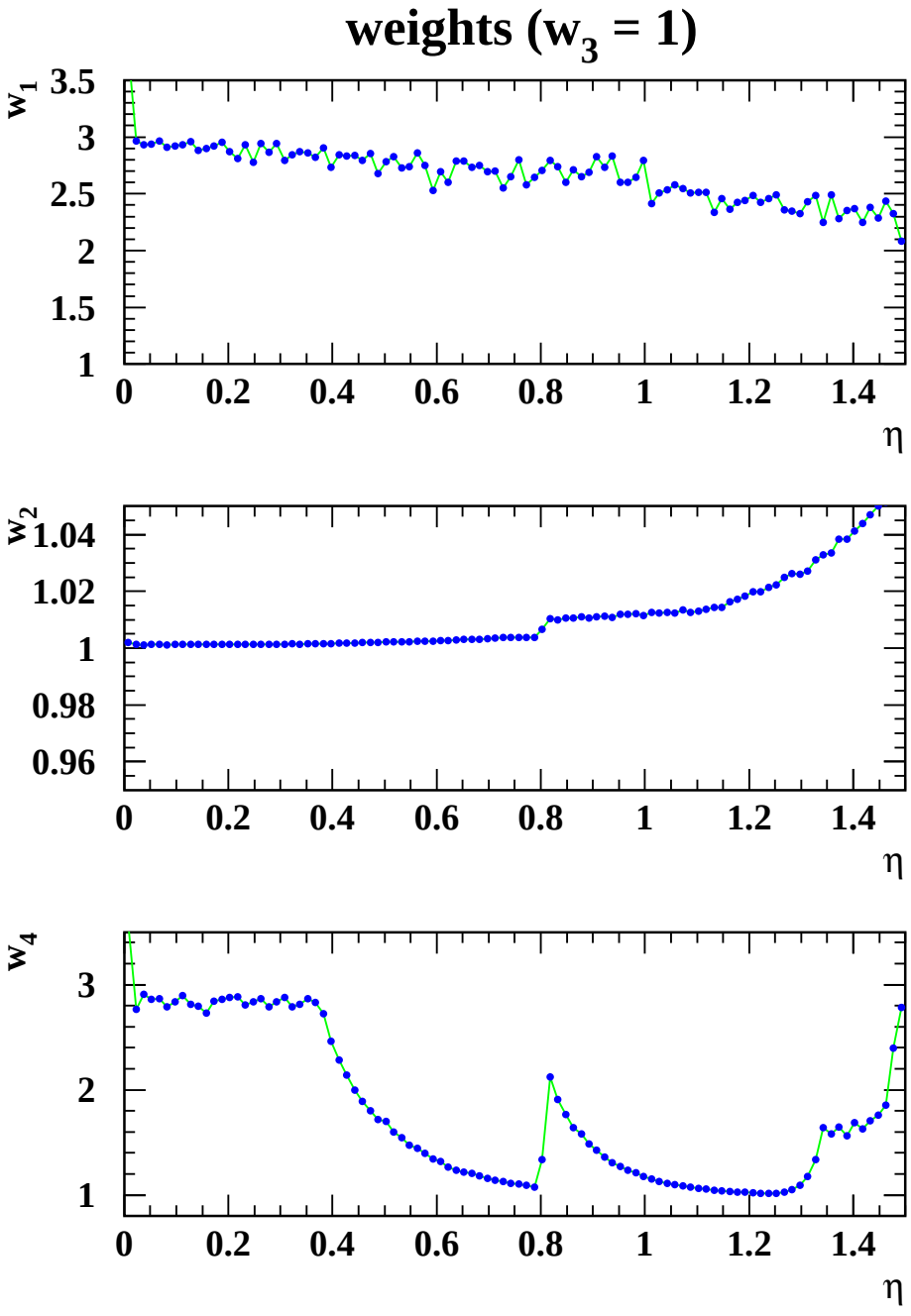

Figure 6.6: EMB Energy recovering weights for an e.m. cascade induced by a 245 GeV electron, as a function function of η. The weights are computed with "toy" MonteCarlo (see text for details). Presampler weight (top); Strips weight (middle); Back weight (bottom).

The total energy resolution $\sigma[E_{\rm tot}]/\langle E_{\rm tot}\rangle$ is therefore:

$$\frac{\sigma[E_{\rm tot}]}{\langle E_{\rm tot}\rangle} = \frac{\sqrt{\vec{w}^T C \vec{w}}}{\vec{w}^T \vec{\mu}} \tag{6.9}$$

The minimization is directly performed with respect to the $\vec{w}$ vector. The extremals of (6.9) are vectors $\vec{w}$ that satisfy:

$$0 = \frac{\partial}{\partial \vec{w}} \left(\frac{\sqrt{\vec{w}^T C \vec{w}}}{\vec{w}^T \vec{\mu}} \right) = \frac{1}{(\vec{w}^T \vec{\mu})^2} \left[\frac{(C\vec{w})(\vec{w}^T \vec{\mu})}{\sqrt{\vec{w}^T C \vec{w}}} - \vec{\mu}\sqrt{\vec{w}^T C \vec{w}} \right] \tag{6.10}$$

$$= \frac{\left[C\vec{w}\vec{w}^T\vec{\mu} - \vec{\mu}\vec{w}^T C\vec{w} \right]}{(\vec{w}^T \vec{\mu})^2 \sqrt{\vec{w}^T C \vec{w}}} \tag{6.11}$$

which is equivalent to:

$$\left(\vec{w}^T \vec{\mu}\right) \vec{w} = \left(\vec{w}^T C \vec{w}\right) C^{-1} \vec{\mu} \tag{6.12}$$

provided that the covariance matrix C is invertible[2] If $\vec{w}$ is a solution, then it must have the same direction as $C^{-1}\vec{\mu}$. Conversely, any vector $\vec{w} \propto C^{-1}\vec{\mu}$ is a solution of (6.12), as can be easily verified by substitution. Therefore, the (1-dimensional vector space of) extremals $\vec{w}$ have the form:

$$\vec{w} = \lambda (C^{-1}\vec{\mu}) \quad \lambda \in \mathbb{R} \tag{6.13}$$

that is easily reduced to the standard notation:

$$w_i = \lambda \sum_k C^{-1}_{ik} \mu_k \tag{6.14}$$

Some considerations are needed:

- All the weights are defined up to an overall multiplicative constant λ, that affects the total energy scale. This result should not be surprising, since the starting

[2] A generic $n \times n$ covariance matrix C is by definition symmetric and semi–defined positive. It can always be written as

$$C = \begin{pmatrix} C_{11} & \rho_{12}\sqrt{C_{11}C_{22}} & \cdots & \rho_{1m}\sqrt{C_{11}C_{nn}} \\ \rho_{21}\sqrt{C_{11}C_{22}} & C_{22} & \cdots & \rho_{2m}\sqrt{C_{22}C_{nn}} \\ \vdots & \vdots & \ddots & \vdots \\ \rho_{n1}\sqrt{C_{11}C_{nn}} & \cdots & \rho_{(n-1)n}\sqrt{C_{(n-1)(n-1)}C_{nn}} & C_{nn} \end{pmatrix}$$

where ρ_{ij} is the correlation coefficient

$$\rho_{ij} = \frac{C_{ij}}{\sqrt{C_{ii}C_{jj}}}$$

It can be shown [66] that C is defined positive (and therefore invertible) if there is no perfect linear correlation between any two of the n variables, namely if $\rho_{ij} \neq \pm 1$. This is always the case for the energy measurements in different calorimeter compartments, due to the stochastic mechanism of shower development. In case $\rho_{ij} = \pm 1$, C is singular.

point was the optimization of the *relative* energy spread $\sigma[E_{\rm tot}]/\langle E_{\rm tot}\rangle$. The way to set an absolute scale for the weights, and therefore the energy, must come from further considerations. The choice adopted here is to assume that the sampling layer recording the largest energy release (call it the M-th layer) does not need any correction, i.e. $w_M = 1$, and the remaining weights are scaled accordingly. This fixes λ, and the weights so normalized are:

$$\tilde{w}_i = \frac{\sum_k C^{-1}_{ik}\mu_k}{\sum_k C^{-1}_{Mk}\mu_k} \tag{6.15}$$

- The minimization of $\sigma[E_{\rm tot}]/\langle E_{\rm tot}\rangle$ must be carried out *simultaneously* as a function of *all* the weights. Figure 6.7 shows the dependence of the relative energy resolution on the Presampler and Back weights, for the EMB (Strips and Middle weights are set to 1, see Section 6.4 for explanation). Clearly, the effects of the two weights are not separable.

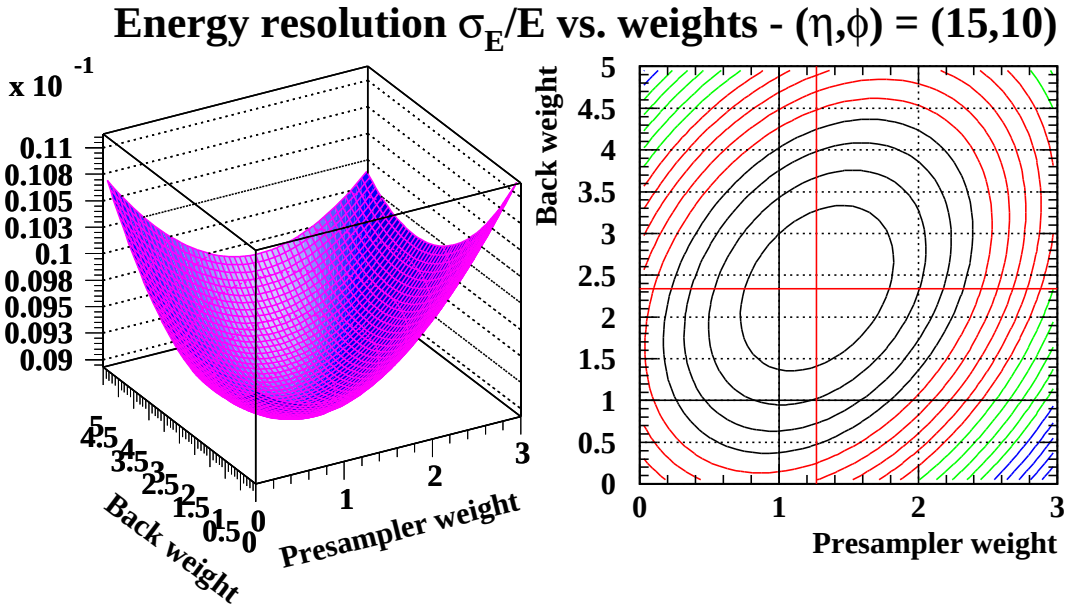

Figure 6.7: Relative energy resolution $\sigma[E_{\rm tot}]/\langle E_{\rm tot}\rangle$ as a function of the Presampler and Back weights (3-D plot and level curves). The weights for Strips and Middle layer are constrained to 1.

- The minimization algorithm is exact, therefore it does not introduce any systematic error to the w_i's. However, the variables μ_i's and C_{ij}'s, as extracted according to equations (6.5),(6.6) from the finite data sample under exam, are affected by statistical fluctuations, that propagate into the evaluation of the weights[3]. An estimate of their effect is described in Section 6.3.

[3]Notice that these fluctuations are completely unrelated to the "errors" that could be obtained from an iterative minimization algorithm (e.g. MINUIT), which are due to the way the algorithm handles the function to minimize. In the case under exam, the minimum is known analytically with absolute precision,

6.3 Statistical fluctuations on the weights

The uncertainties on the quantities μ_i's and C_{ij}'s are in general correlated. An analytical error propagation on formula (6.14) or (6.15) is not suitable, therefore a numerical MC approach can be followed. The steps are the following:

- Find a linear transform of the variables E_i's:
$$\hat{E}_r = \sum_i U_{ri} E_i$$
such that the covariance matrix
$$\hat{C}_{rs} = \mathrm{Cov}[\hat{E}_r; \hat{E}_s]$$
is diagonal. This is always possible since the matrix C is symmetric; the transform matrix U is therefore orthogonal ($U^{-1} = U^T$), and
$$\hat{C}_{rs} = \sum_{ij} U_{ri} U_{sj} C_{ij}$$

- The variables $\hat{E}_r$'s are now uncorrelated. Their average values are:
$$\langle \hat{E}_r \rangle = \hat{\mu}_r = \sum_i U_{ri} \mu_i$$
and their spreads are:
$$\hat{\sigma}_r = \sqrt{\hat{C}_{rr}}$$
For a sample of N events, the statistical uncertainty on $\hat{\mu}_r$ is:
$$\mathrm{RMS}[\hat{\mu}_r] = \frac{\hat{\sigma}_r}{\sqrt{N}}$$
Under the hypothesis of large N and gaussian distribution, the uncertainty on $\hat{\sigma}_r$ is uncorrelated with that on $\hat{\mu}_r$, and amounts to:
$$\mathrm{RMS}[\hat{\sigma}_r] = \frac{\hat{\sigma}_r}{\sqrt{2N}}$$

- For each of the $\hat{\mu}_r$'s and $\hat{\sigma}_r$'s one can generate the corresponding smeared quantity $\hat{\mu}_r^*$ (randomly sampled from a gaussian distribution centered in $\hat{\mu}_r$, with standard deviation equal to $\hat{\sigma}_r/\sqrt{N}$) and $\hat{\sigma}_r^*$ (randomly sampling the quantity $(\hat{\sigma}_r^*/\hat{\sigma}_r)^2$ from a χ^2 distribution with $(N-1)$ degrees of freedom). Applying the inverse transform U^T one obtains $\mu_i^* = \sum_r U_{ri} \hat{\mu}_r^*$ and $C_{ij}^* = \sum_r U_{ri} U_{rj} (\hat{\sigma}_r^*)^2$, from which a new set of weights w_i^*'s can be evaluated.

- The previous procedure is to be repeated several times[4], in order to get a histogram for each w_i^* (see Figure 6.8). The RMS spread of each histogram is then used as an estimate of the statistical uncertainty on w_i.

once the function is given. However, the function itself is affected by uncertainties of statistical origin (through the quantities C_{ij}'s and μ_i's), and their effect must be studied.

[4] $N_{\mathrm{MC}} = 10000$ would provide at least 1%precision on the central values of the weights distributions.

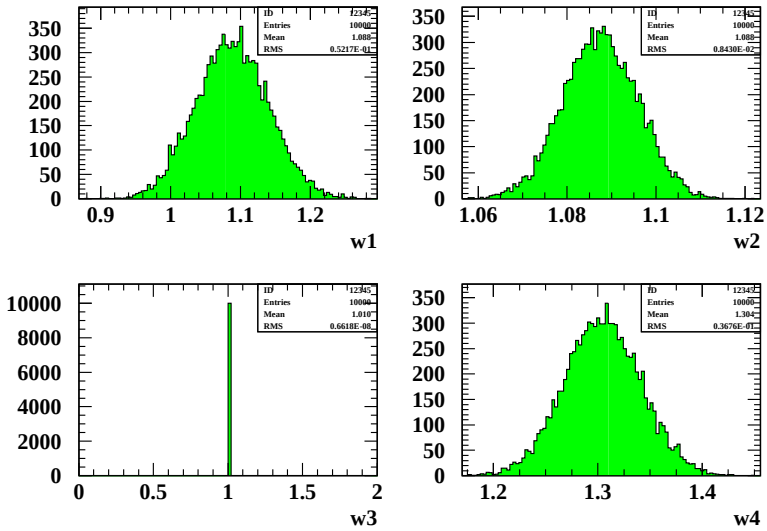

Figure 6.8: Example of typical distributions for the weights w_i^*, as obtained from the MC errors propagation. The values of μ_i's and C_{ij}'s are from an EMB test beam run, and the weights normalization is $w_3 = 1$.

6.4 Application to the EMB test-beam data samples

The optimal weights are computed using equation (6.15) from the data samples collected from the EMB production modules test-beam sessions (in this chapter, the module P15 data are used[5]), and then applied to the same measurements. For each selected cell, only "electron" events are used to evaluate the covariance matrix C_{ij} and the average energies μ_i. The data selection used to evaluate the weights values are extensively described in Section 7.3.

6.4.1 Normalization strategies

As it is discussed in Section 6.2, the energy measure of a M-th layer has to be chosen to define an overall normalization constant for the weights set. The most natural choice here would be the Middle layer (i.e. the sampling that collects the largest energy signal), therefore $\tilde{w}_3 = 1$. On the other hand, the "toy" MC study (Section 6.1) suggests that a Strips weight may not help in improving the total energy measurement accuracy. A variation of the first normalization approach consists then in considering the Strips and Middle samplings as one single layer with weight $\tilde{w}_{2+3} = 1$. Strips and Middle are contiguous and homogeneous in terms of constituent materials, and should not suffer of longitudinal containment effects. Since the energies $E^{\rm cluster}_{\rm Strips}$ and $E^{\rm cluster}_{\rm Middle}$ recorded in Strips and Middle are strongly anti-correlated ($\rho_{23} \sim -0.97$), the spread of $E^{\rm cluster}_{\rm Strips} + E^{\rm cluster}_{\rm Middle}$ is much narrower than that of $E^{\rm cluster}_{\rm Middle}$ alone. For test–beam electrons of $E_0 = 245$ GeV

[5] An analogous procedure has been applied to the other EMB modules test–beam data analysed in Chapter 7

it is found $\sigma_{E^{\text{cluster}}_{\text{Strips}}+E^{\text{cluster}}_{\text{Middle}}} \sim 4$ GeV, instead of $\sigma_{E^{\text{cluster}}_{\text{Middle}}} \sim 11$ GeV. Since the choice of the weights scale λ in equation (6.14) always involves some arbitrariness, we believe the sum of Strips and Middle measurements to be the most reasonable energy reference. On the other hand this normalization does not correct for the possibility that some shower develops in the material between the Presampler and the Strips.

6.4.2 Weights patterns and symmetries

The resulting weights from the EMB production module P15 are shown in Figure 6.9 and Figure 6.10, for normalizations $\tilde{w}_3 = 1$ and $\tilde{w}_{2+3} = 1$ respectively. Qualitatively, the trends obtained in the two cases are similar. For all layers, the weights are clustered around "main distributions", with some exceptions of points scattered away, that however are affected by large statistical errors. The Presampler weight is slightly geater than 1 ($\sim 1 \div 1.3$), and weakly increases with η, while that of the Strips, for the normalization $\tilde{w}_3 = 1$, regularly rises with η_{cell}, from 0.96 to 1.03, indicating that the material between Presampler and Strips also increases, as it is intuitive from projectivity considerations.

The weight of the Back has a more complicate structure, that can be understood in terms of the depth of the sampling layers (Section 6.1). For $\eta_{\text{cell}} \geq 16$ the depth of Strips+Middle is constant, while that of the Back increases with η_{cell} in the two ranges $16 \leq \eta_{\text{cell}} \leq 31$ and $32 \leq \eta_{\text{cell}} \leq 47$; the trend of the Back weight tends to compensate the resulting variation of containment. For $\eta_{\text{cell}} \leq 15$ the depth of the Middle decreases for decreasing η_{cell}, while that of the Back is constant, therefore the longitudinal leakage is even larger, but more energy flows through the Back; as a result, the Back weight does not need to increase further as $\eta_{\text{cell}} \to 0$.

The dependence of the weights on ϕ_{cell} does not exhibit any evident trend. For this reason, their values at each η_{cell} can be averaged over all the ϕ_{cell}'s (see Figures 6.11 and 6.12 for the choices $\tilde{w}_3 = 1$ and $\tilde{w}_{2+3} = 1$). To reduce the local fluctuations, the profiles as a function of η_{cell} have been fit with a combination of exponential functions in the three mentioned η ranges.

6.4.3 Resolution improvements and measurement accuracy

The total energy released in the EMB (sum of the cluster energies of all the layers) can be plot as a function of the hit cell position $\eta^{\text{hit}}_{\text{cell}}, \phi^{\text{hit}}_{\text{cell}}$. The bare sum of cluster energies (i.e. without applying weights) from the P15 module test-beam data is displayed in Figure 6.13. The trend of the total energy as a function of $\eta^{\text{hit}}_{\text{cell}}$ shows a slight slope for the region $\eta^{\text{hit}}_{\text{cell}} < 31$ (electrode A); a similar effect is observed at the beginning for the electrode B region ($32 < \eta^{\text{hit}}_{\text{cell}} < 35$). These two effects can be attributed to the longitudinal leakage of the shower. The drop of few GeV at $\eta^{\text{hit}}_{\text{cell}} = 31, 32$ is instead due to energy loss in the small gap between electrodes A and B.

Applying the fit weights displayed in Figure 6.12, with the normalization $\tilde{w}_{2+3} = 1$, the total energy profile as a function of $\eta^{\text{hit}}_{\text{cell}}$ changes slightly, as in Figure 6.14. There is a small but visible improvement in the profile in the electrode A region, that is now flatter; the profile at the beginning of the electrodes B region is also improved. As expected, the

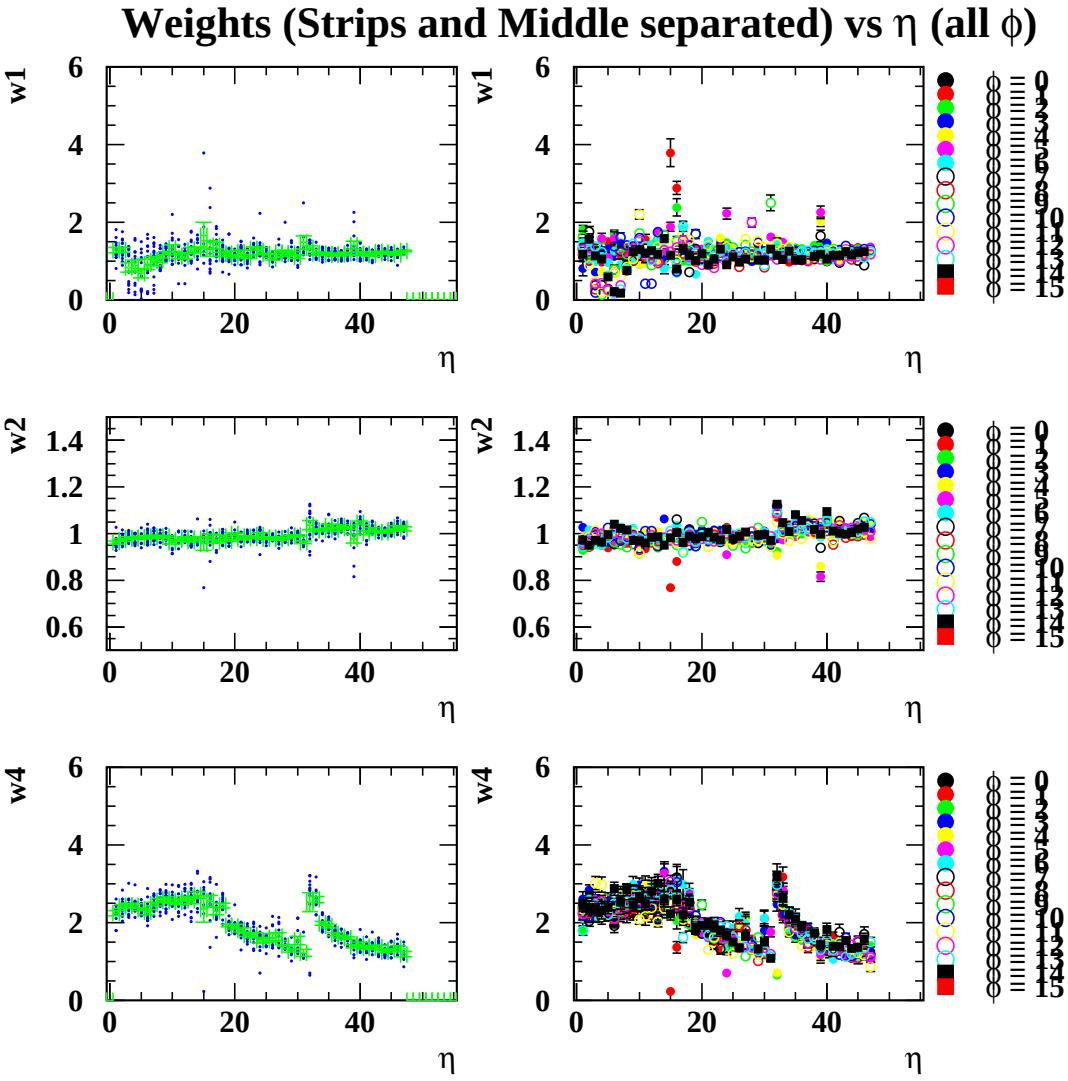

Figure 6.9: Weights evaluated for Presampler, Strips and Back (w1, w2, w4), as a function of $\eta_{\mathrm{cell}}^{\mathrm{hit}}$, with Middle weight set to 1. In the left column all weights at several $\phi_{\mathrm{cell}}^{\mathrm{hit}}$ are displayed together with their profile histogram. In the right column, different symbols and gray levels refer to different $\phi_{\mathrm{cell}}^{\mathrm{hit}}$.

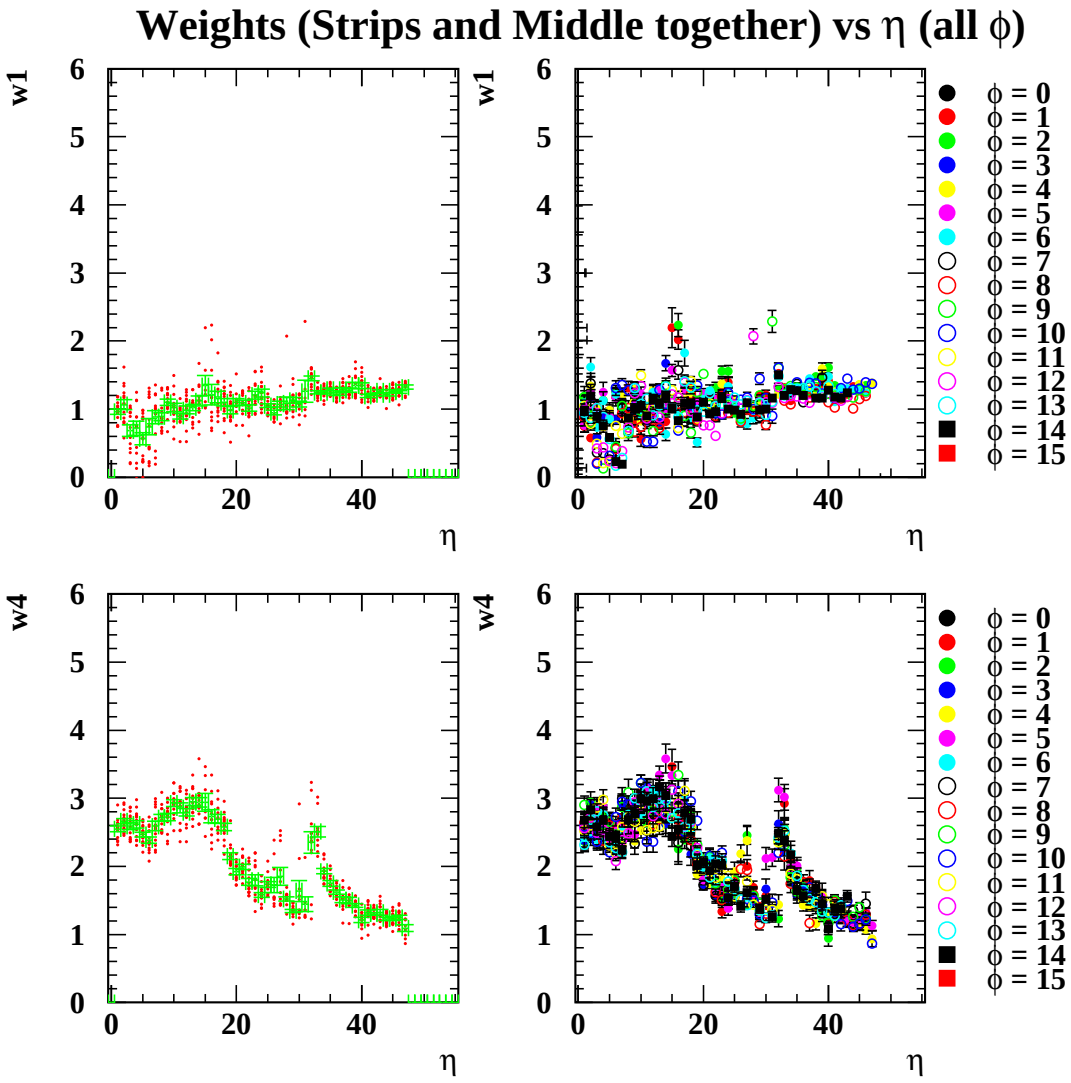

Figure 6.10: Weights evaluated for Presampler and Back (w1, w4), as a function of $\eta_{\text{cell}}^{\text{hit}}$, with Strips and Middle weights set to 1. In the left column all weights at several $\phi_{\text{cell}}^{\text{hit}}$ are displayed together with their profile histogram. In the right column, different symbols and gray levels refer to different $\phi_{\text{cell}}^{\text{hit}}$.

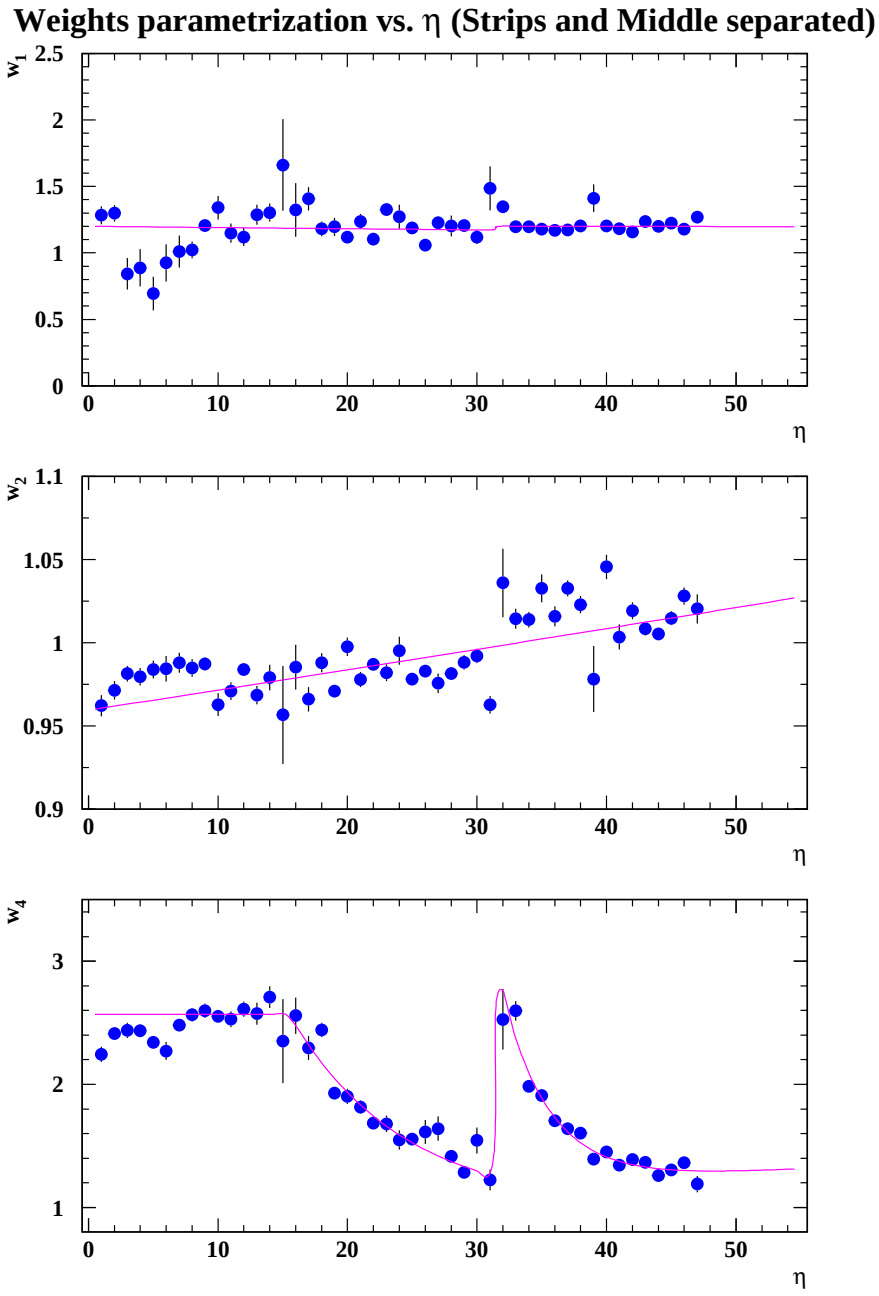

Figure 6.11: Profile of weights evaluated for Presampler, Strips and Back (w1, w2, w4), with Middle weights set to 1, as a function of $\eta_{\text{cell}}^{\text{hit}}$. At each $\eta_{\text{cell}}^{\text{hit}}$ the values are averaged over $\phi_{\text{cell}}^{\text{hit}}$. The fit is also displayed.

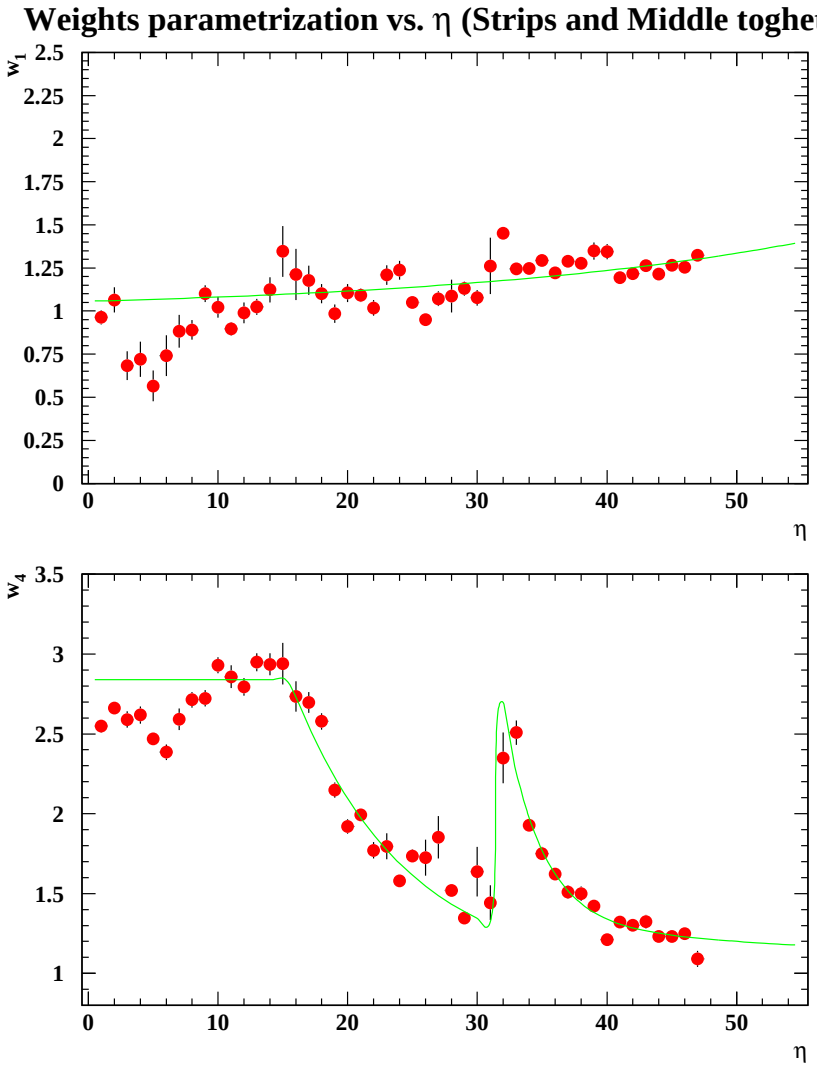

Figure 6.12: Profile of weights evaluated for Presampler and Back (w1, w4), with Strips and Middle weights set to 1, as a function of $\eta^{\text{hit}}_{\text{cell}}$. At each $\eta^{\text{hit}}_{\text{cell}}$ the values are averaged over $\phi^{\text{hit}}_{\text{cell}}$. The fit is also displayed.

Weighting recipes	$\frac{\mathrm{RMS}[E_{\mathrm{peak}}]}{\langle E_{\mathrm{peak}}\rangle}\Big\vert_{\mathrm{module}}$	$\frac{\mathrm{RMS}[E_{\mathrm{peak}}]}{\langle E_{\mathrm{peak}}\rangle}\Big\vert_{\mathrm{FT0}}$	$\frac{\mathrm{RMS}[E_{\mathrm{peak}}]}{\langle E_{\mathrm{peak}}\rangle}\Big\vert_{\mathrm{FT-1}}$
no weights	**1.03%**	**0.84%**	**1.05%**
single cell weights, $\tilde{w}_3 = 1$	1.13%	1.00%	1.08%
single cell weights, $\tilde{\mathbf{w}}_{\mathbf{2+3}} = \mathbf{1}$	**0.98%**	**0.77%**	**1.01%**
fit weights, $\tilde{w}_3 = 1$	1.57%	1.71%	1.31%
fit weights, $\tilde{\mathbf{w}}_{\mathbf{2+3}} = \mathbf{1}$	**0.97%**	**0.67%**	**1.08%**

Table 6.1: Uniformity of the energy E_{peak} obtained with different weighting recipes for the full EMB module P15 coverage (module), and in the FT0 ($0 \leq \phi_{\mathrm{cell}} \leq 7$) and FT-1 ($8 \leq \phi_{\mathrm{cell}} \leq 15$) regions.

energy drop at $\eta_{\mathrm{cell}}^{\mathrm{hit}} = 31, 32$ is still present in the weighted energies; the *ad–hoc* correction for this effect is behind the scope of this work, as well as the correction of the response of the remaining misbehaving cells.

With the fit weights displayed in Figure 6.11, i.e. with the normalization $\tilde{w}_3 = 1$, the energy profile becomes as in Figure 6.15. The evident deterioration is due to the few % variation of the Strips weight. This does not necessarily mean that leaving the Strips weight as a free parameter is wrong: probably the explanation is that the choice of the normalization $\tilde{w}_3 = 1$ is too arbitrary. At least from an empirical point of view, one can conclude that this normalization is not suitable.

The uniformity, without weights and with weights evaluated in different ways (i.e. with normalizations $\tilde{w}_{2+3} = 1$ and $\tilde{w}_3 = 1$, and with or without fitting) are summarized in Table 6.1[6] for the full EMB module extension, and for the FT0 ($0 \leq \phi_{\mathrm{cell}} \leq 7$) and FT-1 ($8 \leq \phi_{\mathrm{cell}} \leq 15$) regions. The reason for such a distinction is related to the EMB test–beam setup, that can be considered ATLAS–like only in the FT0 region (see Chapter 7 for a details). The FT0 region results should be looked as a reference to judge the weighting algorithm performances.

As expected, the relative energy resolution shows an improvement when computing the total energy as the weighted sum of the layer measurements. In Figure 6.16 the values of $\sigma[E_{\mathrm{tot}}]/\langle E_{\mathrm{tot}}\rangle$ as a function of $\eta_{\mathrm{cell}}^{\mathrm{hit}}$, mediated over $\phi_{\mathrm{cell}}^{\mathrm{hit}}$, are shown, for different weights normalizations, using the weights evaluated cell by cell. The best energy resolution is obtained with the normalization $\tilde{w}_3 = 1$, as expected since it has the largest degree of freedom. Figure 6.17 displays the same quantities, but using the weights from the fits. In this case, the normalization $\tilde{w}_{2+3} = 1$ yields the best energy resolution. In both cases, the improvement is at the level of $0.1\% \div 0.2\%$, and is essentially due to the application of weights, the difference between the two normalizations being almost negligible.

[6] The energy response uniformity values quoted in Table 6.1 for the P15 module are slightly worse than the ones proposed in Table 7.1 in Chapter 7. This is due to the fact that in the full data analysis a further gaussian fit is performed is on the E_{peak} distribution, in order to get rid of the remaining misbehaving cells.

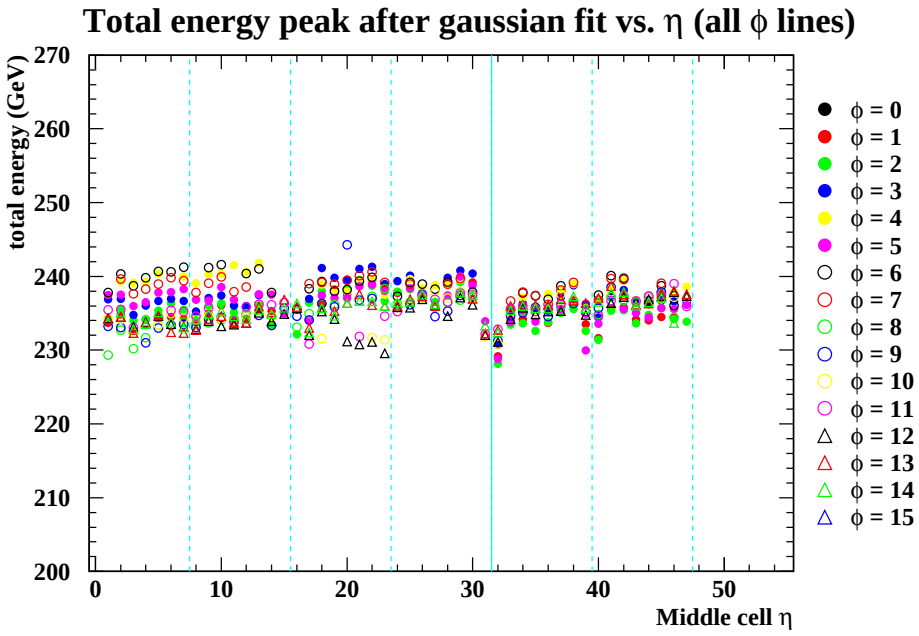

Figure 6.13: Total energy vs $\eta_{\text{cell}}^{\text{hit}}$ at several $\phi_{\text{cell}}^{\text{hit}}$ (no weights applied).

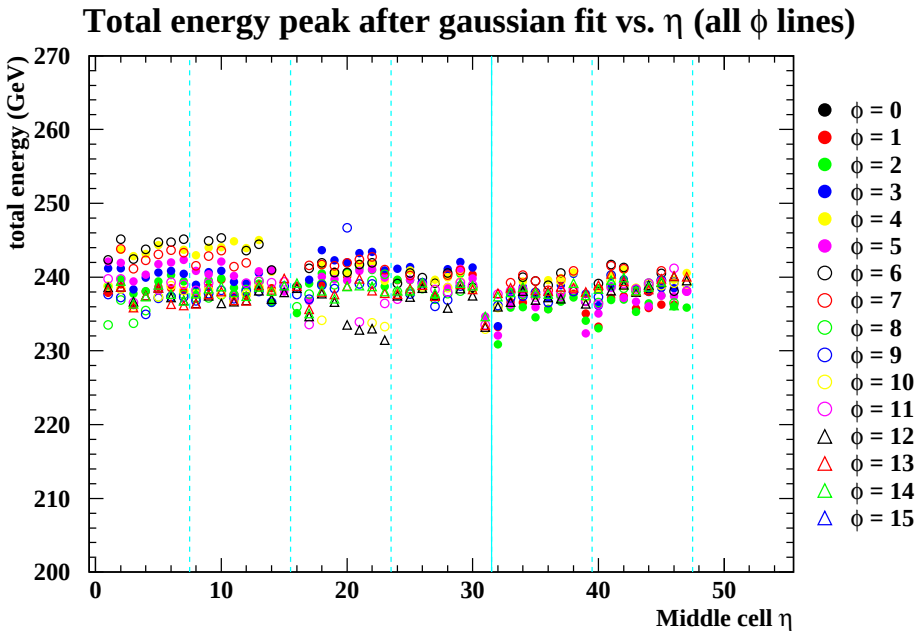

Figure 6.14: Total energy vs $\eta_{\text{cell}}^{\text{hit}}$ at several $\phi_{\text{cell}}^{\text{hit}}$ (weights normalization: $\tilde{w}_{2+3} = 1$).

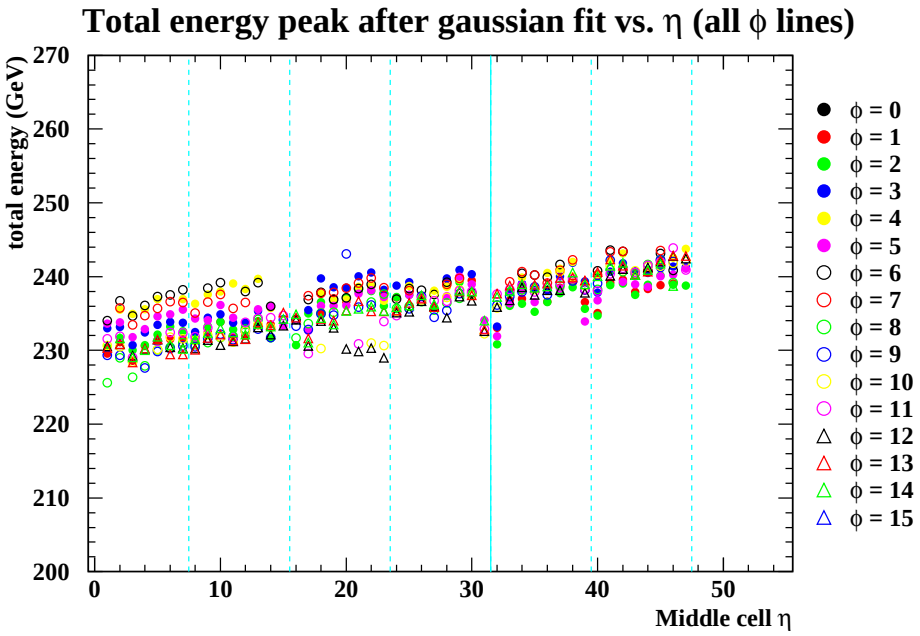

Figure 6.15: Total energy vs $\eta^{\rm hit}_{\rm cell}$ at several $\phi^{\rm hit}_{\rm cell}$ (weights normalization: $\tilde{w}_3 = 1$).

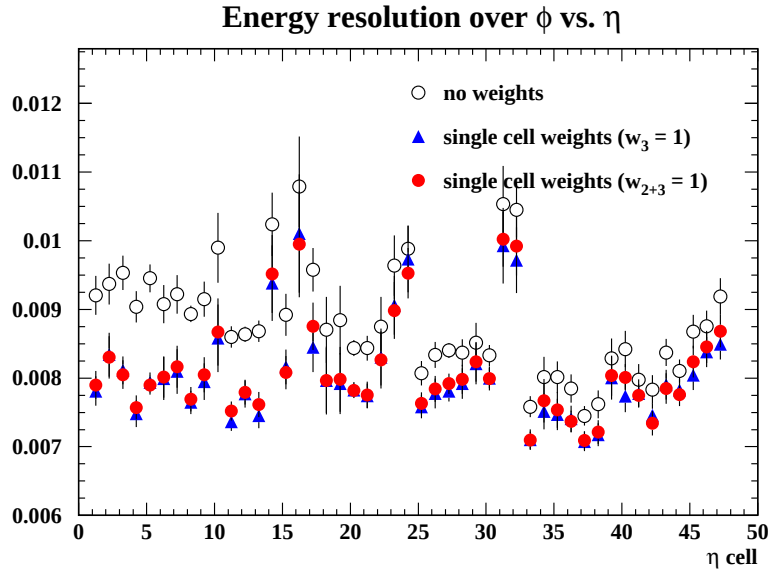

Figure 6.16: Values of the $\sigma[E_{\rm tot}]/\langle E_{\rm tot}\rangle$ energy resolution, mediated over $\phi^{\rm hit}_{\rm cell}$, as a function of $\eta^{\rm hit}_{\rm cell}$, for different weighting recipes. The weights evaluated cell by cell are used.

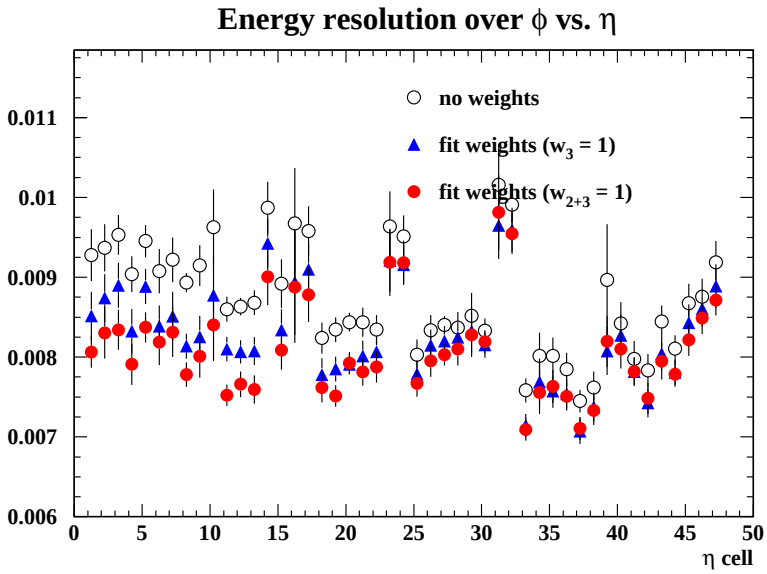

Figure 6.17: Values of the $\sigma[E_{\rm tot}]/\langle E_{\rm tot}\rangle$ energy resolution, mediated over $\phi^{\rm hit}_{\rm cell}$, as a function of $\eta^{\rm hit}_{\rm cell}$, for different weighting recipes. The weights from the fits are used.

6.5 Summary and perspectives

The energy resolution of the ATLAS electromagnetic barrel calorimeter (EMB) can be improved by reconstructing the total energy as the weighted sum of the measurements in all the longitudinal layers. The set of optimal weights can be obtained through an exact analytical minimization of the energy resolution, expressed as a function of the averages and covariance matrix elements of the layers measurements. Statistical fluctuations on the optimal weights can be efficiently evaluated through a numerical MC approach.

Since the optimal weights are defined up to an overall multiplicative constant, two different normalizations have been developed and tested, consisting in constraining the weight of Middle layer, or that of the Strips+Middle pseudo–layer, to be equal to 1. Both the "toy" MC study of the energy losses in the dead zone of the detector, and the results obtained from the EMB module P15 test-beam data samples, suggest that — at least for high energy shower — the Strips+Middle pseudo–layer normalization is the most performing, providing a sensible improvement in the energy uniformity and scale. In the case of the module P15 electrons data the relative energy resolution improves by $0.1\% \div 0.2\%$ with both normalizations. The algorithm proves to be a powerful tool in order to complete the EMC calibration, and it will be used in Chapter 7 as a complementary correction in the uniformity study.

There are several questions related to the calibration weights that should be investigated, but that are certainly behind the direct scope of this work. The weights computation algorithm should be tested on data from different EMB production modules, in order to study the stability of the optimal weights. The behavior of the optimal weights

at different beam energies should be investigated. In order to state the feasibility of the energy weighting calibration technique in the ATLAS framework (for what concerns the first attempts, see for example [21]), it would indeed necessary to study the scaling of the weights values with the amount of material in front of the calorimeter. This could be done in the EMB test–beam setup, with the aim to find a possible parametrization to be extended to the full ATLAS environment.

Chapter 7

Energy response uniformity of the EMC

7.1 Energy response non–uniformity sources

The quality of the energy response uniformity of the ATLAS LAr EMC depends on several factors, each being expected to contribute to the relative energy resolution constant term c in equation (2.4). The main sources of the EMC energy response non–uniformity have been extensively studied [4], and can be summarized as follows:

- **Detector mechanical non–uniformity** (absorber and gap thickness). They are minimized thanks to an accurate detector components design, production and assembly (see for example [60]).
- **Detector geometry** ("ϕ modulation"). The *accordion* geometry induces a variation in the sampling fraction of the calorimeter along the ϕ coordinate, because of the imperfect overlap among the absorbers due to finite bending radius.
- **Finite size of the readout cluster** ("η modulation"). The readout cluster has a finite dimension, that is usually relatively small along the η coordinate. The shower energy is not fully contained, the EMC response depends on the impact point of the incoming particle with respect to the cell position. The response is maximum when the particle hits the center of the cell, and decreases at the edges.
- **Calibration quality** (amplitude accuracy and stability, difference between the calibration an ionization signals). Chapter 3 and 4 of this work are dedicated to show how the signal reconstruction and the electronic calibration technique contribute to the quality of EMC response uniformity.
- **Upstream material** (low energy tails). It can cause the shower to start developing before the EMC, so that its energy is not fully contained in the detector. In this case the EMC energy resolution is worsened by the appearance of low energy tails in the calorimeter energy distribution (see Chapter 6).

- **Longitudinal leakage** of high energy showers (see Chapter 6).
- **Long range non–uniformity sources**, such as signal dependence on the LAr purity and temperature, HV variations, cables lengths, mechanical deformations, localized discontinuities (e.g. between the EMB A and B electrodes, or between the EMB and the EMC).

The detailed discussion of all the non–uniformity contributions, as well as the optimization of the relative corrections, is well behind the scope of this work. On the other hand, it is reasonable to assume that the non–uniformity sources contribute independently to the final energy response performances of the EMC.

This chapter is dedicated to study the energy response uniformity of the EMB production modules exposed to 245 GeV electrons test–beam at CERN during the 2001 ans 2002 sessions (Section 7.2), using the SR algorithms based on the OF technique discussed in Chapter 4 and 5, in association with the "dead" material and leakage correction based on the weighting technique developed in Chapter 6. In order not to be dependent on the ϕ and η modulations effects discussed above, the analysis is conducted on the electrons events hitting the center of the cell (see Section 7.3 for details).

7.2 EMB modules test–beam setup

The beam tests of the EMB modules were conducted on CERN's H8 beam line For the modules uniformity study secondary beams of $e^{\pm}$ of 245 GeV producted by the SPS were used [44].

The EMB module under test is housed in a dedicated cryostat built with 4 cm thick aluminum walls separated by a 5 cm vacuum gap (Figure 7.1). Two feed-through's are needed to read out the whole EMB module and the corresponding Presampler sectors. FT-1 covers the $0 < \phi < 0.2$ region, FT0 the $0.2 < \phi < 0.4$ one; only FT0 is equipped with the ATLAS gold–plated pin carriers, thus ensuring the required low–cross–talk connections. The cryostat is mounted on a movable table, so that each readout position of the EMB module can be aligned to the beam line, respecting the projective design (Figure 7.2).

A system of three scintillators in front of the cryostat provides the trigger to the DAQ system [45]. The beam acceptance is defined by the $4{\times}4$ cm^2 size of the first two. Four multi–wire proportional chambers [46] ("beam chambers", BC's) are located along the beam line in front of the EMB module cryostat; they provide the position of the incoming particle track. Since the trigger is asynchronous with respect to the 40 MHz DAQ clock, the time difference between the trigger and the next clock cycle is measure by a fast Time Discriminator Counter (TDC), whose counting period is $\sim$50 ps, and whose resolution is $\sim$300 ps. Two additional scintillators follow the cryostat: the first one is allocated after a lead block corresponding to 3 X_0, and is used as a threshold counter to discriminate the pions contaminating the electrons beam. The second one follows after a 5 λ_I iron block, its signal is used to detect the muons in the beam. The different elements disposition along the beam line is schematized in Figure 7.2; details on the test–beam line instrumentation can be found in [47].

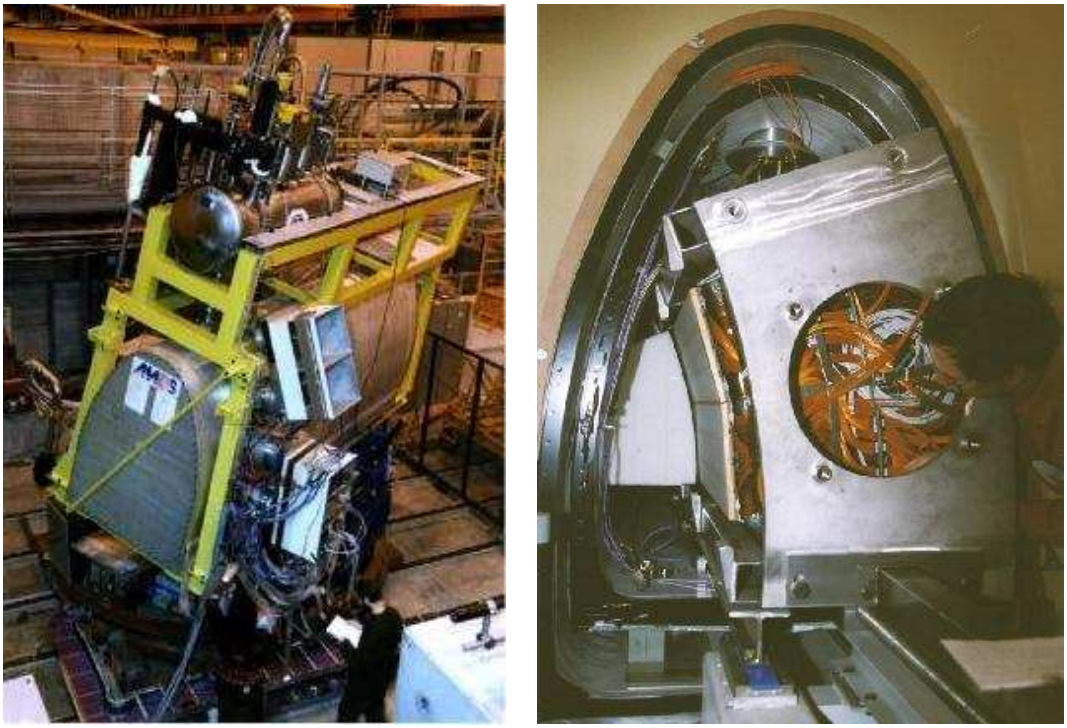

Figure 7.1: The EMB module test–beam cryostat on the movable table (left). An EMB production module is being inserted in the cryostat (right).

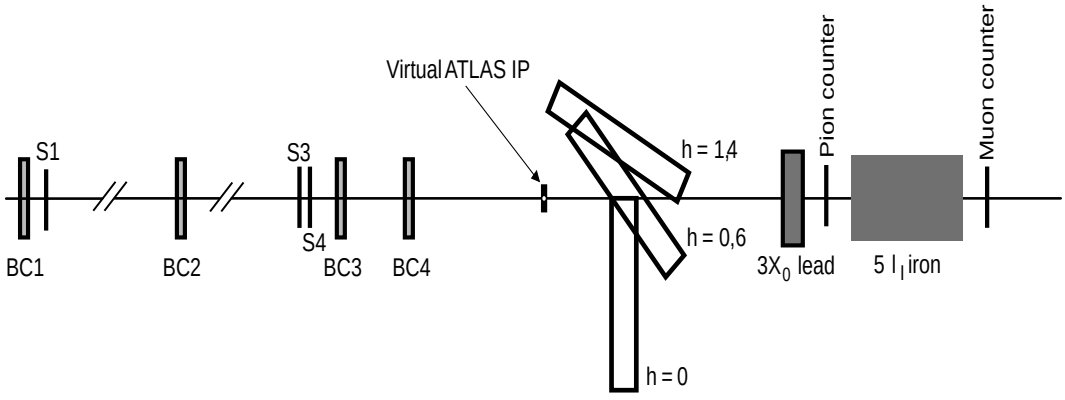

Figure 7.2: CERN H8 beam line setup. Three different positions of the EMB module under test are shown.

The DAQ system used in the EMB modules test–beam sessions is based on the system developed by the RD13 collaboration (see for example [48]). The data emerging from the readout system located on the FEC (see Chaper 2) are stored in FIFO registers on the miniROD system [49], that is read by a RIO8061(2) processor. The whole system is controlled by different software applications that are detailed described in [50].

7.3 Data sample selection and analysis outline

The data sets under exam come from the position scans performed in 2001 and 2002 on different EMB production modules[1]with electron beams at energy $E_{\text{beam}} = 245$ GeV. In each modules the scanned region spans most of the interval $1 \leq \eta_{\text{cell}} \leq 45$ ($0.025 \leq \eta \leq 1.15$) for $1 \leq \phi_{\text{cell}} \leq 15$.

The data are processed off-line through the EMTB [52] package, and the energy recorded by each readout cell is reconstructed using the OF technique [30], in the OF4 incarnation [32].

For each event, in the Middle layer, a 3×3 cells cluster is formed around the cell with the largest energy content. Similar clusters are formed for Presampler, Strips and Back layer, made of 3×1, 24×1 and 2×3 cells respectively, in order to cover at least the same region of the Middle cluster. The η and ϕ coordinates of the impact point are estimated as the barycentre of the shower contained in the Middle cluster:

$$\left(\eta_{\text{bary}}^{\text{Middle}}, \phi_{\text{bary}}^{\text{Middle}}\right) = \frac{\sum_{k\in\text{cluster}} \left(\eta_{\text{cell}}^{\text{Middle}}, \phi_{\text{cell}}^{\text{Middle}}\right) \times E_k^{\text{Middle}}}{\sum_{k\in\text{cluster}} E_k^{\text{Middle}}} \qquad \text{(Middle cell units)} \quad (7.1)$$

For each run, the position $(\eta_{\text{cell}}^{\text{hit}}, \phi_{\text{cell}}^{\text{hit}})_{\text{Middle}}$ of the cell hit by the beam is extracted as the average values of $\eta_{\text{bary}}^{\text{Middle}}$ and $\phi_{\text{bary}}^{\text{Middle}}$ from events where the energy in the Middle cluster in greater then 30 GeV (Figure 7.3).

The η impact point of the events is obtained also from the Strips sampling records. The η coordinates of the impact point is estimated as the barycentre of the shower contained in the Strips cluster using the analogous of equations (7.1); for each run the position $(\eta_{\text{cell}}^{\text{hit}})_{\text{Strips}}$ of the cell hit by the beam is extracted as the average values of $(\eta_{\text{bary}})_{\text{Strips}}$, and conveniently converted in Middle cells units. This value is used to check the quality of the analized run (see Section 7.3.2).

7.3.1 Event selection

For each run, the following event selection is applied:

A1 all events from random trigger, or compatible with muons or pions are rejected; only events with a physics trigger are selected;

A2 the signal from the 3$^{\text{nd}}$ scintillator upstream (S3) must be compatible with one MIP, otherwise the event is rejected (Figure 7.4);

[1]M13 (July–August 2001), M10 (October 2001), P15 (June 2002), P13 (July–August 2002)

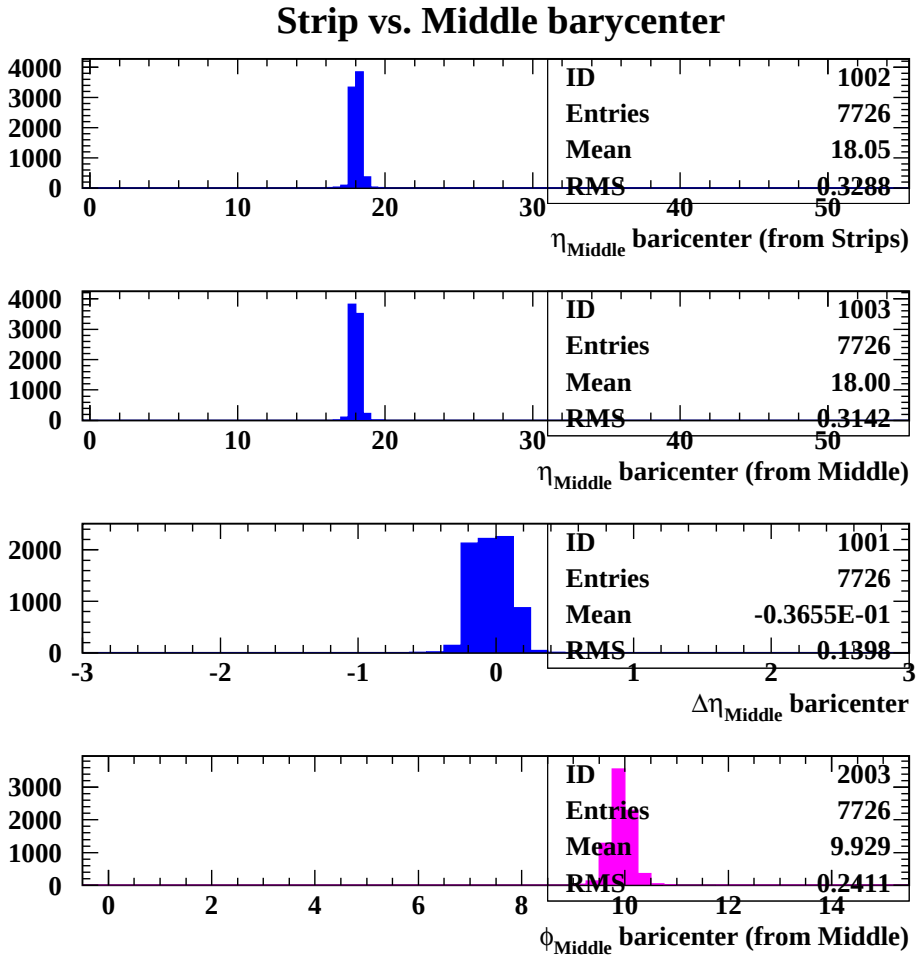

Figure 7.3: Example of estimation of the η and ϕ coordinates of the impact point in a P15 EMB module test–beam run. The nominal position of the cryostat table was ($\eta_{\rm cell} = 18$, $\phi_{\rm cell} = 10$). From to bottom: $(\eta^{\rm hit}_{\rm cell})_{\rm Middle}$ distribution; $(\eta^{\rm hit}_{\rm cell})_{\rm Strips}$ distribution; $\Delta\eta^{\rm hit}_{\rm cell}$ distribution (see text for details); $(\phi^{\rm hit}_{\rm cell})_{\rm Middle}$ distribution.

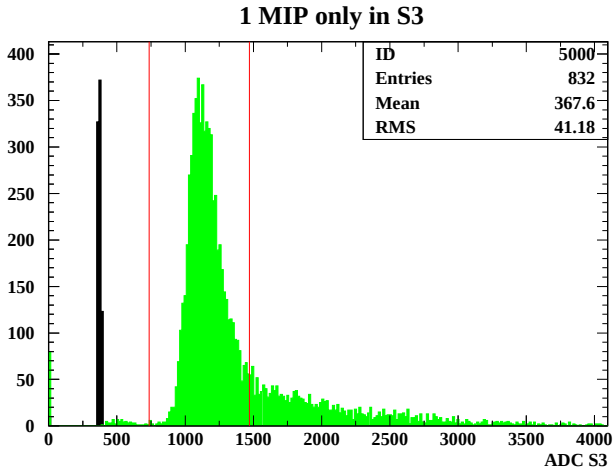

Figure 7.4: Spectrum of the S3 ADC counts. The pedestal peak (black) is estimated with the random trigger events. The first peak of the distribution, compatible with a single MIP particle, is selected.

A3 to achieve a further pions and muon rejection, the cluster energy in the Strips must be > 4 GeV.

A4 a check is performed on the particle track extrapolated from the BC's system spatial hits. For each of the BC's (x, y) coordinates, the residual from the track fit must be within 1 RMS around the mean of the corresponding residuals distribution (Figure 7.5), thus avoiding events in which the track reconstruction has been difficult. The reconstructed η (ϕ) shower barycentre in the Middle sampling is required to be consistent with the x (y) coordinate of each of the 4 BC's (Figure 7.6).

Due to the limited size of the cluster and to the *accordion* geometry, the cluster energy exhibits a dependence on the impact position (η and ϕ "modulations" respectively). As the optimization of corrections for such effects is behind the scope of this work, it is necessary to restrict the selection to only those events where the impact point is close to the center of the hit cell:

A5 $|\eta_{\text{bary}} - \eta^{\text{hit}}_{\text{cell}}| < 0.1$ and $|\phi_{\text{bary}} - \phi^{\text{hit}}_{\text{cell}}| < 0.1$ (Middle cell units)

This requirement is quite tight: in general only $\sim 6\%$ of the events match it.

After this selection, the cluster energies from all the layers are summed together, and the total energy E_{tot} for the selected events is plot into a histogram in the range $0.8 \cdot E_{\text{beam}} \div 1.1 \cdot E_{\text{beam}}$. The distribution exhibits a large non-gaussian lower tail, due to a sizable contamination from pions and electrons that lost energy upstream (Figure 7.7). The histogram peak is fit with a gaussian in a range between -1.5σ and $+2.5\sigma$ from the peak. The result of the fit provides a peak value E_{peak} and a width σ_{gauss}. The events satisfying the following requirement:

A6 $|E - E_{\text{peak}}|/\sigma_{\text{gauss}} < 3$

are considered as "electrons" from now on.

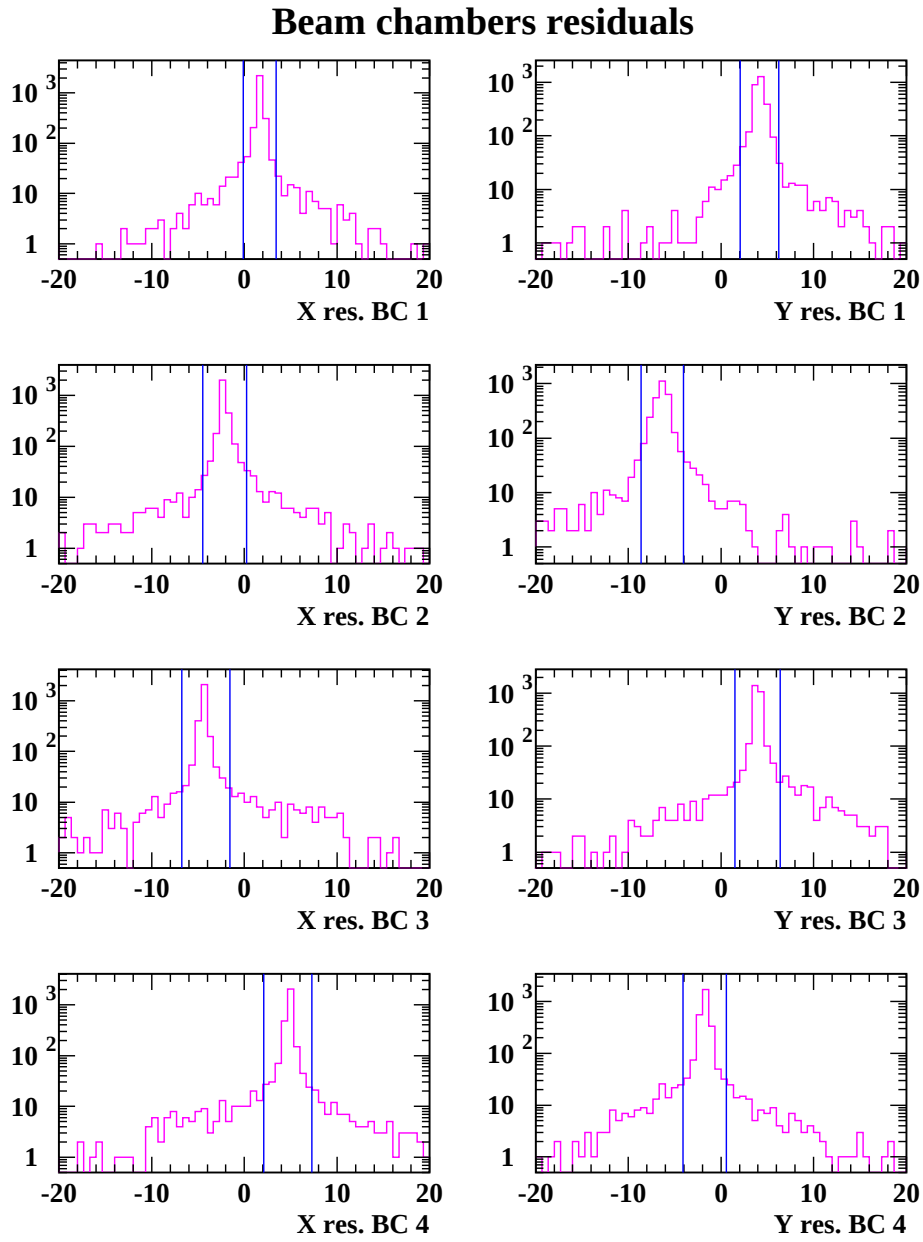

Figure 7.5: Distributions of the residuals of the tracks interpolation fit in each of the four BC's coordinates. The events which residuals are within 1 RMS from the mean of each distributions are selected.

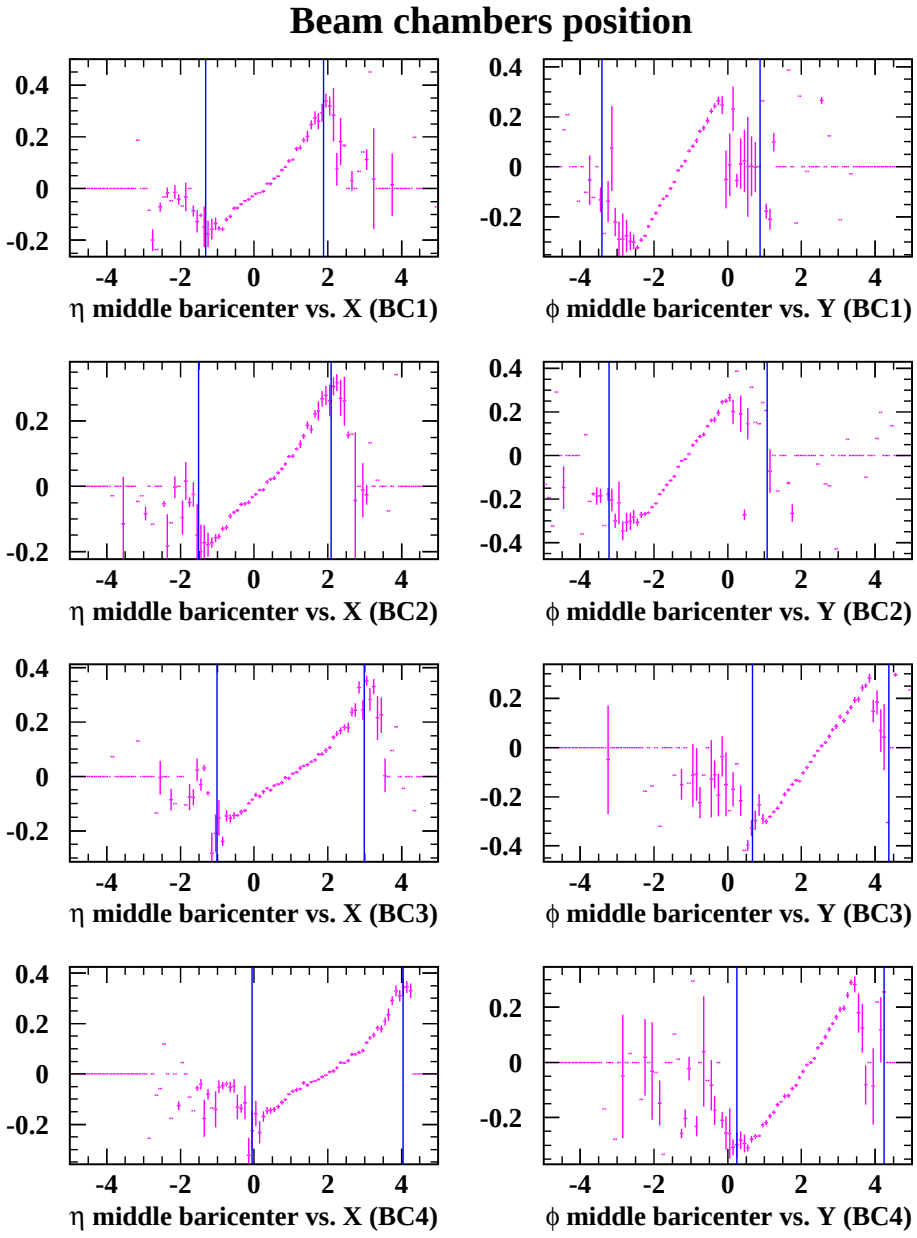

Figure 7.6: Correlations between the event η (ϕ) barycentre, as reconstructed in the Middle section, and the BC's x (y) coordinate. The events for which the two values are compatible are selected.

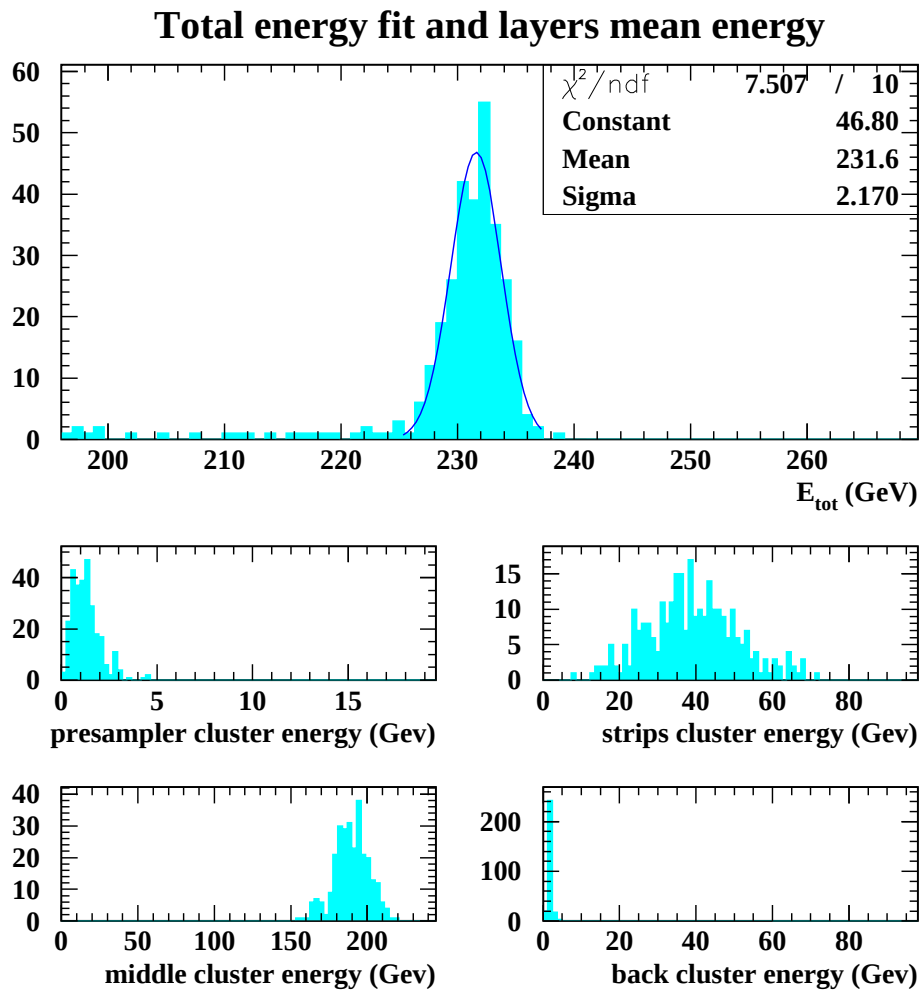

Figure 7.7: Example of the final total energy distribution (top), and of the corresponding energy distributions in the four calorimeter layers, as obtained after the **A6** selection (see text for details). The plots refers to electrons data from a run taken on the EMB production module P15 at $\eta_{\rm cell} = 18$, $\phi_{\rm cell} = 10$ and $E_{\rm beam} = 245$ GeV. The gaussian fit to the peak is shown, and the labels **Mean**, **Sigma** are $E_{\rm peak}$ and $\sigma_{\rm gauss}$ respectively.

7.3.2 Run and cell selection

Not all the runs can be used for uniformity study and weights optimization, because of the limited statistics and due to local problems. Therefore:

B1 the position of the hit cell must be extracted from at least 50 events;

The η impact points of the incoming particle as extracted from the Strips and Middle compartments are required to be compatible. The distribution of

$$\Delta\eta_{\text{bary}} = (\eta_{\text{bary}})_{\text{Middle}} - (\eta_{\text{bary}})_{\text{Strips}}$$

is histogrammed (Figure 7.3), the following requirements on the distribution parameters are required:

B2 the bare values of $(\eta^{\text{hit}}_{\text{cell}})_{\text{Middle}}$ and $(\eta^{\text{hit}}_{\text{cell}})_{\text{Middle}}$ must be the same;

B3 the mean value of the $\Delta\eta_{\text{bary}}$ distribution must be comprise within ± 0.15 Middle cell units;

B4 the $\Delta\eta_{\text{bary}}$ distribution RMS must be smaller than 0.25 Middle cell units;

For each run, the cluster energy spectrum for all layers is histogrammed, using events matching criteria **A1** and **A2**, and the fraction of events above a given energy threshold is evaluated (Figure 7.8). If such fraction is too low, then the hit cell is probably dead or misbehaving, and the run is rejected. The selection criteria are:

B5 at least 50% of events must have $E^{\text{cluster}}_{\text{Presampler}} > 0.5$ GeV;

B6 at least 50% of events must have $E^{\text{cluster}}_{\text{Strips}} > 10$ GeV;

B7 at least 50% of events must have $E^{\text{cluster}}_{\text{Middle}} > 100$ GeV;

B8 at least 50% of events must have $E^{\text{cluster}}_{\text{Back}} > 1$ GeV;

The Strips pass a further control: even if the total energy from the Strips cluster has a reasonable value and distribution, in fact, a few of them (namely one or two out of the eight corresponding to the hit Middle cell) could be dead or misbehaving. The checking algorithm is based on the comparison of the mean energy deposit in each Strip with the deposit in the neighbors and with the mean deposit along the Strips cluster, and on a threshold comparison of the mean energy variation between adjacent Strips (Figure 7.9).

B9 no "dead" Strips must be found by the Strips efficiency check algorithm;

To reject runs where the gaussian fit to the energy peak fails (e.g. due to neighboring dead cells or calibration problems), a loose cut on the energy resolution is applied:

B10 $\sigma_{\text{gauss}}/E_{\text{peak}} < 1.5\%$

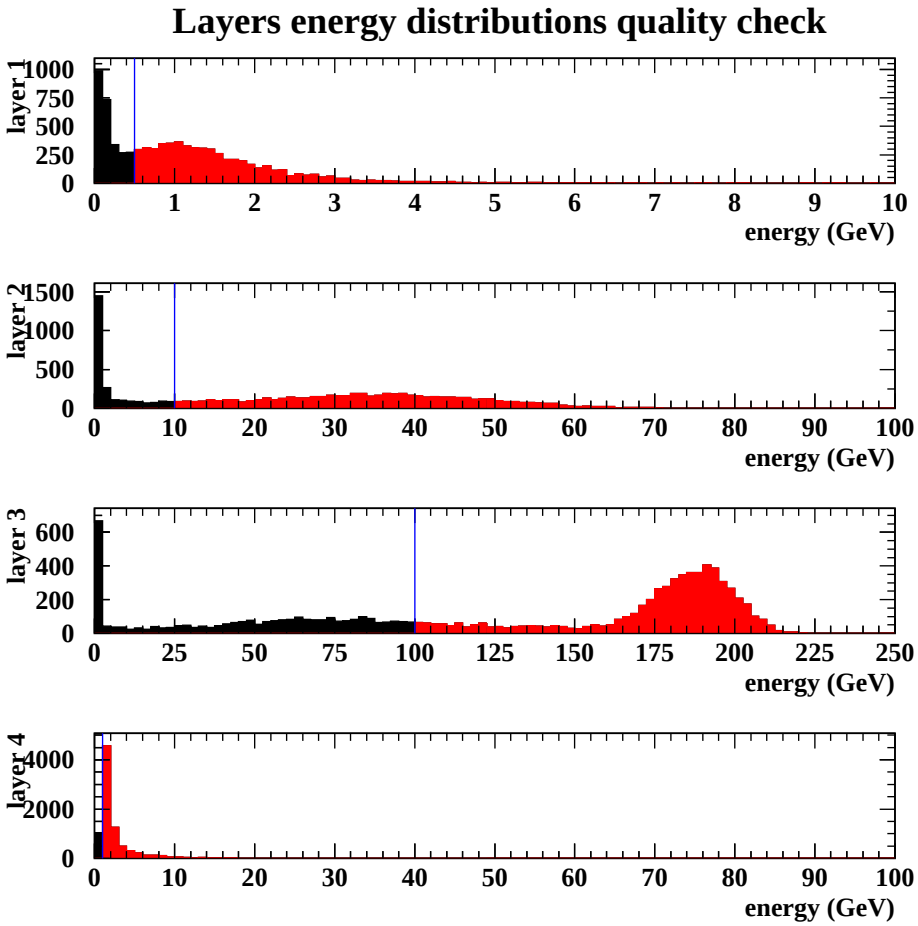

Figure 7.8: Example of the cluster energy spectra for all EMC layers (from top to bottom, Presampler, Strips, Middle and Back): total (black) and above a given energy threshold (red) (see text for details).

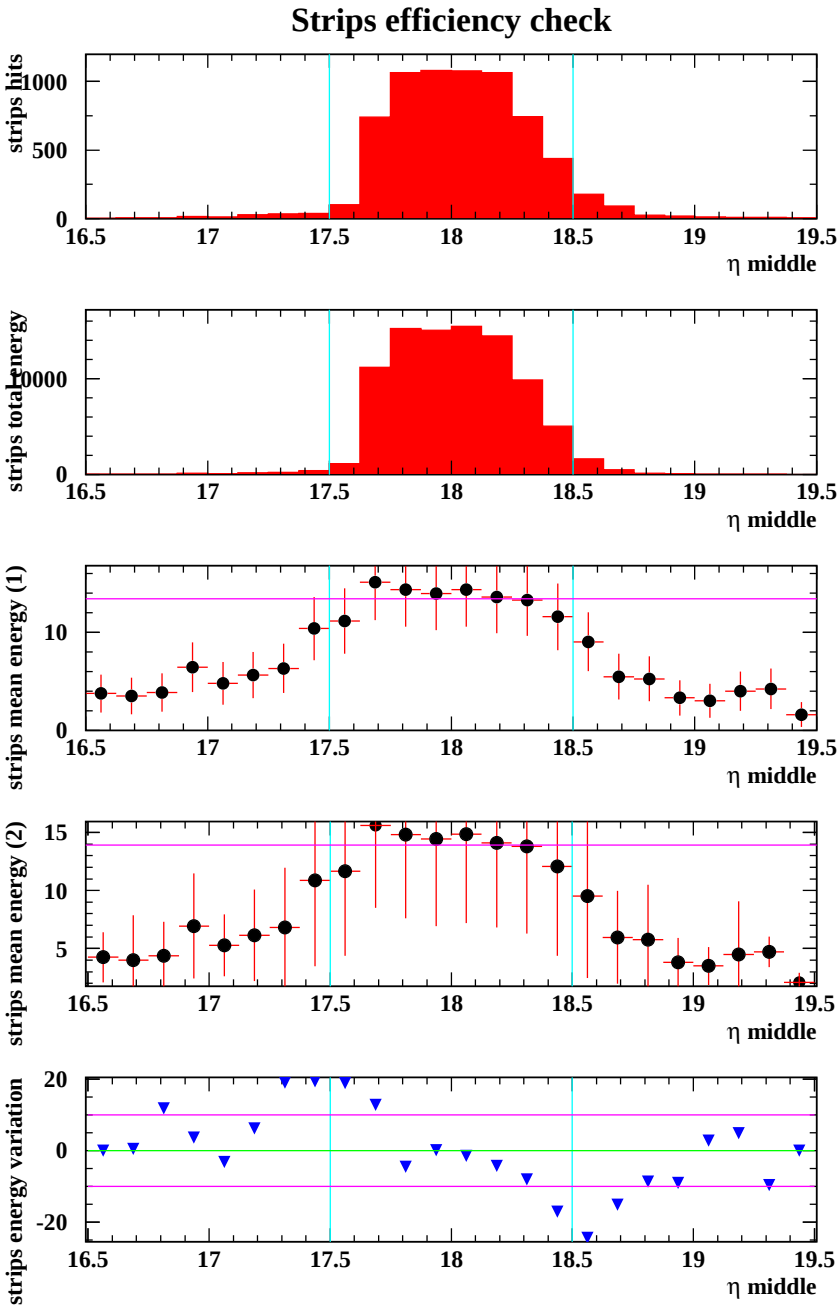

Figure 7.9: Strips efficiency check algorithm summary. From top to bottom, in the exposed Strips region: total number of hits distribution; total energy distribution; mean energy deposit per events (two different estimation procedures); mean energy variation between adjacent Strips.

The **B1**—**B10** criteria are only used to select runs: if a run pass the previous selection, then the event selections **A1**—**A6** are used for the analysis. After these selections, data from different runs belonging to the same hit cell are merged together to increase the statistics, and the gaussian fit is repeated.

B11 the analysis is performed only on the cells where at least 5000 selected events are collected, of which at least 100 are flagged as "electron" events.

The last requirement is quite loose: on average, in each cell ~ 10000 events are collected, of which ~ 650 are "electrons".

7.4 Uniformity of the production modules

Once the analysis is conducted on the full region of the EMB module under test, the energy response uniformity is estimated as follows:

- the E_{peak} values from all the $(\eta^{\text{hit}}_{\text{cell}}, \phi^{\text{hit}}_{\text{cell}})$ positions that pass the selection criteria put in a histogram;
- the E_{peak} distribution is expected to be gaussian, apart for some residual misbehaving cells that pass the run selections. Since these values populate the non–gaussian tail of the E_{peak} distribution, and the correction of these local problems is anyway behind the scope of this work, the E_{peak} histogram is fit with a gaussian function to get rid of this residual deviation (see Figure 7.10 for an example).
- the *uniformity* estimator is computed as the ratio between the $\sigma[E_{\text{peak}}]$ width and the $\langle E_{\text{peak}} \rangle$ mean value of the E_{peak} distribution gaussian fit.

The same uniformity computation procedure is separately applied to the $(\eta^{\text{hit}}_{\text{cell}}, \phi^{\text{hit}}_{\text{cell}})$ positions belonging to the FT0 ($\phi^{\text{hit}}_{\text{cell}} \geq 8$) and to the FT-1 ($\phi^{\text{hit}}_{\text{cell}} < 8$) regions. Since the FT-1 is not equipped with the ATLAS gold–plated pin–carriers, in fact, the cross-talk between the corresponding neighboring cells and the noise contribution are expected to be higher than in FT0. These effects are expected to worsen the detector performance: for this reason only the FT0 energy response uniformity will be taken as the reference value in order to quote the detector performance and the effectiveness of the energy reconstruction and calibration algorithm used.

The global uniformity results are extensively listed in Table 7.1 for the M10, P13 and P15 EMB production modules. Values are quoted for different weighting recipes; the sum of the Strips and Middle energies is used as the reference measurement to normalize the weights values[2]

It is immediately noticed that the uniformity, already good at the $\sim 1\%$ level on the full modules extension thanks to the OF4 signal reconstruction, furtherly improves with the use of the energy weighting technique. In agreement with the Chapter 6 results, in

[2] $w_{2+3} = 1$, that is shown in Chapter 6 to be the best performing weights normalization scheme.

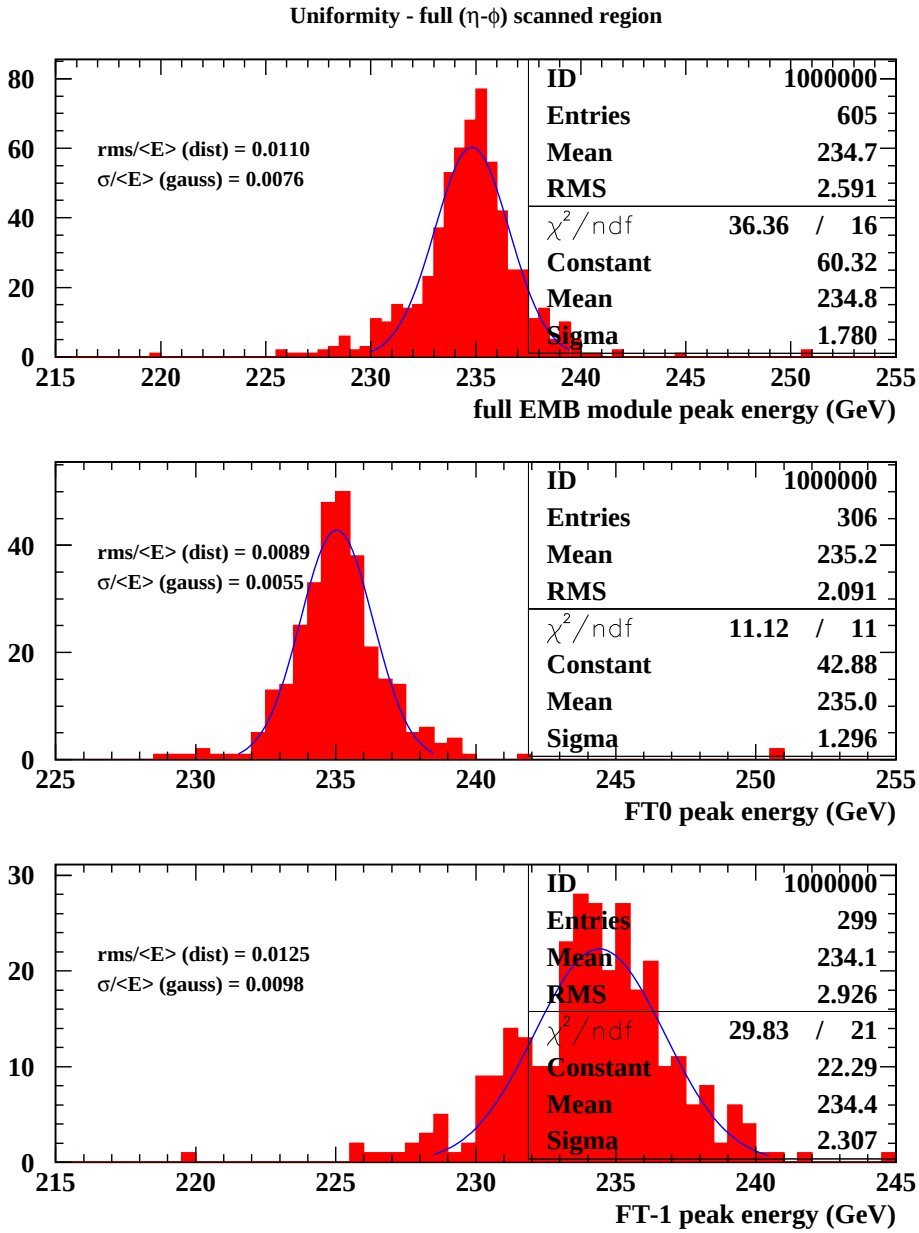

Figure 7.10: EMB production modules M10 energy response uniformity evaluation, through the fit of the E_{peak} distribution. From top to bottom, full module after selections, FT0 and FT-1.

Uniformity (% RMS)	weighting recipes	M10	P13	P15
$\frac{\sigma[E_{\rm peak}]}{\langle E_{\rm peak}\rangle}\Big\vert_{\rm module}$	no weights	0.91	0.97	0.93
	weights (single cell)	0.78	0.87	0.80
	weights (fit)	0.76	0.87	0.66
$\frac{\sigma[\mathbf{E_{peak}}]}{\langle \mathbf{E_{peak}}\rangle}\Big\vert_{\mathbf{FT0}}$	**no weights**	**0.77**	**0.68**	**0.73**
	weights (single cell)	**0.59**	**0.52**	**0.50**
	weights (fit)	**0.55**	**0.46**	**0.44**
$\frac{\sigma[E_{\rm peak}]}{\langle E_{\rm peak}\rangle}\Big\vert_{\rm FT-1}$	no weights	1.04	0.94	1.08
	weights (single cell)	1.03	0.78	1.07
	weights (fit)	0.98	0.99	1.10

Table 7.1: Energy response uniformity of the EMB production modules M10, P13 and P15

all the modules the best uniformity is obtained using the weighting recipes that takes advantage of the averaging along ϕ and the parametrization along η.

In all the three modules the FT0 region ($\Delta\eta \times \Delta\phi = 1.4 \times 0.2$) shows the best uniformity ($\sim 0.5\%$). This results confirm the power of the OF signal reconstruction technique implementing the injection–point and signal–difference corrections (Chapter 4), and of the energy weighting calibration (Chapter 6). As we mentioned before, the $\sim 1\%$ uniformity in FT-1 is to be attributed to the test–beam setup.

Uniformity FT0 (% RMS)	M10	P13	P15
$\frac{\sigma[E_{\rm peak}]}{\langle E_{\rm peak}\rangle}\Big\vert_{\rm A}$	0.51	0.45	0.47
$\frac{\sigma[E_{\rm peak}]}{\langle E_{\rm peak}\rangle}\Big\vert_{\rm B}$	0.74	0.90	0.61

Table 7.2: Energy response uniformity of the EMB production modules M10, P13 and P15 in the FT0 region.

In Table 7.2 the energy response uniformity for the FT0 cells are quoted, as obtained splitting the electrode A ($\eta_{\rm cell} \leq 31$) from electrode B region ($\eta_{\rm cell} > 31$): since the sampling fraction is different in the two zones of the EMC (see Chapter 2), the detector performances could be expected to differ. The uniformity is in fact slightly better in the electrode A region.

7.5 Summary and perspectives

The aim of this EMB test–beam data analysis is to show the effectiveness of the signal reconstruction and calibration techniques that are detailed in the previous chapters. The analysis tests the reconstruction algorithm based on the OF technique that implements

the necessary signal corrections (Chapter 4), applied to the test–beam data in association with the energy weighting technique developed in Chapter 6.

The energy response uniformity results are indeed very good. The non–uniformity effects related to the detector electrical properties, to the material in front of the module and to the longitudinal leakage can be treated so that a $\sim 0.5\%$ RMS uniformity is obtained on the whole extensions of the EMB modules that share the ATLAS–like cabling setup.

The effects of local misbehaving cells and of the energy response modulations due to the detector geometry are not faced in this analysis and need of course to be separately studied.

Conclusive remarks

The ATLAS LAr electromagnetic calorimeter (EMC) is designed to provide a precise energy measurement of electrons and photons, in order to meet the requirements coming from the LHC physics program. Such a quest for precision poses the problematic of the reconstruction of the signals emerging from the detector, as well as of the electronic calibration of the EMC readout cells. This thesis is dedicated to investigate the EMC signal properties, and to the study and development of adequate energy reconstruction and calibration algorithms.

The EMC system is in fact shown to be affected by an intrinsic non–uniformity, that is proved to be related to the detector electrical properties (Chapter 3). These properties are conveniently analysed using equivalent circuit models with lumped elements. The development of such models has been complemented by the construction and the study of a hardware model of a part of the EMC detector (*mock–up*). The electrical behavior of the EMC electrodes are now understood, as well as the ionization and calibration waveforms properties.

The EMC response non–uniformity is demonstrated to be correlated to the inductive behavior of the the readout channels ground reference. This inductive component in the ground connections is proved to be different for the readout cells sharing the same connector, even if both the two ground springs foreseen in the detector design are present. Furthermore, this distortion effect is worsened by the fact that the calibration signal, used as a reference to complete the readout channels equalization, is generated in a different point in the detector with respect to where the ionization current is produced by the physics events.

The intrinsic non–uniformity of the system is also magnified by the existing signal reconstruction (SR) algorithm ("*parabola*" SR), that was used in the preliminary EMC prototype module test–beam data analysis. The aim of such an algorithm would be to extract the correct value of peak and arrival time of the sampled signals: the need of an improved reconstruction and calibration procedure is demonstrated (Chapter 4). The EMC energy response uniformity can in fact be improved using a SR technique that takes into account the detector cell–dependent electrical properties discussed in Chapter 3 ("injection-point" correction and "ionization–to–calibration signal shape difference" correction): this is extensively demonstrated using the signals from the EMC hardware model.

The implementation of such corrections to the real experimental data reconstruction (e.g. the data from the EMC production module test–beam sessions) finds its natural

way in the framework of the optimal filtering (OF) SR technique. In order to perform the computation of the OF coefficients, that are used to reconstruct the peak and the arrival time of an ionization pulse from its digitized sampling, the noise information and the "normalized" shape of the ionization signal are needed for each readout channel. The "injection-point" and "ionization–to–calibration signal shape difference" corrections are then implemented through a correct definition of the ionization pulse "normalization". The ionization waveform is in fact to be deduced from the corresponding calibration pulse, through a transformation that takes into account the different injection points of the currents in the detector, as well as the different injected pulse shapes (Chapter 5).

Performing such a transformation implies the knowledge of a set of parameters that characterize the readout cell model. If the mean ionization pulse shape is known, these parameters can conveniently be retrieved using a fit procedure involving both the ionization and the calibration pulses (OF4 SR technique [32]). The effectiveness of this SR method is extensively demonstrated in the energy response uniformity analysis on the EMC barrel production modules test–beam data analysis (Chapter 7).

In Chapter 5 a possible extension of the OF signal reconstruction technique to the ATLAS experimental framework is developed. The main characteristics of this method is that the OF coefficients computation relies only on the information available from the calibration pulses ("stand–alone" procedure). The ionization signal shape and its correct normalization can in fact be predicted from the calibration waveform using a time–domain convolution procedure. The stand–alone procedure is conceived to directly retrieve all the parameters needed to complete the ionization signal prediction directly from the calibration waveform itself (i.e. without accessing any information from the test–beam mean ionization pulses). Even if some aspects of the parameters extraction need a further investigation, the present status of stand–alone ionization pulse prediction procedure looks promising, also in view of its implementation within the ATLAS framework.

There are anyway some open points that still need to be clarified if the advertised calibration accuracy is to be achieved using only the calibration information. They are discussed in details at the end of Chapter 5, and can be summarized as follows:

- the relevance of the resistive term in the LAr readout cell model;
- the change in rise time of the calibration pulse due to the skin effect in the calibration injection cables;
- the determination of the drift time of the ionization electrons in the LAr gaps, that affect the physics signal pulse;
- the cross-talk contribution to the ionization signal.

The energy resolution and uniformity of the ATLAS LAr EMC can be improved by reconstructing the total energy as the weighted sum of the measurements in all the longitudinal layers. We show in Chapter 6 that the the optimal weights can be obtained through an exact analytical minimization of the energy resolution, expressed as a function

of the averages and covariance matrix elements of the layers measurements. The energies–weighting algorithm proves to be a powerful tool in order to complete the EMC calibration provided by the OF signal reconstruction.

As we mentioned before, an EMB test–beam data analysis completes the thesis work (Chapter7). This analysis is conceived to test the effectiveness of the signal reconstruction and calibration techniques discussed and developed in the rest of the work. The energy response uniformity obtained from the EMB production modules test–beam data analysis is at the level of $\sim 0.5\%$, proving the power of the developed algorithms.

Appendix A

Signals description

A.1 Ionization signal

After the passage of the ionizing particles produced in the shower, electrons and positive ions drift in the LAr gap, forced by the electric field provided between the electrodes and the absorber by the HV. Due to the different mobilities in LAr, the interesting (faster) signal is the one generated by the electrons drift. The produced current is a typical ionization–chamber triangular waveform (Fig. A.1), with a rise time of the order of a few nanoseconds followed by a linear decay for the duration of the electrons maximum drift time T_d [29].

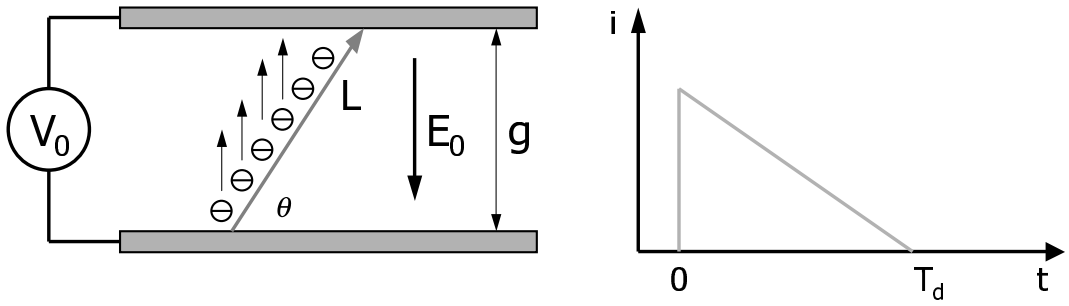

Figure A.1: Charge collection scheme and current characteristic for a LAr ionization chamber, assuming uniform ionization over the gap.

In fact, under the (reasonable) assumptions of a uniform electric field E_0 and of uniform ionization along the LAr gap, a current di is generated by the charge dq that drift for a length dl:

$$\begin{aligned} dq &= \frac{Q}{L} dl \\ di &= v_d \frac{E_0}{V_0} dq = \frac{Q}{L} v_d \frac{E_0}{V_0} dl \end{aligned} \tag{A.1}$$

where Q is the ionization charge deposited along the ionization track length L that will be

collected by the readout electrode, and v_d is the electrons drift velocity. The peak current I_0^{phys} is:

$$\begin{aligned} I_0^{\text{phys}} &= \int_0^L di = \frac{Q}{L} v_d \frac{E_0}{V_0} \int_0^L dl \\ &= \frac{Q}{L} v_d \frac{E_0}{V_0} L = \frac{Q}{T_d} \end{aligned} \tag{A.2}$$

being $g = \frac{V_0}{E_0}$ the LAr gap width and $T_d = \frac{g}{v_d}$ the maximum drift time. The current $I^{\text{phys}}(t)$ at time $t \in [0, T_d]$ is then:

$$\begin{aligned} I^{\text{phys}}(t) &= \frac{Q}{L} v_d \frac{E_0}{V_0} \int_0^{L - \frac{v_d t}{\cos\theta}} dl = I_0^{\text{phys}} \frac{1}{L} \int_0^{L - \frac{v_d t}{\cos\theta}} dl \\ &= I_0^{\text{phys}} \frac{1}{L} \left(L - \frac{v_d t}{\cos\theta} \right) = I_0^{\text{phys}} \left(1 - \frac{v_d t}{L \cos\theta} \right) \\ &= I_0^{\text{phys}} \left(1 - \frac{v_d t}{g} \right) \end{aligned} \tag{A.3}$$

where $g = L\cos\theta$ is again the LAr gap width, as a function of the ionization track length L and of the angle θ between the track and the electrode; or, recalling the definition of maximum drift time T_d:

$$I^{\text{phys}}(t) = I_0^{\text{phys}} \left(1 - \frac{t}{T_d} \right) \tag{A.4}$$

Adding the correct Heaviside θ functions the expression (A.4) can be extended to the full time domain:

$$I^{\text{phys}}(t) = I_0^{\text{phys}} \left(1 - \frac{t}{T_d} \right) \theta(t)\ \theta(t - T_d) \tag{A.5}$$

In the frequency (Laplace) domain it reads:

$$I^{\text{phys}}(s) = I_0^{\text{phys}} \left[\frac{1}{s} - \frac{1 - e^{-sT_d}}{s^2 T_d} \right] \tag{A.6}$$

A.2 Calibration signal

The calibration signal is a known current pulse that mimics the ionization signal. It is injected as near as possible to the LAr gap where the ionization signals are generated, and then it is read and reconstructed through the corresponding cell readout chain. In this way the actual gain of the channel can be computed and the cell can be calibrated each time it is needed. Details of the ATLAS EMC calibration strategy are discussed in Section 2.3.5.

The calibration signal should be as similar as possible to the ionization triangular pulse (see Section A.1). An exponential signal with decay time τ_{cali} as been chosen; the decay

constant τ_{cali} has been appropriately trimmed to mimic the EMC ionization signal decay slope:

$$I^{\text{cali}}(t) = I_0^{\text{cali}} e^{-\frac{t}{\tau_{\text{cali}}}} \tag{A.7}$$

In the frequency (Laplace) domain it reads:

$$I^{\text{cali}}(s) = I_0^{\text{cali}} \frac{\tau_{\text{cali}}}{1 + s\tau_{\text{cali}}} \tag{A.8}$$

A.2.1 A more detailed description of the calibration signal

In the ATLAS experimental framework the EMC calibration signals are generated by the *calibration boards* (CB) [27, 28]. The CB exponential pulser is based on a LR circuit: a current step of programmable height flows through the parallel of a resistance R and an inductance L. The values of the R and L components are chosen in order to obtain the proper exponential decay constant $\tau_{\text{cali}} = \frac{2L}{R}$ [3]. The exponential voltage pulse is then converted to current signal by the calibration resistor located on the MB [23].

For the *mock–up* measures and analysis we generate the exponential calibration pulse injecting a voltage step through the series of a resistance R and a capacitance C, thus obtaining an exponential decay constant $\tau_{\text{cali}} = RC$.

Both the CB pulser circuit and in the *mock–up* calibration pulser contains discrete real elements. In both cases the generated pulse is only approximately exponential, because of the non-ideal nature of the components. A more detailed description is needed, especially in the case on CB LR pulser.

Calibration board pulser

The non-ideal inductance L of the CB pulser circuit has a resistive component r that alters the exponential waveform baseline. According to the simplified scheme in Figure A.2, in the frequency domain the output pulse is:

$$I^{\text{cali}}(s) = I_0^{\text{cali}} \left[\frac{\left(\frac{r}{r+\frac{R}{2}}\right) + s\left(\frac{L}{r+\frac{R}{2}}\right)}{s\left(1 + s\left(\frac{L}{r+\frac{R}{2}}\right)\right)} \right] \tag{A.9}$$

$$= I_0^{\text{cali}} \left[\frac{f_{\text{step}} + s\tau_{\text{cali}}}{s(1 + s\tau_{\text{cali}})} \right] \tag{A.10}$$

$$= I_0^{\text{cali}} \left[\frac{(1 - f_{\text{step}})\,\tau_{\text{cali}}}{1 + s\tau_{\text{cali}}} + \frac{f_{\text{step}}}{s} \right] \tag{A.11}$$

where:

$$\begin{cases} f_{\text{step}} = \left(\frac{r}{r+\frac{R}{2}}\right) & \text{is the fraction of the total resistance } (r + \frac{R}{2}) \\ & \text{represented by the resistive component } r \text{ of} \\ & \text{the non-ideal inductance } L \ (f_{\text{step}} \in [0,1]); \\ \tau_{\text{cali}} = \left(\frac{L}{r+\frac{R}{2}}\right) & \text{is the effective exponential decay constant.} \end{cases} \tag{A.12}$$

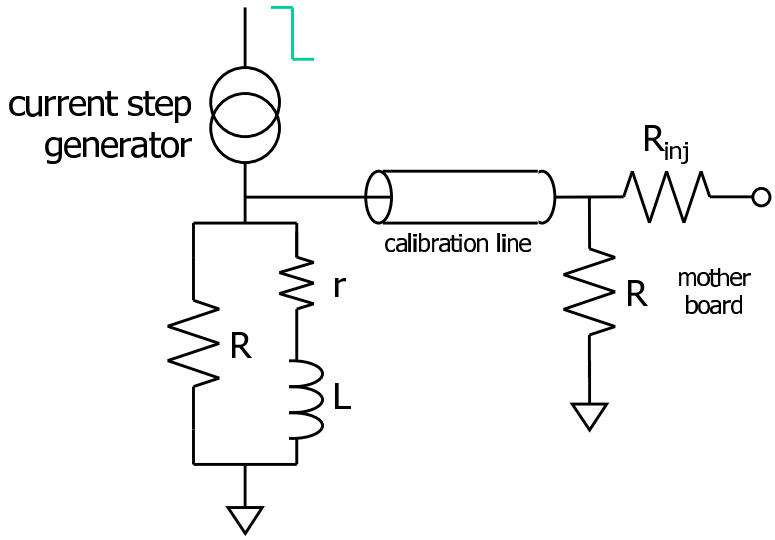

Figure A.2: Simplified calibration board pulser circuit, showing the non-ideal nature of the inductance L in its resistive component r.

In the time domain eq. A.11 becomes:

$$I^{\text{cali}}(t) = I_0^{\text{cali}} \left[(1 - f_{\text{step}})\, e^{-\frac{t}{\tau_{\text{cali}}}} + f_{\text{step}} \right] \tag{A.13}$$

The effective calibration pulse is an exponential waveform that does not go asymptotically to 0, but converges to a non-null baseline. The relative height of this residual baseline is determined by the resistive component r of the non-ideal inductance L of the CB pulser circuit. The nominal value of the resistance on the CB is $R = 50\ \Omega$ [27]. A $r \sim 2\ \Omega$ resistive component of the non-ideal inductance L can be expected [38], leading to a baseline fraction $f_{\text{step}} \sim 7\%$.

The effective expression (A.13) is used in all the computations and analysis proposed in Chapter 5.

Mock–up calibration pulser

All the *mock–up* calibration different pulsers are based on a RC circuit: a voltage step is injected through the serie of a capacitance C and a resistance R: in one case this R element is a real resistive component, in an other it describes the effective behavior of the sum $r_{\text{int}} + Z$ of the step voltage generator internal resistance and of the calibration cables chain effective impedance (see Section 3.3.2 5.4 for details).

The capacitive component C can indeed exhibit a non-ideal behavior, eventually showing a (usually very high) resistive component r in parallel (Figure A.3). In this case the output pulse is:

$$I^{\text{cali}}(s) = I_0^{\text{cali}} \left[\frac{\left(\frac{R}{r+R}\right) + s\left(\frac{rR}{r+R}\right) C}{s\left(1 + s\left(\frac{rR}{r+R}\right) C\right)} \right] \tag{A.14}$$

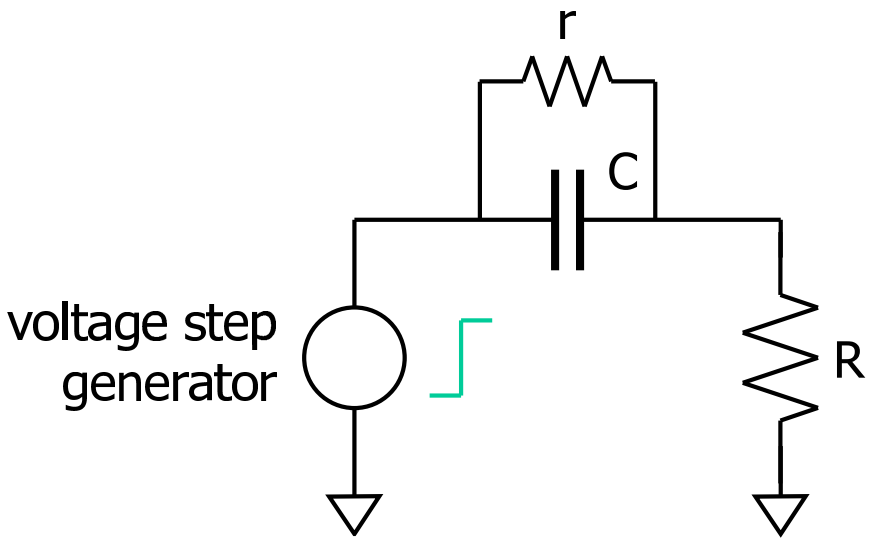

Figure A.3: Example of a *mock–up* calibration pulser circuit, showing the non-ideal nature of the capacitance C in its resistive component r.

that can again be reconducted to the effective expression (A.10) by the definitions:

$$\begin{cases} f_{\text{step}} &= \left(\frac{R}{r+R}\right) &\lesssim 0.1\% \\ \tau_{\text{cali}} &= \left(\frac{rR}{r+R}\right) C &\sim RC \end{cases} \tag{A.15}$$

being indeed $r \gg R$ ($r \sim M\Omega$, $R \simeq 100\ \Omega$) (see Section 5.4).

Appendix B

Optimal filtering

The *optimal filtering* (OF) is a technique used to estimate the *peak amplitude* and the *starting time* of a multiply–sampled signal while *minimizing the noise contributions*. The method as been first proposed in [30] as a reconstruction technique for signals emerging from liquid ionization calorimeters in high rate environments. The need of such a signal reconstruction method in the ATLAS experimental framework is discussed in Section B.1.

The OF reconstructs the signal peak amplitude S and the signal starting time τ as the weighted sums of a set of n signal samples s_i:

$$\left\{ \begin{array}{rcl} S & = & \sum_{k=1,n}^{n} a_k s_k \\ S\tau & = & \sum_{k=1,n}^{n} b_k s_k \end{array} \right. \tag{B.1}$$

Being $g(t)$ the normalized shape of the signal, and $g'(t)$ its first derivative, the coefficients set $\{a_k\}$ ($\{b_k\}$) is obtained as the result of the minimization of the variance of S ($S\tau$), with the constrains that the normalized signal shape peak must be unitary ($\sum_{k=1}^{N} a_k g_k = 1$) and that there must not be a residual time dependence ($\sum_{k=1}^{N} a_k g'_k = 0$). The minimization procedure ensures the required noise suppression; the computation is performed using a standard Lagrange–multiplier technique (Section B.2).

As a particular case in the digital filtering theory, the OF technique provides an additional shaping of the signal: the corresponding transfer function is computed in Section B.3.

B.1 About the need of additional filtering

The signals emerging from the ATLAS EMC suffer of two noise contributions: the electronics noise, that is related to the readout electronics chain characteristics, and the "pile–up" noise, due to the minimum–bias events in the detector, whose intensity depends on the luminosity of the collider. The EMC readout electronic chain has been optimized minimizing the quadratic sum of the two noise contributions, in order to obtain the best performances at the LHC high luminosity conditions ($\mathcal{L} \simeq 10^{34}$ cm^{-2}s^{-1}) [3]. The pile–up noise contribution [36, 37] increases as $\sqrt{\tau_{\rm sh}}$, while the electronics noise contribution decreases as $\tau_{\rm sh}^{-\frac{3}{2}}$ (Figure B.1), at least in case of fast–shaping, when the electronics parallel

noise that scales as $\tau_{\rm sh}^{-\frac{1}{2}}$ an can be omitted. It has been shown ([3], [35]) that at high luminosity the pile–up contribution will be $\sqrt{3}$ times greater that the electronics one. The shaper optimal time constant has then been chosen $\tau_{\rm sh} = 15$ ns over the full EMC rapidity coverage[1] [31].

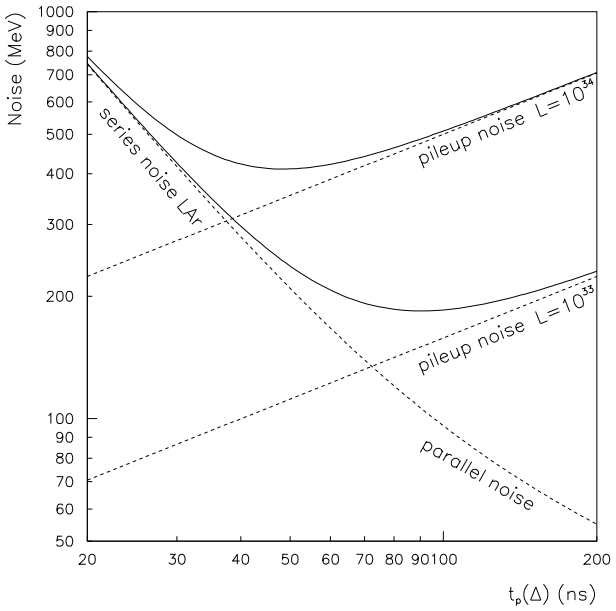

Figure B.1: Optimization of the shaping time for LHC high and low luminosity running conditions. The amount of noise is plotted versus the peaking time of the shaper response to a delta function $t_p(\Delta)$.

In the first years of running the LHC will operate at low luminosity ($\mathcal{L} \simeq 10^{33}$ cm^{-2}s^{-1}); the same optimization would lead to a greater $\tau_{\rm sh}$ (the optimal shaper time constant scales as $\mathcal{L}^{-\frac{1}{4}}$), but the readout hardware has been designed to use an unique $\tau_{\rm sh}$. There is then the need of a software method, to be implemented at the signal reconstruction level, that adds an additional filtering stage to the signals collected at low luminosity.

B.2 Coefficients computation

Let the multiply sampled signal waveform be

$$f(t) = Ag(t - \tau) + n(t) \tag{B.2}$$

where A is the signal amplitude, $g(t)$ the signal shape, and τ the delay at which the signal starts with respect to the sampling trigger time. The function $n(t)$ represents the sum

[1] A shaper time constant $\tau_{\rm sh} = 15$ ns corresponds to a peaking time of the shaper response to a delta function $t_p(\Delta) = 45$ ns.

of the noise contributions that superimpose to the signal during the data acquisition. A small τ approximation leads to:

$$f(t) \simeq A[g(t) - \tau g'(t)] + n(t) \tag{B.3}$$

where $g'(t)$ is the first derivative of the signal shape $g(t)$. The sampled points of the signals at time t_k are then:

$$s_k = A(g_k - \tau g'_k) + n_k \tag{B.4}$$

where the k label indicates the value of the various functions taken at t_k.

The noise is supposed to be a zero–mean function[2], and its *autocorrelation function* to be known or measurable[3]:

$$\langle n(t) \rangle = 0 \qquad \langle n_i n_j \rangle = R_{ij} \tag{B.5}$$

The noise at the shaper output is indeed correlated in time by the shaping function.

As we mentioned before, peak and timing values are computed as linear combinations of the n samplings[4] $\{s_1, \ldots, s_n\}$. Coefficients are chosen for the expressions:

$$U = \sum_{k=1}^{n} a_k s_k \qquad V = \sum_{k=1}^{n} b_k s_k \tag{B.6}$$

such to minimize σ_U and σ_V with the constraints:

$$\langle U \rangle = A \quad \Rightarrow \quad \sum_{k=1}^{N} a_k g_k = 1, \quad \sum_{k=1}^{N} a_k g'_k = 0 \tag{B.7}$$

$$\langle V \rangle = A\tau \quad \Rightarrow \quad \sum_{k=1}^{N} b_k g_k = 0, \quad \sum_{k=1}^{N} b_k g'_k = -1 \tag{B.8}$$

Solving using the expressions (B.4) and (B.5) leads to:

$$\sigma_U^2 = \mathrm{var}[U] = \sum_{ij} a_i a_j R_{ij} \tag{B.9}$$

$$\sigma_V^2 = \mathrm{var}[V] = \sum_{ij} b_i b_j R_{ij} \tag{B.10}$$

[2]This assumption is true for the electronics contribution, and it is assured for the pile–up noise by the shaped signal area being null.

[3]In the ATLAS EMC case, special *pedestal* runs are taken to measure the noise autocorrelation function for each cell.

[4]In the ATLAS EMC case, $n = 5$.

The system can be solved using the Lagrange multipliers technique. Two sets of equations are obtained, one for the *peak amplitude* coefficients:

$$0 = \frac{\partial}{\partial a_k}\left[\frac{1}{2}\sum_{ij} a_i a_j R_{ij} - \lambda\sum_i a_i g_i - \mu\sum_i a_i g'_i\right] \tag{B.11}$$

$$= \sum_i a_k R_{ik} - \left(\lambda g_k + \mu g'_k\right) \tag{B.12}$$

$$a_i = \lambda\sum_k R^{-1}_{ik} g_k + \mu\sum_k R^{-1}_{ik} g'_k \tag{B.13}$$

$$\begin{cases} \lambda = \frac{Q_2}{\Delta} \\ \mu = -\frac{Q_3}{\Delta} \end{cases} \tag{B.14}$$

and one for the *timing information*:

$$0 = \frac{\partial}{\partial b_k}\left[\frac{1}{2}\sum_{ij} b_i b_j R_{ij} - \rho\sum_i b_i g_i - \sigma\sum_i b_i g'_i\right] \tag{B.15}$$

$$= \sum_i b_k R_{ik} - \left(\rho g_k + \sigma g'_k\right) \tag{B.16}$$

$$b_i = \rho\sum_k R^{-1}_{ik} g_k + \sigma\sum_k R^{-1}_{ik} g'_k \tag{B.17}$$

$$\begin{cases} \rho = \frac{Q_3}{\Delta} \\ \sigma = -\frac{Q_1}{\Delta} \end{cases} \tag{B.18}$$

where for equations (B.14) and (B.18) the following relations hold

$$\begin{cases} Q_1 = \sum_{ij} g_i g_j R^{-1}_{ij} \\ Q_2 = \sum_{ij} g'_i g'_j R^{-1}_{ij} \\ Q_3 = \sum_{ij} g_i g'_j R^{-1}_{ij} \\ \Delta = Q_1 Q_2 - Q_3^2 \end{cases} \tag{B.19}$$

To compute the coefficients a_k and b_k the normalized signal waveform $g(t)$, its first derivative $g'(t)$ and the noise autocorrelation matrix $R_{ij} = \langle n_i n_j \rangle$ are needed. The results U and V are *unbiased estimators with optimized uncertainty*:

$$\langle U \rangle = A \quad \langle V \rangle = A\tau \tag{B.20}$$

The coefficients might have a residual dependence on timing τ, introduced in the calculation by the first order approximation in eq. (B.3). In order to get rid of this dependence, coefficients for any τ value are needed to be known. It is then possible to evaluate A and $A\tau$ assuming coefficients for $\tau = 0$, estimate a new τ value, use appropriate coefficients and re–iterate to convergence.

B.3 Transfer function of the OF

According to the digital filtering (DF) theory, computing the peak of a signal as the weighted sum of its samples corresponds to additionally shape the signal with a virtual filter. This virtual filter is usually known as Finite Impulse Response (FIR) filter; its transfer response can be computed using the Z–transform technique.

Let the signal $f(t)$ be sampled at a period T_{samp}, such as the samples of signals are $f_k = f(kT_{\text{samp}})$. The Z–transform $F(Z)$ of $f(t)$ is defined as:

$$F(Z) = \sum_{k=-\infty}^{k=+\infty} f_k Z^{-k} \tag{B.21}$$

The digital filter output y_k is the weighted sum of n samples of the signal f:

$$y_k = \sum_{i=1}^{n} a_i f_{k+i-n} \tag{B.22}$$

The Z–transform of y is:

$$Y(Z) = \sum_{k=-\infty}^{k=+\infty} \sum_{i=1}^{n} a_i f_{k+i-n} Z^{-k} \tag{B.23}$$

By inverting the order of the sums and letting $l = k + i - n$ we obtain:

$$Y(Z) = \sum_{i=1}^{n} a_i Z^{-i-n} \sum_{l=-\infty}^{l=+\infty} f_l Z^{-l} \tag{B.24}$$

$$= \sum_{i=1}^{n} a_i Z^{-i-n} F(Z) \tag{B.25}$$

from which we can isolate the transfer function of the n–samples digital filter:

$$H_{\text{DF}}^{n} = \sum_{i=1}^{n} a_i Z^{-i-n} \tag{B.26}$$

It can be expressed in the frequency domain by the substitution $Z = e^{j\omega T_{\text{samp}}}$. The factor $e^{j\omega T_{\text{samp}}}$ represents a delay T_{samp} in the time domain:

$$H_{\text{DF}}^{n} = \sum_{i=1}^{n} a_i e^{(-i-n)\times(j\omega T_{\text{samp}})} \tag{B.27}$$

Replacing in expression (B.27) the solution (B.13) for the OF coefficients $\{a_k\}$ gives the actual OF transfer function.

It has been shown [31] that at the LHC low luminosity conditions the OF acts as a *low–pass* filter with a cut–off frequency $f_c = 4$ MHz, resulting in a slower output signal. At high luminosity it is a *pass–band* filter, centered around 10 MHz. In each case, the frequency response of the OF has bumps every 40 MHz, corresponding as in every sampling process to the aliasing of the signal spectrum at multiples of the sampling frequency.

Bibliography

Technical Design Reports

[1] *The Large Hadron Collider*. Technical Report CERN/AC/95-05, CERN, 1995.

[2] The ATLAS collaboration. *Technical Proposal for a General–Purpose pp Experiment at the Large Hadron Collider at CERN*. Technical Report CERN/LHCC/94-43, CERN, 1994.

[3] The ATLAS collaboration. *Liquid Argon Calorimeter Technical Design Report*. Technical Report CERN/LHCC/96-41, CERN, 1996.

[4] The ATLAS collaboration. *Calorimeter Performance Technical Design Report*. Technical Report CERN/LHCC/96-40, CERN, 1996.

[5] The ATLAS collaboration. *Detector and Physics performances Technical Design Report* . Technical Report CERN/LHCC/99-14 and 99-15, CERN, 1999.

[6] The ATLAS collaboration. *Inner Detector Technical Design Report*. Technical Report CERN/LHCC/97-16 and 97-17, CERN, 1997.

[7] The ATLAS collaboration. *Pixel Detector Technical Design Report*. Technical Report CERN/LHCC/98-13, CERN, 1998.

[8] The ATLAS collaboration. *Tile Calorimeter Technical Design Report*. Technical Report CERN/LHCC/96-42, CERN, 1996.

[9] The ATLAS collaboration. *Muon Spectrometer Technical Design Report*. Technical Report CERN/LHCC/97-22, CERN, 1997.

[10] The ATLAS collaboration. *Magnet System Technical Design Report*. Technical Report CERN/LHCC/97-18, CERN, 1997.

[11] The ATLAS collaboration. *First Level Trigger Technical Design Report*. Technical Report CERN/LHCC/98-14, CERN, 1997.

[12] The ATLAS collaboration. *High–Level Triggers, DAQ and DCS Technical Design Report*. Technical Report CERN/LHCC/2000-17, CERN, 2000.

LHC Physics

[13] N.V. Krasnikov, V.A. Matveev. *Search for standard Higgs boson at supercolliders. Phys. Part. Nucl.*, 31, 2000.

[14] G. Altarelli. *The Standard Model and Beyond. Nucl. Phys. B, Proc. Suppl.*, 75A, 1999.

[15] J. Ellis. *Decline and fall of the Standard Model? Int. J. Mod. Phys.*, A 17, 2002.

[16] J. Ellis. *Beyond the Standard Model for hillwalkers.* In *1998 European School on High-Energy Physics.*, (CERN-99-04) CERN, Geneva, 1999.

[17] F. Gianotti. *Precision physics at LHC. ATLAS Internal Note*, ATL-PHYS-99-001, 1999.

[18] V. Tisserand. *The Higgs into two photons decay in the ATLAS detector. ATLAS Internal Note*, ATL-PHYS-96-090, 1996.

[19] O. Linossier and L. Poggioli. *$H \rightarrow ZZ^{\star} \rightarrow 4l$ channel in ATLAS. Signal reconstruction and reducible background rejection. ATLAS Internal Note*, ATL-PHYS-97-101, 1997.

[20] A. Amorin, L. Poggioli, A. Maio. *Calibrating the electromagnetic calorimeter using $Z^0 \rightarrow e^+e^-$. ATLAS Internal Note*, ATL-PHYS-93-015, 1993.

[21] L. Carminati. *Photon energy calibration in Athena.* Talk presented at the ATLAS Sotware Workshop, Combined Performance Group, London, September 19$^{\text{th}}$, 2002. `http://documents.cern.ch/AGE/current/fullAgenda.php?ida=a02249#s11`.

LAr electromagnetic calorimeter

[22] B. Aubert et al. (RD3 coll.). *Performance of a liquid Argon electromagnetic calorimeter with an "accordion" geometry. NIM A*, 309, 1991.

[23] The USA ATLAS collaboration. *The Mother Board system for the Liquid Argon barrel calorimeter.* `http://www.usatlas.bnl.gov/detector/lar/mb/`.

[24] J. Ban, S. Negroni, J. Parsons, S. Simion, B. Sippach. *Design and Implementation of the ATLAS LAr Front End Board.*
`http://www.nevis.columbia.edu/~atlas/electronics/ATLASFEB/`.

[25] G. Battistoni et al. *Specification Requirements for Warm Preamplifiers.*
`http://www.mi.infn.it/~battist/preampl2.html`.

[26] R. L. Chase, C. de la Taille, J. P. Richer, N. Seguin-Moreau. *A fast monolithic shaper for the ATLAS e.m. calorimeter.* In *Proc. 5th International Conference on Calorimetry in High-energy Physics*, 1994.

[27] J. Colas et al. *The LAr calorimeter calibration board. ATLAS Internal Note*, ATL-LARG-2000-006, 2000.

[28] E. Marschalkowski, V. Gýartner, K. Jakobs, U. Schýafer. *Design and performance of an integrated pulse generator for the LARG calibration system. ATLAS Internal Note*, ATL-LARG-99-013, 1999.

Signal analysis and reconstruction

[29] W. Willis and V. Radeka. *Liquid Argon ionization chamber as a total absorption detector. NIM A*, 120, 1974.

[30] W.E. Cleland and E.G. Stern. *Signal processing considerations for liquid ionization calorimeter in a high rate environment. NIM A*, 338, 1984.

[31] Y. Jaquier, C. de La Taille, I. Nikolic, L. Serin. *Strenghs and weakness of digital filtering. ATLAS Internal Note*, ATL-LARG-97-080, 1997.

[32] L. Neukermans, P.Perrodo and R. Zitoun. *Understanding the electromagnetic barrel pulse shapes and the absolute electronic calibration. ATLAS Internal Note*, 2001.

[33] F. Lanni et al. *Waveform analysis and parameter extraction with the BNL mock–up.* Talk presented at the 1st ATLAS LAr Signal Reconstruction Workshop, CERN, July 7th, 2001.

[34] W.E. Cleland. *Determination of transformation parameters from calibration waveforms.* Talk presented at the 1st ATLAS LAr Signal Reconstruction Workshop, CERN, July 7th, 2001.

[35] S. Tisserand. PhD thesis, LAL-97-01, 1997.

[36] L. Serin and V. Tisserand. *Study of the pile–up in the ATLAS electromagnetic calorimeter. ATLAS Internal Note*, ATL-LARG-95-075, 1995.

[37] R. A. Davis and P. Savard. *A study of the pile–up noise in the barrel and end–cap calorimetry. ATLAS Internal Note*, ATL-LARG-96-084, 1996.

[38] C. De La Taille. *ATLAS LAr electronics chain.* Talk presented at the 1st ATLAS LAr Signal Reconstruction Workshop, CERN, July 7th, 2001.

[39] I. Wingerter Seez, L. Serin et al. *EMB Modules LC measurements.* Private communication.

[40] C. Le Maner. *EMB P15 module LC values from the OF4 computation procedure.* Private communication.

[41] D. Banfi and M. Fanti. *EMB P15 32–samples delay runs analysis using a FFT algorithm.* Private communication.

[42] H. Przysiezniak. *Cross–talk correction using the Optimal Filtering coefficients.* Talk presented at the LAr EMTB Meeting, CERN, April 16$^{\text{th}}$, 2002.

EMB test–beam

[43] A. Jeremie, N. Massol, P. Perrodo, G. Sauvage. *Channels of the may EMB2000 prototype module.* `http://wwwlapp.in2p3.fr/~perrodo/atlas.html`.

[44] I. Efthymiopoulos and K. Elsener. *H8 Electron beam quality improvement during 2001. SPS/LHC Internal Note*, SL-Note-2002-018 EA, 2002.

[45] M. Abouelouafa, M. Gouanère, P. Perrodo. *Trigger setup in the H8 and H6 test-beam area. EDMS Note*, ATC-TT-EN-0001 (Id. 324406), 2001.

[46] J. Spangaard. *Delay Wire CHambers. A User Guide. SPS/LHC Internal Note*, SL-Note-1998-023 BI, 1998.

[47] P. Puzo et al. *ATLAS EMC test–beam line instrumentations.* `http://atlas.web.cern.ch/Atlas/GROUPS/LIQARGON/EM_Calo/TestBeam/Docs/Beam`.

[48] M. Caprini at al. *The Data Acquisition System of the ATLAS combined test–beam April 1996. ATLAS Internal Note*, ATL-DAQ-96-058, 1996.

[49] F. Chollet, J. Colas, H. Kambara. *MRA - The miniROD data acquisition program on RIO8062. EDMS Note*, ATC-TT-EN-0004 (Id. 324919), 2001.

[50] P. Perrodo. *Software for the ATLAS LAr electromagnetic test–beam setups H6 and H8. EDMS Note*, ATC-TT-EN-0002 (Id. 324407), 2001.

[51] M. Fanti. *2000 EMB "Module 0" test–beam data analysis results.* Private communication.

[52] D. Nicol, D. Zerwas, R. Zitoun (et al.). *EMTB User Guide, Version 1.9.* `http://atlasinfo.cern.ch/Atlas/GROUPS/LIQARGON/EM_Calo/TestBeam/Testbeam/doc/new_emtb.html`.

[53] L. Di Ciaccio, L. Neukermans, P.Perrodo, R. Zitoun. *Uniformity of the 2000 test-beam data with the new optimal filtering coefficients. ATLAS Internal Note*, ATL-LARG-2001-009, 2001.

[54] P. Perrodo. *Material between the presampler and the EMB Module 0. ATLAS Internal Note*, ATL-LARG-2001-002, 2001.

[55] G. Parrour. *Estimate of the amount of material in the EMB calorimeter in term of radiation leghts X_0 using GEANT.* Private communication.

[56] A. Artamonov, A. Dell'Acqua. D. Froidevaux, M. Nessi, P. Nevski, G. Poulard. *DICE–95. ATLAS Internal Note*, ATL-SOFT-95-014, 1995.

[57] *GEANT. Detector description and simulation tool.* CERN Program Library Long Write-up W5013 (CERN, Geneva, 1994).

[58] C. Fabjan. In T. Ferbel, editor, *Experimental technique in high energy physics.* Addison–Wesley, 1987.

[59] D. E. Groom and S. R. Klein. *Passage of particles through matter.* In *Particle Physics booklet.* Springer, 2000.

[60] B. Mansouille. *Non–uniformity of lead plates and gaps: analytical estimates of the shower averaging effect. ATLAS Internal Note*, ATL-LARG-98-099, 1998.

Manuals and reference books

[61] SPICE general-purpose circuit simulation program. *SPICE3F User's Manual.* `http://bwrc.eecs.berkeley.edu/Classes/IcBook/SPICE/`.

[62] F. James. *MINUIT. Function Minimization and Error Analysis. Reference Manual, Version 94.1.* CERN Program Library Long Write-up D506. (CERN, Geneva, 1994).

[63] W. Press, B. Flannery, S. Teukolsky, W. Vetterling, William T. *Numerical Recipes: the art of scientific computing.* Cambridge Univ. Press, 1998.

[64] P. C. Magnusson. *Transmission lines and wave propagation.* Lewis Publisher, 2000.

[65] M.R. Spiegel. *Laplace Transforms.* Schaum, 1965.

[66] H. Crame. *Mathematical Methods of Statistics.* Princeton, 1966.

Errata Corrige and Addendum

Chapter 2

page 15, Table 2.1

At line 5 read "radiation lenght" insted of "radiation lento".

page 16, line 13

Instead of "radiation Lent" read "radiation lenght'.

Chapter 3

page 40, line 12

After "then take a C_s value at a given ω" add "e.g. in correspondence to the C_s minimum before the resonance (see Figure 3.10)".

page 53, Figure 3.20

There are some small differences between the C values measured with one and two ground springs. In principle a constant value of C would be expected, but since the L and C parameters are strongly correlated, the two setup measurements produce slightly different C values. This difference is anyway compatible with the $\delta C = 15$ pF precision quoted at page 44.

page 49, line -4

Instead of "The calibration waveform (right) differs from the physics waveform (left)" read "The calibration waveform (red) differs from the physics waveform (black)".

Chapter 4

page 70, line 4

Instead of "The 25 ns sampling period is too long to allow..." read "The 25 ns sampling points spacing is too large with respect to the signal properties to allow...".

page 72, Figure 4.3

The axis labels are (s) instead of (ns); the number on the axises scales are to be multiplied by 10^7 (the factor is partially covered by the axis label). The black line in the top plot represents the case in which the parabola peak time is equal to the true peak time.

page 74, Figure 4.6

The correct plots are:

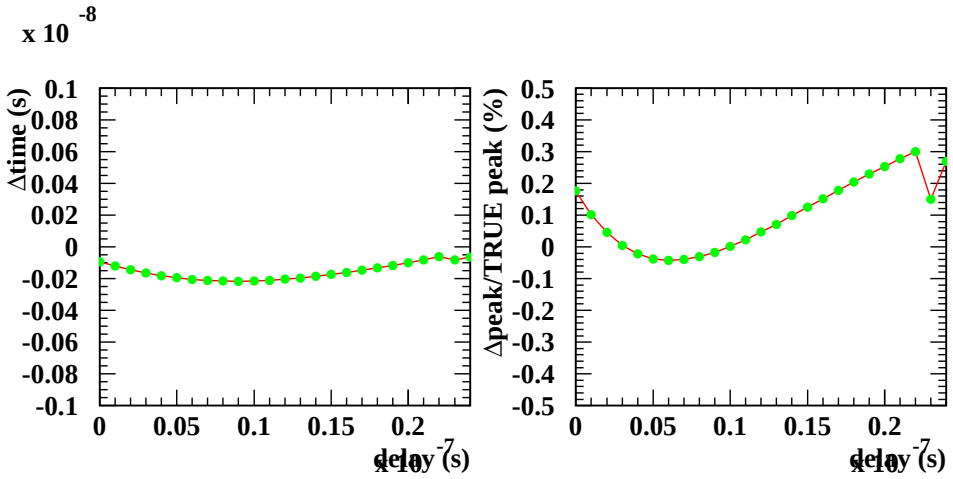

page 75, line 5

Instead of "up to ∼700 ps in..." read "up to ∼200 ps in...".

page 75, line 8

Instead of "up to ∼700 ps is again found" read "up to ∼700 ps is found".

page 75, line 9

Instead of "(Figure 4.7)" read " (Figure 4.5 and 4.7)".

page 76, Figure 4.8

All the symbols labels in the three plot are inverted: open and solid black symbol correspond to 2 ground returns connected, open and solid red symbol correspond to 1 ground returns connected.

page 78, Table 4.1

The uniformity values for the two different ground configuration are inverted. The table should read:

uniformity (%)	non–corrected	with LC correction
1 ground	0.60	0.15
2 ground	0.36	0.14

page 82, Figure 4.12

The absence of red symbols (OF4 SR serie) for $\eta_{\text{cell}} \geq 44$ is related to the difficulty in reconstructing and fitting the mean ionization signal shape in that region of the detector.

Chapter 5

page 87, equation 5.8:

the ionization-to-calibration signal shape difference correction function is:

$$g^{\text{exp} \rightarrow \text{tri}}(t) = \delta(t) + \left[\frac{1 - f_{\text{step}}}{\tau_{\text{cali}}} e^{-f_{\text{step}} \frac{t}{\tau_{\text{cali}}}} - \frac{1 - f_{\text{step}}}{f_{\text{step}} T_d} \left(e^{-f_{\text{step}} \frac{t}{\tau_{\text{cali}}}} - 1 \right) \right] \theta(t) + \frac{1 - f_{\text{step}}}{f_{\text{step}} T_d} \left(e^{-f_{\text{step}} \frac{t - T_d}{\tau_{\text{cali}}}} - 1 \right) \theta(t - T_d)$$